HELLENIC REPUBLIC

National and Kapodistrian University of Athens

Faculty of Geology and Geoenvironment

Dynamic Tectonic and Applied Geology

Tectonometamorphic evolution and exhumation of the metamorphic rocks of Amorgos Island

A study on the architecture and evolution of the Late Eocene-Oligocene Hellenic subduction zone

by

Sofia Laskari, MSc Geologist

Dissertation

Presented to the Faculty of Geology and Geoenvironment

National and Kapodistrian University of Athens, Greece

for the degree of

Doctor of Philosophy

Athens
2022

Approved by

Supervising committee:

Supervisor: _____
Assistant Prof. Konstantinos Soukis

Co- Supervisors: _____
Prof. Daniel F. Stockli

_____
Associate Prof. Stylianos Lozios

Examining committee: _____
Prof. Paris Xypolias

_____
Prof. Maria Triantaphyllou

_____
Associate Prof. Haralambos Kranis

_____
Assistant Prof. Emmanuel Skourtsos

Acknowledgments

I would like to express my great appreciation to the members of the research supervising committee, my supervisor Konstantinos Soukis, and co-supervisors Daniel Stockli and Stylianos Lozios for their priceless knowledge, and guidance, contributions and helpful discussions during my research work. In addition, I am most grateful to Daniel Stockli for his efficient supervision during sample preparation and the dating of the zircons in this dissertation.

I would also like to extend my thanks to Lisa Stockli, Zach Foster-Baril, Rudra Chatterjee, Daniel Arnost and Eirini-Maria Poulaki for training and invaluable assistance at the UTChron laboratory during my staying at Austin, Texas.

My special thanks to my friends for their encouragement throughout my years of study.

Finally, I would like to thank my family for all their love and support during my research.

Tectonometamorphic evolution and exhumation of the metamorphic rocks of Amorgos Island

Sofia Laskari, Ph.D.

National and Kapodistrian University of Athens, 2022

Abstract

The Hellenides constitute an integral part of the Alpine mountain chain in the eastern Mediterranean. They were shaped during the Cretaceous to Tertiary Africa-Eurasia convergence-collision and subsequent overprinting by extensional tectonics forming the Aegean domain. Exhumed HP rocks have been affected by extensional processes, concealing their syn-orogenic history that is essential for understanding the regional configuration of the Attic-Cycladic during the subduction-related stage.

This dissertation concentrates on the southeastern Cyclades of the Aegean domain. Field-based observations and structural measurements combined with novel lab techniques are used to investigate the deformation and exhumation of the low-grade HP rocks of Amorgos Island. The new findings are further compared to the neighboring Iraklia island to understand better the exhumation mechanisms and the different tectonometamorphic records of the exhumed subduction-type rocks.

In Chapter II, a new lithostratigraphic configuration for the Amorgos Unit is presented, and a new paleogeographic position is proposed. Based on along-strike variations in the sedimentary facies, the Amorgos Unit is subdivided into three stratigraphic columns representative of the island's northeast, central and southwest parts, respectively. Furthermore, the structural evolution is briefly discussed, and a retro-wedge setting is proposed for the top-NW kinematics of the early syn-HP deformation. The detrital zircon U-Pb geochronology and zircon (U-Th)/He dating results are described in detail, providing fundamental knowledge for the provenance signatures and the timing of exhumation processes. Our results show that the

Amorgos Unit was paleogeographically located at the southern Pelagonian margin and structurally above the CBU.

In Chapter III, we present new structural data and integrate our results with those of Chapter II. A multi-stage deformation is described as evolving from a consistent syn-orogenic compressional phase during the Late Eocene-Oligocene to a post-orogenic extensional phase in the early-mid Miocene. An alternative tectonic model for the Amorgos structural evolution is proposed that includes a short-lived SE-directed subduction zone that was eventually developed at the retrowedge side of the late Eocene-Oligocene subduction zone. Based on our results, a composite double-verging orogen is proposed for the Late Eocene-Oligocene collisional phase. Detachment faulting has affected the Amorgos Unit by top-SE kinematics during the Early-mid Miocene extensional phase, associated with the Santorini Detachment System.

Chapter IV presents a structural analysis of the Iraklia Island CBU rocks combined with detrital zircon U-Pb geochronology. Based on the provenance signatures of the schists, the stratigraphy of Iraklia is reviewed and the record of distinct geodynamic environments is discussed. The structural evolution of Iraklia revealed the retrogression/decompression stage during exhumation. An intra-CBU shear zone with top- N kinematics is recorded associated with the Paros-Naxos Detachment System. Relics of the prograde path is preserved as blue amphibole inclusions in feldspars. Zircon rim U-Pb ages indicate an early Eocene subduction-related HP event, typical for the CBU rocks documented in the neighboring islands.

Table of Contents

Acknowledgments **2**
Abstract **3**
Chapter I: Introduction **6**
1. Motivation 6
2. Techniques 11
   2.1. Detrital Zircon U-Pb Geochronology 11
   2.2. (U-Th)/He low-T thermochronometry 13
3. Hellenides 14
   3.1. The Geology of the Hellenides 14
   3.2. Tectonic Evolution of the Aegean domain 19
   3.3. The Attic-Cycladic Crystalline Core Complex 23

Chapter II: Reconstructing the southern Pelagonian domain in the Aegean Sea: Insights from U-Pb detrital zircon analysis, lithostratigraphic and structural study, and zircon (U-Th)/He thermochronology on Amorgos Island (SE Cyclades, Greece) **26**
1. Introduction 27
2. Geological Setting 29
3. Lithostratigraphy of Amorgos Island 33
   3.1. Northeastern Amorgos 33
   3.2. Central/Southwestern Amorgos 34
4. Structures 36
   4.1. Progressive compressional deformation stage $Dn_{a\text{-}b}\text{-}D_{n+1}$ 36
   4.2. Extensional deformation phase $Dn_{+2/3}$ 41
5. Detrital zircon U-Pb geochronology and results 43
   5.1. Methodology 43
   5.2. Results 44
      5.2.1. Metaflysch 44
      5.2.2. Kapsala Formation 46
6. (U-Th)/He zircon dating 47
   6.1. Methodology 47
   6.2. Results 48
7. Discussion 48
   7.1. Lithostratigraphy of the Amorgos Unit 48
   7.2. Provenance of detrital zircons 52
      7.2.1. Kapsala Formation 53
      7.2.2. Metaflysch 56
   7.3. Structural evolution of the Amorgos Unit 56
   7.4. Regional correlations 58
   7.5. Permo-Triassic to Miocene paleogeographic evolution of Amorgos Unit 61
      7.5.1. Late Permian 61
      7.5.2. Early-Mid Triassic 62
      7.5.3. Mid-Late Triassic 62
      7.5.4. Late Triassic-Early Cretaceous 64
      7.5.5. Late Cretaceous 64

7.5.6. Early-Mid Eocene 65
7.5.7. Late Eocene-Oligocene 65
7.5.8. Early-Late Miocene 66
8. Conclusions 67
Chapter III: A composite Late Eocene-Oligocene double-vergent orogen in the Aegean domain: Insights from the retro-ward internal duplicated structure of the low-grade HP Amorgos Unit (SE Cyclades, Greece) 68
1. Introduction 68
2. Geological setting 70
2.1. Geology of Amorgos Island 73
3. Structural Evolution of the Amorgos Unit 76
3.1. Dn_a structures 76
3.2. Dn_b structures 78
3.3. Dn_{+1} structures 82
3.4. Dn_{+2} structures 84
3.5. Dn_{+3} structures 86
3.6. Dn_{+4} structures 86
4. Discussion 87
4.1. Structural evolution of the Amorgos Unit 87
4.2. Alternative scenarios for the Amorgos Unit and Regional Implications 91
5. Conclusions 95
Chapter IV: Structural study and Detrital Zircon Provenance Analysis of the Cycladic Blueschist Unit Rocks from Iraklia Island: From the Paleozoic Basement Unroofing to the Cenozoic Exhumation 97
1. Introduction 98
2. Geological Setting 100
3. A New Geological Map of Iraklia 104
3.1. Lithostratigraphic Subdivision 104
3.2. Structures 106
3.2.1. D1 Syn-Blueschist Facies Structures 106
3.2.2. D2 Ductile to Brittle Deformation 107
3.2.3. D3 Late Brittle Deformation 109
4. Detrital Zircon U-Pb Geochronology 109
4.1. Methodology 109
4.2. U-Pb Results 110
5. Discussion 114
5.1. Review of the Lithostratigraphy of Iraklia 114
5.2. Structures and Metamorphism 115
5.3. Provenance of Detrital Zircons 116
5.4. Regional Implications 119
6. Conclusions 121
Chapter V: Conclusions 123
Appendix A: Supplementary material for the Chapter II 127
Appendix B: Supplementary material for the Chapter IV 151
Bibliography 168

Chapter I

Introduction

1. Motivation

The Aegean domain of Greece presents a complicated tectonic evolution that resulted from several geodynamic processes, including subduction and tectonic emplacement of geotectonic units during Late Cretaceous-Cenozoic convergence-collision, orogenic built-up, back-arc extension, and the formation of metamorphic core complexes (Jacobshagen 1986; Pe-Piper and Piper 2002; Jolivet and Brun 2010; Ring et al., 2010; Papanikolaou 2021). The distribution of HP metamorphic rocks throughout the Hellenides is compatible with an NNE-directed subduction zone (Pe-Piper and Piper 2002; Jolivet and Brun 2010; Ring et al., 2010; Papanikolaou 2021). Underplating and accretion of these rocks reveal evidence for sustained HP conditions, indicating a clear southward younging in the metamorphic ages towards structurally lower nappes, reflecting the southward migration of the Hellenic orogen (Pe-Piper and Piper 2002; Jolivet and Brun 2010; Papanikolaou 2021). The exhumation of the Aegean HP rocks initially occurred during an Eocene- Oligocene syn-orogenic stage followed by a Miocene post-orogenic extensional stage along lithospheric scale detachment fault systems (Jolivet and Brun 2010; Ring et al., 2010; Glodny and Ring 2022). The exhumed HP rocks are direct witnesses of the complex interaction between deformation and metamorphism generated along the subducting plate and subsequent overprinting processes during their return to the surface. However, some of the observed HP rocks are associated with a retroward vergence (Schneider et al., 2018; Gerogiannis et al., 2019; Grasemann et al., 2021), which opposes the principal frontal orogenic wedge, indicating that the structural evolution of the Hellenic orogenic belt does not fit with a simple tectonic scenario.

This dissertation represents a multidisciplinary study on the low-grade HP rocks exposed on Amorgos Island in the SE Cyclades, the back-arc domain of the Hellenic subduction zone. Amorgos Island is located between HP metamorphosed tectonic units, which constitute the lower plate (Cycladic Blueschist Unit CBU/Cycladic basement CB Jolivet and Brun 2010; Ring et al., 2010) and the high-grade to

unmetamorphosed units of the upper plate (e.g., Anafi Soukis and Papanikolaou 2004; Martha et al., 2016, Santorini Schneider et al., 2018, Astypalea Ring 2001, Kalymnos Grasemann et al., 2021), which preserve different tectonometamorphic records of the orogenic history. Based on previous studies, Amorgos consists of low-grade metamorphosed Mesozoic-Cenozoic clastic sequences and neritic to pelagic carbonates capped by an Eocene metaflysch with olisthostromes. Similar flyschoid sequences are observed in the surrounding islands, but no detrital zircon studies have been executed, and no correlation with Amorgos has been established. Overall, controversial views have been proposed regarding the lithostratigraphic configuration and tectonic position with respect to the nearby tectonic units. The rocks of Amorgos have been correlated to the Basal Unit, the Plattenkal Unit, the CBU, the Phyllite-Quartzite Unit or the Mnederes Cover (Minoux, 1980; Fytrolakis et al., 1981; Dürr, 1985; Rosenbaum et al., 2007; Ring et al., 2009; Chatzaras et al., 2011).

The HP rocks of Amorgos reveal early top to NW kinematics (Minoux, 1980; Fytrolakis et al., 1981; Dürr, 1985; Chatzaras et al., 2011), which is not typical for the Hellenic subduction zone in the Cenozoic. Similar kinematics have been reported from the neighboring Santorini and Kalymnos islands (Schneider et al., 2018; Grasemann et al., 2021). Differences in the lithostratigraphic and provenance signatures, metamorphic grade, structural style, and exhumation ages and mechanisms compared with the nearby Cycladic islands can provide fundamental insights into the paleogeography, syn- and post-orogenic stages. Therefore, Amorgos is a key area for better defining the geodynamic evolution of the Hellenic subduction zone in the SE Aegean domain during the Eocene-Oligocene collisional and Miocene post-orogenic stages.

The main questions targeted in this dissertation are:

- What is the tectonostratigraphy of Amorgos Island and the provenance signatures of the siliciclastic sequences?
- What are the main differences regarding the structural evolution and metamorphic record of Amorgos compared to the neighboring Cycladic

Islands that were not affected by the Barrovian metamorphism (e.g., Iraklia Island)?

- What are the main differences regarding the provenance signatures between the Amorgos and Iraklia clastic sequences?
- How is the closure of Paleotethyan and Neotethyan basins reflected in the CBU and Amorgos siliciclastic formations?
- What is the paleogeographic and geotectonic position of Amorgos?
- How is the Amorgos Unit affected by the Miocene detachment faulting?
- In a regional view, what is the record of the retroward kinematics during prolonged subduction and successive coherent underplating of thrust sheets in the frontal wedge?
- What is the Late Eocene-Oligocene structure and evolution of the Hellenic subduction system in the SE Aegean?

The following published and in-preparation manuscripts are the main results of the work related to this dissertation. The co-authors have thoroughly contributed to these manuscripts by reviewing and editing, assisting in fieldwork, sample preparation and analytical lab procedures. Fieldwork was funded by the National and Kapodistrian University of Athens ELKE, and awarded to K. Soukis and S. Lozios.

PUBLISHED

Laskari S., Soukis K., Stockli F. D., Lozios S., Zambetakis-Lekkas A., (2022). Reconstructing the southern Pelagonian domain in the Aegean Sea: Insights from U-Pb detrital zircon analysis, lithostratigraphic and structural study, and zircon (U-Th)/He thermochronology on Amorgos Island (SE Cyclades, Greece). *Gondwana Research*, 106, p. 329-350 (**Chapter II**).

Laskari S., Soukis K., Stockli F. D., Lozios S., Poulaki M. E., Stouraiti C., (2022). Structural Study and Detrital Zircon Provenance Analysis of the Cycladic Blueschist

Unit Rocks from Iraklia Island: From the Paleozoic Basement Unroofing to the Cenozoic Exhumation. *Minerals*, *12*(1), p.83 (**Chapter IV**).

IN-PREPARATION

Laskari S., Soukis K., Lozios S., Stockli D. F., (to be submitted).
A composite Late Eocene-Oligocene double-vergent orogen in the Aegean domain: Insights from the retroward internal duplicated structure of the low-grade HP Amorgos Unit (SE Cyclades, Greece) (**Chapter III**).

2. Techniques

2.1. Detrital Zircon U-Pb geochronology

Detrital zircon U-Pb dating is a very powerful and widely used geochronology technique for determining the provenance signatures and constraining the maximum depositional ages of clastic sequences. Provenance studies play a fundamental role in comparing the ages of potential source terranes to define ultimate sediment sources. The state of knowledge of provenance, the age, and characteristics of source terranes are determined and can be compared to decipher possible linkages between different sedimentary sequences. On the other hand, the maximum depositional age defines the youngest age mode in a clastic sequence, providing the oldest possible deposition age. The DZ U-Pb geochronology is especially valuable for metamorphosed stratigraphic units that lack preserved fossils. In this case, detrital provenance can shed light on the tectonic affinity of different tectonic units and is capable of unravelling the paleogeography.

In this dissertation, zircon U-Pb analysis was conducted using the depth-profile Laser-Ablation-Inductively Coupled Plasma-Mass Spectrometry (LA-ICP-MS) technique. All zircons were separated at the UT Chron Laboratory at the University of Texas at Austin, using standard mineral separation methods that include crushing, pulverizing, water table concentrating, magnetics and heavy geo-liquids (Bromoform and Methylene Iodide). Zircon separates were sprinkled/mounted onto 1-inch polycarbonate discs with double-sided adhesive tape. Following the procedures of Marsh and Stockli (2015) and Hart et al., (2016), unpolished zircons were ablated via depth profile LA-ICP-MS with the use of a PhotoMachine Analyte G.2 excimer laser fitted with a large-volume Helex cell, connected to Thermo Element2 ICP-MS. Ablation was applied for 30 s with an energy of 4 mJ and a repetition rate of 10Hz. Ablation rates of 0.5 µm/s result in profiles of the outer -15 µm of each grain. At least 130 zircon grains were analyzed per sample, in which the laser focused on the prism surfaces perpendicular to the grain's c-axis. Depth profile U-Pb analysis allows for distinguishing metamorphic rims from magmatic core zircon ages highly significant for maximum depositional age determination (e.g., Poulaki et al., 2021). GJ1 (601.7±13 Ma, Jackson et al., 2004) and Plešovice (337.1±0.4 Ma, Sláma et al.,

2008) were used as the primary and secondary reference standards, respectively. Data corrections were applied using the VisualAge data reduction scheme (Petrus and Kamber 2012) based on IgorPro addition to Iolite 3.4 software (Paton et al., 2010). U-Pb ages for each grain were reported with 2σ error. $^{206}Pb/^{238}U$ and $^{207}Pb/^{206}Pb$ were considered as the U-Pb ages for dates less and greater than 850 Ma, respectively. A 10% error filter and 15% $^{206}Pb/^{238}U$ vs. $^{207}Pb/^{235}U$ discordance filter were used for $^{206}Pb/^{238}U$ ages. On the other hand, a 30% $^{206}Pb/^{238}U$ vs. $^{207}Pb/^{206}Pb$ discordance filter was applied to $^{207}Pb/^{206}Pb$ ages. Zircon U-Pb data from metasedimentary samples were plotted in Kernel Density Estimates (KDEs) histograms using the DetritalPy Python script (Sharman et al., 2018). The Maximum depositional ages (MDAs) were estimated by taking the average of the three youngest zircon ages, which overlap within analytical error. Zircon rims were distinguished from cores during data reduction by the presence of a step function in the elemental concentrations and age and by selecting a well-defined plateau in the $^{206}Pb/^{238}U$ final age.

2.2. (U-Th)/He low-T thermochronometry

Zircon (U-Th)/He low-temperature thermochronometry is a powerful technique for resolving thermal histories to quantify cooling and exhumation histories of upper crustal tectonic units during extension (Stockli, 2005). (U–Th)/He dating is based on the decay of 235U, 238U, 232Th, and 147Sm by alpha (4He nucleus) emission. The decay energy, up to ~8 MeV, is taken up by a combination of α-recoil of the parent nucleus and emission of the energetic α particle that travels ~18–20 µm before coming to a stop, leading to potential α loss from the grain during decay (Farley et al., 1996). Zircon is characterized by a He closure temperature ranging from ~180 to 200 °C (e.g., Reiners et al., 2004) and a He Partial Retention Zone (PRZ) spanning a temperature range from ~130 to 180 °C (Stockli, 2005; Wolfe and Stockli, 2010).

All zircons used for (U-Th)/He dating were analyzed at the UT Chron facilities at the University of Texas at Austin following the procedures of Wolfe and Stockli (2010). After mineral separation, the most appropriate zircon grains, in terms of their similarity in geometry, clarity, and size (60-70 µm in width), were selected and handpicked. Morphometric analysis of each grain was executed by measuring length and width. Zircon grains were sealed into Pt tubes for in-vacuum laser heating and He analysis by quadrupole noble-gas mass-spectrometry using a ^{3}He isotopic tracer. Degassed zircons were dissolved using HF-HNO_3 pressure vessel digestion and U, Th, and Sm concentrations were determined by isotope-dilution solution ICP-MS analysis. zHe ages are presented as both individual aliquot ages and mean sample ages. Cited zHe uncertainties for single aliquots are standard errors derived from intra-laboratory standard reproducibility of 8%. Uncertainties for mean samples ages are given as the standard deviation.

3. Hellenides

3.1. The geology of the Hellenides

The geology of Hellenides resulted from the convergence of African-Eurasian plates since the Mesozoic (Fig. 1), and it has been the subject of numerous studies (Jacobshagen 1986; Papanikolaou 2021; Papanikolaou et al.,2004; van Hinsbergen et al., 2005; Jolivet and Brun 2010). Several tectonic models have been proposed regarding the paleogeographic organization, and the identification of tectonostratigraphic terranes involved. Most importantly, all studies dealt with the number of ophiolitic zones and corresponding oceanic basins, which is still a matter of a strong debate (van Hinsbergen et al., 2005; Jolivet and Brun 2010; van Hinsbergen et al.,2005; Ring et al., 2010; Jolivet et al., 2012; Robertson 2012; Bortolotti et al., 2013; Ferriere et al., 2016; van Hinsbergen et al., 2020 and references therein; Papanikolaou 2021). Despite differences, the researchers mentioned above agree that these terranes represent Godwanan-derived fragments that drifted northwards and amalgamated into Eurasia during the Late Paleozoic to Tertiary. The continental fragments were distinguished based on prevalent lithostratigraphy, pre-subduction, and syn-orogenic tectonometamorphic history (Robertson et al., 2001). They were all consumed along with the in-between oceanic domains in a single subduction zone at least since the Late Cretaceous (Faccenna et al.,2003, Jolivet et al., 2003, 2010, 2015, van Hinsbergen et al., 2005, Jolivet and Brun 2010; Ring et al., 2010; Papanikolaou 2021). However, an alternative proposed tectonic model for the evolution of the Hellenides involves an additional SW-dipping subduction zone (Xypolias et al., 2003; Xypolias et al., 2012; Gerogiannis and Xypolias 2017; Gerogiannis et al., 2019, 2021).

A transect from the innermost to the outermost part of the Aegean includes the following domains: (i) the Serbomacedonian-Rhodope continental domain, (ii) the Axios/Vardar oceanic domain, (iii) the Pelagonian continental domain, (iv) the Pindos oceanic or deep marine basin (v) the Attic-Cycladic Crystalline Complex which will be described in the following paragraph (vi) the External Hellenides continental domain which includes mainly Gavrovo-Tripoliza and Ionian-Paxos, and (vii) the East

Mediterranean oceanic crust (Jacobshagen 1986; Pe-Piper and Piper 2002; van Hinsbergen et al., 2005; Jolivet and Brun 2010; Ring et al., 2010; Papanikolaou 2021).

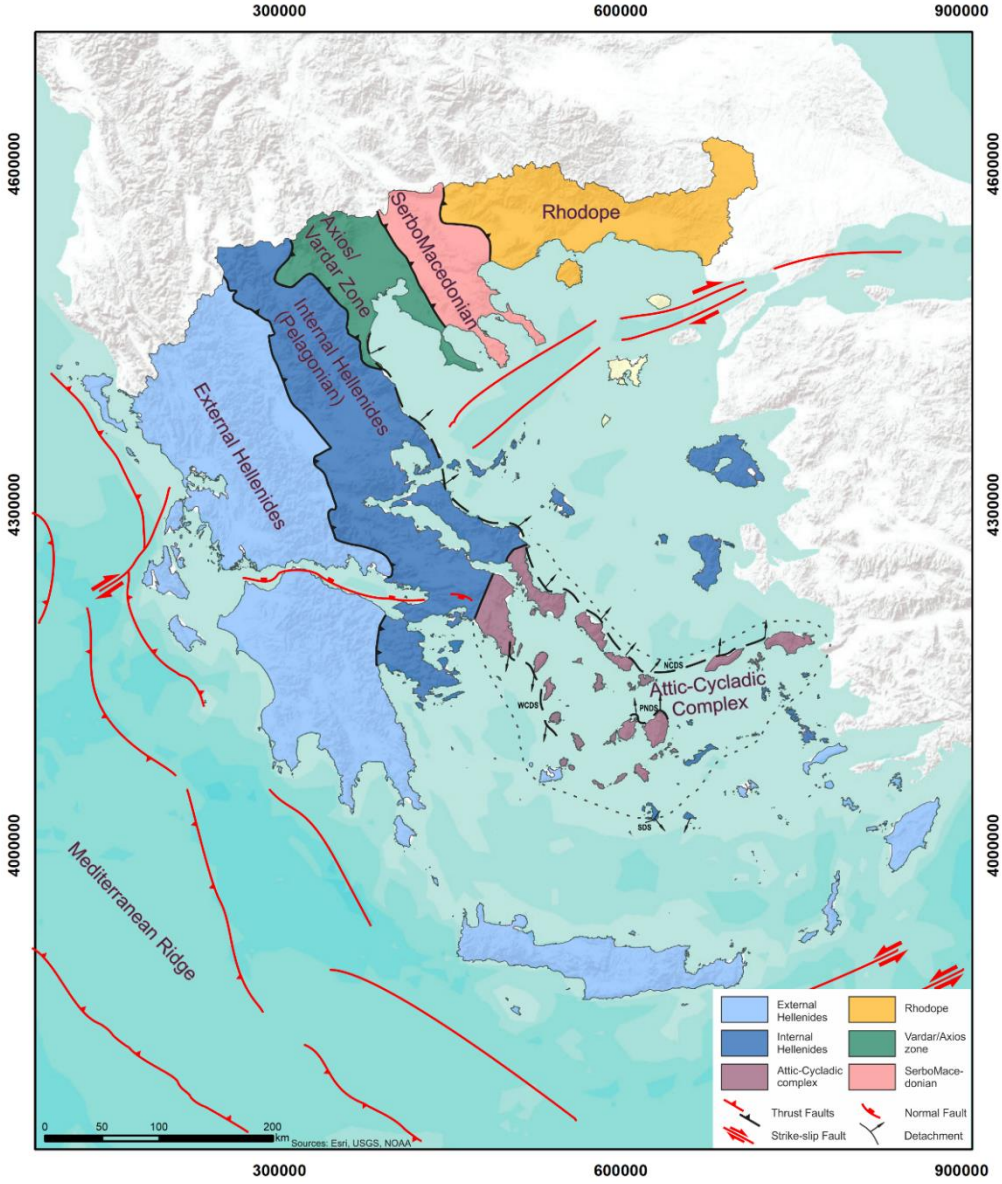

Figure 1: Simplified geotectonic map showing the major tectonic units in the Hellenides (Jacobshagen 1986; Pe-Piper and Piper 2002; van Hinsbergen et al., 2005; Jolivet and Brun 2010; Ring et al., 2010; Papanikolaou 2021)

The Serbomacedonian -Rhodope domain represents the innermost continental tectonostratigraphic terrane. It is a poly metamorphosed and poly-deformed complex made of smaller blocks that are either viewed as part of the Eurasian margin or as Godwanan-derived fragments that accreted to two Eurasia since the Paleozoic (Jacobshagen 1986; Ricou et al., 1998; Stampfli and Borel 2002; Mposkos

and Kostopoulos 2001; Papanikolaou et al., 2004; Papanikolaou 2021). It is characterized by a heterogeneous and complex nappe stack that has caused much confusion regarding the tectonic units and the observed ophiolites whose origin is still controversial. However, all researchers agree that the Serbomacedonian-Rhodope domain is fringed to the south by the Axios/Vardar oceanic domain suture.

The Axios/Vardar domain corresponds to the main Tethyan oceanic basin, represented by ophiolitic rocks that appear in two NNW-SSE striking belts. It includes Triassic-Jurassic ophiolitic rocks formed by seafloor spreading along mid-ocean ridge and supra-subduction zone ophiolites in an intra-oceanic subduction setting (Robertson et al., 1991; Robertson 2002, 2004; Stampfli and Borel 2004; Ferriere 1982, 2015). The inception of the Axios/Vardar subduction below the Serbomacedonian-Rhodope domain in the Middle Jurassic resulted in the development of a volcanic arc in southern Bulgaria (von Quadt et al., 2005; Ring et al., 2010). The final closure of the Axios/Vardar is associated with the westward obduction and emplacement of the Triassic-Jurassic ophiolites on top of the former eastern passive margin of the Pelagonian domain (Celet and Ferriere 1978; Papanikolaou 2009, Robertson et al., 2012; Ferriere et al., 2012; Bortolotti et al., 2013; Ferriere et al., 2016). This is the Paleo-Alpine orogenic event of the so-called Internal Hellenides during the Late Jurassic-Early Cretaceous (Papanikolaou 2021; Papanikolaou et al., 2004).

The Pelagonian domain can be subdivided into internal and external nappes of the eastern active and western passive margins of the platform respectively. The critical difference between these nappes is the complex polyphase tectonic evolution of the internal margin since it has been involved in two orogenic events: the late Jurassic – early Cretaceous Paleo-Alpine orogeny, following the obduction of the Vardar ophiolites and the main Alpine Eocene phase that corresponds to the collision of the Pelagonian and External Hellenides microcontinents. On the other hand, the external margin of the Pelagonian domain represents the units that have participated only in the Eocene tectonic event (Jacobshagen et al., 1976; Papanikolaou et al., 2004; Papanikolaou 2021). Therefore, the stratigraphic columns are differentiated

regarding the complexity of the eastern and western margins of the Pelagonian domain.

The units with Internal Hellenides affinities, initially referred to as the Pelagonian zone (s. str.), show complex stratigraphic columns. The lower part includes a Hercynian basement overlain by a Late Paleozoic- Early Jurassic sedimentary sequence (clastic rocks-mélanges and carbonates), capped by the Axios/Vardar ophiolitic nappe (e.g., the Paleo-Alpine orogeny). The upper part starts with the Late Cretaceous (Cenomanian) transgression basal conglomerate, followed by the deposition of neritic limestones topped by Late Cretaceous-Eocene flysch (Papanikolaou 2021; Papanikolaou et al., 2004). The Pelagonian zone is further subdivided into the unmetamorphosed Sub-Pelagonian zone of the western part (Othrys mt, Argolis peninsula, Poros, Aegina, Hydra) and the metamorphosed units of the eastern part (Thessaly, Pelion, N. Sporades, Attic-Cycladic, Jacobshagen 1986; Papanikolaou 2021).

The external part shows continuous Triassic - Maastrichtian stratigraphic columns covered with Paleocene-Eocene flysch (e.g., Parnassos Unit). No ophiolitic nappe is observed but rather ophiolitic detritus and blocks within clastic flysch-type mélanges (e.g., W Thessaly, Boeotia), implying their proximity to the Internal Hellenides units (Papanikolaou 2009, 2021). Despite the differences above, internal and external units have shown periods of emersion similarly, evinced by bauxite deposits and stratigraphic unconformities in different time intervals (e.g., Parnassos, Sub-Pelagonian).

Metamorphosed units from the Pelagonian domain constitute the upper plate to the tectonically denudated Attic-Cycladic Crystalline Complex. An Early Cretaceous HP metamorphic event followed by an amphibolite-facies overprint has been postulated (Schenker et al., 2014). There is also evidence for two HP metamorphic episodes during the Late Paleocene to Eocene, which affected the Pelagonian and the underlying units around the Olympos-Ossa window. Based on 39Ar/40Ar on phengite, hornblende and biotite, the first event occurred at around 61-53 Ma and is related to the intense deformation within the same unit, while the second took place

at 40-36 Ma related to the underthrusting of the Basal Unit (Schermer 1990, 1993; Lips et al., 1998). Notably, a Miocene (24-21 Ma) greenschist event seems to have locally affected the Pelagonian unit, evinced by zircon Fission track data, which have been attributed to the normal faulting and exhumation during back-arc extension in the Aegean (e.g. Tinos, Olympos Mt) (Brocker and Franz, 1998; Zeffren et al., 2005; Schenker et al., 2015).

The Pindos domain mainly comprises the unmetamorphosed Pindos unit, a coherent Late Triassic to Cretaceous age pelagic sequence covered by Maastrichtian flysch (Papanikolaou 2021). Its deformation style of folds and thrusts devoid of metamorphic record indicates superficial conditions within the accretionary wedge. The heterogeneous HP metamorphosed equivalent Cycladic Blueschist Unit (CBU) is considered either an oceanic or hyper-extended continental margin, where both oceanic crust and Variscan basement (CB) overlain by Mesozoic metasedimentary cover (metapelites and marbles) are observed. The CBU is marked by a composite metamorphic history making correlations with Pindos unit difficult. As in the Pelagonian domain, the CB outcrops are limited and are only found in the Cyclades (Ios, Paros, Naxos) (Papanikolaou 1977, 1980; Jansen et al., 1977; Durr et al., 1978; Andriessen et al., 1987; Keay 1998; Engel and Reischmann 1998) and W. Crete (Sitia) (Siedel et al., 1982; Zulauf et al., 2015). The main argument for correlating these two units is their similar tectonic position between the continental platforms of the overlying Pelagonian zone and the underlying Tripolitza unit Additionally, controversy still exists regarding the origin of the ophiolites of the Pindos domain, which are either assigned to the Pindos or the Vardar oceanic basin (Papanikolaou 2009, 2021; Papanikolaou et al., 2004; Ferriere et al., 2012; Robertson 2012; van Hinsbergen and Schmid 2012; Bortolotti et al., 2013; Ferriere et al., 2016). The age of their tectonic emplacement is Middle- Late Eocene (e.g. N. Pindos, Koziakas Mt.) (Papanikolaou 2009), while in the Attic-Cycladic (e.g. Syros, Tinos, Samos), Late Cretaceous (80-76 Ma) ophiolitic rocks are incorporated within the Cycladic blueschists (Katsikatsos 1979; Brocker and Enders, 1999; Tomaschek et al., 2003; Brocker and Keasling, 2006; Katzir et al., 2007; Papanikolaou 2009,2021; Brocker et al., 2013). Despite this long-lasting debate, the final closure of the Pindos domain

took place during the Eocene-Oligocene, leading to the tectonic emplacement of the Pelagonian domain over the External Hellenides platform (Apulia platform).

The Gabrovo- Tripolitza and Ionian-Paxos domain corresponds to the external carbonate platform of the Tethyan realm. The Gavrovo-Tripolitza represents the innermost nappe of the carbonate platform made up of shallow-water Triassic to Eocene age carbonates topped by a Late Eocene – Oligocene flysch. The Pindos nappe tectonically overlies this locally very low-grade metamorphosed unit in Peloponnese and Crete (Papanikolaou 2021 and references therein). In contrast, the lateral metamorphosed equivalent Basal Unit occurs in tectonic windows below the CBU in Evia, Samos and Olympos Mt (Godfriaux 1968; Dubois and Bignot 1979; Theodoropoulos 1979; Papanikolaou 1979; Ferriere 1982; Papanikolaou 1986; Godfriaux and Ricou 1991; Ring et al., 1999; Shaked et al., 2000). Subduction and accretion of the Tripoliza unit started during Oligocene time (35-30 Ma) and the pronounced HP event of the Basal Unit is dated as Early Miocene (24-21 Ma) (Ring et al., 2001; Ring et al., 2010). Based on the ages of subduction and metamorphism, the duration of subduction of the Basal Unit lasted ~10 Ma. Tectonically underlying the Tripoliza unit is the HP Quartzite-Phyllite unit, which shows similar P-T trajectories to the Basal Unit (Jolivet et al., 1996; Ring et al., 2001). On the other hand, the outermost nappes of Ionian and Paxi units are made up of Mesozoic carbonate sequence topped by Oligo-Miocene turbidites (Papanikolaou, 2021).

The Eastern Mediterranean domain represents the last remnant of the Tethyan oceanic crust of probably Late Triassic age (van Hinsbergen et al., 2005), whose subduction initiated during Early-Middle Miocene and it is still subducting below the outermost parts of the Hellenides (Le Pichon et al., 2002). South of Crete, the oceanic crust is wholly consumed, and the African crust has entered the subduction zone leading to the development of the Mediterranean accretionary prism (Finetti 1982; Underhill 1989; Papanikolaou, 2021).

3.2. The Attic-Cycladic Crystalline Complex

The Attic-Cycladic Crystalline complex consists of a tripartite tectonic group, which are differentiated form island to island and can be subdivided into two or more

structural groups (Fig. 2). In the Cyclades, the lowermost group that constitutes the footwall of the major detachment systems, is composed of the Cycladic Basement (CB) and the Cycladic Blueschist Unit (CBU), and originally located below the uppermost heterogeneous group. The latter represents the remnants of the Pelagonian unit, also known as the Upper Cycladic Nappe, and hence forms the hangingwalls to these detachments. In Evia and Samos islands, where the pre-extensional nappe stack is better preserved, a slightly different configuration is observed, including from bottom to top: the Basal Unit, the CBU and the Pelagonian Unit.

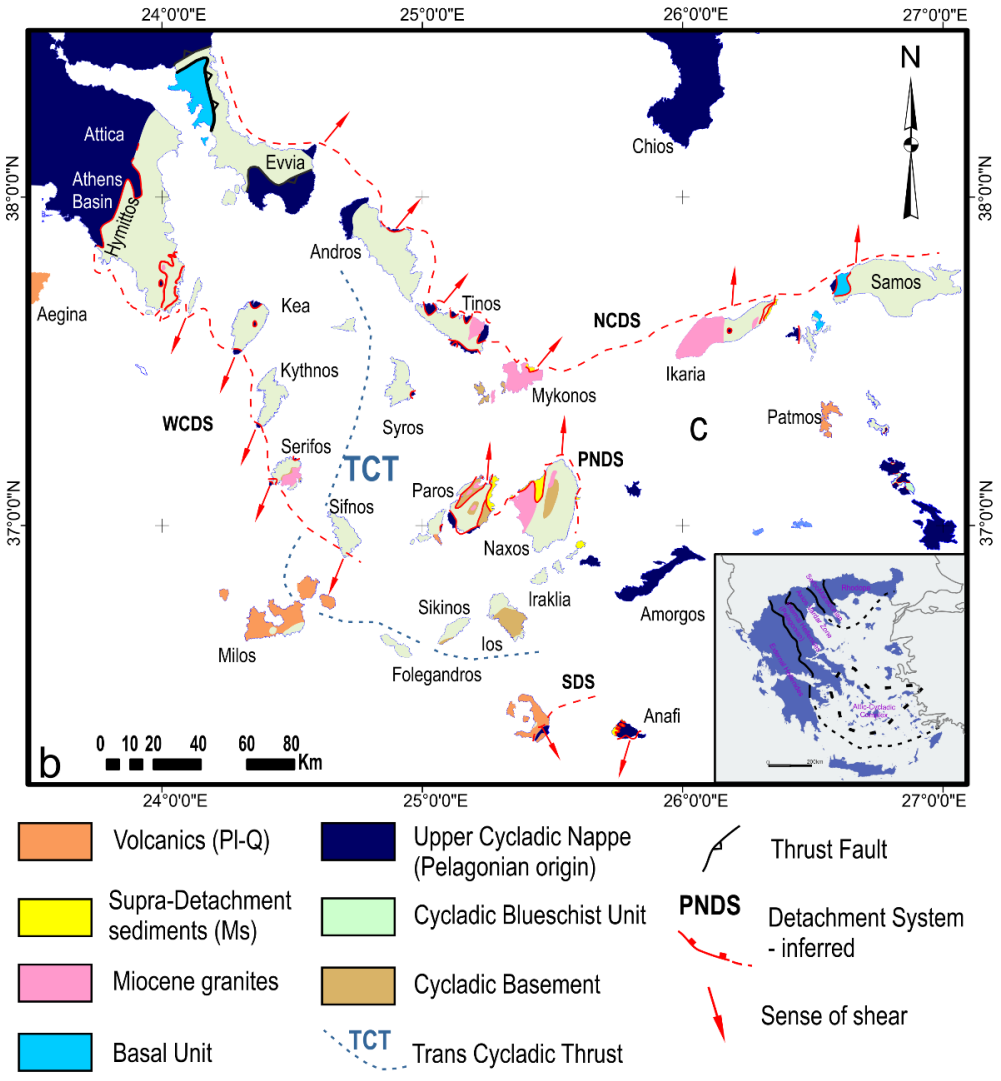

Figure 2: Tectonic map of the Attic-Cycladic Complex (ACC), illustrating the main tectonic units and structures. NCDS: North Cycladic Detachment System, PNDS: Paros-Naxos Detachment System, WCDS: West Cycladic Detachment System, and SDS: Santorini

Detachment System, compiled from Avigad and Garfunkel, 1991, Gautier and Brun, 1994, Pe-Piper and Piper 2002, Soukis and Papanikolaou 2004, Brichau et al., 2007, Ring et al., 2010, Jolivet et al., 2010, Lekkas et al., 2011, Grasemann et al., 2012, 2018, 2021, Schneider et al., 2018).

The relative autochthonous Basal unit crops out in tectonic windows below the CBU in Evia, Samos and Olympos-Ossa mts. and it is widely regarded as the metamorphosed equivalent of the Gavrovo-Tripolitza unit. The Basal Unit consists of a monotonous stratigraphic sequence, characterized by Triassic to Eocene neritic carbonates, topped by an Eocene-Oligocene flysch (Godfriaux 1968; Durr et al., 1978; Dubois and Bignot 1979; Theodoropoulos 1979; Papanikolaou 1979; Avigad and Garfunkel 1989; Ring et al., 1999). $^{40}Ar/^{39}Ar$ ages show that the Basal unit has recorded an HP metamorphic event at ~24-21 Ma (Early Miocene) (8-10 kbar, 350-400 °C) induced by the overthrusting of the CBU (e.g., Evvia, Samos) (Shaked et al., 2000; Ring et al., 2001). In addition, a greenschist-facies overprint is also identified, whose age is still unresolved (Brocker et al., 2004).

In the Cycladic islands, the lowermost unit corresponds to the CB that is the generally accepted equivalent of the external Apulia/Adria platform (Bonneau and Kienast 1982; Keay and Lister 2002; Stampfli and Borel, 2002; Jolivet and Brun, 2010; Ring et al., 2010). However, an alternative view of an internal position relative to the Pelagonian domain has been proposed (Zlatkin et al., 2018). It is mainly observed in the southern and central Cyclades (Ios, Sikinos, Paros, Naxos, Mykonos), comprising a Variscan granitic core that has intruded into Neoproterozoic-Ordovician metasedimentary rocks, involving a polyphase deformation history and metamorphic record reaching locally partial melting (e.g., Paros, Naxos) (Jansen 1977; Papanikolaou 1977, 1980; Durr et al., 1978; van der Maar, 1981; Andriessen et al., 1987; Engel and Reischmann, 1998; Reischmann 1998; Keay and Lister 2002; Zlatkin et al., 2018; Flansburg et al., 2019; Poulaki et al., 2019). Zircon U-Pb data show that the crystallization age of the granites of the CB is ~330-305 Ma (Reischmann 1998; Engel & Reischmann, 1998; Photiades and Keay, 2003; Bargnesi et al., 2013;

Flansburg et al., 2019), while the detrital zircon (dz) age distributions of the host rocks revealed a peri-Godwanan affinity (Flansburg et al., 2019).

The intermediate unit in the entire Cycladic domain corresponds to the CBU, which is considered as the metamorphosed equivalent of the Pindos unit and is structurally overlies either the Basal unit or the CB (Bonneau 1984; Pe-Piper and Piper 2002; Avigad et al., 2007; Xypolias et al., 2007; Huet et al., 2009; Jolivet and Brun 2010; Ring et al., 2010). The CBU comprises passive-margin facies rocks of marble and metapelites within which metabasic pods are observed (Papanikolaou 1976, 1977, 1978; Jansen 1977; Blake et al., 1981; Bonneau et al., 1984; Avigad and Garfunkel 1991; Pe-Piper and Piper 2002; Keiter et al., 2004; Papanikolaou 2009, 2021). U-Pb dz studies on the CBU rocks revealed a Godwanan provenance with a significant change by the time the CBU approached the trench (Seman et al., 2017; Poulaki et al., 2019). The metamorphic history of the CBU has involved a consistent HP event during the Eocene (~55-40 Ma), followed by a greenschist- amphibolite facies overprint in the Oligocene-Miocene (~25-15 Ma) (Jansen 1977; Wijbrans and McDougall 1988; Brocker et al., 1993; Keay et al.,2001; van Hinsbergen et al., 2005b; Denele et al.,2011; Laurent et al.,2015; Beaudoin et al.,2015; Peillod et al., 2017; Cao et al., 2017; Ring et al., 2010; Ring et al., 2018). Significant differences in the estimated peak P-T conditions led to the subdivision of CBU in two nappes e.g., the blueschist-bearing Lower Cycladic Nappe (LCN) and the eclogite-bearing Upper Cycladic Nappe (UPN) (Grasemann et al., 2018), or three nappes with different HP ages (e.g., Upper, Middle and Bottom CBU) (Glodny and Ring 2022; Kotowski et al., 2022). The exhumation of these rocks was achieved in two successive stages, including an Eocene syn-orogenic exhumation process within an extrusion wedge or subduction channel and an Oligo-Miocene post-orogenic unroofing via major extensional detachments, causing the formation of the MCCs and their final juxtaposition against the Upper Cycladic Nappe (Ring et al.,2003; Huet et al., 2009; Jolivet and Brun 2010; Jolivet et al., 2010; Ring et al.,2010; Bargnesi et al., 2013; Soukis and Stockli 2013; Menant et al.,2016; Roche et al.,2016; Grasemann et al., 2018).

The uppermost unit appears in the Attic-Cycladic in two fashions. In Attica-Evia, a Pelagonian-derived sequence of middle Triassic to Early Jurassic carbonates capped by ophiolitic rocks and transgressive limestones constitutes the upper plate of Cenozoic core complexes. In the Cyclades, isolated klippen mainly from the Pelagonian domain are observed as extensional allochthons formed during the ?Oligo-Miocene extension, commonly comprising the Upper Cycladic Nappe. This unit is a diverse group that consists of ophiolitic rocks (Andros, Tinos, Mykonos, Kea, Serifos) (Melidonis 1980; Jolivet et al., 2010; Grasemann et al., 2012; Augier et al., 2014), marine to continental supra-detachment sediments (Paros, Naxos, Ikaria, Anafi, Mykonos) (Jansen 1977; Angelier et al., 1978; Papanikolaou 1980; Boger 1983; Sanchez-Gomez et al., 2002; Kuhlemann et al., 2004) and high-grade schists, gneisses (Tinos, Syros, Anafi, Donousa) (Durr et al., 1978; Reinecke et al., 1982; Maluski et al., 1987; Patzak et al., 1994; Katzir et al., 1996; Soukis and Stockli 2013). Amongst the Pelagonian formations, the hanging wall of the Santorini detachment includes low-grade Late Triassic carbonates and Eocene flysch, exhumed above 200°C in the Early-Middle Miocene (25-18 Ma) (Schneider et al., 2018). Finally, geochronological data from the uppermost unit have shown a prolonged tectonometamorphic history spanning the Early Cretaceous to early Cenozoic and including high-pressure and high-temperature metamorphic assemblages (Durr et al., 1978b; Maluski et al., 1987; Patzak et al., 1994; Huet et al., 2014). These rocks have also recorded a Miocene (24-21 Ma) greenschists-facies overprint in the Cyclades (e.g. Tinos) (Brocker and Franz 1998; Zeffren et al., 2005).

3.3. Tectonic Evolution of the Aegean domain

Since the latest Oligocene-Early Miocene, a pronounced post-orogenic back-arc extension in an N-S direction, particularly in the south Aegean region has reworked the previously thickened crust, causing a regional extreme thinning of the overriding plate as a result of the southward roll-back of the slab (Brun and Sokoutis 2010; Jolivet and Brun 2010; Ring et al., 2010; van Hinsbergen and Schmid 2012; Jolivet et al., 2015). However, alternative views regarding the extension in the Aegean domain point to a non- classic back-arc domain, but rather as related to the faster SW-ward velocity of the Aegean microplate relative to Anatolia (Agostini et al., 2010).

Nonetheless, extension resulted in the exhumation of previously HP metamorphosed rocks in several metamorphic core complexes via symmetric shallow-dipping detachment systems that exhibit opposite sense of shear. Top-to-the NE sense of shear for the North Cycladic Detachment (Andros, Tinos, Mykonos, Ikaria, Syros), top-to-the N for the Naxos-Paros Detachment (Paros, Naxos) and top-to-the SW-SE sense of shear for the West Cycladic Detachment (Kea, Kythnos, Serifos) and the Santorini Detachment (Santorini) (Urai et al., 1990, Buick 1991; Brichou et al., 2007; Jolivet et al., 2010; Ring et al., 2010; Soukis and Stockli 2013; Grasemann et al., 2012;, Schneider et al., 2018), in a warm geothermal area induced by the direct contact of the denudated crust with the asthenosphere that caused partial melting (e.g., Naxos dome) (Jolivet and Brun 2010; Ring et al., 2010; Jolivet et al., 2015). Based on thermochronological data, all detachment systems were active from at least the Early until Late Miocene (Brichau et al 2006; Jolivet et al.,2010; Grasemann et al., 2012; Bargnesi et al., 2013; Soukis and Stockli 2013; Schneider et al., 2018), while the largest amount of displacement at about 50-70 km was accommodated by the NCDS (Jolivet et al.,2004, 2010). The activity on some of these detachments ceased after the emplacement of syn-tectonic I and S- type granitic intrusions (Altherr et al., 1982; Pe-Piper and Piper 2002; Brichau et al., 2007; Bolhar et al., 2010; Bargnesi et al., 2013). Additionally, some authors have argued for the existence of a South Cycladic Shear Zone with top-to-the S sense of shear, which corresponds to the CB/CBU contact and is exposed on southern Ios island. This contact is either viewed as a detachment (Lister et al., 1984; Ring et al., 2011) or a thrust (Huet et al., 2009), while a recent study by Poulaki et al. (2019), suggested a parautochthonous relationship between CB and CBU.

In the internal areas (Rhodope domain), extension probably started much earlier, in the Eocene, the based on the deposition of marine sediments during that time (Brun and Sokoutis 2010). Nonetheless, this event is not related to the same roll-back described in the Cyclades, but more likely, corresponds to a primary slab retreat whose velocity was much slower, as evinced by the steady magmatic arc during that period (Jolivet and Brun 2010). Moreover, from another point of view, a part of the extensional history of the Cyclades is ascribed to arc-parallel extension that was

accommodated along the Mid-Cycladic lineament or detachment, in which the orientation of lineations rotated significantly from NE-SW to N-S direction (Walcott and White 1998; van Hinsbergen and Schmid 2012; Philippon et al., 2012, 2014). According to van Hinsdergen and Schmid (2012), these major dislocations have been assigned to trench- parallel extensional deformation along the Mid-Cycladic detachment since 15 Ma. Despite that, the non-existence of an apparent discontinuity led Jolivet et al. (2015) to suggest a wide left-lateral gradient of extension involving a mantle flowing driven by the development of a slab tear beneath the eastern Aegean region. However, the concept of an extensional feature is recently corroborated by paleomagnetic data from Paros island, where the detachment is exposed (Malandri et al., 2017). It is worthwhile noting that in the Cyclades, the extension has been accompanied by E-W compression and shortening leading to the development of several reverse and strike-slip faults along with upright folds during Miocene time at about 9-8 Ma (Ring et al., 1999; Avigad et al., 2001; Philippon et al., 2012; Menant et al., 2013). This tectonic event is considered to be a consequence of the westward extrusion of the Anatolia block and the westward propagation of the North Anatolian Fault (NAF) within the Aegean domain since ~5 Ma (Armijo et al., 1999; Menant et al 2013; Roche et al., 2019). The NAF is linked to the Hellenic trench through the Central Hellenic Shear Zone (Papanikolaou and Royden 2007; Royden and Papanikolaou 2011) and forms a large structure responsible for the northwestern separation of the continental Greece from the Aegean domain that moves at a fast rate towards to the southwest based on the referred GPS velocities (Armijo et al., 1999; McClusky et al., 2000; Jolivet et al., 2001).

Finally, the present-day stress filed is compatible with N-S to NNE-SSW extension related to mainly E-W striking steeply-dipping normal faults, that notably control the current Neogene basins (e.g. Corinth Gulf, Evia) and are straightforwardly linked to the faster southward slab retreat and slab tearing below the Aegean (Jolivet et al., 2015).

Chapter II

Reconstructing the southern Pelagonian domain in the Aegean Sea: Insights from U-Pb detrital zircon analysis, lithostratigraphic and structural study, and zircon (U-Th)/He thermochronology on Amorgos Island (SE Cyclades, Greece).

Sofia Laskari[1,*], Konstantinos Soukis[1], Daniel F. Stockli[2], Stylianos Lozios[1], Alexandra Zambetakis-Lekkas [1]

[1.] Faculty of Geology and Geoenvironment, National and Kapodistrian University of Athens, Greece.
[2.] Department of Geological Sciences, Jackson School of Geosciences, University of Texas at Austin, USA.

Abstract

In the Attic-Cycladic Crystalline Complex (Aegean Sea, Greece), following early syn-convergence exhumation processes, the extensional tectonics resulted in the extreme denudation of the upper plate, preserved today in a few places. The Cycladic Blueschist Unit (CBU) and the underlying Cycladic Basement and the Basal Units have been exhumed in the footwall of detachment systems, juxtaposed against the Pelagonian-derived hanging wall fragments. Traditional views accept that Amorgos Unit occupies a structurally lower position, correlated to the Basal Unit. This study presents lithostratigraphic and structural data, integrated with detrital zircon MDA, provenance analyses, and (U-Th)/He ages, showing a new investigation of the paleogeographic and structural position of Amorgos in the Cycladic archipelago.

The low-grade metamorphosed Amorgos Unit presents a tripartite lithostratigraphy: a basal metaconglomerate, a middle carbonate sequence with shallow-water to pelagic facies, and an Eocene (meta)flysch. An HP/LT metabasite huge block is incorporated within the metaconglomerate either by gravitational movements as an isolated olistolith or tectonic processes as a slice during the early deformation stage. Detrital zircon U-Pb analysis on the meta-siliciclastic deposits revealed that the basal metaconglomerate shows a dominant Ediacaran input with Mid-Permian and Precambrian MDAs for the matrix and the high-grade clasts, respectively. The metaflysch shows Paleozoic affinity (e.g., mainly Pelagonian-sourced) and Triassic-Jurassic MDAs. The deformation history of Amorgos includes an early-stage top-to-

NW thrusting in the retro-wedge setting of the Late Eocene–Oligocene subduction zone and a late-stage top-to-SE extensional low- and high-angle normal faulting. Zircon (U-Th)/He ages reveal an Early–Mid Miocene (18-14Ma) exhumation below ~200°C. Similarities on lithostratigraphy, structural inventory, exhumation history, and structural position of Amorgos Unit with the Santorini Detachment System Pelagonian hanging wall imply their close spatial relationship. From all the above, we propose that Amorgos belongs to the upper plate of the CBU and is paleogeographically located at the southern Pelagonian margin.

1. Introduction

In the Early Paleozoic, the opening of the Paleotethys was associated with the detachment of Gondwana-derived terranes (Hunic terranes), eventually involved in the Variscan orogeny during subduction of the Paleotethys. Subduction and accretion lasted up to the Ladinian or Norian, when the collision of the Cimmerian ribbon continent with the southern Eurasian margin signified the final closure of Paleotethys (eo-Cimmerian event, Robertson et al., 1991; Stampfli and Borel 2002; Stampfli et al., 2003; Robertson, 2006; Zulauf et al., 2015, 2018). The diachronous Carboniferous to Triassic closure of Paleotethys resulted in widespread magmatic activity, documented in the pre-Apline basement of Rhodope, Pelagonian, the Cycladic domain, and the External Hellenides (e.g., Crete, Kythira, Peloponnese) (Henjes-Kunst and Kreuzer, 1982; Ring et al., 1999; Vavassis et al., 2000; Keay et al., 2001; Xypolias et al., 2006; Anders et al., 2007; Zulauf et al., 2007; Meinhold et al., 2010). The Paleozoic basement was overlain by Permo-Triassic volcano-clastic sequences, viewed as fore-arc, volcanic-arc, back-arc basin, or rift-related units (Robertson et al., 1991; Pe-Piper and Piper 2002; Stampfli and Borel 2002; Stampfli et al., 2003; Robertson, 2006; Papanikolaou 2009, 2013; Zulauf et al., 2018). These sequences occupy the stratigraphic base in almost all units of the Hellenides (Papanikolaou 2021) and can encode significant clues regarding the tectonic setting and processes since they originate from the supply of older basement rocks. Therefore, the Permo-Triassic clastic lithologies are the best candidates for shedding light on paleogeography and the passage from the Paleotethyan to the Neotethyan cycle.

In the Aegean domain, the pre-Variscan crustal fragments of Gondwanan and peri-Gondwanan affinities and the juvenile Variscan basement were affected by the complex tectonometamorphic evolution of the Alpine orogeny. Successive episodes of rifting, intra-oceanic subduction, ophiolite obduction, and passive margin subduction overprinted previous records of the Paleotethyan cycle (Pe-Piper and Piper 2002; Papanikolaou 2009, 2013; Jolivet and Brun 2010; Ring et al., 2010; Zulauf et al., 2018). As a result, paleogeographic reconstructions are often hard to unravel.

Amorgos Island lies at the southeastern edge of the southeastern Cycladic archipelago, between the HP/LT metamorphosed Cycladic Blueschist Unit (CBU), the Cycladic Basement (CB) (Jolivet and Brun 2010; Ring et al., 2010), and the Asteroussia Unit (e.g., Nikouria, Anafi, Dürr et al., 1978; Reinecke et al., 1982; Koutsovitis et al., 2021), and very close to the Pelagonian-derived units of Kalymnos and Leros islands (Dodecanese islands Franz et al., 2005; Grasemann et al., 2021). Previous studies have shown that the stratigraphy of Amorgos includes metamorphosed clastic sequences and carbonates of both neritic and pelagic affinities topped by flysch deposits (Minoux, 1980; Fytrolakis et al., 1981; Dürr, 1985; Rosenbaum et al., 2007; Ring et al., 2009; Chatzaras et al., 2011). However, there are strikingly different views concerning the paleogeographic and tectonic position of Amorgos. The most disputable topics include the number of the exposed units and the structural evolution of Amorgos.

This paper combines classic field methods such as geological mapping, lithostratigraphic and structural study with detrital zircon U-Pb analyses, and (U-Th)/He low-T thermochronometry applied to the Amorgos rocks. The new DZ U-Pb ages provide valuable information regarding the potential provenance areas, which offer significant insights into the paleogeographic organization. Additionally, these U-Pb ages, together with new fossil findings preserved in the carbonate rocks, and specific lithological criteria, are used as anchoring points providing an alternative view of the Amorgos lithostratigraphy. Finally, the new (U-Th)/He ages presented in this study shed light on the structural position of Amorgos in the Attic Cycladic edifice and assist in robust regional correlations.

2. Geological Setting

The Hellenides and the Aegean domain resulted from the northward subduction beneath the Eurasian plate and final collision of several Gondwanan-derived continental fragments, separated by oceanic or deep marine basins (Stampfli and Borel 2002; Papanikolaou et al., 2004, 2009; van Hinsbergen et al., 2005; Jolivet and Brun 2010; Ring et al., 2010; Jolivet et al., 2013; Menant et al., 2016; Gerogiannis and Xypolias 2017). In the Attic-Cycladic area, the deeply buried rocks were exhumed in two stages: an Eocene syn-orogenic exhumation stage and a Late Oligocene to Miocene post-orogenic unroofing via symmetric shallow-dipping detachment systems exhibiting an opposite sense of shear (Ring and Layer 2003; Thomson et al., 2009; Brun and Sokoutis 2010; Jolivet and Brun 2010; Ring et al., 2010, 2011; Menant et al., 2016; Grasemann et al., 2018). These are the top-to-the NE North Cycladic Detachment System (NCDS), the top-to-the N Paros-Naxos Detachment System (PNDS), the top-to-the SW West Cycladic Detachment System (WCDS), and the top-to-the SE Santorini Detachment System (SDS), respectively (Urai et al., 1990; Avigad and Garfunkel, 1991; Buick 1991; Brichau et al., 2006, 2007; Jolivet et al., 2010; Lekkas et al., 2011; Grasemann et al., 2012; Soukis and Stockli 2013; Schneider et al., 2018; Coleman et al., 2019, 2020) (Fig.1).

The Pelagonian-derived rocks are seen with a more or less complete tectonostratigraphy in Attica and Evia, comprising a lower sequence of Triassic-Jurassic carbonates overlain by a Late Jurassic - Early Cretaceous wildflysch and ophiolitic rocks followed by an upper sequence of Late Cretaceous transgressive limestone (the co-called Cenomanian transgression) and Maastrichtian to Eocene flysch (Papanikolaou 2021 and references therein). In the Attic-Cycladic Crystalline Complex (ACCC), the upper plate is tectonically denudated, forming fragments observed as isolated klippen or extensional allochthons (Upper Cycladic Nappe). These fragments can include ophiolitic rocks (Katzir et al., 1996; Jolivet et al., 2010; Grasemann et al., 2012; Mavrogonatos et al., 2021), clastic marine to continental sediments (Böger 1983; Sánchez-Gómez et al., 2002; Bargnesi et al., 2013), schists and gneisses locally intruded by Late Cretaceous granitoids (Dürr et al., 1978; Reinecke et al., 1982; Maluski et al., 1987; Patzak et al., 1994; Soukis and Stockli

2013; Koutsovitis et al., 2021). The upper plate is best exposed on Anafi and Santorini Island (Reinecke et al., 1982; Soukis and Papanikolaou 2004; Martha et al., 2016). The latter comprises low-grade Late Triassic-Jurassic carbonates and Paleogene flysch (Schneider et al., 2018).

The dominant Cycladic Blueschist unit (CBU) consists of metavolcanic rocks, metapelite, and marble (Dürr et al., 1978; Blake et al., 1981; Papanikolaou 2021). According to traditional views, the CBU has recorded an HP event during the Eocene (~55-40 Ma), followed by greenschist- amphibolite facies overprint in the Oligocene-Miocene (~30-15 Ma) (Jansen 1977; Wijbrans and McDougall 1988; Bröcker et al., 1993; Keay et al.,2001; Ring et al., 2010, 2018; Denèle et al., 2011; Beaudoin et al., 2015; Laurent et al., 2015; Peillod et al., 2017). However, recent studies argue for a prolonged HP event from the Early Eocene to Early Oligocene (Kotowski et al., 2020; Ring et al., 2020). On a few islands (e.g., Paros, Naxos, Ios, Sikinos) below the CBU lies the Cycladic Basement unit (CB), which is regarded as part of the external Apulia platform or the Pelagonian domain (Keay and Lister 2002; Stampfli and Borel, 2002; Jolivet and Brun, 2010; Ring et al., 2010; Augier et al., 2014). It consists of a Carboniferous granitic core that has intruded into Neoproterozoic-Ordovician metasedimentary rocks, involving a polyphase deformation history and metamorphic record reaching locally partial melting (e.g., Paros, Naxos) (Papanikolaou 1980; Andriessen et al., 1987; Engel and Reischmann 1998; Reischmann 1998; Keay and Lister 2002; Photiades and Keay, 2003; Bargnesi et al., 2013; Zlatkin et al., 2018; Flansburg et al., 2019). The CB/CBU contact on Ios has been described as a top-to-the S detachment (South Cycladic Shear Zone Lister et al., 1984; Ring et al., 2011) or a thrust (Huet et al., 2009), while a recent study suggested a parautochthonous relationship (Poulaki et al., 2019).

The Basal unit crops out in tectonic windows below the CBU in Evia, Samos, and Olympos-Ossa-Pelion Mts. This unit is regarded as the metamorphosed equivalent of the Gabrovo-Tripolitza unit and consists of Triassic to Eocene platform-facies carbonates, topped by Eocene-Oligocene flysch (Godfriaux 1968; Dubois and Bignot 1979; Papanikolaou 1979; Theodoropoulos 1979; Ring et al., 1999) with a peak HP at

24-21 Ma (Early Miocene) (8-10 kbar, 350-400 °C) (Shaked et al., 2000; Ring et al., 2001; Ring and Layer 2003).

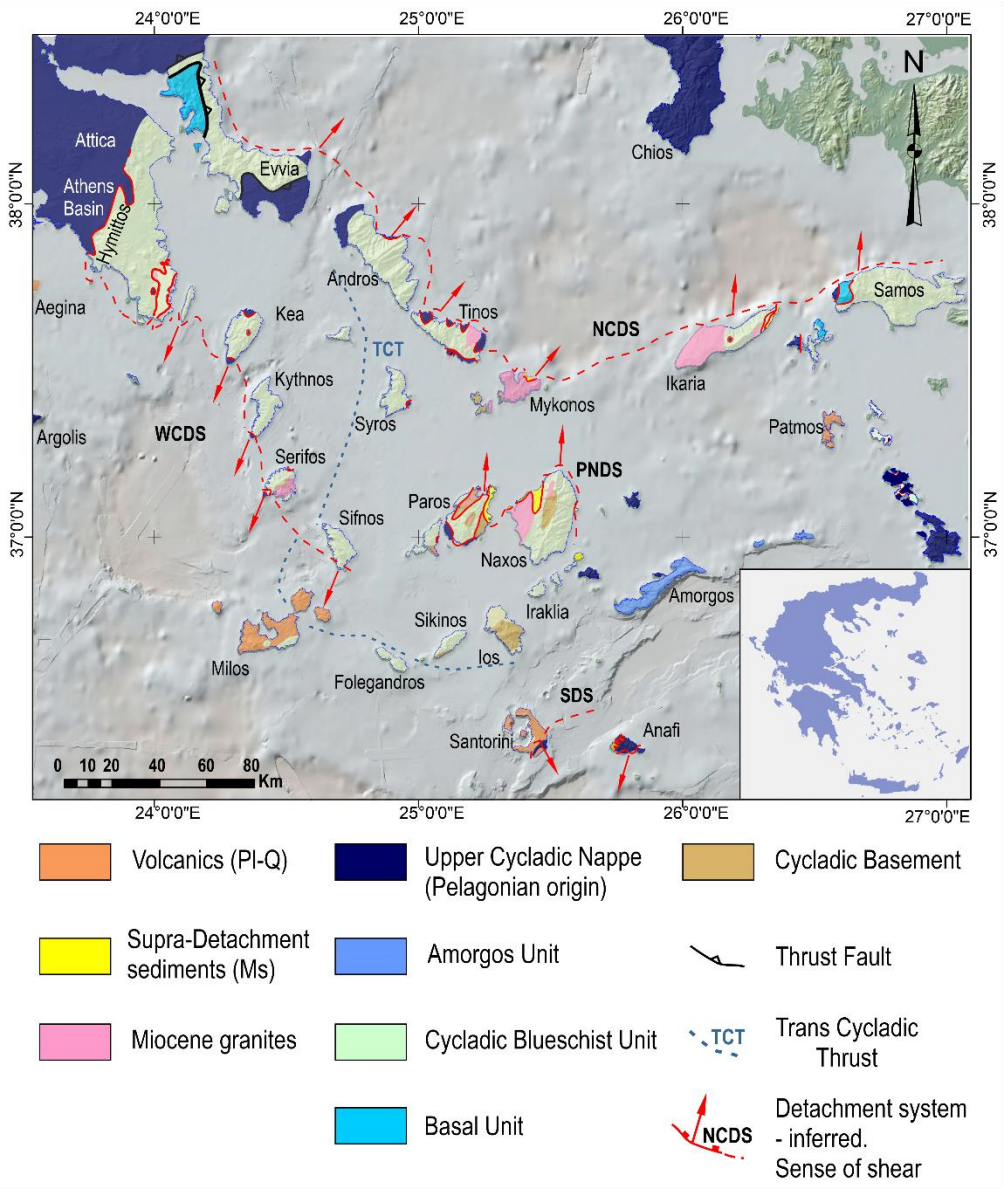

Figure 1: Detailed tectonic map of the Attic-Cycladic complex, portraying the main tectonic units, the structures, and the location of the study area. NCDS: North Cycladic Detachment System, PNDS: Paros-Naxos Detachment System, WCDS: West Cycladic Detachment System, and SDS: Santorini Detachment System, compiled from Avigad and Garfunkel, 1991, Gautier and Brun, 1994, Pe-Piper and Piper 2002, Soukis and Papanikolaou 2004, Brichau et al., 2007, Ring et al., 2010, Jolivet et al., 2010, Lekkas et al., 2011, Grasemann et al., 2012, 2018, 2021, Schneider et al., 2018).

Amorgos is considered as one of the Cycladic islands where the Basal Unit is cropping out. In general, it is made of a Mesozoic massive marble series that is interleaved

with one or more clastic lithologies and capped by Eocene metaflysch. According to Minoux (1980) and Dürr (1985), the lower marble series is rich in Late Triassic age fossils (e.g., corals, large *Megalodontidae*). It corresponds to the neritic formation found in most units of the Hellenides (Pantokrator facies) at that time. On the other hand, poorly preserved fossils (*Rudist sp*. fragments, Campanian-Maastrichtian *Rhapydionina, or Murciella* of the subfamily *Rhapydionininae*) have been reported from the upper marble series, providing a Late Cretaceous age (Minoux, 1980). In the lower clastic lithologies, the age given by the microfauna of *Ammonites and Corals* (*Placites cf. oldhami MOJSISOVICS*) of Richti Formation, and large *Megalodontidae* of the Kryoneri Formation was Carnian to Norian (Minoux, 1980; Dürr, 1985). Based on specific lithological features and preserved nummulite fossils, an external origin near the Tripolitza (Basal unit) or the Ionian unit has been suggested (Minoux, 1980; Fytrolakis et al., 1981; Dürr, 1985; Papanikolaou 1987). Rosenbaum et al. (2007) and Ring et al. (2009) have distinguished two metamorphosed units, which they have correlated to the Phyllite-Quartzite and the Tripolitza unit (Basal unit). According to these authors, the two units are separated by a detachment fault, which is the northern continuation of the Cretan detachment. The P-T conditions have been estimated at 13 MPa and 500-600 ^{o}C and >8MPa, 300-400 ^{o}C for the underlying and the overlying unit, respectively (Theye et al., 1997; Rosenbaum et al., 2007; Ring et al., 2009). Chatzaras et al. (2011) suggested a different tectonostratigraphy and correlation. They identified an HP metamorphosed metaconglomerate, which they have correlated to the CBU. This HP unit is tectonically over- and underlain with thrust faults by a carbonate sequence, which they have assigned to the Menderes cover. These authors concluded that unroofing of Amorgos involved a southward exhumation of the HP rocks within an extrusion wedge under blueschist-facies conditions during the Eocene and a subsequent Oligo-Miocene NW-directed back thrusting concurrent with greenschists facies retrogression.

From the latest Miocene, the island is under the neotectonic stress field resulted in the development of E-W to NW-SE normal faults. A major offshore NE-SW normal fault seems to control the geomorphology and structural evolution of the southern

coast of Amorgos Island (Papadopoulos and Pavlides, 1992; Tsampouraki et al., 2021).

3. Lithostratigraphy of Amorgos Island

Lithological and structural observations, supplemented by new geochronological and paleontological data, elucidate the lithostratigraphy of the Amorgos Unit. This unit presents notable lithostratigraphic variations from northeast to southwest. Consequently, we propose three lithostratigraphic columns for the northeastern, central, and southwestern parts of Amorgos (Fig. 2a, b).

3.1. Northeastern Amorgos

Northeastern Amorgos mainly includes a sequence of massive to well-foliated light to dark gray marble, underlain by Verrucano-type deposits (Kryoneri Formation) and capped by a metaflysch.

The lowermost Kryoneri Fm. is observed near the port of Aigiali and comprises light grey to yellow, fine-grained, dolomitic layers alternating with reddish-violet and light yellow slate (Fig. 3a). The Kryoneri Fm. gradually transits in shallow-water fossiliferous calcitic-dolomitic marble (Tholaria Fm.). Along the footpath from Tholaria to Langhadha village (~400m from the beginning of the path from Tholaria), 3-4 cm long fossils were detected. These fossils correspond to bivalves, e.g., small *Megalodontidae* and *Lithiotidae,* indicating a Late Triassic to Early Jurassic age (e.g., Pantokrator-facies) (Fig. 3b). The foraminifer *Orbitopsella* sp. has also been identified in the optical and scanning electron microscope, providing an Early Jurassic (Lias-Pliensbachian) age (Fig. 3c, d). The Tholaria Fm. is overlain by a massive to well-foliated marble (Krikelas Fm.). A remarkable feature of the northeastern part is the occurrence of at least one and possibly two metabauxite layers, observed in many outcrops near Krikelas Mt. and near Tholaria. The transition to the overlying metaflysch is defined by a conglomeratic/brecciated marble with quartzitic and calcitic pebbles of variable size (locally fossiliferous) and a calcitic matrix that quickly becomes rich in phyllosilicates and quartz. The metaflysch consists of weakly metamorphosed dark brown to green shale, sandstone conglomerate alternations,

and rare boudinaged marble layers. Graphite-rich layers form the stratigraphic base of the metaflysch.

3.2. Central/Southwestern Amorgos

The central and southwestern parts of Amorgos include pelagic and shallow-water carbonates and clastic sequences with substantial thickness variations. It should be stressed that the complete Amorgos stratigraphic column is observed only at the central part.

The lowermost lithology is a basal metaconglomerate (Kapsala Fm.) best exposed at Kapsala, Xylokeratidi (central), and Vroutsi (southwest). It is heterogeneous, comprising quartzitic and purple, green, or light brown phyllitic layers, representing more or less the matrix and a polymictic, poorly sorted conglomeratic part. Lenses/clasts originate from higher-grade rocks such as mica-schists, quartzite, metatuff, metachert, carbonates, and metabasite, varying from a few mm to a few meters. A few meters thick and a few tens of meters long metabasite is observed within the Kapsala Fm. It represents a coarse-grain and well-foliated metabasic rock, including blueschist-facies minerals (e.g., glaucophane). Interestingly, the foliation and stretching lineation of the metabasite show similar geometrical characteristics with the enveloping metaconglomerate (Fig. 3e, f). The Kapsala Fm. is either overlain by the Verrucano-type Kryoneri Fm. or an equivalent light green to yellow phyllite with marble lenses (Richti Fm.). The Kryoneri and Richti Fm. are overlain by a light grey calcitic, partly dolomitized, Pantokrator-facies marble (Xylokeratidi Fm. = lateral equivalent to the Tholaria Fm). This marble locally contains haematite-rich layers (Dürr, 1985; this study). The Xylokeratidi Fm. gives place to light-blue-gray, platy, fine to medium-grained metachert marble of the Chozoviotissa Fm. In the central part, the Chozoviotissa Fm. passes through a conglomeratic/brecciated marble to a massive, strongly karstified marble of the Asfondilitis Formation. It should be noted that Asfondilitis Fm. is devoid of metabauxite or haematite layers and not found in the southwestern Amorgos. At the central part, the transition to the metaflysch is recorded by a conglomeritic/brecciated marble. This lithology also includes transported fossils, some of which strongly resemble *Nummulites sp*., despite

recrystallization (Fig. 3g, h). The metaflysch appears in two fashions: i) a less than 50m thick continuous clastic layer, often graphitic, which is isoclinally folded with the underlying Asfondilitis Fm. (central Amorgos) and occupies the core of macroscale NE-SW recumbent folds, ii) a more than 400m thick, low-grade metamorphosed and isoclinally folded, clastic sequence, which occupies a fault-bounded graben, at the center of the island. The upper part is a wildflysch with metabasic and carbonate olistoliths, while the lower part consists of calc-rich and often graphitic layers. At the southwestern part, the metaflysch overlies both Chozoviotissa and Xylokeratidi Fm.

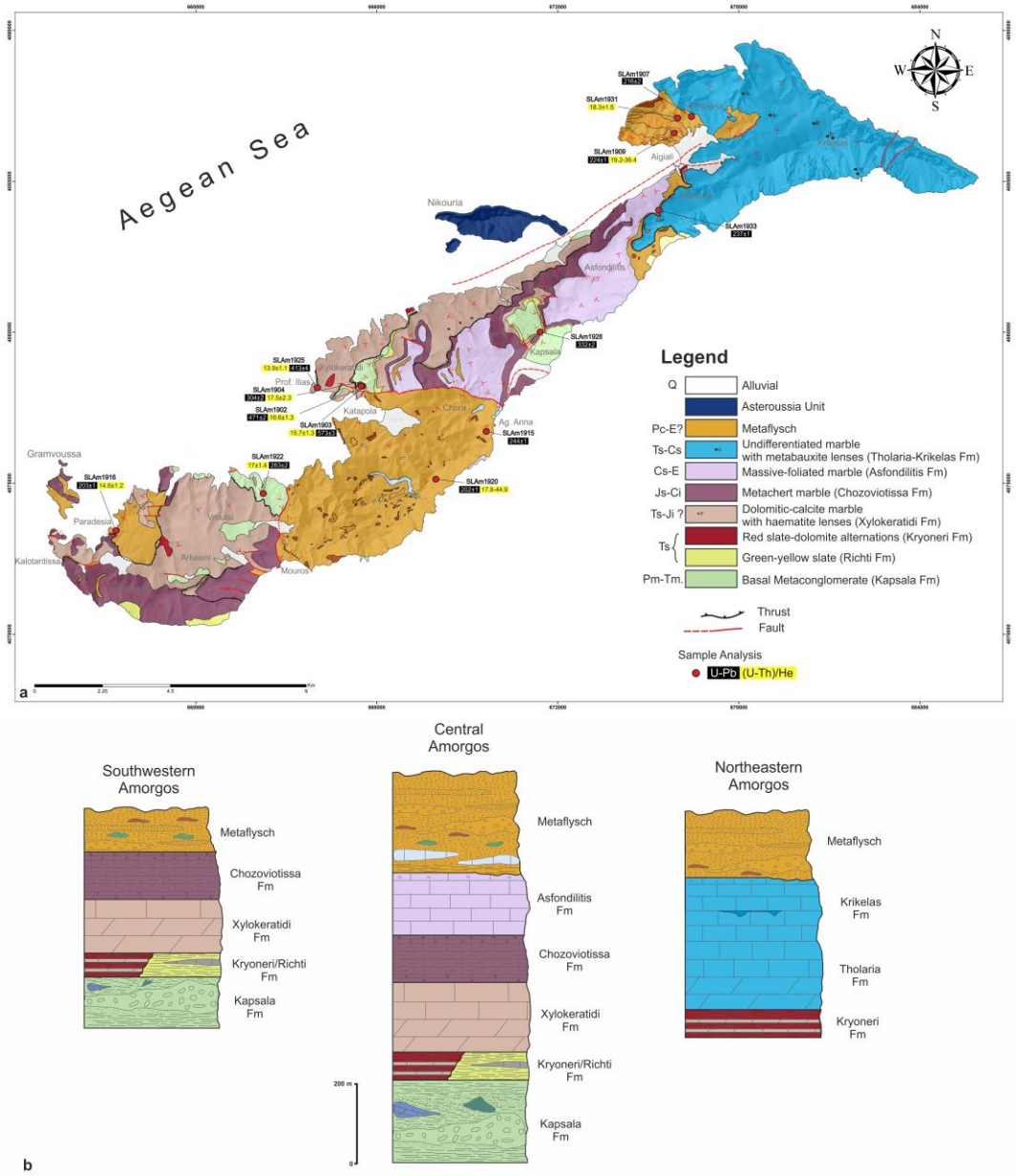

Figure 2: Geological map of Amorgos Island showing the main formations and sample locations of DZ U-Pb and (U-Th)/He analyses. Nikouria and Gramvoussa islets adapted from

Dürr, (1985). (b) Lithostratigraphic columns of southwestern, central, and northeastern Amorgos Island.

4. Structures

Based on our observations, Amorgos Unit comprises complexly deformed rocks with structures developed during two distinct deformation stages. The first deformation stage is characterized by structures formed during a continuous and progressive compressional phase under ductile to brittle-ductile and finally to brittle conditions. The second stage comprises structures developed into the brittle regime during an incipient stage of an extensional event. In this chapter, we summarize the structural evolution of Amorgos, which will be the subject of a more detailed forthcoming paper. The neotectonic fault activity is not part of this study and will be very briefly mentioned.

4.1. Progressive compressional deformation stage Dn_{a-b} -D_{n+1}

The main Dn_a syn-metamorphic ductile deformation episode is associated with the development of ductile Fn isoclinal folds with NW-SE fold axes (Bn), resulting in a dominant penetrative fine-grained Sn foliation. An NW-SE-trending stretching lineation (Ln) is formed on Sn (Fig. 4a), defined by the alignment and stretching of quartz- calcite- phyllosilicate aggregates elongated clasts, and Fe-Mg carpholite (Fig. 4b). It is more pronounced in the structurally lowermost sequences but only weakly developed in the metaflysch. The resultant mean Sn plane is shallow to moderately -dipping SE, while Ln is gently plunging to the SE, having a single maximum cluster in stereo-plots (Fig. 4c, d). However, field observations revealed that the stretching lineation is strongly folded during subsequent progressive deformation. During Dn_a, several ductile to brittle-ductile thrusts were formed, parallel to the long axis of the island, and are responsible for older-over-younger relationships (Fig. 2). Along these thrusts, Sn displays an ultramylonitic to mylonitic texture, which is more pronounced towards the structurally lowermost thrust sheets.

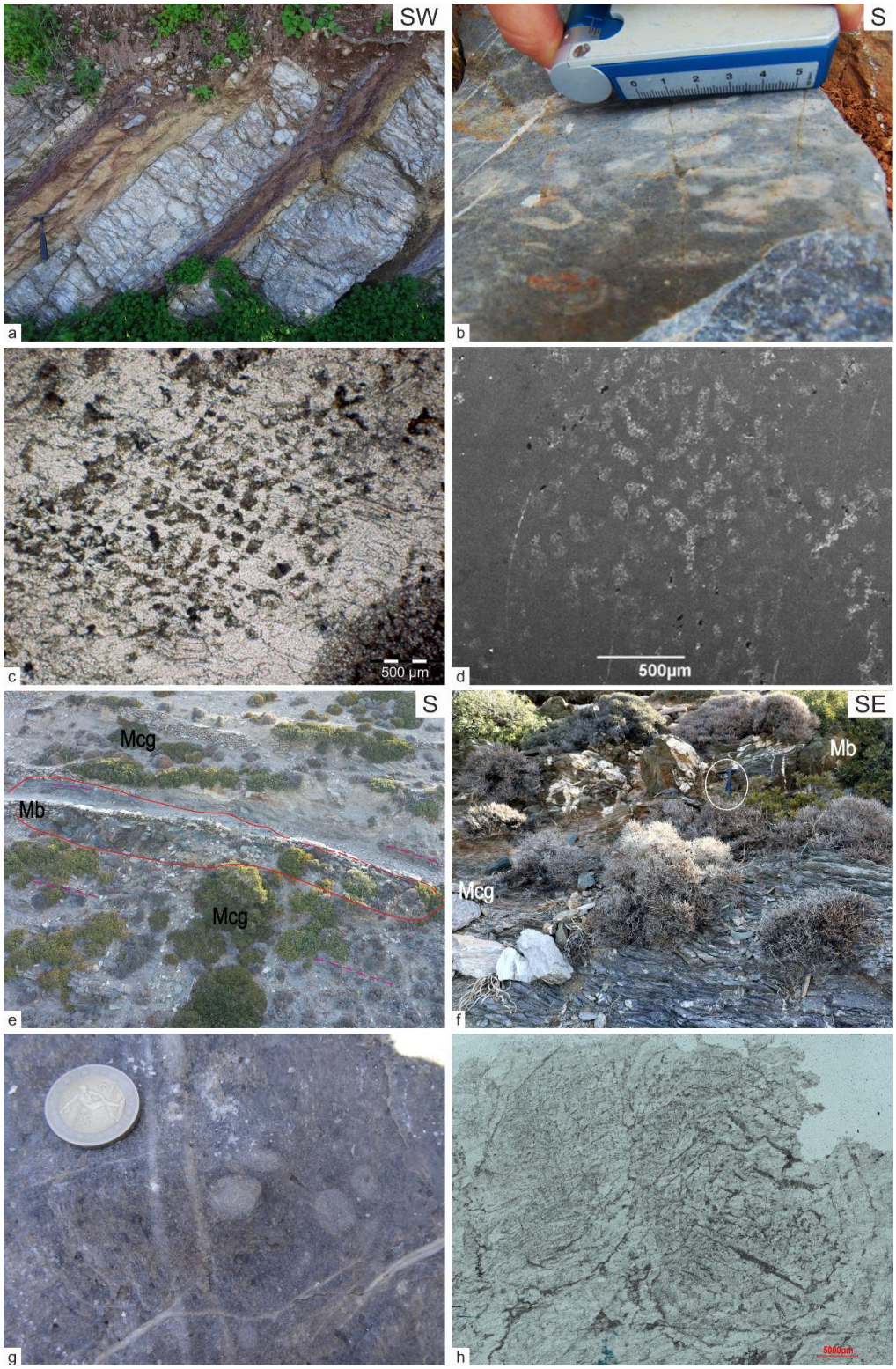

Figure 3: (a) Red-violet to yellow slate (Verrucano) and dolomite alternations of the Kryoneri Formation, in which cleavage fanning can be observed (*36⁰ 54′05′′ N, 025⁰ 58′40′′ E*). (b) Fossiliferous marble (Tholaria Fm.) with gastropods, bivalves (small Megalodontids and Lithiotids) near Tholaria village (*36⁰ 54′56′′ N, 025⁰ 59′35′′ E*). (c-d) Microphotograph (c- random section) and Scanning Electron Microscope (d- SEM) photo of Orbitopsella sp. (e) Drone

picture of the metabasite within the basal metaconglomerate (Kapsala Fm.). The boundaries of the metabasite (red solid line) are illustrated. Note the foliation of both the metabasite and the basal metaconglomerate (pink dotted line). (f) Close-up view of the well- foliated metabasite and metaconglomerate (*36⁰ 50′15′′ N, 025⁰ 51′21′′ E*). (g) Well-preserved. fossils (probable Nummulites sp.) in the conglomeratic/brecciated marble of the Asfondilitis Fm. (*36⁰ 53′06′′ N, 025⁰ 57′44′′ E*). (h) Microphotograph of probable Nummulites sp.

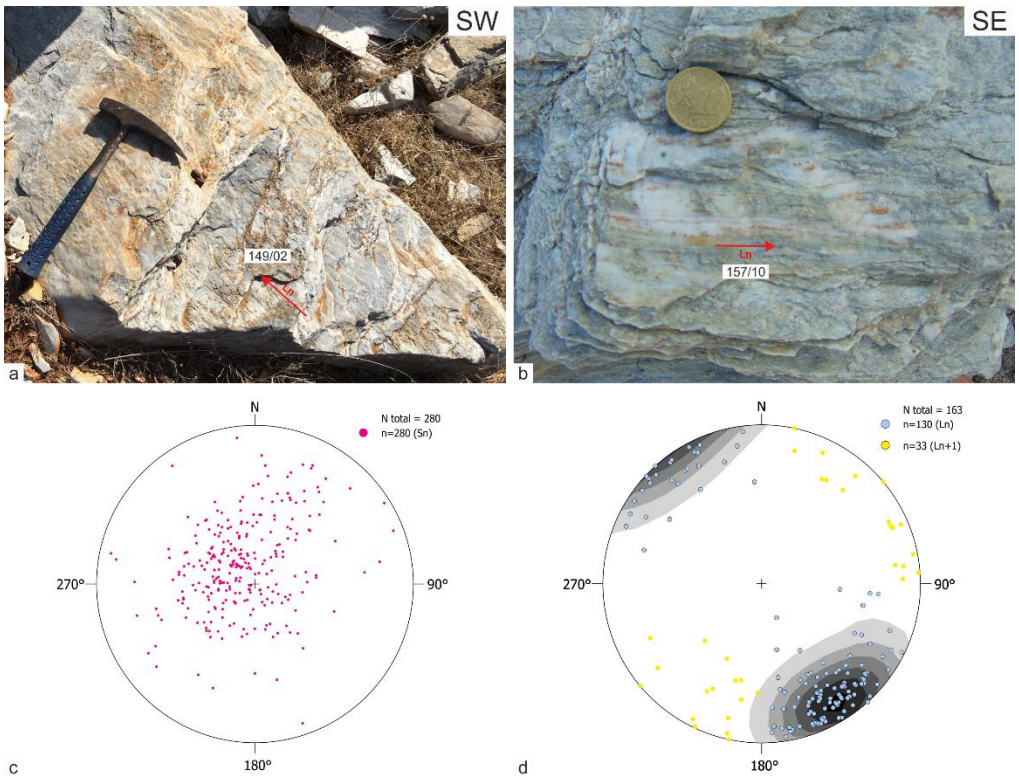

Figure 4: (a) NW-SE stretching lineation on the Sn foliation plane (red arrow) (*36⁰ 50′ 27′′ N, 025⁰ 52′ 01′′ E*). (b) NW-SE stretching lineation of the fibrous carpholite in the basal metaconglomerate of the Kapsala Fm. (red arrow) (*36⁰ 50′ 16′′ N, 025⁰ 51′ 22′′ E*). (c) Stereoplots of the poles to Sn foliation planes (equal-area projection, lower hemisphere). (d) Stereoplots of the Ln stretching and Ln_{+1} intersection lineation (equal-area projection, lower hemisphere). Note the contour diagram illustrating a main maximum of the Ln in the SE quadrant.

Several kinematic indicators such as δ-clasts, asymmetric shear bands, and domino boudinage reveal a dominant top-to-the NW sense of shear (Fig. 5a). A consistent NW-ward shear sense is also recorded in the proto-mylonitic fabric of the metabasite thin section (Fig. 5b). Analyzed kinematic criteria in the structurally

higher thrust sheets (e.g., flanking structures) display opposing kinematics with top-to-the NW and SE sense of shear (Fig. 5c).

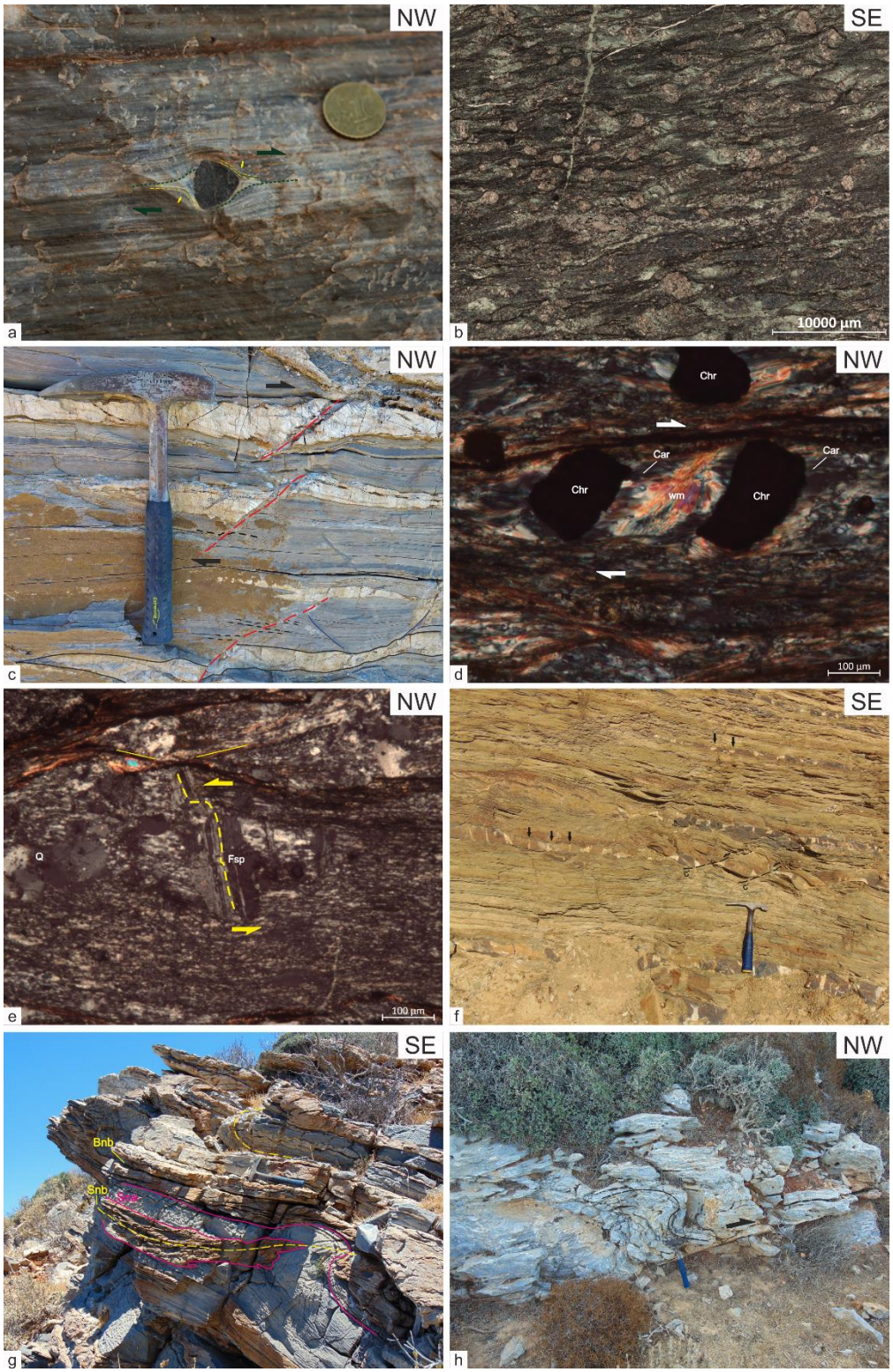

Figure 5: (a-e) All sections parallel to the stretching lineation Ln and perpendicular to the main foliation Sn. (a) Delta-type clast in the ultramylonitic blue gray marble, indicating top-to-the NW shearing. The green dotted lines depict the trace of the tails, while the yellow

dotted lines and arrows indicate the embayment of the foliation (*36⁰ 51′13′′ N, 025⁰ 53′52′′ E*) (b) Top-to-the NW S-C' shear bands in the proto-mylonitic fabric of the metabasite. (c) Antithetic-type flanking structures displaying top-to-the NW shear sense with counter-shearing slip along secondary shear zones in the metachert marble of the Chozoviotissa Fm. Note that the marker horizons (black dotted lines) exhibit a reverse drag along the secondary shear zone (red dotted line). Conjugate shear bands (blue solid lines) display opposing kinematics (*36⁰ 47′40′′ N, 025⁰ 45′59′′E*). (d) Photomicrograph of fibrous Ferro-Mg carpholite between a boudinaged chromite grain in the basal metaconglomerate. The alignment of the carpholite parallel to the main foliation within the matrix, shows its syn-tectonic growth. The rotated boudinaged chromite indicates top-to-the NW shearing. Mineral abbreviations: Car= carpholite, Chr= chromite, wm=white micas. (e) Fractured feldspar, rotated towards the SE (yellow dotted line). Note that phyllosilicate aggregates develop opposing C' planes (yellow solid lines) (Q=quartz, Fsp=feldspar). (f) Asymmetric shear band boudinage in the Late Triassic Richti Fm., indicating top-to-the NW shearing (black dotted lines). Symmetric torn blocky boudinage indicates general shear. Note the white calcite infill in the interboudin areas (black arrows) (*36⁰ 51′34′′ N, 025⁰ 55′25′′ E*). (g) Type-3 interference fold pattern (pink solid line-trace of Sn_a foliation, yellow dotted line-trace of the axial planar foliation). Bn_b isoclinal progressive folds refold Sn_{a-b} foliations. Note the shear band boudinage of the metachert layer (orange dotted line) (*36⁰ 51′44′′ N, 025⁰ 54′59′′ E*). (h) NE-SW folding accompanied by Dn_b brittle-ductile to brittle thrusting with top-to-the NW kinematics (*36⁰ 51′10′′ N, 025⁰ 53′36′′ E*).

Similar kinematics are also observed in thin sections of the clastic sequences. Boudinaged chromite grains in the metaconglomerate matrix indicate top-to-the NW shearing (Fig. 5d, e), while phyllosilicate aggregates in the metaflysch and the metaconglomerate matrix show both top-to-the NW and SE shear sense.

The progressive Dn_b deformation stage includes isoclinal to tight NW-vergent Fn_b folds with NE-SW Bn_b axes which refold the previous Sn foliation. An axial planar foliation Sn_b is developed, associated with a NE-SW intersection lineation (Ln_b) parallel to the (Fn_b) fold axes. These folds are partly responsible for stratigraphic repetitions observed throughout the island. In the fold limbs, symmetric boudinage and pinch-and-swell structures are formed in the Chozoviotissa and Richti Fm. (Fig. 5f). Refolding structures are most evident in the Chozoviotissa Fm. since the

metacherts are marker layers, revealing a hook-shaped type-3 interference pattern (Fig. 5g). Eventually, the Fn_b folds show a brittle-ductile to brittle character often accompanied by mesoscale thrusting, defining an internal deformation pattern with a dominant top-to-the NW shearing (Fig. 5h). As previously mentioned, thrusting probably commenced earlier in Dn_a.

It is noteworthy that the shear sense indicators of the Dn_{a-b} deformation episodes indicate a consistent top-to-the NW sense of movement. However, opposing top-to-SE kinematics are also observed. This signifies the contribution of an additional coaxial component, suggesting an overall general shear deformation developed under NW-SE contraction. The involvement of the coaxial component is also evident by the development of symmetric boudinage, implying that the pure shear component was significant.

The subsequent Dn_{+1} episode represents the last stage of the compressional phase. The most characteristic features of Dn_{+1} are mesoscale gently SW-dipping thrust planes, and kink-type folds. On some outcrops, several arrays of en echelon quartz or calcite-filled tension gashes are observed in the upper stratigraphic levels of the metaflysch. Kinematic criteria such as striations on the thrust planes revealed opposing kinematics of both top-to-the NE and SW shear sense (Fig. 6a, b). In thin sections, the intense pressure solution cleavage and shortened calcite veins indicate a high coaxial component. Although these structures are also generated during a general shear, the main difference with the previously described stages of the Dn_{a-b} is the change of the maximum principal axis (σ1) orientation, implying contraction in a NE-SW direction.

4.2. Extensional deformation phase $Dn_{+2/3}$

The Dn_{+2} includes low-angle discrete shear zones and shallow to steep faults. Often, these faults represent discrete zones involving cm to m thick non-cohesive meso- to ultra-cataclasites observed primarily on the meta-siliciclastic lithologies of the Amorgos Unit. Moderate to high-angle normal faults, dipping towards ESE root into these cataclastic zones (Fig. 6c, d). Shear sense criteria such as normal drag

geometries combined with fault striations indicate overall top-to-the ESE movements.

Late high-angle normal faulting (Dn_{+3}) is related to the final stage deformation and cut through all previous structures observed throughout the island. Two sets of normal faults were identified, trending NW-SE to E-W and NE-SW, respectively. The first set includes moderate to steeply dipping faults, and based on cross-cutting relationships, is older. The second set, comprising the neotectonic normal faults, is mainly located along the southern and northern coasts and coincides with the long axis of Amorgos Island.

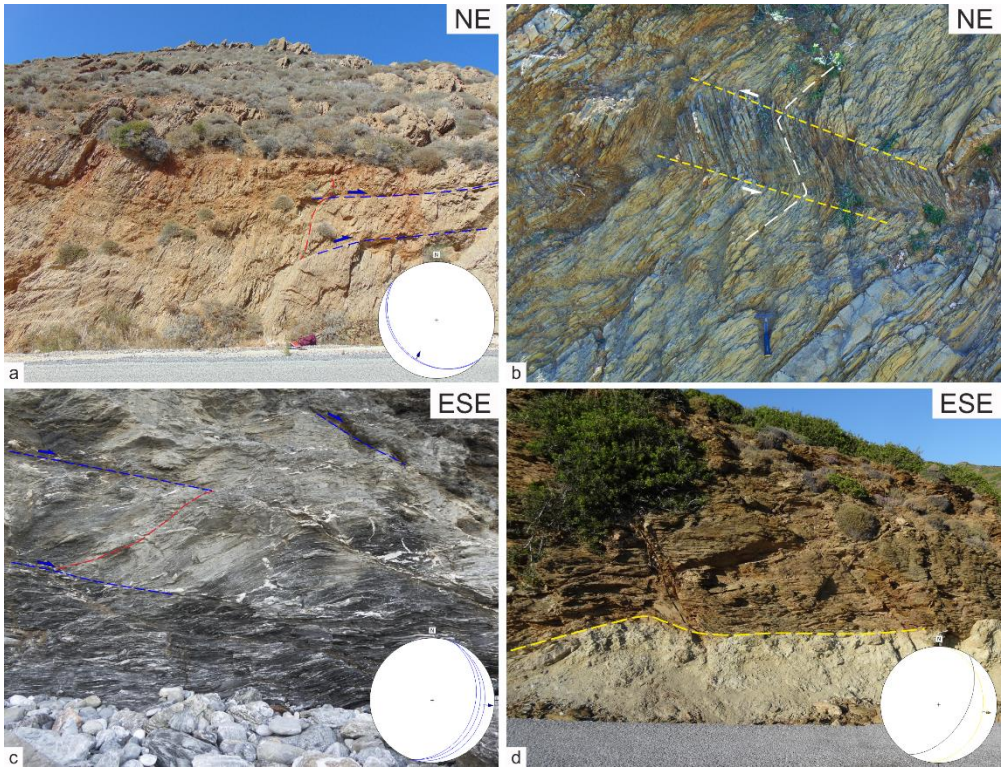

Figure 6: (a) Thrust planes in the metaflysch indicating top-to-the NE thrusting (blue dotted line). Note the drag on either side of the thrusts (red solid line). Stereoplot of the thrust plane and striation is depicted in the lower right corner (*36⁰ 54′ 32′′ N, 025⁰ 58′ 28′′ E*). (b) Kink-type fold in the metaflysch developing an angular relationship between the kinked and unkinked foliation (yellow dotted lines- trace of the kinked boundaries) (*36⁰ 54′ 50′′ N, 025⁰ 58′ 45′′ E*). (c) Low-angle discrete SSE-dipping brittle fault zones (blue dotted line) in the graphite-rich layers of the metaflysch. The normal drag is also depicted (red dotted line) (*36⁰ 47′ 10′′N, 025⁰ 49′ 40′′E*). Stereoplot of the fault plane and striation is depicted in the lower right corner. (d) Non-cohesive cataclasite at higher structural levels in the metaflysch (yellow

dotted line). Note the high-angle fault with normal drag rooting into the cataclastic zone (black dotted line) (*36⁰ 47′ 20′′N, 025⁰ 49′ 45′′E*). Stereoplot of the thrust plane and striation is depicted in the lower right corner.

5. Detrital zircon U-Pb geochronology and results

5.1. Methodology

Detrital zircon (DZ) U-Pb geochronology was applied to meta-siliciclastic samples spanning all tectono-stratigraphic units exposed on the island of Amorgos (1) to provide constraints on the maximum deposition ages (MDAs) and (2) unravel detrital provenance to shed light on the tectonic affinity of the different tectonic units.

Zircons from all samples were separated at the UT Chron Laboratory at the University of Texas at Austin, using standard mineral separation techniques, including crushing, pulverizing, water table concentrating, magnetic and heavy liquid (Bromoform and Methylene Iodide) separations. Extracted zircon grains were sprinkle-mounted on double-sided adhesive tape on 1-inch polycarbonate discs.

Zircon U-Pb analysis was performed by depth-profile Laser Ablation- Inductively Coupled Plasma- Mass Spectrometry (LA-ICP-MS), following procedures detailed by Marsh and Stockli (2015) and Hart et al. (2016), on unpolished zircons via depth-profile LA-ICP-MS using a PhotonMachine Analyte G.2 excimer laser with a large-volume Helex cell connected to a Thermo Element2 ICP-MS. Depth profile U-Pb analysis allows differentiating between metamorphic and magmatic zircon ages – critically important for the determination of maximum depositional ages (e.g., Poulaki et al., 2020, 2021). GJ1 was used as the primary reference standard (601.7±13 Ma) (Jackson et al., 2004) and Plešovice as secondary reference standard (337.1±0.4 Ma) (Sláma et al., 2008). Corrections were applied using the IgorPro based on Iolite 3.4 software (Paton et al., 2010) with the VisualAge reduction scheme (Petrus and Kamber 2012). Individual grain U-Pb ages are reported with 2σ uncertainties. For U-Pb dates <850 Ma, the $^{206}Pb/^{238}U$ dates are taken for the reported U-Pb age, and for dates >850 Ma, the $^{207}Pb/^{206}Pb$ date is reported. A 15% $^{206}Pb/^{238}U$ vs. $^{207}Pb/^{235}U$ discordance filter and 10% error filter is applied to $^{206}Pb/^{238}U$ ages. A 30% $^{206}Pb/^{238}U$ vs $^{207}Pb/^{206}Pb$ discordance filter was applied to

$^{207}Pb/^{206}Pb$ ages. The detritalPy Python script (Sharman et al., 2018) is used for data representation and plot samples in Kernel Density Estimates (KDEs). Concordant ages and all analytical data are reported in the Supplementary Data (Figure S1, S2, Table S1). All sample localities are also shown in Fig. 2.

5.2. Results

5.2.1. Metaflysch

The analyzed samples from the metaflysch are strongly foliated, fine to medium-grained, composed mainly of calcite, quartz, and minor phyllosilicate minerals. Zircon is also included as asseccory.

The youngest DZ age cluster of the sample SLAm1907 yielded MDAs at about 216±2 Ma (Norian) (Fig. 7a). It is dominated by Precambrian DZ age mode (27%), an Early Paleozoic (22%) age mode and a major Carboniferous (36%) DZ age mode with a prominent peak at ~340 Ma. The sample also contains subordinate Permian (6%) and Triassic (6%) DZ age modes.

Sample SLAm1909 yielded an MDA estimate of 224±1 Ma (Norian). The DZ age spectrum is quite similar to SLAm1907, containing Precambrian (31%), Early Paleozoic (13%), and a prominent Carboniferous (33%) DZ age component. The sample is characterized by a slightly higher proportion of Permian (7%) and Triassic (15%) age modes.

Sample SLAm1933 yielded older MDAs at ~237±1 Ma (Ladinian-Carnian). The DZ age spectra exhibit slightly smaller Precambrian (22%) and early Paleozoic (17%) DZ age modes – with the early Paleozoic showing an Ordovician (13%) age peak at ~446 Ma but lacking any Silurian ages. The sample also comprises a major Carboniferous (36%) age mode and subordinate Permian (4%) and Triassic (9%) DZ ages.

Sample SLAm1915 yielded the oldest Triassic MDAs at about 244±1 (Anisian) compared to the metaflysch samples described above. It is dominated by Precambrian (44%) ages, with a prominent peak at ~620 Ma, but exhibits fewer early Paleozoic (16%) zircons with minor Silurian (10%) and Devonian (6%) modes, while

total lacking Cambrian DZ ages. Like the other samples, it comprises a significant Carboniferous (30%) age mode and only a few Triassic (8%) ages.

Sample SLAm1920 yielded the youngest MDA of ~202±1 (Rhaetian) of all samples. As with the other flysch samples, its DZ age spectra is dominated by Precambrian (30%), early Paleozoic (14%), and Carboniferous (33%) age modes and minor Permian (4%), Triassic (11%), and Jurassic (4%) DZ age components.

Sample SLAm1916 yielded an MDA of ~203±1 Ma (Rhaetian) and contains equal major Precambrian (26%) and Carboniferous (26%) DZ age components. In contrast, the early Paleozoic (10%) is only minor, while the Triassic (21%) and Permian (8%) DZ age modes are more prominent.

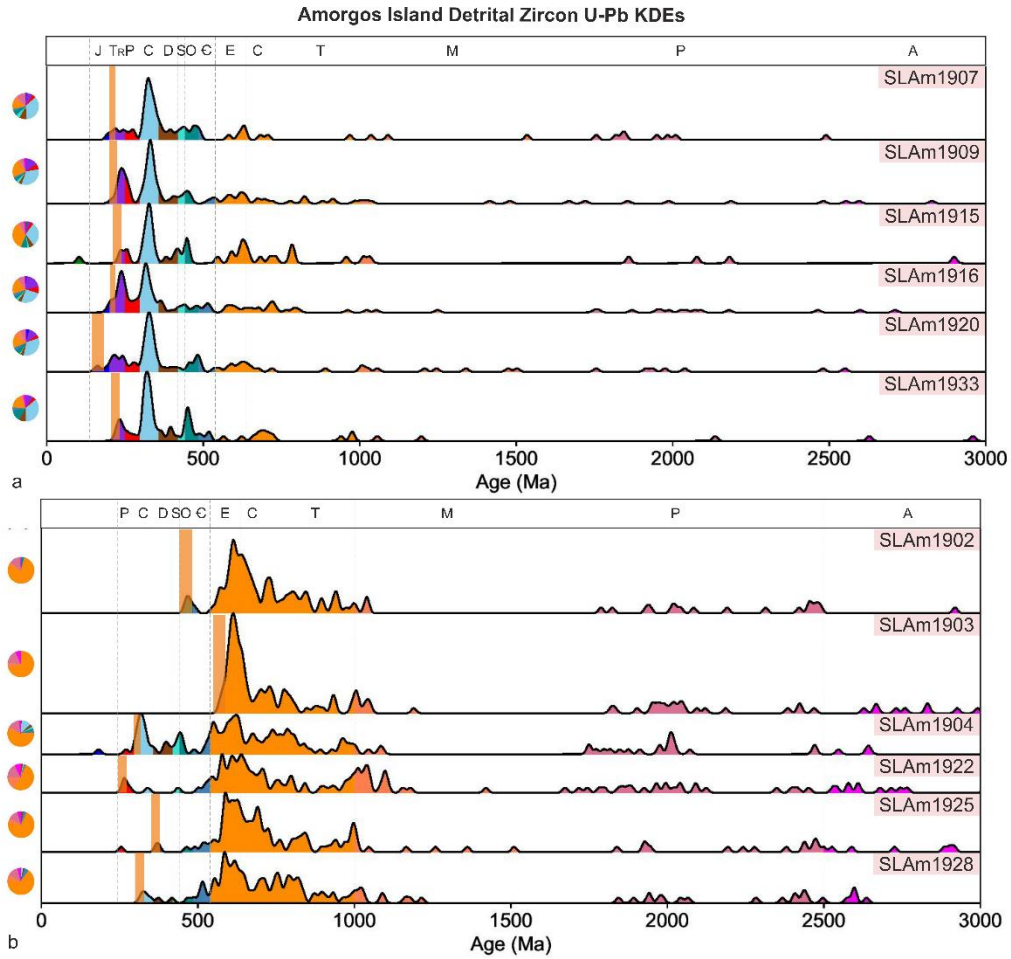

Figure 7: (a) U-Pb KDEs results displaying the detrital zircon population for the metaflysch. (b) U-Pb KDEs results displaying the detrital zircon population for the basal metaconglomerate (Kapsala Fm.). Compiled data from 3000-0 Ma for each sample and

proportions of each age mode in the pie diagrams are illustrated. MDAs are depicted in orange bars.

5.2.2. Kapsala Formation

Samples collected from Kapsala Fm. are both from the matrix and the clasts (Fig. 7b). The samples SLAm1904, SLAm1922, SLAm1925, and SLAm1928 are inequigranular medium-coarse grained, representing the matrix of Kapsala Fm. The main minerals are quartz, feldspar, micas, and zircon, and hematite as accessory. The samples SLAm1902 and SLAm1903 represent quartzite and quartz-mica schist clasts, respectively. The quartzite is non-foliated coarse-grained, composed entirely of quartz with minor micas. Zircon is also observed as accessory. The quartz-mica schist is well-foliated medium to coarse-grained, consisting of quartz, feldspar, white micas, chlorite, and zircon as accessory.

Sample SLAm1902 yielded an MDA of 471±2 Ma (Lower Ordovician). It contains minor Paleoproterozoic (13%) and Mesoproterozoic (4%) age modes and a dominant Neoproterozoic (80%) DZ component, comprising Tonian (29%), Cryogenian (21%), and Ediacaran (30%) zircon ages. Only very few DZ are Cambrian (4%) and Ordovician (4%) in age.

Sample SLAm1903 yielded an Ediacaran MDA of 573±3 Ma and is characterized by subordinate Archean (6%), Paleoproterozoic (16%), and Mesoproterozoic (6%) ages and predominant Neoproterozoic (70%) age mode comprising Tonian (20%), Cryogenian (19%), and Ediacaran (32%) ages.

Sample SLAm1904 from the Xylokeratidi area was collected from the metaconglomerate matrix and yielded an MDA of 304±2 Ma (Late Pennsylvanian). It contains a moderate Archean-Paleoproterozoic (15%) age mode but largely lacks Mesoproterozoic (3%) DZ ages. The spectrum is dominated by Neoproterozoic ages (58%), but unlike the clasts, contains younger early Paleozoic (8%) and Carboniferous (12%) with a prominent Pennsylvanian peak.

Sample SLAm1922 yielded an MDA of 263±2 Ma (Middle Permian). The DZ spectrum is characterized by Archean-Paleoproterozoic (25%), Mesoproterozoic (15%), and

Neoproterozoic (50%) DZ age modes. The dominant Neoproterozoic mode includes similar proportions of Tonian (15%), Cryogenian (16%), and Ediacaran (19%) ages. Subordinate Paleozoic zircon ages comprise Cambrian (2%) and Permian (5%) DZ modes but lack Ordovician and Carboniferous zircons.

Sample SLAm1925 was collected from Profitis Ilias Cape. The youngest detrital zircons yielded a Lower Devonian MDA of 413±4 Ma. The DZ spectrum exhibits diminished Archean-Paleoproterozoic (17%) and Mesoproterozoic (6%) age modes and a dominated Neoproterozoic (69%) component, consisting of Tonian (22%), Cryogenian (21%), and Ediacaran (26%) zircons. A minor DZ component comprises Cambrian DZ ages (3%).

Sample SLAm1928 yielded a Carboniferous (Middle Mississippian) MDA of 332±2 Ma. The DZ age spectrum is quite similar to that of sample SLAm1925 with Archean-Paleoproterozoic (15%), Mesoproterozoic (8%), and dominant Neoproterozoic (66%) DZ age components. The Neoproterozoic DZ component comprises Tonian (27%), Cryogenian (15%), Ediacaran (24%) ages. The sample also exhibits minor Cambrian (5%), Devonian (1%), and Carboniferous (4%) DZ ages.

6. (U-Th)/He zircon dating

6.1. Methodology

Zircon (U-Th)/He low-temperature thermochronometry has become a powerful tool for obtaining thermal histories to quantify the cooling and exhumation history of upper-crustal rocks (e.g., Stockli, 2005). It is characterized by a nominal closure temperature of ~180-200 °and a zircon He Partial Retention Zone (PRZ) spanning from ~130-180 °C (Reiners, 2005; Wolfe and Stockli, 2010). Nine samples from the Kapsala Fm and the metaflysch were analyzed, focusing on the exhumation history of the Xylokeratidi area, where a detachment or a thrust plane has been proposed (Rosenbaum et al., 2007; Ring et al., 2009; Chatzaras et al., 2011). Zircon grains were handpicked and sealed into Pt tubes for in-vacuum laser heating and He analysis by quadrupole noble-gas mass-spectrometry using a ^{3}He isotopic tracer. Degassed zircons were dissolved using HF-HNO_3 pressure vessel digestion and U, Th, and Sm concentrations determined by isotope-dilution solution ICP-MS analysis. zHe are

presented as both individual aliquot ages and mean sample ages. Cited zHe uncertainties for single aliquots are standard errors derived from intra-laboratory standard reproducibility of 8%. Uncertainties for mean samples ages are given as the standard deviation. All results are described below and are presented in the Supplementary Data (Table S2).

6.2. Results

Five samples were analyzed from the Kapsala Fm. and yielded mean ages that range from 17.5±2.3 to 13.9±1.1 Ma. More specifically, from the Xylokeratidi area, sample SLAm1902 yielded zHe ages that range from 47.2±3.8 to 5.2±0.4. Excluding two outliers (47.2±3.8 and 5.2±0.4), the mean age for this sample is 16.6±1.3 Ma. Sample SLAm1903 yielded ages that span from 17.8± 1.4 to 14.9±1.2 Ma with a mean age of 15.7±1.3 Ma, while the sample SLAm1904 a mean age at about 17.5±2.3 Ma. Sample SLAm1925 yielded the youngest mean age of 13.9±1.1 Ma. Sample SLAm1922 yielded a similar mean age to the sample SLAm1904 of 17.0±1.4 Ma. From NE Amorgos, metaflysch samples SLAm1931 and SLAm1907 were analyzed. SLAm1931 yielded a mean age of 18.3±1.5 Ma, while SLAm1907 exhibits ages ranging from 36.4±2.9 to 19.2±1.5 Ma, indicative of partial resetting. Similarly, sample SLAm1920 from the central part of the island yielded ages ranging from 44.9±3.6 to 17.8±1.4 Ma, suggestive of partial resetting. In contrast, a metaflysch sample (SLAm1916) from the southwestern part of Amorgos yielded a completely reset mean age of 14.6±1.2 Ma.

7. Discussion

7.1. Lithostratigraphy of the Amorgos Unit

Amorgos Unit presents a complex stratigraphy and structural architecture that has been the subject of considerable debate in the literature. Some authors have argued for the existence of two tectonometamorphic units separated either by a detachment or a thrust fault (Dürr, 1985; Rosenbaum et al., 2007; Ring et al., 2009; Chatzaras et al., 2011) and assigning them to the External Hellenides. This view has stemmed from field observations and distinctive high pressure/low temperature mineral occurrences observed in rocks on Amorgos (Theye et al., 1992; Rosenbaum

et al., 2007). Rosenbaum et al. (2007) and Ring et al. (2009) proposed a folded brittle-ductile detachment with top-to-the NW shearing, juxtaposing a higher-grade HP metabasite unit against the low-grade Amorgos Unit. On the other hand, Chatzaras et al. (2011) suggested NW-ward imbrication of HP rocks correlated to the CBU between the equivalent Menderes Cover of the Amorgos Unit. An alternative view for a single unit affected by internal thrusting was originally proposed by Minoux (1980) and Fytrolakis et al. (1981).

Geological mapping and structural analysis revealed that Amorgos Unit consists of sedimentary rocks characterized by vertical and lateral sedimentary facies variations that recorded significant differences in the paleogeographic and tectonic depositional setting. In several locations, the metaconglomerate Kapsala Fm. forms the base of the Amorgos Unit. No tectonic contact or a tectonic fault was identified in the field between the metabasite and the surrounding over- and underlying metaconglomerate layers. Furthermore, all the rocks share the same Sn_a foliation and the NW-SE Ln_a stretching lineation. No angular relationship was observed between the foliation planes. The metabasite shows a protomylonitic fabric with a top-to-NW sense of shear, the same as the kinematics of Dn_a. These are strong indications that the metabasite and the country rocks have been affected by the Dn_a event. (U-Th)/He zircon ages obtained from the high-grade clasts/olistoliths, the matrix, next to the metabasite, and the metaflysch, have all recorded similar Burdigalian – Langhian ages. Ring et al. (2009) report similar apatite FT ages for the metabasite. Therefore, these rocks have been together since the Dn_a stage, excluding the existence of a detachment fault.

However, the distinctly different P-T history of the metabasite and the country metaconglomerate (Rosenbaum et al., 2007; Ring et al., 2009) cannot exclude a possible thrust fault, as was previously suggested by Chatzaras et al. (2011). Since there are no geochronological data for the HP event of the metabasite, two feasible scenarios are proposed. First, assuming that the HP event could be as old as Carboniferous (Variscan), the higher HP conditions (Rosenbaum et al., 2007) reflect a different event, unrelated to the Cenozoic lower-grade HP event recorded in the Fe-Mg carpholite-bearing country rocks. In this concept, it appears possible that the

metabasite could represent an exotic huge block/olistolith within the metaconglomerate matrix, and possibly reflects product of transport processes associated with Paleotethys closure. Such olistoliths are commonly resulted from gravitational movements (Festa et al., 2016). Alternatively, the metabasite represents a tectonic slice incorporated within the Kapsala Fm. in association with advancing thrust sheets during the NW-ward back-thrusting. In such a scenario, the juxtaposition should be an early event later overprinted by the Dn_a structures. Either way, the similar characteristics and zHe cooling ages of both the metabasite and metaconglomerate suggest their common exhumation history.

The characteristic features of the terrigenous Kapsala Fm. suggest a tectonic depositional environment in a Permian isolated rift basin setting, in which exhumed high-grade rocks were eroded and redeposited within proximal coarse-clastics conglomerates. The high-grade clasts/olistoliths are characterized by latest Neoproterozoic MDAs and Pan-African/Gondwanan provenance signatures. In contrast, the metaconglomeratic matrix exhibit mainly Permian MDAs and a more complex provenance signature containing both Pan-Africa/Gondwanan and Carboniferous (Variscan s.l.) affinities. Occurrences of carbonate blocks and other variable lithologies of intra-conglomerate lenses indicate both erosion of basement as well as syn-rift carbonate sedimentation. The Mid-Permian DZ MDA estimates for the Kapsala Fm. appear reasonable or slightly older than the actual dispositional age as constrained by the overlying Triassic sequences that bear similarities with the Permo-Triassic clastic sequences elsewhere in the Hellenides (e.g., Attica, central Evia, Crete). All these sequences are associated with the closure of Paleotethys (Clement, 1968; De Bono 1998; De Bono et al., 2001; Stampfli and Borel 2002; Stampfli et al., 2003; Zulauf et al., 2015, 2018). As a result, the terrigenous Kapsala Fm. cannot be placed at a higher stratigraphic level as proposed by Minoux (1980) and Fytrolakis et al. (1981), but rather forms the Permo-Triassic stratigraphic base of the Amorgos Unit.

The transition from the Kapsala Fm. to the overlying carbonates is marked by the Kryoneri Fm., a Verrucano-type unit, and its lateral equivalents, the greenish/yellowish slates of the Richti Fm. These lithofacies characterize an oxidizing

environment and can be compared with similar lithologies found in several regions in the Alpine-Mediterranean realm (Baud et al., 1990; De Bono 1998; De Bono et al., 2001; Zulauf et al., 2008; Cassinis et al., 2018). The Upper Triassic- Early Jurassic carbonates, constrained by microfossils of *Megalodonts*, *Corals* (Minoux, 1980; Fytrolakis et al., 1981; Dürr, 1985; this study), *Lithiotids* and *Orbitopsella* (this study, Tholaria Fm.), indicate a shallow marine depositional setting, commonly observed in all parts of the island. In the northeastern Amorgos, the carbonate sequence age-wise extended into the Cretaceous (Krikelas Fm.), preserving *Rudist* fossils (Minoux, 1980; Fytrolakis et al., 1981; Dürr, 1985), suggesting a steady shallow-water depositional environment, with at least one episode of bauxite formation.

The nummulite-bearing debris limestone (now marble) over the Krikelas Fm. signifies that at least part of the Amorgos Unit was in the vicinity of reefal areas during the Early Eocene. However, the central and southwestern parts document pelagic facies as evidenced by the metachert marble of the Chozoviotissa Fm. This differentiation reveals the platform drowning events during the Lower Jurassic (Lias), reflecting the effect of the geodynamic processes at a regional scale. Such different lithological features imply that shallow-water sedimentation probably took place on underwater topographic highs adjacent to basins, where deep-water sediments were deposited. Shallow-water conditions were re-established in the central Amorgos, as evidenced by the non-bauxite bearing Asfondilitis Fm. on top of the Chozoviotissa Fm. via a conglomeratic marble. This conglomeratic marble implies the proximity to the carbonate platform. In stark contrast, the southwestern Amorgos lacks Cretaceous neritic carbonates, and the Chozoviotissa Fm. transitions directly to the metaflysch.

The metaflysch is characterized by significant thickness variations throughout the island. However, there are no significant differences concerning the MDA estimates and the detrital zircon provenance signatures. Hence, the differentiation of a stratigraphically intermediate schist formation at Potamos proposed by Fytrolakis et al. (1981) is not supported by the data. It is far more likely that it is a structural intercalation that belongs to the same metaflysch. Similarly, the metasediments in Paradesia, assigned variably to the basal metaconglomerate (Minoux, 1980) or the

metaflysch (Dürr, 1985), appear to be part of the metaflysch based on similar MDA estimates and almost identical DZ provenance signatures.

The onset of metaflysch deposition is undoubtedly Eocene as constrained by underlying nummulite-bearing conglomeratic marbles (Minoux, 1980; Fytrolakis et al., 1981; Dürr, 1985; this study). However, no syn-depositional DZ ages were observed. The youngest zircons from the metaflysch cover a narrow range from Ladinian to Lower Jurassic in age. The lack of younger than Jurassic DZ ages from all our metaflysch samples is interesting and is likely attributable to a lack of post-Triassic/Jurassic arc-related volcanic zircon input as observed in other Eocene flysch samples (Seman et al., 2017; Poulaki et al., 2019; Laskari et al., 2022). The lack of such zircons in the source area due source-rock infertility (e.g., carbonates) or sediment transport/bypass. A migration of the depocenters far from an overfilled trench could also play an essential role for MDAs variations (Žák et al., 2020 and references therein). A combination of the above reasons could explain the total absence of younger DZ grains in the Eocene metaflysch. Hence, the depositional age of the metaflysch cannot be constrained by the youngest component of DZ ages. Importantly, the metaflysch overlies both pelagic and shallow-water carbonates of variable age, ranging from Triassic to Eocene, which clearly implies the existence of a significant unconformity at the base of the metaflysch. This unconformity likely reflects syn-depositional shortening deformation and orogenic processes during Eocene flysch deposition.

Hence, the complex stratigraphy of Amorgos appears to record the impact of several major tectonic events: (1) back-arc extension during or after final the closure of Paleotethys in the Permo-Triassic, (2) early Mesozoic tectonic stability and shallow-water carbonate sedimentation, (3) Mid-Late Jurassic to Early Cretaceous obduction of the Axios-Vardar, (4) syn-tectonic flysch deposition during early Cenozoic closure of NeoTethys.

7.2. Provenance of detrital zircons

The new DZ U-Pb age data obtained from the meta-siliciclastic rocks of Amorgos helps to illuminate the possible source terranes and tectonic affinity of the rocks

making of Amorgos. Additionally, these data have the potential to provide important insights into the tectonic setting and the original characteristics of the basins in which the sediments were accumulated.

7.2.1. Kapsala Formation

The DZ age distributions from both the matrix and the clasts/lenses share two main characteristics. They are both (1) dominated by a Neoproterozoic (0.54-1.0 Ga) DZ age mode with varying individual age peaks and (2) exhibit a marked early-middle Mesoproterozoic age gap, containing only Stenian DZ ages (6-16%). The DZ ages of the matrix are predominantly Neoproterozoic, with pronounced Ediacaran age peaks at ~550-575 Ma and 600-625 Ma. This advocates for a dominant recycled Neoproterozoic basement source for the Kapsala Fm. in order to account for the high proportion of Precambrian ages. This assumption is also reinforced by the DZ ages derived from the clasts that show a dominant amount of Neoproterozoic (60-80%) and Paleoproterozoic (13-17%) DZ age proportions. In addition to this major Precambrian DZ input, this formation also exhibits minor Cambrian and Ordovician (1-5%) DZ ages and is notable for a significant Permo-Carboniferous (5-12%) DZ age component.

Based on similar detrital zircon U-Pb provenance characteristics of rocks, four different peri-Gondwanan terranes have been suggested (Dörr et al., 2015 and references therein): (1) the Minoan terranes whose DZ age spectrum contain prominent Cryogenian than Ediacaran age components, with age peaks at around 0.6 Ga and 1.0 Ga, and a clear Mesoproterozoic age gap between 1.1 and 1.6 Ga is recognized, (2) the Armorican terranes that display a higher proportion of Ediacaran than Cryogenian with a notable peak at around 0.54-0.57 Ga, a minor amount of Tonian/Stenian DZ ages (0-3%), and a Mesoproterozoic age gap, (3) the Avalonian terranes characterized by middle-late Neoproterozoic ages, a lack of Tonian ages and minor to moderate Mesoproterozoic input (9-30%), and (4) Baltic terranes that display a similar DZ age spectrum, but a lower proportion of Ediacaran DZ ages (~10%) and elevated Mesoproterozoic DZ ages. Tonian/Stenian zircons (up to 40%) with a peak at around 1.0 Ga, are restricted to the Eastern Gondwana and more

specifically to the eastern Sahara Metacraton margin along the contact with the Arabian-Nubia Shield that also involves Cryogenian crust and Tonian/Stenian (Grenvillian) basements (Abdelsalam et al., 2002; Dörr et al., 2015). However, rare modes of Tonian DZ ages are observed in NW Africa, suggesting recycled Precambrian basement rocks (e.g., Morocco, Algeria, Meinhold et al., 2013).

The Minoan terranes that are related to the eastern Gondwana margin appear to be characteristic of the pre-Alpine basement of the External Hellenides (Crete, Peloponnese, Kythira, Xypolias et al., 2006; Zulauf et al., 2007, 2015, 2018; Kydonakis et al., 2014; Dörr et al., 2015). DZ U-Pb ages from the Cycladic basement have also provided evidence for a distinct peri-Gondwanan (Cadomian) affinity (Keay and Lister, 2002; Zlatkin et al., 2018; Flansburg et al., 2019), containing Tonian/Stenian ages (Reischmann, 1998; Keay and Lister, 2002). The Pelagonian zone encompasses an Avalonian-Armorican type terrane highlighted by intrusions of 600-700 Ma and ~530-570 Ma ages (Anders et al., 2005, 2006, 2007; Meinhold et al., 2010; Zlatkin et al., 2018), which are related to the Avalonian-Cadomian orogeny and late Cadomian magmatism, respectively. This Avalonian type terrane served as the basement onto which the Carboniferous-Permian magmatic arc formed in response to northward subduction of a branch of the Paleotethys (Vavassis et al., 2000; Reischmann et al., 2001; Anders et al., 2007). Voluminous Permo-Carboniferous magmatism took place in the most external realm of the Hellenides (Xypolias et al., 2006; Dörr et al., 2015; Zulauf et al., 2015, 2018) and the Attic-Cycladic complex (Engel and Reischmann, 1998; Ring et al., 1999; Tomaschek et al., 2001; Flansburg et al., 2019; Poulaki et al.,2019), suggesting diachronous subduction-related magmatic activity.

The patterns of DZ ages obtained from the Kapsala Fm. (matrix and clasts) point to a contribution of recycled Cadomian and Carboniferous magmatic arc (Variscan) affinities in the source area, suggesting a large catchment and diverse basement source area. DZ signature differences between conglomerate matrix and clast samples in terms of MDA and provenance show that the matrix received more detritus from Paleozoic magmatic sources and/or second-order recycled sediments, better reflecting the entire source area. In contrast, clasts are more locally sourced and more restricted to Neoproterozoic components. The observed 1.1-1.6 Ga age

gap from all samples excludes the westernmost African craton and Laurussian/Baltica sources (Stephan et al., 2019). Tonian-Stenian ages are undoubtedly present in the Kapsala Fm., invoking non-juvenile basement rocks involved in the East African orogeny, making up NE Africa and Arabia. Late Ediacaran- Cambrian magmatic rocks, often referred to as the "younger granites" are exposed in the Eastern Desert of Egypt, and the Sinai (e.g., Eyal et al., 2010; El-Bialy, 2020) and can readily explain the predominant Ediacaran peaks in the Kapsala Fm. Grenvillian-aged basement is rare in Cadomian-type terranes, however, Grenvillian-aged detrital zircons are abundant in the Paleozoic cover of NE Africa (e.g., Stephan et al., 2019). Given these new DZ data, a possible source terrane candidate for supplying sediment for the Kapsala Fm. is the basement and cover rocks from the northern Gondwana margin in NE Africa/Arabia. The prominent Ediacaran age clusters of the Kapsala Fm. with prominent peaks at around ~550-575 Ma and 600-625 Ma point to a basement source with Avalonian-Cadomian or Arabian-Nubian Shield affinities that strongly resembles DZ age patterns observed within the Pelagonian domain. The combination of these DZ ages and a strong Carboniferous input point to the Pelagonian domain as the most likely sediment source for the Upper Permian to Lower Triassic strata on Amorgos. However, these characteristics are also not uncommon for parts of the CB, implying a shared basement history for the Pelagonian and parts of the CB domains. It is also noteworthy that the Phyllite-Quartzite Unit shows very similar provenance signatures, but lacks a prominent Cambrian-Carboniferous signature (Kydonakis et al., 2014; Dörr et al., 2015; Zulauf et al., 2015, 2018; Chatzaras et al., 2016; Seybold et al., 2020), making an unlikely candidate supplier for the Kapsala metaconglomerate. While otherwise dissimilar, the Talea Ori Group, structurally below the Phyllite-Quartzite Unit, contains ample early Paleozoic and Carboniferous detrital zircons (Seybold et al., 2020). In either case, a direct correlation with the Phyllite-Quartzite Unit can be excluded. Hence, it seems most probable that the Kapsala Fm. accumulated in a more internal basin receiving both prominent Precambrian and Carboniferous input, probably from both the CB and the Pelagonian domain. This assumption supports a genetic link or spatial proximity of the CB and the Pelagonian basement as previously proposed by Zlatkin et al. (2018). Importantly, the Kapsala Fm. is characterized by the absence of Triassic

DZ ages, suggesting that either it predated Triassic syn-rift magmatism or, less likely, was spatially excluded from receiving any detritus from the regional volcanic activity.

7.2.2. Metaflysch

The DZ U-Pb age spectra of the metaflysch point to a dominant sediment source, derived from a Carboniferous (Variscan) continental-arc crust, with subsidiary contributions from pre-Variscan crustal sources. This is manifested by a dominant Carboniferous DZ age component (26-32%), compared to a reduced Proterozoic distribution (3-14%). Distinct additional components include Triassic (8-21%) and Jurassic (4%) DZ ages that are present in some metaflysch samples. Similar age spectra have commonly been recognized in Mesozoic sedimentary units derived from the Internal Hellenides (Pelagonian zone) (Seman et al., 2017). The input of Triassic DZ ages is likely linked to protracted syn-rift magmatic activity in either the Pelagonian (Anders et al., 2007) and the ACCC (Reischmann 1998; Tomaschek et al., 2001; Bröcker and Keasling 2006; Bröcker and Pidgeon 2007). It appears most plausible that the Carboniferous and Triassic DZ age components of Amorgos metaflysch were derived from dominant arc- and rift-related felsic magmatic sources with only minor contributions from an older crust.

7.3. Structural evolution of the Amorgos Unit

As briefly described in this study, the structural evolution Amorgos Unit can be subdivided into discrete deformation stages, which involve compressional and extensional episodes. The age of the structural history is bracketed between Late Eocene to Early- Mid Miocene and reflects the different episodes of the Cenozoic Alpine orogenic evolution and the final exhumation in the Aegean domain.

The earliest syn-metamorphic Dn_a episode is responsible for the penetrative structures under low-grade HP metamorphic conditions on the Amorgos Unit, as indicated by the syn-tectonic growth of fibrous Ferro-Mg carpholite. This episode produced ductile fold and thrusts documenting a dominant top-to-the NW shearing that formed the dominant NW-SE stretching lineation and agrees with observations pointed out by Chatzaras et al. (2011). Based on the age of the metaflysch, this stage could be post-Late Eocene. Subsequently, the Dn_a episode is evolved in Dn_b refolded

structures developing an intersection lineation Ln_b with similar kinematics in the frame of a progressive deformation pattern. However, subordinate opposing kinematics with top-to-the SE shearing suggests a general shear deformation developed under NW-SE contraction. These episodes and their kinematics are not compatible with the SW to W-ward translation of the nappes in the Hellenides, pointing to back-thrusting as already proposed by Chatzaras et al. (2011). The development of the back thrusts can be associated with ongoing accretion of sediments and possibly basement rocks, which resulted in the growth and uplift of the wedge (Doglioni et al., 2007; Encinas et al., 2021) and is compatible with a retro-wedge setting. Similar observations have also been documented from different areas in the Hellenides (Clift 1996; Ferriere et al., 2004; Xypolias et al., 2012; Gerogiannis and Xypolias 2017), implying that back-thrusting was not a local process.

Interestingly, the latest Dn_{+1} episode of the compressional stage revealed kinematic criteria that indicate the change of the maximum principal axis (σ1), implying contraction in a NE-SW direction but still under general shear. Therefore, a straightforward assumption is that up to Dn_{+1}, the structural evolution of the Amorgos Unit is characterized by several imbricated thrusts that could explain the intense deformation in the structurally lower lithologies developing the mylonitic texture. Furthermore, these deformational stages are associated with a progressive deformation pattern in a continuous compressional phase, characterizing a Late Eocene- Oligocene successive nappe stacking in an overall syn-orogenic setting in the southern Aegean region (Jolivet and Brun, 2010).

The final stage of the structural evolution of the Amorgos Unit is associated with post-orogenic tectonics in the frame of an extensional deformation setting, accommodated through shallow SSE-dipping normal faults (Dn_{+2}). These brittle structures suggest that this late-stage exhumation process was controlled by structurally shallower normal faults and/or a structurally lower detachment fault. The timing of this extensional event is constrained on the basis of cross-cutting relationships and our new zircon (U-Th)/He data that revealed rapid Early- Mid Miocene (Burdigalian-Langhian) exhumation and cooling below 180-200°C of the Amorgos Unit. These zHe ages partly coincide with the apatite fission-track data

(AFT) reported by Ring et al. (2009) and document exhumation at 18-14 Ma from greater than 200°C to less than 60°C during the Early to Middle Miocene. Only stratigraphically higher flysch samples appear to have resided in the zHe PRZ (<140°C) prior to final exhumation and unroofing, limiting the maximum burial to less than 4 km.

In light of the structural and thermochronometric data discussed above, we conclude that the Cenozoic deformational history of the Amorgos Unit is bracketed between Late Eocene to Early-Middle Miocene. The earliest episodes (Dn_a-Dn_{+1}) were associated with a compressional deformation linked to a Late Eocene-Oligocene compressional syn-orogenic phase affecting the southern Aegean region (Jolivet and Brun, 2010). This phase also coincides with the syn-tectonic deposition of the metaflysch that unconformably overlies various Triassic-Cretaceous carbonates. During Oligo-Miocene times, the convergent deformation front migrated southward (e.g., Crete), where accretion and underplating involved the more external Hellenide units. This resulted in regional back-arc extension dominating most of the Aegean region.

7.4. Regional Correlations

This study of the Amorgos Unit provides critical new insights into its paleogeographic position, tectonic affinity, structural evolution, and exhumation history. In terms of paleogeographic position, previous studies mainly assigned the Amorgos rocks either to the External Hellenides on the basis of *Nummulites* (e.g., Tripolitza-Basal Unit, Minoux, 1980; Fytrolakis et al., 1981; Rosenbaum et al., 2007; Ring et al., 2009) or the Mesozoic Menderes cover sequence (Chatzaras et al., 2011).

However, based on our observations, the Mesozoic carbonates of the Amorgos Unit show a strong pelagic character that is not observed in the Tripolitza and the typical Basal Unit, as this is exposed in Olympus mt. or Evvia Island. The Late Triassic-Early Jurassic Pantokrator-facies carbonates overly a Verrucano-type formation that is comparable to the lithofacies observed in the Pelagonian domain as exposed on Evia, Hydra, or Attica (Baud et al., 1990; De Bono 1998; De Bono et al., 2001) and more external units (e.g., Crete, Zulauf et al., 2008), all of which signal the transition from

the Paleotethyan to the Neotethyan cycle. A metaconglomerate sequence (Kapsala Fm.) is overlain by the Verrucano-facies that resemble the successions observed in Attica (Clement, 1968; Baud et al., 1990).

Our new DZ U-Pb provenance data from the Kapsala Fm. revealed the contribution of a prominent Carboniferous (Variscan) age component that is non-existent in the Phyllite-Quartzite Unit of Crete and Peloponnese (Kydonakis et al., 2014; Dörr et al., 2015; Zulauf et al., 2015, 2018; Chatzaras et al., 2016) therefore a correlation of the two units is unlikely. The same data also argue against a correlation with the units overlying the Menderes basement since the latter completely lacks Carboniferous ages, and thus is incompatible with dominant Variscan DZ signature of the Kapsala Fm. In addition, the low-grade HP/LT record of the Amorgos Unit is also inconsistent with the higher metamorphic conditions (P=10-12 kbar, T= 440 ^{o}C) obtained from the Menderes cover (Rimmelé et al., 2003).

A characteristic lithology of the Amorgos Unit is an Upper Cretaceous bauxite-bearing marble. This marker unit is typical for the internal units of the Hellenides (e.g., Parnassos Unit-B3 bauxite horizon, Sub-Pelagonian Unit) and non-existing in more external units (e.g., Tripolitza Unit- Eocene bauxites). This correlation to the Parnassos B3 bauxite horizon further supports the attribution of the Amorgos Unit to the Pelagonian domain as previously proposed by Minoux (1980) and Laskou and Economou (1991). While nummulite fossils have generally been reported from the external Hellenides (e.g., Gavrovo, Tripolitza, Basal, Ionian), they have also been described from the Pelagonian domain (s.l.) on the northern Argolis peninsula, where the Nummulite-bearing clasts within the Eocene flysch correspond to Lower Eocene reefal facies (Photiades and Skourtsis-Coroneou 1994; Richter et al., 1996). These lithological features show marked similarities between the Amorgos Unit and the Pelagonian flysch in northern Argolis, suggesting that Nummulites are not restricted in the external units. Interestingly, nummulite-bearing clasts have also been found in supra-detachment sediments of Naxos, thought to have originated from the eroded upper plate above the CBU (Jansen 1977). The Amorgos nummulitic limestones might represent an example of these upper-plate limestones.

Most importantly, the structural evolution of the Amorgos Unit in the retro-arc realm is incomparable with the geodynamic setting of the External Hellenides that occupied a frontal position in the Hellenic trench during the Late Eocene. During this time, Amorgos experienced low-grade HP/LT metamorphic conditions synchronous with retro-arc thrusting. In contrast, the external units did not undergo HP/LT metamorphism until early Miocene times (e.g., Phyllite-Quartzite, Crete and Basal Unit, Samos, Ring et al., 1999, 2001), followed by a Late Miocene unroofing.

Despite the temporal similarities of Eocene HP/LT metamorphism in the CBU and the Amorgos Unit, their metamorphic, kinematic, and tectonic evolution are not directly correlated. While the CBU is being subducted and underplated, the Pelagonian Amorgos Unit occupies a retro-arc position in the upper plate of the convergent margin. Similar conclusions can be drawn from their exhumation history that demonstrates slightly diachronous cooling. Widespread middle to late Miocene apatite and zircon (U-Th)/He and fission-track ages record the exhumation history of the CBU (Brichau et al., 2006, 2010; Grasemann et al., 2012; Bargnesi et al., 2013; Bröcker et al., 2013; Soukis and Stockli, 2013; Schneider et al., 2018). In contrast to the lower plate CBU rocks, which have experienced a Late Miocene exhumation, the upper-plate rocks experienced slightly earlier Early-Middle Miocene (~19-13 Ma) cooling (Grasemann et al., 2012; Soukis and Stockli, 2013; Schneider et al., 2018). Published zHe data from rocks in the hanging wall of the Santorini detachment yielded reset at 19-17 Ma and partial reset ages between 36 and 15 Ma (Schneider et al., 2018). We obtained very similar ages from Amorgos, with the Kapsala Fm. recording totally reset ages of 14-18 Ma and the metaflysch exhibiting partially reset zHe ages dispersed between 36 and 17 Ma, implying maximum post-depositional temperatures between 140-180°C. However, two structurally lower metaflysch samples yielded reset ages between 14-18 Ma, suggesting post-depositional burial exceeding ~6 km, likely due to retro-arc thrust sheet burial. It appears plausible that the observed diachronous cooling histories reflect the fact that upper-plate units (e.g., Amorgos or Santorini) record and preserve the onset of upper-crustal extension. In contrast, the lower-plate CBU units record the younger history of progressive extension and exhumation from deeper structural levels. This apparent

diachroneity has been observed in other large-magnitude extensional systems, such as in the Basin and Range (e.g., Stockli, 2005; Singleton et al., 2014).

From the above points, we conclude that the Amorgos Unit has experienced a strikingly different exhumation history with zHe cooling ages in the Early-Mid Miocene. This scenario implies a shallower crustal position of Amorgos in the hanging wall structurally above these CBU units. Stratigraphic similarities with other Pelagonian rocks, especially the Santorini hanging wall, further support the attribution of Amorgos to the upper plate units. Given the lack of any ophiolitic nappe and discernable evidence for Paleo-Alpine tectonism, commonly observed in the external parts of the Pelagonian domain (e.g., Parnassos Unit), we propose that Amorgos was paleogeographically located at the southern margin of Pelagonia. In this scenario, Amorgos would have formed the link between the Pelagonian domain of continental Greece and that of the Aegean region. Amorgos and Santorini represent a remnant of the Pelagonian upper plate that is now mostly eroded in the Cycladic archipelago.

7.5. Permo-Triassic to Miocene paleogeographic evolution of Amorgos Unit

Integrating the different aspects of lithostratigraphy, structural evolution, exhumation, and regional correlations of the Amorgos Unit with other units of the Pelagonian domain, a model for the Late Permian to Late Miocene tectonic paleogeographic evolution is developed in the following paragraphs.

7.5.1. Late Permian

In the Late Permian, along the southern margin of SE Europe, composed of previously accreted Gondwanan terranes, the ongoing northward subduction of the Paleotethys resulted in widespread voluminous Carboniferous - Permian continental arc magmatism in the Pelagonian domain (Fig. 8a). The southern passive continental margin of the Paleotethys formed the depositional environment of the Phyllite-Quartzite Unit (Stampfli et al., 2003; Zulauf et al., 2015, 2018). During ongoing Paleotethys subduction, Cimmerian terranes detached from the northern Gondwana margin, resulting in the nascent opening of the Neotethys (Robertson et al., 1996; Stampfli and Borel 2002; Zulauf et al., 2018). Paleotethys slab roll-back results in the

development of Permian intra-arc and back-arc basin(s) (Stampfli and Borel 2002; Stampfli et al., 2013; Flansburg et al., 2019). The onset of basin formation during early stages of rifting was marked by early Verrucano-type deposits exposed in Evia, Hydra, and Salamina (Baud et al., 1991; De Bono 1998; De Bono et al., 2001). These extensional basins within the back-arc realm of the northern Paleotethyan margin also formed the depositional environment of the syn-tectonic Kapsala Fm., receiving detritus from the exhumed and eroding Variscan and Cadomian rocks (Vavassis et al., 2000; Poulaki et al., 2019).

7.5.2. Early-Mid Triassic

During the Early to Mid Triassic, Neotethyan seafloor spreading accelerated during final closure of the Paleotethys (Fig. 8b). The Pelagonian margin continued to extend and neck probably in response to the ongoing slab roll-back, leading to major rifting and continental break-up, forming the future Pindos–CBU domain (Stampfli and Borel 2002). A second cycle of syn-rift Verrucano-type facies deposition occurs in Hydra (Miras formation) Attica, and Evia (Baud et al., 1990; De Bono et al., 2001). Phyllite-Quartzite Unit sedimentation continued along the passive northern margin of the Cimmerian microplate (Zulauf et al., 2015, 2018). In Amorgos, the Kapsala Fm. metaconglomerate continued to accumulate in this back-arc rift basin setting. The recycled material was likely derived from locally sourced fault blocks and regional erosion of Late Proterozoic to Late Paleozoic sequences occupying the Pelagonian hinterland, as suggested by detrital zircon U-Pb data presented in this study.

7.5.3. Mid-Late Triassic

By the Mid to Late Triassic, the Paleotethys was completely subducted, resulting in a soft collision/docking as no evidence for significant crustal thickening is apparent (Stampfli and Borel 2002; Stampfli et al., 2013; Zulauf et al., 2015, 2018) (Fig. 8c). This collision led to the amalgamation of the External Hellenides domain. Deposition of Ravdoucha beds seals the Paleotethyan suture. This appears to be concurrent with a second stage of rifting that took place in the area that will later become the Pindos-CBU domain, possibly enhanced by lithospheric removal. By Carnian times, Amorgos and Santorini are situated at the rifted proximal parts of the southern

Pelagonian continental margin. The Verrucano-type Richti and Kryoneri Fms. were depositing atop the Kapsala Fm.

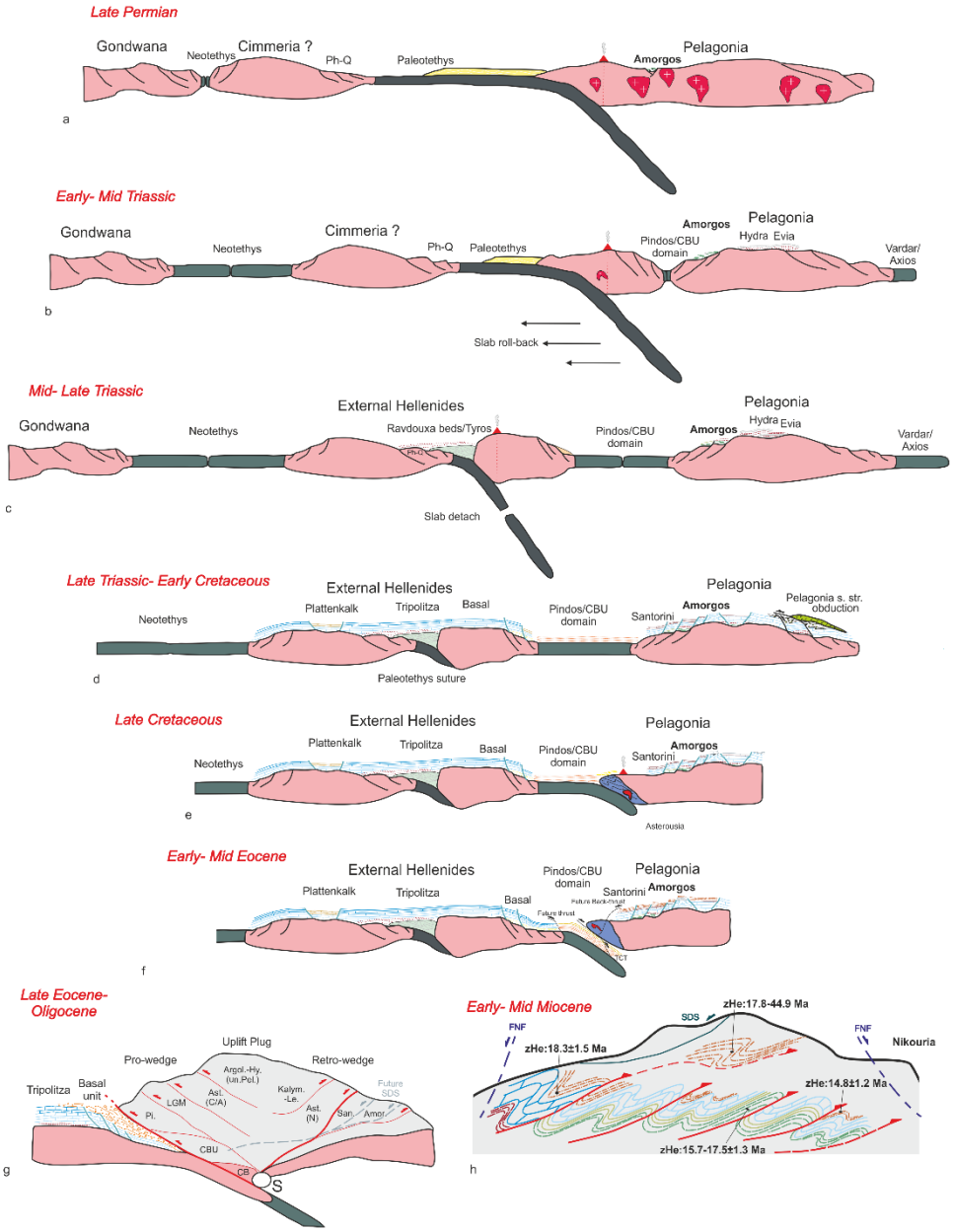

Figure 8: (a-h) Late Permian to Early Late Miocene paleogeographic and tectonic evolution of Amorgos Island. Ph-Q= Phyllite-Quartzite unit, LGM= Low Grade Metamorphic units, CBU= Cycladic Blueschist Unit, TCT= Trans Cycladic Thrust, Pi= Pindos Unit, CB= Cycladic Basement, Ast. (C/A)= Asteroussia (Crete/Anafi), Ast. (N)= Asteroussia (Nikouria), San.= Santorini, Amor.= Amorgos, Kalym.-Le.= Kalymnos-Leros, Argol.-Hy. (un.Pel.)= Argolis-Hydra unmetamorphosed Pelagonian Units, S= Singularity (the point S where one plate underthrusts the other, Willet et al., 1993), SDS= Santorini Detachment System, FNF= Future Neotectonic Faults.

7.5.4. Late Triassic-Early Cretaceous

The Late Triassic – Early Jurassic appears to be characterized by tectonic quiescence and passive margin sedimentation (Fig. 8d). The External Hellenides and Pelagonian domains were characterized by stable shallow-water sedimentation - Pantokrator facies carbonates- along the proximal continental margin, while the deep marine and oceanic domains (Pindos-CBU, Vardar/Axios, East Mediterranean Neotethys) were expanding. In the Middle Jurassic, intra-oceanic subduction initiated in the Vardar Ocean, culminating in ophiolite obduction onto the Pelagonian domain in the Late Jurassic - Early Cretaceous. Drowning of the stable Triassic carbonate platform led to pelagic sedimentation and contemporaneous local uplifts marked by regionally observed bauxite formation (Plattenkalk - Ionian Units Parnassos Unit, Sub-Pelagonian Unit, Baumgartner, 1985; Photiades and Skourtsis-Coroneou 1994; De Bono 1998; Bortolotti et al., 2003, 2013; Papanikolaou et al., 2004; Papanikolaou 2009; Scherreiks et al., 2010; Robertson, 2012; Ferriere et al., 2012, 2016; Schneider et al., 2018). In Amorgos, the Tholaria/Xylokeratidi Fm. represent this shallow-water carbonate depositional episode along the southern Pelagonian margin, while areas characterized by tectonic subsidence shifted to siliceous deep-sea sedimentation, e.g., the Chozoviotissa Fm.

7.5.5. Late Cretaceous

During the Late Cretaceous, shallow to deep marine sedimentation resumed in the Pelagonian domain following the Cenomanian transgression, after a period of erosion (Papanikolaou 2021 and references therein). In contrast, carbonate sedimentation continued uninterrupted in the External Hellenides domain (Fig. 8e). Incipient subduction of the Pindos/CBU domain beneath the southern Pelagonian margin resulted in underplating and accretion synchronous with the development of the Anafi/Asteroussia unit magmatic arc, around ~79-69 Ma (Thomson et al., 1998; Martha et al., 2016, 2018; Koutsovitis et al., 2021). Shallow-water conditions prevailed along the southern Pelagonian margin, and the Krikelas/Asfondilitis Fm. were deposited atop the Tholaria and Chozoviotissa Fm., respectively. The Krikelas - Tholaria sequence occupied a persistent structural high throughout the Mesozoic,

with a short-lived emergence and bauxite formation episode. The pelagic areas shifted to shallow marine sedimentation, and the overlying Upper Cretaceous limestones (Asfondilitis Fm.) were deposited.

7.5.6. Early- Mid Eocene

During the Early-Mid Eocene, the main Alpine orogenic event is fully developed and mainly involves the Pindos/CBU domain (Fig. 8f). The Cycladic units, the Arvi Unit, and the Greenschist Unit were subducted beneath the southern Pelagonian margin, extending from the Argolis to Santorini and Amorgos (Papanikolaou 2009; Martha et al., 2016, 2017, 2018; Menant et al., 2016; Koutsovitis et al., 2021). This mixed siliciclastic-carbonate system was characterized by the input of clastic material shed from the Pelagonian hinterland and shallow carbonates as evidenced by nummulite-bearing limestone clasts (Tataris et al., 1970; Jansen, 1977; Photiades and Skourtsis-Coroneou 1994). In the External Hellenides, carbonate sedimentation continued until the mid-Eocene, when the Basal Unit (e.g., the Tripolitza metamorphosed equivalent) received the first siliciclastic material. In Amorgos, the Cretaceous phase of shallow-water sedimentation was succeeded by a depositional phase characterized by a conglomeratic limestone with Nummulites sp., marking the transition to syn-tectonic flysch sedimentation. The flysch deposits received detritus from the internal units of the Hellenides, as revealed by the DZ U-Pb provenance data. Considering the thickness variations of the flysch from the northeastern to the southwestern Amorgos, overlying both pelagic and shallow-water carbonates, a series of wedge-top basins probably developed.

7.5.7. Late Eocene-Oligocene

The main Alpine orogenic event culminated in the final closure of the Pindos/CBU domain, collision of the Pelagonian domain with the External Hellenides, and subduction/accretion and underplating of the neritic Tripolitza and Basal Units (Fig. 8g). On the pro-wedge side of the subduction zone, the nappes of the overriding plate (Anafi/Asteroussia Unit, Low Grade Metamorphic units of Crete) were thrust southward over the Pindos Unit (Thomson et al., 1998; Martha et al., 2016, 2017; Koutsovitis et al., 2021). After underplating of the Basal Unit, top-to-NW back-thrusting started shortly after or likely during deposition of the Amorgos flysch on

the retro-wedge side. NW-ward back-thrusting caused structural duplication of the stratigraphy, crustal thickening, and high-pressure metamorphism (Minoux 1980; Fytrolakis et al., 1981; Chatzaras et al., 2011; this study). The metabasite could have been incorporated within the basal metaconglomerate during that time. The Anafi/Asteroussia Unit, exposed on Nikouria and Donousa (Dürr 1985), the Upper Cycladic Nappe and the unmetamorphosed Pelagonian-derived units exposed on Argolis, Hydra, Kalymnos and Leros possibly represent remnants of the overthrust units (Baud et al., 1990; Franz et al., 2005; Jolivet et al., 2010; Roche et al., 2019; Grasemann et al., 2021), tectonically burying the Amorgos Unit, including the metaflysch. Subsequently, the entire package was thrust over the more external Hellenic units (Martha et al., 2016, 2017, 2018; Koutsovitis et al., 2021).

7.5.8. Early-Late Miocene

Back-arc extension, due to rapid Hellenic subduction roll-back, started to dominate the Aegean domain, characterized by low-angle detachment systems, exhuming deeply buried units from below the overriding Pelagonian upper plate (Buick 1991; Gautier et al., 1993; Brichau et al., 2006; Jolivet et al., 2010; Grasemann et al., 2012; Schneider et al., 2018) (Fig. 8h). During the Early - Mid Miocene, the Amorgos Unit experienced rapid exhumation as revealed by low-T thermochronometry (Ring et al., 2009, this study). Similar exhumation ages have been documented in Santorini (Schneider et al., 2018), suggesting a simultaneous exhumation history of these Pelagonian upper-plate rocks. The activation of structurally higher, top-to-SSE, brittle normal fault zones associated with the Santorini Detachment System (SDS) led to the final exhumation of the Amorgos Unit and regional juxtaposition with the structurally deeper CBU. In the Plio-Quaternary, the Amorgos Unit was cut by high-angle normal faults associated with Aegean extensional and wrench-faulting, such as the Amorgos Fault, resulting in the modern physiography of the island that is characterized by a precipitous, fault-controlled southern edge of the island (e.g., Papadopoulos and Pavlides 1992; Hooft et al., 2017; Tsampouraki et al., 2021).

8. Conclusions

The following conclusions can be drawn from the new data for Amorgos Island:

- In the SE Aegean domain, the Amorgos Unit presents a coherent stratigraphic sequence throughout the Mesozoic to Cenozoic (Mid Eocene), belonging to the southern margin of the Pelagonian domain.
- The higher-grade HP/LT metabasite is either a late Carboniferous olistolith/ huge block within the basal metaconglomerate or a tectonic slice incorporated during the Late Eocene – early Oligocene top to NW thrusting.
- The Permo-Triassic metaconglomerate of the Kapsala Fm. constitutes the stratigraphic base of Amorgos. The Variscan and Cadomian input revealed by the DZ age distributions shows a position in the vicinity of the Pelagonian and Cycladic basement rocks.
- The structural evolution of Amorgos is mainly controlled by a regional compressional phase under general shear in a convergent setting. The NW-directed back thrusts are compatible with a retro-wedge position and synchronous with a low-grade HP metamorphic event. The subsequent shift of the σ1 towards NE – SW probably reflects the impact of the ongoing SW to S-ward nappe translation.
- (U-Th)/He low-T thermochronometry revealed that Amorgos experienced Early-Mid Miocene cooling ages at ~19-14 Ma suggesting a higher structural position above the CBU and the Basal Unit.
- The top-to-the SSE moderate to shallow-dipping brittle fault zones are associated with the Santorini Detachment System.
- The striking similarities between the Amorgos Unit and the Santorini hanging wall imply their comparable paleogeographic and structural position.

Chapter III

A composite Late Eocene-Oligocene double-vergent orogen in the Aegean domain: Insights from the retroward internal duplicated structure of the low-grade HP Amorgos Unit (SE Cyclades, Greece).

Sofia Laskari[1,*], Konstantinos Soukis[1], Stylianos Lozios[1], Daniel F. Stockli[2]

[1.] *Faculty of Geology and Geoenvironment, National and Kapodistrian University of Athens, Greece.*
[2.] *Department of Geological Sciences, Jackson School of Geosciences, University of Texas at Austin, USA.*

Abstract

In the Hellenides, underplating and accretion of HP rocks have provided evidence for a unidirectional SW-vergent orogen. On Amorgos Island, the preserved Fe-Mg carpholite-bearing rocks and the record of retroward top-NW kinematics contradict such a tectonic scenario. Based on our new field-based structural observations, the earlier Dn_a stage resulted in tectonic burial by top-NW thrusting and low-grade HP conditions, along a SE-dipping subduction zone. The progressive Dn_b stage is related to internal imbrication with subsequent top-NW fold-verging and refolding structures within a retro-wedge setting. The Dn_{+1} stage corresponds to a shift from top-NW to top-SE fold vergence, reflecting the proward advancing nappe stacking of the Late Eocene-Oligocene compressional syn-orogenic phase. The Dn_{+2} deformation stage represents fabrics with top-SE to ESE kinematics that were formed in response to Early Miocene extension and exhumation and can be linked to the Santorini Detachment System (SDS). Finally, the tectonic evolution of Amorgos Unit recorded a Dn_{+3} late-stage high-angle normal faulting. From all the above we propose a composite double vergent orogen that involved a short-lived SE-directed intracontinental subduction zone along with a retrobelt during the Late Eocene- Oligocene collisional phase, affected by the Miocene post-orogenic extensional stage.

1. Introduction

Collision of continental plates usually involves the formation of back-to-back bivergent orogens (doubly vergent of Willett et al., 1993), in which thrust wedges are developed on both sides (Willett et al., 1993; Jamieson and Beaumont, 2013). This type of orogen can be explained in terms of the down-going lithosphere, slab pull, and convergence rates between plates (Royden and Burchfiel, 1989). Deep events,

such as the seismicity along the subducting slab play a fundamental role in the slab geometry. However, the different behavior of the metamorphic evolution and the kinematics associated with the development of accretionary wedges are also considered a function of the subduction polarity (Doglioni et al., 1999 and references therein). The polarity of the subducting plate imparts a characteristic asymmetry to the wedge, resulting in the subdivision of the orogen into pro- and retro- wedge components. These components exhibit opposite kinematics, in which the frontal and back-thrust belt is synthetic and antithetic to the subduction, respectively (Willett et al., 1993).

Such doubly vergent structures are responsible for the built-up of an elevated orogen that is more frequently developed along E- to NE-directed class of subduction zones, associated with the accretion of crystalline basement rocks (Doglioni et al., 1999; Doglioni et al., 2007). The structure of such complex orogens is also associated with the distribution of different metamorphic belts generated and exhumed in different domains within the orogen. On the pro-wedge side, the exhumation mechanisms of the HP rocks are well-understood, following a unique proward flow. On the other hand, multiple exhumation mechanisms are involved in the retro-wedge side, including a former frontal and a subsequent backward flow (Jamieson and Beaumont, 2013; Zanchetta et al., 2012, 2015), direct backward exhumation during unidirectional subduction (figure 6, Doglioni et al., 1999) and two-sided subduction system (Faccenda et al., 2008).

The Hellenides represent an arcuate orogenic system that formed and still forming along an N- to NE-directed subduction zone as a result of convergence-collision processes throughout Mesozoic-Cenozoic (Papanikolaou et al., 2004; van Hinsbergen et al., 2005; Jolivet and Brun 2010; Ring et al., 2010; Papanikolaou, 2021). Tectonic models have considered the Hellenides either as a single SW-vergent (Jolivet and Brun 2010) or doubly SW- and NE/NW-vergent orogenic belt (pro- and retro-wedge, Doglioni et al., 1996, 2007) or two-sided subduction system (Xypolias et al., 2012; Gerogiannis et al., 2019, 2021). The initial Late Cretaceous- Early Paleogene subduction system resulted in an S- to SW-ward nappe stacking, which developed in

the frontal belt (pro-wedge), as opposed to the N-directed backthrust of the retrobelt in the Rhodope-Balkan zone (Doglioni et al., 1996).

In the Cyclades, the defined composite HP nappe stack of different peak HP ages (e.g., the Cycladic Blueschist and Basal Units) suggests successive accretion to the overriding plate during the Paleocene-Oligocene (Grasemann et al., 2018; Glodny and Ring, 2022; Kotowski et al., 2022; Uunk et al., 2022). This diachronous activity is compatible with developing a younger top- N/NW backthrust system (retrobelt) on the overriding plate, observed in parts of the unmetamorphosed Pelagonian domain (Grasemann et al., 2021). An analogous retro-wedge model was proposed for the Late Eocene-Oligocene Pelagonian-derived Amorgos Unit based on the observed top-NW backthrust-related structures (Laskari et al., 2022a). However, the occurrence of carpholite-bearing rocks in the Amorgos Unit suggests that the distribution of the metamorphic units in different domains does not fit with a simple tectonic scenario. In this case, Amorgos represents a key area for understanding the complex structure of the Hellenic orogen and poses the question of how the successively frontal accretion affected parts of the overriding plate during the Late Eocene- Oligocene collisional stage.

In this paper, we present new structural data and integrate our results with a synthesis of a previously published structural evolution of the Amorgos Unit to propose alternative tectonic models for the tectonometamorphic history of the upper plate rocks on Amorgos Island. Our study provides insights into the kinematics and metamorphic conditions in different parts of the Hellenic orogen and presents evidence for a more complex deformation in the Attic-Cycladic domain during the prolonged Eocene- Oligocene compressional phase.

2. Geological Setting

The Hellenic orogen resulted from the convergence and final collision of Gondwanan-derived continental fragments to the Eurasian margin, following the closure of Neotethyan deep marine or oceanic strands (Papanikolaou et al., 2004; 2009; van Hinsbergen et al., 2005; Jolivet and Brun 2010; Papanikolaou, 2021). The original architecture of this orogen is preserved in mainland Greece, while it has

been strongly affected by bivergent large-scale detachment faulting, forming the Attic-Cycladic area (Gautier et al., 1993; Ring and Layer 2003; Jolivet and Brun 2010; Jolivet et al., 2010; Ring et al., 2011; Soukis and Stockli 2013; Grasemann et al., 2012; Schneider et al., 2018). Despite the relatively simple succession of subduction-exhumation processes that eventually led to the formation of several SW-ward advancing nappes in mainland Greece, the structure and distribution of subduction-related HP and low-grade crustal rocks exposed in the Attic-Cycladic Crystalline Complex (ACCC) points to a more complex tectonic evolution of the Hellenic subduction zone.

The ACCC consists of the following units: (i) the Upper Cycladic Nappe (UCN), (ii) the Cycladic Blueschist Unit and its underlying Cycladic basement (CB), and (iii) the Basal Unit (Fig. 1).

The Upper Cycladic Nappe (UCN) is a highly diverse group of Pelagonian-derived units, such as metamorphosed ophiolites (e.g., Upper Unit s.s.), low-grade to amphibolite facies metasedimentary rocks, and gneisses with locally Late Cretaceous granitic intrusions (Dürr et al., 1978; Reinecke et al., 1982; Böger 1983; Maluski et al., 1987; Patzak et al., 1994; Katzir et al., 1996; Sánchez-Gómez et al., 2002; Jolivet et al., 2010; Grasemann et al., 2012; Bargnesi et al., 2013; Soukis and Stockli 2013; Koutsovitis et al., 2021; Mavrogonatos et al., 2021). The UCN represents locally exposed fragments on top of the CBU, considered the upper plate in the Aegean region. The upper plate rocks are exposed on Anafi Island (Reinecke et al., 1982; Soukis and Papanikolaou 2004; Martha et al., 2016), on Santorini and on Amorgos island where a more or less complete stratigraphy of the recently attributed rocks to Pelagonian-derived units is also observed (Schneider et al., 2018; Laskari et al., 2022a).

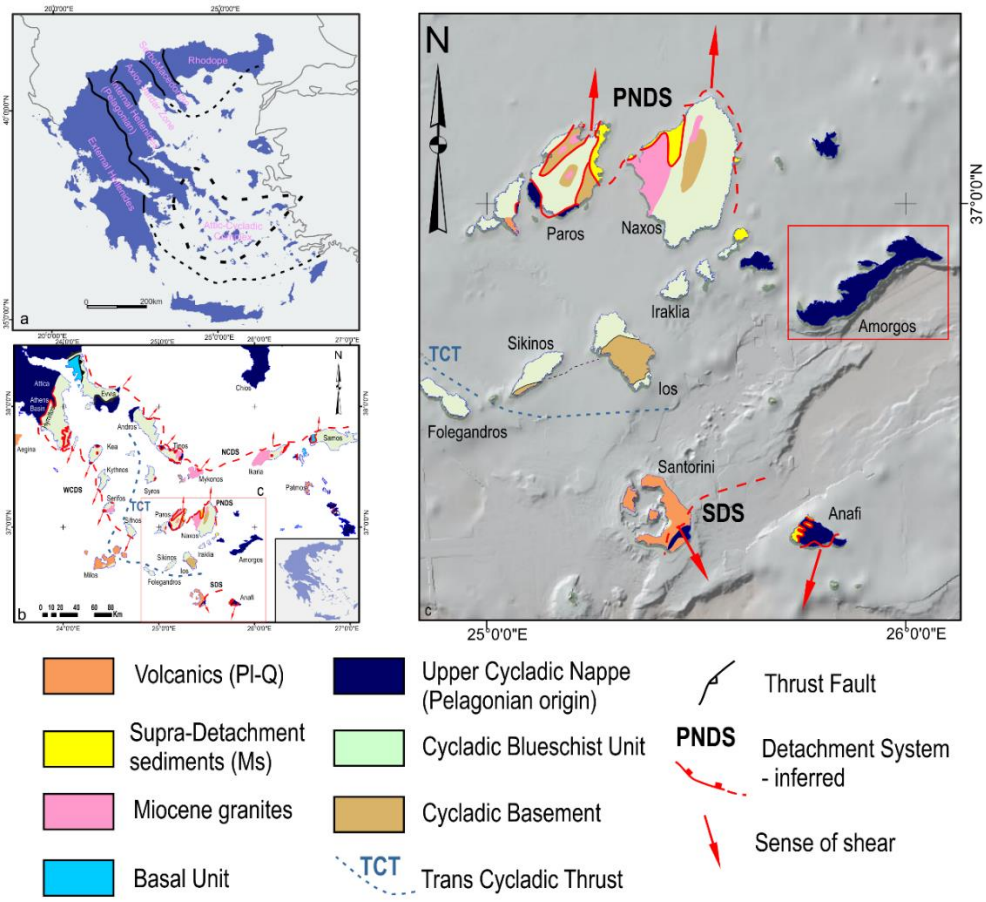

Figure 1: (a) Schematic map of major domains in the Hellenides, (b) Regional tectonic map depicting the tectonic units and structures observed in the Attic-Cycladic Complex, (c) location of Amorgos Unit and simplify geology of the neighboring Cycladic islands. NCDS: North Cycladic Detachment System, PNDS: Paros-Naxos Detachment System, WCDS: West Cycladic Detachment System, and SDS: Santorini Detachment System, compiled from Avigad and Garfunkel, 1991, Gautier and Brun, 1994, Pe-Piper and Piper 2002, Soukis and Papanikolaou 2004, Brichau et al., 2007, Ring et al., 2010, Jolivet et al., 2010, Lekkas et al., 2011, Grasemann et al., 2012, 2018, 2021, Soukis and Stockli 2013; Schneider et al., 2018).

Underneath the Pelagonian rocks, distinct subduction-related HP tectonic nappes of the dominant Cycladic Blueschist Unit (CBU) are observed, reflecting different time intervals of underplating and exhumation processes (Grasemann et al., 2018; Kotowski et al., 2020, 2022; Ring et al., 2020; Glodny and Ring 2022). The CBU includes a Permo-Mesozoic passive-margin to deep-marine sequence of marble, metapelite, and metavolcanic rocks (Dürr et al., 1978; Jolivet and Brun 2010; Seman et al., 2017; Poulaki et al., 2019; Papanikolaou 2021; Laskari et al., 2022b). A composite exhumation history characterizes the CBU, including an Eocene syn-

orogenic and a Late Miocene post-orogenic unroofing through symmetric bivergent detachment faults. The various HP stages of the CBU nappes range from the Early Eocene to Early Oligocene (~55-30 Ma, Grasemann et al., 2018; Ring et al., 2020; Glodny and Ring 2022; Kotowski et al., 2022) and record a greenschist- amphibolite facies overprint during decompression at Oligocene-Miocene time (~30-15 Ma, Jansen 1977; Wijbrans and McDougall 1988; Bröcker et al., 1993; Keay et al.,2001; Denèle et al., 2011; Beaudoin et al., 2015; Glodny and Ring, 2022). In the southern Cyclades (e.g., Paros, Naxos, Ios, Sikinos), the CBU is underlain by the Cycladic Basement unit (CB) made up of Carboniferous granitoids, intruded into Proterozoic – Lower Paleozoic metasedimentary rocks of Gondwanan affinities (Jansen 1977; Reischmann 1998; Keay and Lister 2002; Zlatkin et al., 2018; Flansburg et al., 2019). The CB has locally reached partial anatexis (e.g., Paros, Naxos, Mykonos) (Jansen 1977; Papanikolaou 1980; Andriessen et al., 1987; Keay and Lister 2002; Bargnesi et al., 2013; Laurent et al., 2018; Jolivet et al., 2021). Controversial interpretations have been reported for the CB/CBU contact (e.g., Ios, Sikinos), which include either a tectonic (Lister et al., 1984; Huet et al., 2009; Ring et al., 2011; Augier et al., 2015) or a deformed depositional contact based on similar detrital zircon U-Pb signatures (Poulaki et al., 2019, 2021).

In a structural position below the CBU (e.g., Evia, Samos, Olympos-Ossa-Pelion Mts), crops out a younger HP nappe, the Basal unit, which is considered equivalent to the Tripolitza Unit of the External Hellenides. This unit is made up of a monotonous Triassic to Eocene platform-facies carbonate sequence capped by Eocene-Oligocene flysch (Godfriaux 1968; Dubois and Bignot 1979; Papanikolaou 1979; Theodoropoulos 1979; Ring et al., 1999), and recorded an Early Miocene (24-21 Ma) HP metamorphism estimated at 8-10 kbar and 350-400 ^{o}C (Shaked et al., 2000; Ring et al., 2001; Ring and Layer 2003).

2.1. Geology of Amorgos Island

Amorgos Island, located at the southeastern part of the Cycladic archipelago, probably represents a complete Pelagonian-derived fragment of upper plate rocks on top of the deeply exhumed HP nappes of the CBU (Laskari et al., 2022a). Amorgos

Unit consists of a low-grade Mesozoic to Cenozoic stratigraphic sequence deposited in different environments due to significant switches in sedimentary facies, including both neritic and pelagic characters (Fig. 2) (Minoux, 1980; Fytrolakis et al., 1981; Dürr, 1985; Rosenbaum et al., 2007; Chatzaras et al., 2011; Laskari et al., 2022a). These variations led to the subdivision of Amorgos into two segments, the northeastern carbonate-platform and central/southwestern, with variable sedimentary facies, respectively (Laskari et al., 2022a). The oldest and stratigraphically lowermost sedimentary succession is the Kapsala metaconglomerate, which includes quartzitic, multicolored phyllitic matrix, and a conglomeratic part with inliers of higher-grade olistolith (e.g., metabasite, mica-schists, quartzite). Detrital zircon (DZ) U-Pb ages of the metaconglomerate matrix and clasts yielded Mid-Permian and Precambrian maximum depositional ages, respectively. The overlying Triassic-Cretaceous and partly Eocene metasedimentary sequences include a Verrucano-type formation and its lateral equivalents, shallow marine and metachert marble with the contribution of conglomeratic marble, capped unconformably by an Eocene metaflysch.

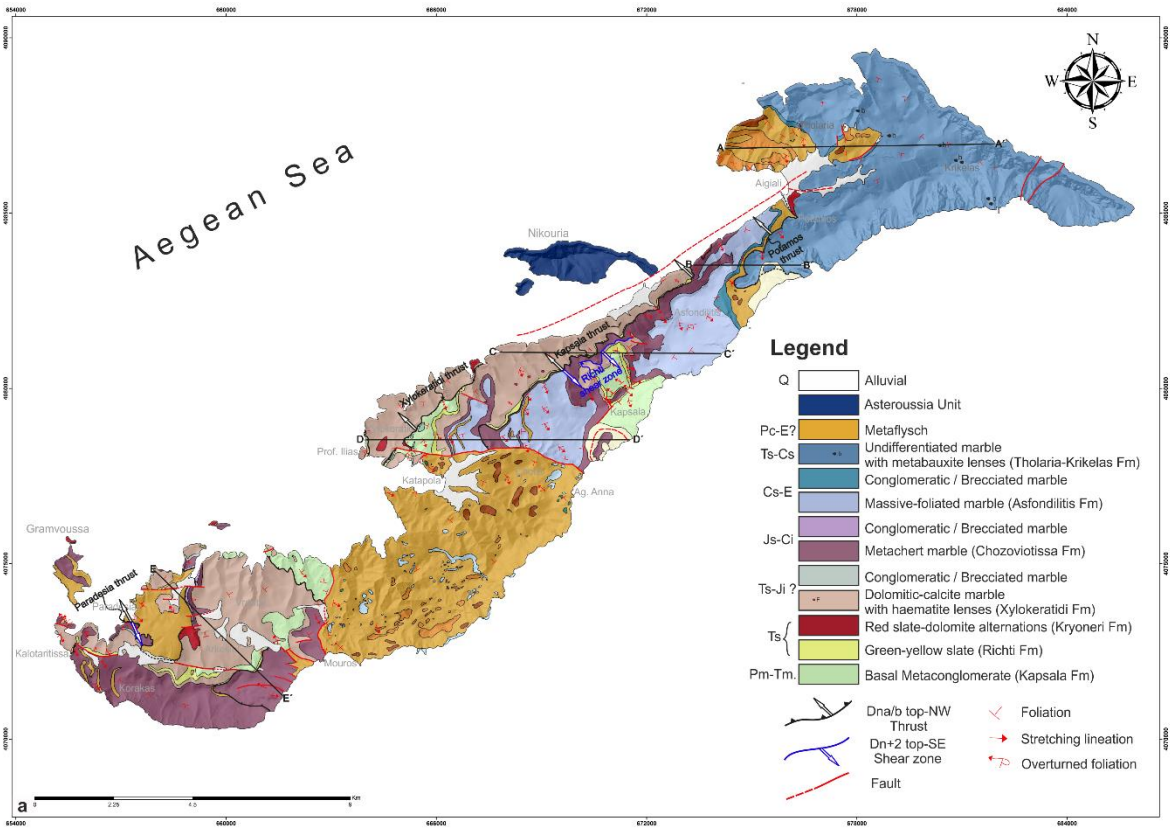

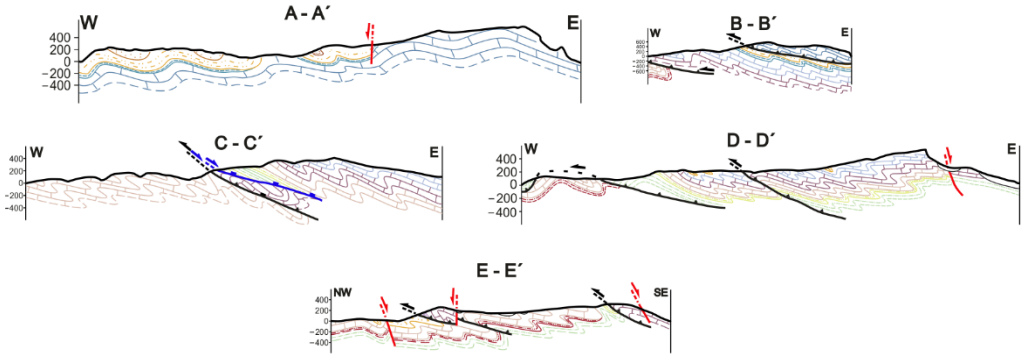

b

Figure 2: (a) Geological map of Amorgos Island, modified from Laskari et al. (2022a). The main formations and structural elements are illustrated. Nikouria and Gramvoussa islets adapted from Dürr, (1985). (b) cross-sections A-A′, B-B′, C-C′, D-D′, E-E′.

The reported P-T conditions for the metabasite have been estimated at 13 kbar and 500-600 °C, while the metaconglomerate part indicated conditions of 10-14 kbar and 300-450 °C (Rosenbaum et al., 2007; Ring et al., 2009). Interestingly, the differences in P-T conditions are more pronounced in the metabauxite -bearing Cretaceous marble sequence, where carpholite was found, based on which Theye et al. (1997) estimated at about 8 kbar and 300-350 °C. These differences in metamorphic conditions led to the conclusion of two distinct metamorphic units, accommodated by different tectonic models that include either a top-to-the NW detachment faulting or a bivergent geometry developing NW-directed thrusts (Rosenbaum et al., 2007; Ring et al., 2009; Chatzaras et al., 2011). However, as recently suggested and briefly described, Amorgos Unit experienced a compressional Late Eocene-Oligocene syn-orogenic phase in a retro-wedge setting, developing the backthrust-related structures before its final unroofing. Based on cross-cutting relationships and zircon (U-Th)/He data, extensional deformation affected the Amorgos Unit during Early-Mid Miocene (14-18 Ma, Laskari et al., 2022a). These ages are similar to the AFT data obtained by Ring et al. (2009), marking the onset of upper-crustal exhumation rocks quite earlier than the lower-plate CBU rocks.

3. Structural Evolution of Amorgos Unit

In the following paragraphs, we describe the deformation stages that constitute the structural evolution of the Amorgos Unit as observed in the studied area. Field-based structural analysis revealed that the Amorgos Unit has a complex deformation history, evolving from ductile to brittle-ductile and finally to brittle conditions. We have used oriented thin sections cut parallel to the shear direction from marble mylonites and siliciclastics, focusing on the deformation mechanisms and the kinematic indicators to constrain the relative temperature conditions and document the shear-sense movement. Dn-Dn_{+1} structures resulted from a progressive multi-stage deformation, forming domains with different kinematics under a compressional setting. The Dn stage is further distinguished into Dn_a and Dn_b sub-stages and associated with the development of large-scale folds and thrusts, exhibiting a dominant top-NW sense of shear. The Dn_{+1} stage shows a non-steady period of deformation (see Fossen et al., 2019; Fossen and Tikoff, 1997), displaying top-SE to SW kinematics. On the other hand, the Dn_{+2} and $Dn_{+3/4}$ structures represent the late stages of the Amorgos structural evolution, recording the exhumation history during an extensional deformation phase.

3.1. Dn_a structures

The earlier structures recorded on the Amorgos Unit correspond to the Dn_a syn-metamorphic HP ductile deformation stage, associated with Fn_a isoclinal folds and NW-SE axes (Bn_a). In the marble, the main Sn_a foliation is evident by the compositional layering of metachert-calcite intercalations, calcite bands, and dolomitic layers, forming a coarse-grained foliation. In siliciclastic rocks, Sn_a is defined by phyllosilicate minerals flattened and elongated quartz and calcite aggregates. The poles to foliation (Sn_a) diagram is characterized by a well-defined maximum plunging steeply to the NW, corresponding to a shallow-dipping resultant-mean Sn_a plane towards the SE, as observed throughout the island. However, a scattered concentration pattern suggests variations in the foliation plane due to subsequent folding (Fig. 3a).

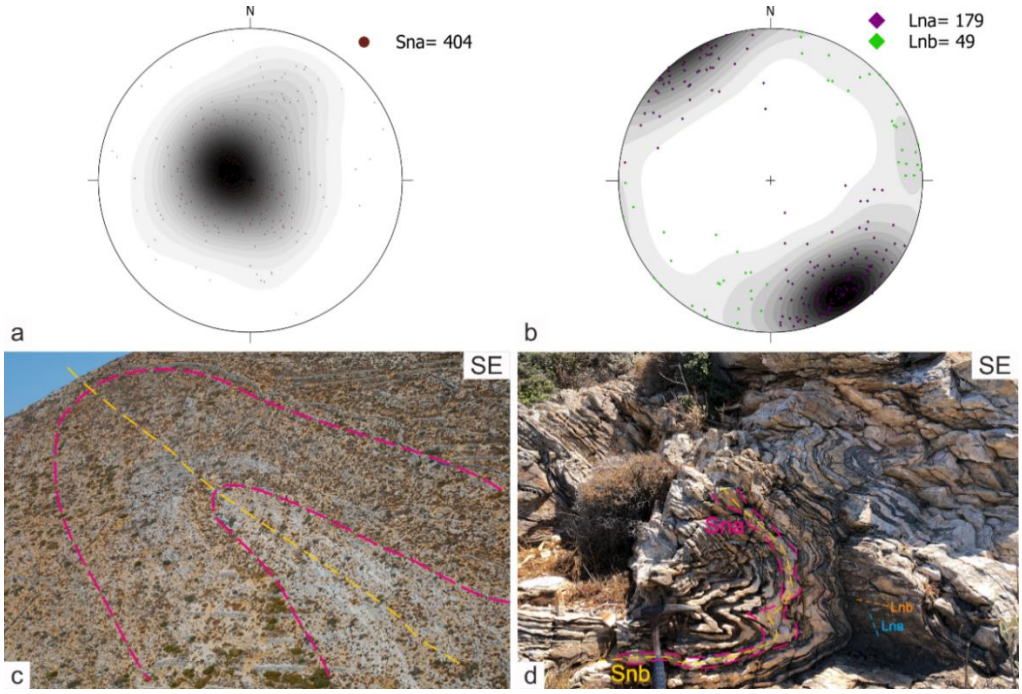

Figure 3: (a) Stereoplots of the poles to Sn_a foliation (equal-area projection, lower hemisphere). The contour diagram illustrates a well-defined maximum of the Sn_a poles in the NW quadrant. (b) Stereoplots of the stretching Ln_a and intersection Ln_b lineation (equal-area projection, lower hemisphere). The contour diagram reveals a main maximum of the Ln_a in the SE quadrant. (c) Outcrop Fn_b NW-vergent folds forming an axial planar cleavage (Sn_b) (*36⁰ 52′ 24′′ N, 025⁰ 56′ 13′′ E*). (d) Refolded structures produce type-III interference pattern (*36⁰ 51′ 44′′ N, 025⁰ 54′ 59′′ E*).

A shallow plunging stretching/mineral lineation (Ln_a) is formed on the Sn_a plane, more pronounced in the marble and clastic sequences but weakly developed in the upper structural levels of the metaflysch. Ln_a is defined by the alignment and stretching of quartz-calcite-phyllosilicate aggregates, elongated clasts and locally fibrous Fe-Mg carpholite. Carpholite is found within fibrous quartz aggregates of the basal metaconglomerate (Kapsala Fm.), indicating HP metamorphic conditions. Lineation (Ln_a) stereo-plot diagram shows a single cluster plunging gently to the SE (Fig. 3b). However, folding of Ln_a during subsequent progressive deformation is also observed.

3.2. Dn_b structures

The Dn_b structures correspond to the progressive deformation stage, manifested by outcrop and mesoscale Fn_b NW-vergent folds with NE-SW Bn_b axes (Fig. 3c). Fn_b folds refold the previous Sn_a foliation and are partly responsible for stratigraphic repetitions observed throughout the island. Fn_b folds vary in style, from isoclinal to tight, forming a discrete axial planar cleavage (Sn_b), resulting in a composite $Sn_{a/b}$ foliation. Fn_b folds also show variable amplitude, wavelength and interlimb angles. Locally, crenulation cleavages are developed. Based on foliation-cleavage angle relationships and fold asymmetry (e.g., S-, Z- asymmetry), fold vergence indicates an overall top-to-the NW sense of shear. An intersection lineation (Ln_b) trending NE-SW (Fig. 3b) formed parallel to the Fn_b folds and crenulation axes. Often, the fold limbs are stretched, producing spectacular symmetric pitch-and-swell and boudinage structures, primarily observed in the characteristic marker layers of the metachert marble (e.g., Chozoviotissa Fm.). Occasionally, refolding folds have produced a type-III interference pattern, indicative of high strain accomplished during Dn_b (Fig. 3d). Several map-scale NE-SW- striking, brittle-ductile thrusts are developed in different stratigraphic levels of the Amorgos Unit. Thrusting probably commenced during the earlier Dn_a stage and progressively evolved in the Dn_b stage. As a result, four major gently SE-dipping thrust zones are recognized based on old-over-young relationships (Fig. 2). These thrusts are responsible for internal imbrication and duplication of the Amorgos stratigraphy. Secondary thrusts also contributed to a further increase in internal deformation and overall crustal thickening. Occasionally, a mylonitic foliation (Sm) is developed in the hanging walls of these thrust zones.

The structurally highest Potamos thrust zone, extending from the Asfondilitis hill to Aigiali bay, has emplaced the Tholaria-Krikelas marble sequence above the metaflysch. A mylonitic foliation is developed in the hanging wall of this thrust. The most distinct feature is the calcite clasts that define δ-type porphyroclasts in both mesoscopic and microscopic scale (Fig. 4a). Thin sections from this zone revealed a medium to high strain intensity in which inequant to sub-equant calcite grains are aligned subparallel or at small angles to the Sm mylonitic foliation. Larger calcite

grains that define the Sn_a coarse-grained domains are ductilely deformed, showing subgrains. These grains also exhibit at least two sets of twins, corresponding to geometric types I and II. Most twins have curved boundaries implying that calcite recrystallization post-dates twinning. Twins with straight boundaries likely formed during the last deformation stages. The large calcite grains with subgrains pass into domains of sub-equant twin-free calcite grains formed by bulging (BLG) recrystallization. In general, calcite grains form a significant oblique shape preferred orientation (SPO) in the bulging recrystallization regime, which revealed an overall top-to-the NW sense of shear. However, within the same high-strain zone, there are also domains of subordinate opposing top-to-the SE kinematics (Fig. 4b, c). It is worth noting that calcite grains also develop an oblique shape fabric in the lineation-normal plane with top-NE shear sense, indicating variations of the flow pattern (Fig. 4d).

Structurally below the Potamos thrust and to the central part of the island, the rocks of the Kapsala thrust sheet (e.g., Kapsala, Richti, Xylokeratidi, Chozoviotissa, and Asfondilitis Fms) are overthrust above the Xylokeratidi Fm. Within the Kapsala thrust, high to ultra-high strain small σ-type and complex porphyroclasts are observed, indicating a top-to-the NW shearing (Fig. 4e, f).

The structurally lowest Xylokeratidi thrust, located at the central part of the island, is restricted within the clastic sequences and it has emplaced the Kapsala Fm. above the Kryoneri and Xylokeratidi Fms. Thin sections from this zone show dynamically recrystallized quartz grains forming mainly bulges. Larger relic quartz grains have developed subgrains, deformation lamellae, and undulose extinction. Feldspar grains show intra-crystalline deformation with twinning and fracturing, while the phyllosilicate minerals occupy the cleavage domains and they are often folded. Sigmoidal calcite and quartz lenses and boudinaged-rotated chromite grains reveal a dominant NW sense of shear (Fig. 5a).

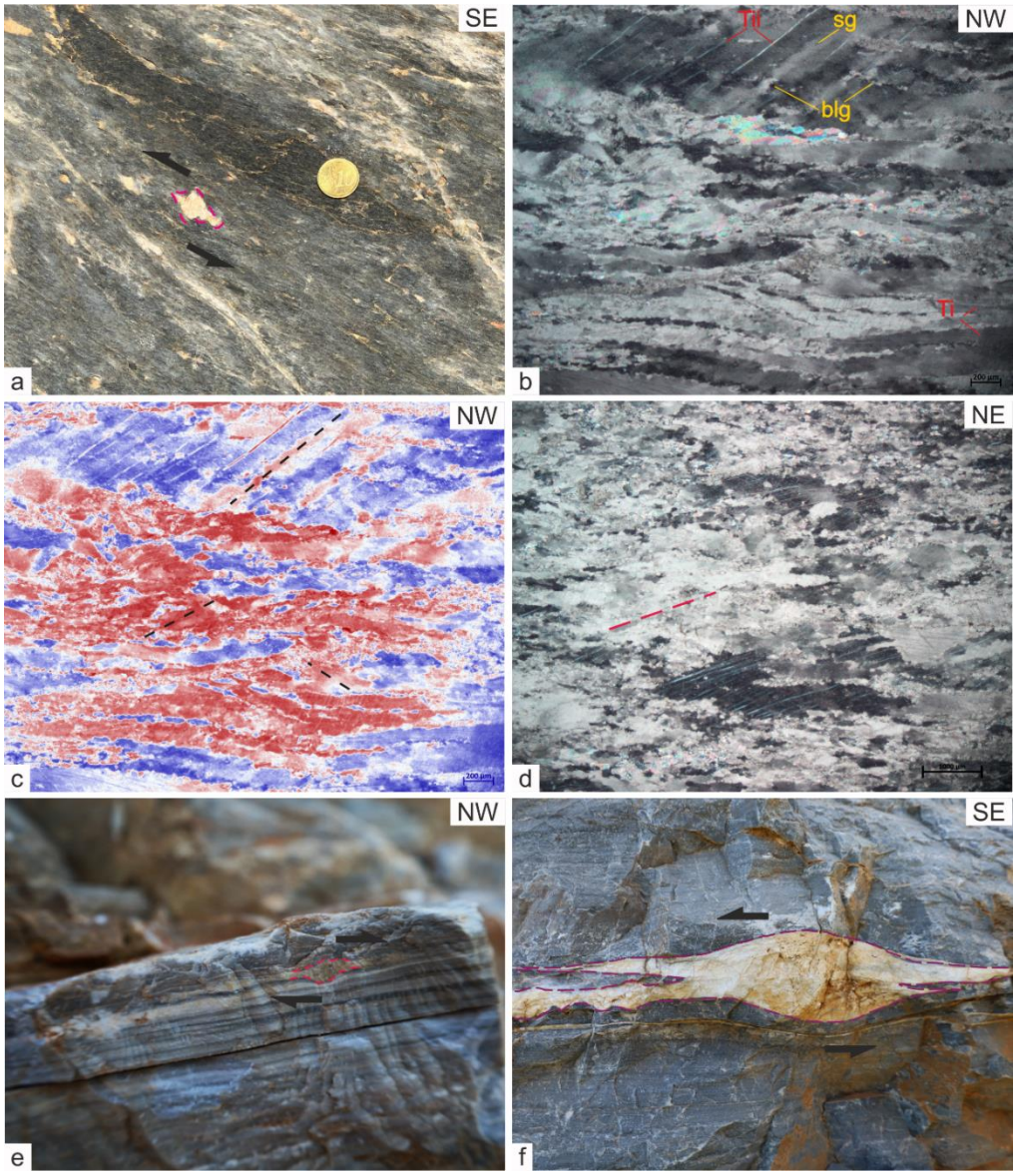

Figure 4: (a) Mesoscopic calcite δ-type clast from the Potamos thrust zone, indicating top-NW sense of shear (*36⁰ 53′ 21′′ N, 025⁰ 58′ 13′′ E*). (b) and (c), Representative photomicrographs (crossed polars and colored) from the Potamos mylonitic marble (sections parallel to stretching lineation Ln_a) showing calcite subgrains and bulging recrystallization and twinning. Ti and Tii correspond to calcite twins type I and II, respectively. Calcite shape preferred orientation indicates top-NW sense of shear. (d) Photomicrograph (section normal to stretching lineation Ln_a) from the Potamos thrust zone, exhibiting an oblique calcite fabric with top-NE sense of shear. (e) Delta-type clast from the Kapsala thrust zone indicating top-to-the NW shearing (section parallel to stretching lineation Ln_a) (*36⁰ 51′ 14′′ N, 025⁰ 53′ 52′′ E*). (f) Complex porphyroclast from the metachert marble displaying top-NW shearing (*36⁰ 53′ 27′′ N, 025⁰ 57′ 28′′ E*).

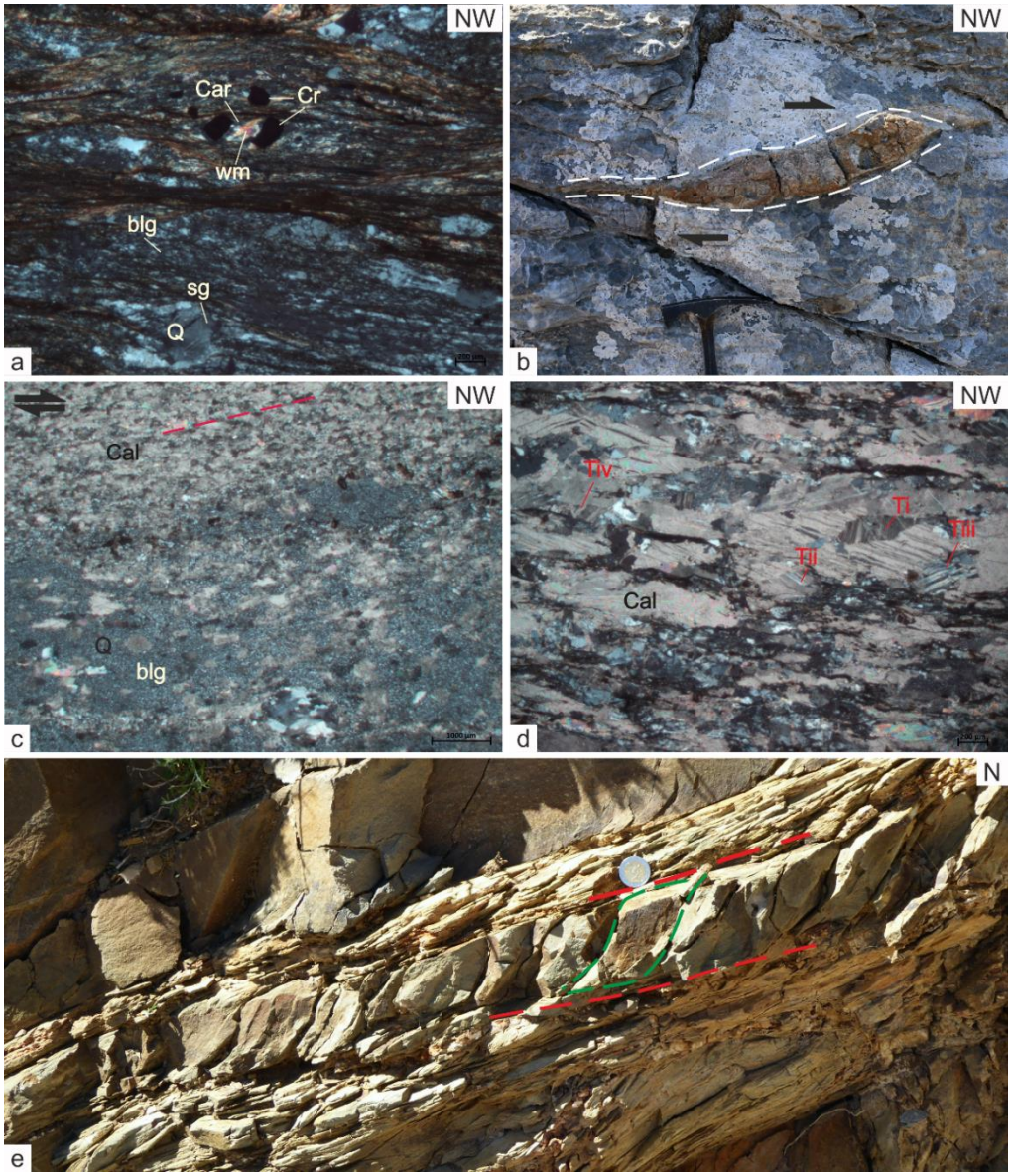

Figure 5: (a) Photomicrograph (crossed polars, section parallel to Ln_a) from the Kapsala metaconglomerate showing dynamically recrystallized quartz grains forming bulges. Larger grains indicate subgrains, deformation lamellae, and undulose extinction. Fibrous Fe-Mg carpholite is syn-tectonically grown within the matrix. Phyllosilicates form the cleavage domains. Rotated boudinaged chromite grains indicate top-NW shearing. Abbreviations: sg= subgrains, blg= bulging, car= carpholite, wm= white micas, Q= quartz, cr= chromite. (b) Sigmoidal metachert clast from the Paradesia thrust zone (section parallel to Ln_a), indicating top-to-the NW shear sense (*36^0 47′ 39′′ N, 025^0 45′ 59′′ E*). (c) Representative photomicrograph (crossed polars, section parallel to Ln_a) from the Paradesia thrust zone showing the calcite oblique shape-fabric with top-NW sense of shear (red dotted line). Quartz grains form bulges. Cal= calcite, Q= quartz, blg= bulging. (d) Representative photomicrograph (crossed polars, section parallel to Ln_a) from the metaflysch illustrating coarse (Sn_a) calcite grains with

inequigranular-interlobate boundaries and twinning. Cal= calcite, Ti-iv= type I-IV twins. (e) Mesoscopic duplex structure from the metaflysch displaying top-N shearing. Roof - base thrusts and horses are depicted in red and green, respectively (*36^0 54′ 51′′ N, 025^0 58′ 46′′ E*).

To the southwest, the Paradesia thrust, extending from Paradesia to Kato Kambos bay, occupies a structurally lower position in this region, bringing the Triassic-Cretaceous marble sequence over the metaflysch. This thrust zone either represents the structurally lowermost thrust of the Amorgos island or is located in a similar structural position to the Xylokeratidi thrust zone. The Paradesia mylonitic zone is developed within the metachert marble. Dynamically recrystallized quartz grains formed by bulging, characterize the fine-grained domains. Contrary, sub-equant calcite recrystallized grains display bulges, defining the coarser-grained parts of this sample. Calcite grains also exhibit an oblique shape preferred orientation (SPO). The sigmoidal metachert clasts, sheared quartz veins forming flanking structures, and oblique metachert clasts indicate a more pronounced top-to-the NW shear sense (Fig. 5b, c).

The metaflysch, located at the footwalls of the thrusts, shows an axial planar fine-grained foliation of recrystallized phyllosilicate and calcite grains, which is often refolded. Away from the thrust zones, Sn_a formed by calcite grains with inequigranular-interlobate boundary geometry reveals that twinning is the dominant deformation mechanism. Curved-thick and twinned twins are present, corresponding to geometric type III. Occasionally, thick twins with sutured boundaries are recorded, suggesting type-IV twins. However, types II and I twins are also observed (see Burkhard, 1992 for calcite- twin classification) (Fig. 5d). Often, the calcite grains of the metaflysch show pressure solution and the development of stylolitic structures. Mesoscopic scale structures are also the duplexes (Fig. 5e) and the development of shallow-dipping to moderate thrust planes.

3.3. Dn_{+1} structures

The less penetratively developed Dn_{+1} structures correspond to a later phase of refolding in which the fold vergence changes towards the SE, and are associated with

a NE-SW Dn_{+1} fold axes. These Dn_{+1} folds have affected the earlier NW-verging folds and have refolded the $Sn_{a/b}$ composite foliation, developing an oblique axial planar cleavage (Sn_{+1}), dipping gently towards NW. The refolded structures are often cut by the Dn_{+1} axial planar cleavage, which is well-observed in the metachert marble. An overall top-to-the SE movement is also recorded by stretched and rotated calcite veins (Fig. 6a, b). Sn_{+1} represents a pressure solution cleavage producing microlithons within which overprinting of the composite $Sn_{a/b}$ foliation is well-preserved on both meso- and microscopic scale of the graphitic layers of the metaflysch.

The Dn_{+1} folding is followed by the last stage of folding that varies from open to kink-type folding. The NE-SW open folds have a wavy appearance forming a NE-SW antiform on the macroscopic scale (Fig. 2). Kink-type folding shows variable sets, displaying weak NE-SW and NW-SE trending axial surfaces. Kink bands occur in conjugate systems, mainly observable in the lowermost siliciclastic sequences.

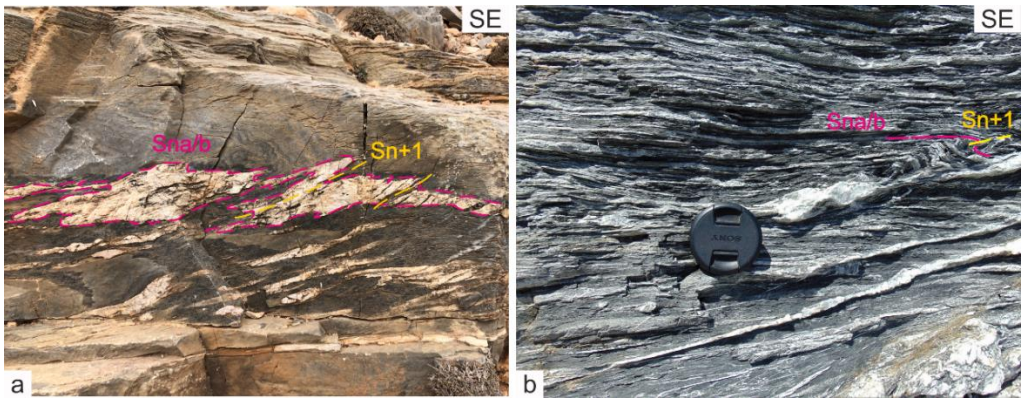

Figure 6: Sections parallel to stretching lineation Ln_a. (a) Refolded composite foliation ($Sn_{a/b}$) from the metachert marble cut by the Sn_{+1} axial planar cleavage, indicating top-SE kinematics (*36⁰ 46′ 41′′ N, 025⁰ 48′ 24′′ E*). (b) Refolded structures form the graphite-layers of the metaflysch, producing an axial planar Sn_{+1} cleavage. Rotated calcite veins indicate top-SE movements (*36⁰ 47′ 10′′ N, 025⁰ 49′ 38′′ E*).

Kinematically, the geometry of kink-type folds reveals rotational movements of limbs along fixed kink hinges towards the SW, mainly recognized in the upper stratigraphic levels of the metaflysch. However, most of the conjugate kink bands reveal NW-SE shortening. In this case, the Dn_{+1} structures could include at least two sets,

depending on their orientation with respect to the kinematic frame generated during a complex deformation pattern. Therefore, the variable orientations and rotational movements of kink bands and kink-type folds indicate a change in the maximum principal axis (σ1) orientation.

3.4. Dn_{+2} structures

The Dn_{+2} structures include late-stage localized ductile to brittle-ductile shear zones that represent domains with top-to-the SE sense of shear. These zones are localized at the intermediate Kapsala and Richti zones, causing ultra-mylonitization of the calcitic marble. The related structures include a gently SE-dipping mylonitic foliation (Sm'), characterized by a SE-plunging stretching lineation (Ln_{+2}) parallel to Ln_a lineation. Within Richti mylonitic zone, Sn_a dolomite grains are cataclastically fractured and rotated in the shear direction to form δ-type clasts, indicating top-to-the SE sense of shear in both meso- and microscopic scale (Fig. 7a, b, c). In microscopic scale, thin sections from the Kapsala zone revealed that equant recrystallized calcite grains surrounding aggregates of coarse-grained calcite, display a strong oblique shape-preferred orientation (SPO) with a dominant top-SE component (Fig. 7d). As previously mentioned, the Kapsala zone also includes complex and σ-type clasts with top-NW sense of shear. In this case, the Kapsala mylonitic zone could represent a pre-existing top- NW thrust zone that was active during the earlier Dn_b stage, and was subsequently reactivated as a shear zone with opposing top-SE kinematics. S-C fabrics and shear bands are the most common fabrics observed at all scales. Although almost all of these kinematic indicators, reveal top-to-the SE shear sense, individual shear bands occur as an antithetic system, exhibiting conflicting kinematics of both top-NW and SE shearing (Fig. 7e).

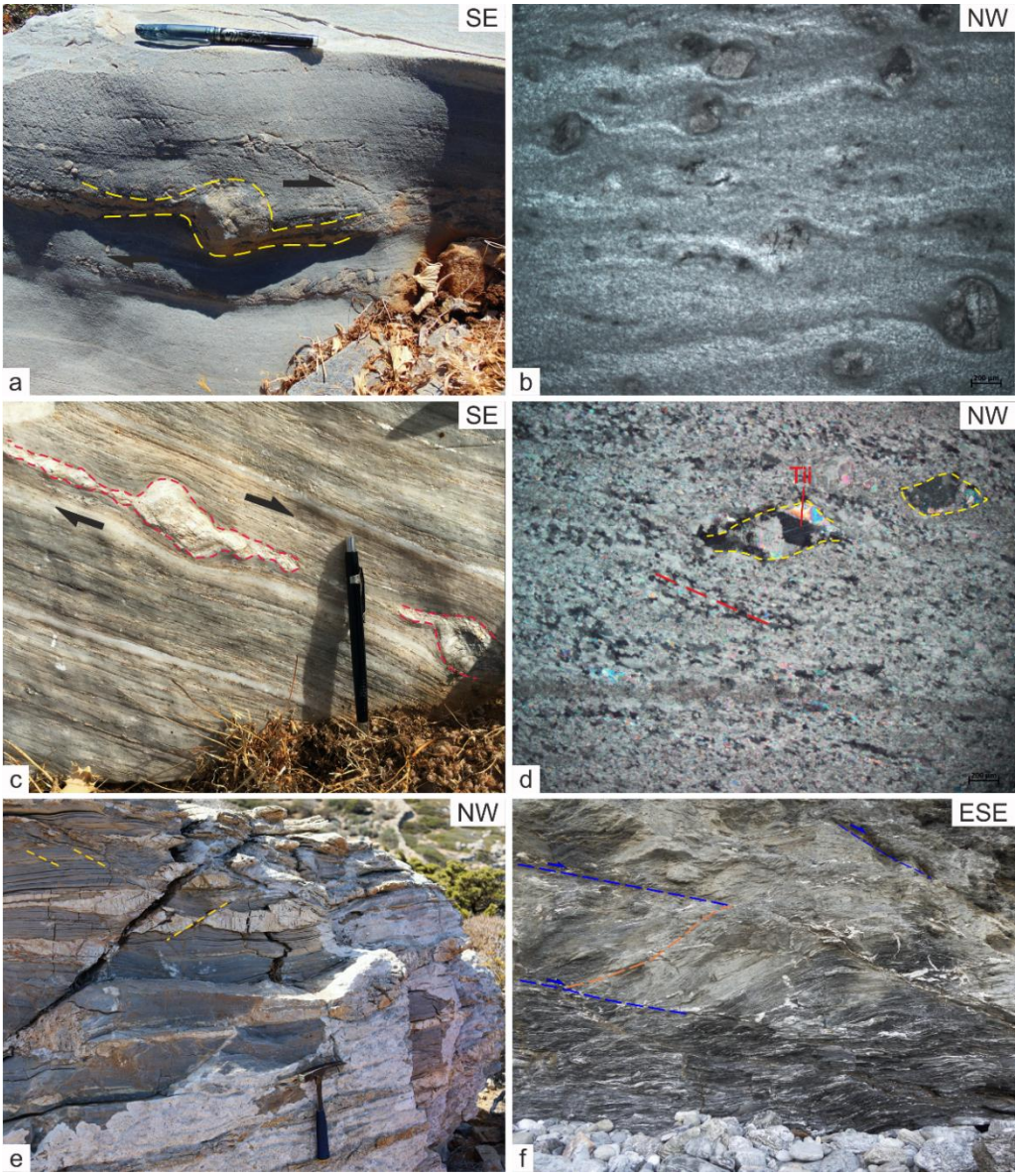

Figure 7: (a) Delta-type clast (yellow dotted line) from the Richti mylonitic zone indicating top-to-the SE shearing (section parallel to Ln_{+2} stretching lineation) (*36⁰ 51′ 44′′ N, 025⁰ 55′ 00′′ E*). (b) Photomicrograph (crossed polars, section parallel to Ln_{+2} stretching lineation) of the Richti mylonitic zone showing top-SE delta-type clasts. (c) Rotated boudinaged clast from the Kapsala zone indicating top-SE shearing (*36⁰ 51′ 13′′ N, 025⁰ 54′ 22′′*). Photomicrograph from the Kapsala zone (section parallel to Ln_{+2} stretching lineation) showing recrystallized calcite grains that display a strong oblique shape-preferred orientation (SPO) (red dotted line) with a dominant top-SE component. Sigmoidal aggregates of coarse-grained calcite (yellow dotted line) exhibit a pre-existing top-NW shearing. Tii= calcite type-II twins. (e) Antithetic system of individual shear bands, exhibiting conflicting kinematics of both top-NW and SE shearing in the Paradesia zone (*36⁰ 47′ 40′′ N, 025⁰ 45′ 59′′*). (f) Top-to-the SE brittle-ductile low-

angle (blue dotted lines) with normal-sense drag geometries and minor displacement in the graphite layers of the metaflysch (*36⁰ 47′ 10′′ N, 025⁰ 49′ 40′′*).

It should be noted that in the graphitic layers of the metaflysch, the associated top-to-the SE shear bands are gradually replaced by top-to-the SE brittle-ductile low-angle faults, in which the foliation records normal-sense drag geometries with only minor displacement (Fig. 7f).

3.5. Dn_{+3} structures

Dn_{+3} stage is associated with structures that are solely developed under brittle conditions. Discrete zones involving multi-generations of cm to m thick non-cohesive meso- to ultra-cataclasites are observed primarily in the meta-siliciclastic sequences of the Amorgos Unit (Fig. 8a). Moderate to high-angle ESE- dipping faults are recognized that root into low-angle cataclastic fault zones. Striations on the fault planes are consistent with top-to-the ESE shearing.

3.6. Dn_{+4} structures

Late high-angle normal faulting can be attributed to the Dn_{+4} structures, which cut through all previous structures observed throughout the island. A protracted extension produced two sets of normal faults trending NW-SE to E-W and NE-SW, respectively (Fig. 8b). NW-SE set shows moderate to steeply dipping fault planes, predating the NE-SW normal faults based on cross-cutting relationships. The latter comprise the neotectonic normal faults, mainly located along the southern and northern coasts and coincide with the long axis of Amorgos Island.

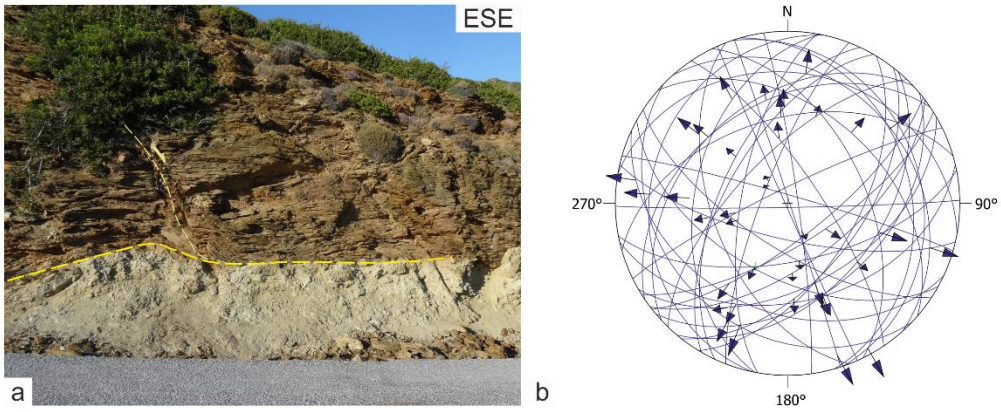

Figure 8: (a) Non-cohesive cataclasite in the higher structural levels of the metaflysch (yellow dotted line). High-angle normal faults root into the cataclastic zone (white dotted line) (*36⁰ 47′ 20′′ N, 025⁰ 49′ 45′′*). (b) Lower hemisphere/equal-area stereo plots of Dn_{+4} normal faults.

4. Discussion

4.1. Structural evolution of the Amorgos Unit

Based on field observations and structural analysis, the deformation history of the Amorgos Unit can be distinguished into discrete deformation stages evolving from a compressional syn-orogenic phase to a post-orogenic extensional episode. The mid-late Eocene age of the metaflysch combined with the Early-Mid Miocene (U-Th)/He (Laskari et al., 2022a) and AFT data (Ring et al., 2009), brackets the time of deformation between Late Eocene to Early-Mid Miocene. These ages correspond to the culmination of the Cenozoic collisional Alpine phase that affected the Hellenides and the final exhumation during back-arc extension dominating most of the Aegean.

The earliest penetrative ductile deformation (Dn_a) is characterized by a well-developed NW-SE oriented stretching lineation (Ln_a), observed on the preserved penetrative Sn_a foliation. The syn-tectonic growth of fibrous Fe-Mg carpholite observed on both meso- and microscopic scale in the basal metaconglomerate (Kapsala Fm.) (Laskari et al., 2022a), indicates that Dn_a structures were synchronous with low-grade HP metamorphic conditions (Fig. 9a). Therefore, the Amorgos Unit was buried in low-grade blueschist facies conditions, where shortening was accommodated by top-to-the NW shearing. These observations agree with previous studies (Rosenbaum et al., 2007; Ring et al., 2009; Chatzaras et al., 2011). Fe-Mg

carpholite is also found within the structurally higher metabauxite lenses of the Cretaceous Krikelas marble (Minoux, 1980; Theye et al., 1997). The peak P-T conditions were estimated at 8 kbar and 300-350° C (Theye et al., 1997). Our microstructural observations from the mylonitic marble zones (e.g., Potamos thrust zone) revealed that dynamic recrystallization evolving from the subgrain to the BLG field and twinning were the dominant deformation mechanisms for calcite, indicative of low-temperature conditions (Passchier and Trouw, 2005). BLG recrystallization is also the dominant mechanism for quartz observed in the metachert marble (e.g., Paradesia thrust zone), suggesting deformation temperatures between 400 and 300°C. In the basal metaconglomerate, the intra-crystalline deformation in feldspar, including grain-scale faults and twinning, implies deformation temperatures below 400°C (Passchier and Trouw, 2005). Based on the above, we assume that the microstructural features were formed under low-grade conditions below 400°C. Significantly different P-T conditions for the basal metaconglomerate were given by Rosenbaum et al. (2007), who estimated 10-14 kbar and 300-450° C. In this case, further geochronological data for the HP event is needed to support the specific conditions under which Amorgos Unit was metamorphosed. Nonetheless, the fibrous carpholite is indicative of low-grade HP metamorphic conditions, and since the age of the metaflysch is mid-late Eocene, the Amorgos HP event probably occurred in the latest Eocene to Early Oligocene.

Subsequently, Dn_a evolved to the progressive deformation Dn_b stage that results in a characteristic generation of NW-verging folds and refolding structures (Fig. 9b), associated with the development of NE-SW intersection lineation Ln_b. The Dn_b structures are associated with increased strain since the higher the strain, the more likely the rocks are to produce refolding structures and overprinting cleavage relations. The Dn_b episode also produced several map-scale thrusts documenting consistent top-to-the NW kinematics. In these mylonitic zones, microstructures suggest a structurally downward increase in strain from high- to ultra-high strain zones, dominated by top-to-the NW sense of shear. Aside from the documented kinematics within some mylonitic zones (e.g., Potamos thrust zone), there are domains within the same thin-section that exhibit opposite top-SE sense of shear.

This could be the result of rheologically-heteregeneous layers and/or switching in strain regime within individual domains. Hence the contrasting indicators may represent the product of strain partitioning and vorticity within domains (Ishii, 1992; Hippert and Tohver, 1999; Passchier and Coelho, 2006). Since most structural features indicate a dominant top-NW shear, structures with apparent reverse shear can also be regarded as consistent with the top-NW kinematics. The coeval shearing in both directions is also evidenced by the fact that overprinting or cross-cutting relationships are ambiguous or absent. In this case, top-NW shearing seemed to involve the contribution of a high coaxial component, suggesting a continuous and progressive general shear in response to a NW-SE compressional phase. Interestingly, the observed oblique fabrics and grain-shape asymmetries in both lineation-parallel and lineation-normal sections indicate a more complex deformation pattern, in which flow probably is distributed in all directions. Such a deformation pattern characterizes a triclinic symmetry (Fossen and Tikoff, 1993; Passchier, 1998; Jiang and Williams, 1998; Xypolias, 2010; Fossen and Cavalcante, 2017). However, in the case of a triclinic deformation, the lineation shows a wide variation in orientation within the shear zone (Forte and Bailey, 2007). In the case of the Amorgos Unit, the observed stretching lineation displays a constant NW-SE orientation on the mylonitic foliation, and it is parallel to the shear direction, which may imply a monoclinic general shear deformation pattern. Aside from the microstructural features, kinematic vorticity values are needed to further understand the flow pattern and the shear style.

The Dn_{+1} deformation stage indicates an abrupt change in fold-phase movement, in which a distinct group of folds shows a top-to-the SE vergence opposite to the general shear recorded in the $Dn_{a/b}$ stages (Fig. 9c). Such a change in fold vergence, points to an opposing transport direction. Based on overprinting relationships, the Dn_{+1} folds should be regarded as a separate folding phase that took place during a secondary deformation stage, unrelated to the progressive $Dn_{a/b}$ stages. This conclusion arises from the opposing fold-vergence and cross-cutting relationships, although fold generations can occur at different times in different parts during the same progressive deformation stage (Fossen, 2000; Fossen et al., 2019). Additionally,

Dn_{+1} kink-like folds with rotational movements towards SE and SW reveal variations in shear direction, implying a switch in the orientation of the maximum principal axis (σ1) and contraction direction from NW-SE to NE-SW. In this concept, these structures may involve a non-steady deformation period, in which σ1 changes during the same deformation stage.

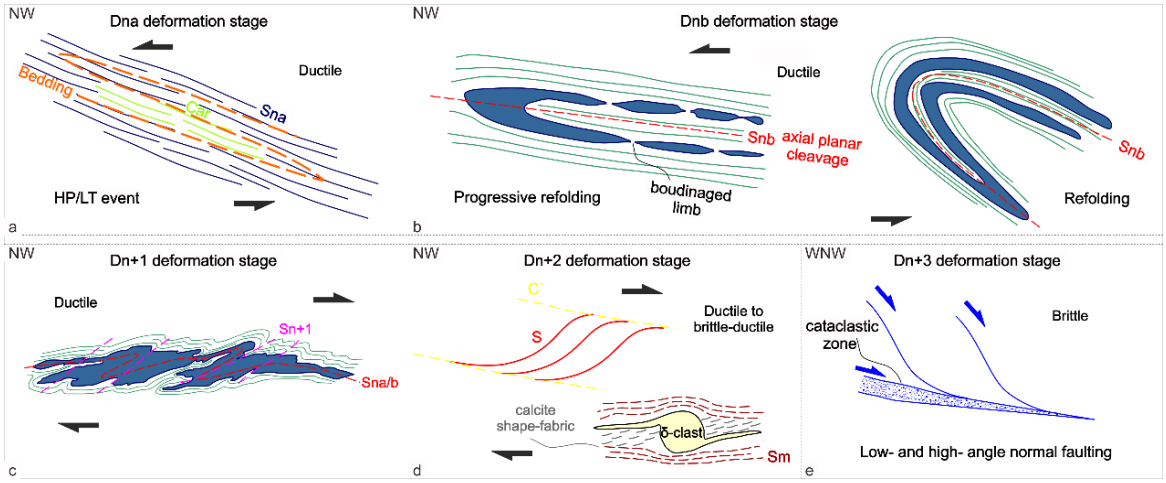

Figure 9: Schematic sketches illustrating the tectono-metamorphic evolution of Amorgos Unit. (a) Formation of fibrous Fe-Mg carpholite related to subduction-related HP event during the Dn_a stage. (b) NW-vergent folding and refolding structures during the progressive Dn_b stage. (c) SE-vergent folding, overprinting the pre-existing composite $Sn_{a/b}$ foliation during the Dn_{+1} deformation stage. (d) Dn_{+2} mylonitic foliation (Sm) indicating top-SE kinematics. (e) Dn_{+3} low- and high- angle normal faulting under brittle conditions.

The Dn_{+2} stage revealed localized deformation in an intermediate structural level of the Amorgos Unit, in which an ultra-mylonitic SE-dipping foliation is developed, accompanied by a SE-plunging lineation. Kinematically, this deformation stage is dominated by top-to-the SE shearing (e.g., Richti shear zone) (Fig. 9d). It should be noted that asymmetric fabrics are observed only in the lineation-parallel section, while a significant symmetry is recognized in the lineation-normal plane. In this case, this shear zone may represent a monoclinic simple shear zone. Furthermore, kinematic indicators (e.g., oblique fabric, σ-type clasts) within the Kapsala zone provide information about a pre-existing foliation affected by a younger one. In this case, the top-SE oblique calcite fabrics may record the last increment, while the top-NW σ-type clasts may record an average of the pre-existing deformation history. For these reasons, the Dn_{+2} stage is differentiated from the previously described general

top- NW shearing. Aside from the described kinematics, most of the observed C- and C'- type shear bands display top-to-the SE sense of shear. Generally, the shear bands seem to represent late syn-mylonitic or early post-mylonitic features, generated at a late stage of an active shear zone when the mylonitic foliation is already established (Passchier and Trouw, 2005). It is possible that the shear bands recognized in the Amorgos Unit, may record the early post-mylonitic deformation and possibly signify the early exhumation stages of the Amorgos Unit. This is also evidenced by the fact that these shear bands are gradually replaced by top-SE semi-brittle low –angle faults with normal-sense drag geometries. These structures probably correspond to the final stages of exhumation of the Amorgos Unit and may be linked to the reported Early-Mid Miocene zircon (U-Th)/He ages (Laskari et al., 2022a). These ages agree with the reported AFT ages (Ring et al., 2009), pointing to rapid cooling at temperatures from 200°C to less than 60°C during that time. The Dn_{+3} deformation stage is solely developed under brittle conditions, producing cataclastic zones and low- high-angle normal faults (Fig. 9e). The final deformation event is related to neotectonic normal faults responsible for the Amorgos morphology.

4.2. Alternative scenarios for the Amorgos Unit and regional Implications

The Amorgos Unit records a complex deformation history, including both top- NW and SE kinematics. Burial and low-grade HP metamorphic conditions were coeval with NW-directed thrusting (Dn_a), suggesting syn-metamorphic shortening during the Latest Eocene, followed by internal imbrication due to progressive deformation (Dn_b). However, such top-NW kinematics show an opposing shear sense relative to the overall kinematic framework of the Hellenides, where the nappes record an SW to W-ward translation (Pe-Piper and Piper 2002; Jolivet and Brun 2010; Ring et al., 2010; Papanikolaou, 2021). In this concept, the proposed tectonic model for these opposed kinematics is consistent with a retro-wedge setting pointing to backthrust-related structures that likely resulted from retro-arc thrust sheet burial (Laskari et al., 2022a). A retro-wedge model requires ongoing accretion of sediments and basement rocks on the pro-wedge side, and differences in subduction velocity rates (Willett et al., 1993; Doglioni et al., 2007; Jamieson and Beaumont, 2013; Thigpen et al., 2017; Encinas et al., 2021). In the Hellenides, the Late Eocene-Oligocene proward

accumulation of the nappes and the slowdown of the subducting continental lithosphere (e.g., Apulia) resulted in the growth and uplift of the wedge. Forethrusts are accommodated by top -W/SW shearing. On the other hand, large-scale back-thrusting documented elsewhere in the Hellenides, is characterized by top- NE/NW sense of shear (Xypolias et al., 2012; Gerogiannis and Xypolias 2017; Grasemann et al., 2021). Therefore, we assume that the initial internal retrobelt that developed in the Rhodope-Balkan zone (Doglioni et al., 1996) must have moved to the south following the southward migration of the Hellenic orogen. In the Aegean domain, the Late Eocene- Oligocene frontal accretion of several imbricated HP CBU nappes (Ring et al., 2020; Glodny and Ring 2022; Kotowski et al., 2022; Uunk et al., 2022), probably resulted in a retrobelt in the Cyclades-Dodecanese, including the top-NW Telendos (back-) thrust observed in Kalymnos (Grasemann et al., 2021) and those of Amorgos Unit. The proposed retro-wedge model could also explain the partial reset zHe ages recorded in the structurally higher metaflysch, suggesting residence in the zHe PRZ and limiting the maximum burial to less than 4 km. In this case, a depositional wedge-top basin of the retro-arc thrust belt must have been developed. On the other hand, the total reset ages of the stratigraphically lower metaflysch and lowermost metaconglomerate (Kapsala Fm.) indicate burial over 6 km depth (Laskari et al., 2022a).

As already mentioned, the Amorgos Unit experienced low-grade conditions based on the occurrence of Fe-Mg carpholite. Overall the carpholite occurs in aluminum-rich metasedimentary rocks and metabauxites, indicating a pressure-dominated metamorphic event (Goffe and Chopin, 1986; Theye et al., 1992; Bousquet et al., 2008). For this reason, the metamorphic conditions recorded in Amorgos Unit are attributed to the thrust sheet burial within the retro-arc in conjunction with the tectonically overlying units, causing the inferred HP event (Laskari et al., 2022a). Additonally, the fact that the top-NW kinematics ($Dn_{a/b}$ stages) predate the top-to-SW (Dn_{+1} stage), suggest a former retroward movement, followed by subsequent proward kinematics.

An alternative tectonic model for the Amorgos tectonometamorphic evolution, is the possible coexistence of a retrobelt along with a short-lived SE-dipping intra-

continental subduction zone within the overriding plate (Pelagonian domain) (Fig. 10). The scenario of an additional subduction zone stems from the fact that Fe-Mg carpholite is considered as a typical mineral for a subduction-related process. It should be noted that during a prograde cold-subduction P-T path (~10° C/km), carpholite forms through the reaction chlorite+ kaolinite= carpholite+ quartz (in the presence of H_2O), while under warm-subduction path carpholite is produced through the reaction chlorite+ pyrophylite= carpholite+ quartz (in the presence of H_2O) (Pourteau et al., 2014 and references therein). In the case of the Amorgos Unit, within the metabauxites the carpholite is intergrown with pyrophyllite (Theye et al., 1997), from which the estimated P-T conditions are 300-350° C and 8kbar. Additionally, higher pressure-dependant minerals, such as aragonite, kyanite and chloritoid, have not recognized by us nor by previous studies, implying that the P-T estimates of the Amorgos Unit do not favor much higher conditions (see petrogenetic grids, Bousquet et al., 2008 and references therein). The absence of chloritoid also indicates that the temperature conditions took place within the stability field of the carpholite. Therefore, we speculate a subduction-type relatively warmer geothermal gradient for the P-T path of the Amorgos Unit related to a short-lived SE-directed subduction zone. In this case, tectonic burial by top-NW thrusting was probably initiated in the Latest Eocene, leading to burial depths of 23- 18 km (equivalent to geothermal gradients of 15-20° C/km) and resulting in low-grade HP metamorphic conditions of the Amorgos Unit (Dn_a stage). The already formed retrobelt (e.g., Telendos thrust) probably affected the Amorgos Unit by causing internal imbrication with subsequent top-NW kinematics (Dn_b stage) and partly exhumation of Amorgos HP rocks to less than 8 kbars. The exhumation mechanism of these HP rocks in the retro side included two-sided subduction and collision process prior to the Miocene extensional deformation and final exhumation.

The scenario of a SE-directed subduction zone is not in accordance with the tomographic models of a long-lived NE-directed subduction zone in the Hellenides, active since the Mesozoic that controlled the regional evolution (Jolivet et al., 2003; Van Hinsbergen et al., 2005; Jolivet and Brun 2010; Papanikolaou, 2021). This single NE-dipping subduction zone is evidenced by the southward migration of trench and

magmatic arc recorded in the Hellenides. However, opposite-dipping intra-continental subduction zones are proposed for the CBU nappes from Andros and Evia islands to explain the top-to-the NE kinematics, although a more internal position is assumed for the CBU (Gerogiannis et al., 2019, 2021). Analogous two-sided subduction system combined with a retro-belt has been observed in other orogenic belts, such as the Variscan orogen (Kroner and Romer, 2013). Therefore, in the case of the Hellenides, kinematically opposing subduction zones cannot be excluded. This speculation suggests that the Hellenic belt was characterized by a complex double-vergent orogen at least during the Latest Eocene-Oligocene. The driving forces of such a combined model, may be generated from the successive advancing nappes and the ongoing push of the incoming external units (e.g., Basal Unit) and the hinterland (Pelagonian domain), representing an expression of a continent-continent collision.

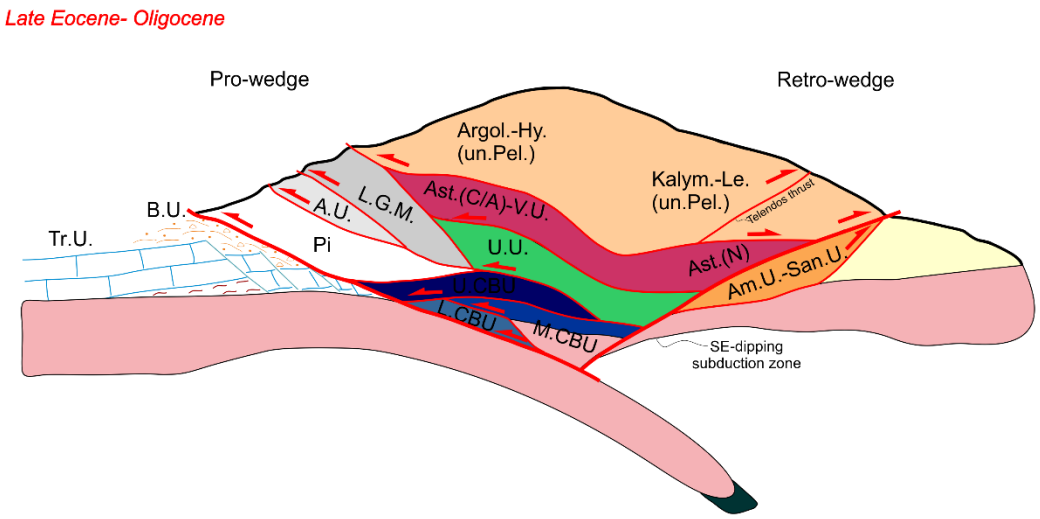

Figure 10: Proposed tectonic model for the Late Eocene- Oligocene evolution of the Hellenides, suggesting a composite double-verging orogen with the development of at least two subduction zones and a retrobelt.

Our structural observations, presented in this study, also demonstrate that the top-NW kinematics are followed by opposite top-SE movements (Dn_{+1}) within a compressional phase. Such kinematics could reflect the nappe stacking in the advancing pro-wedge side. Therefore, a straightforward assumption is that top-NW and SE developed during a protracted compressional phase, characterizing the Late

Eocene-Oligocene nappe stacking in a syn-orogenic setting that affected the southern Aegean (Jolivet and Brun 2010).

After the compressional phase, the Aegean domain transformed to an extensional province, resulted from the southward retreat of the NE-directed subducting slab (Royden, 1993; Jolivet and Faccenna 2000). Lithospheric-scale extension was initiated at Miocene (23-21 Ma) (Ring et al., 2010). In the Amorgos Unit, extensional post-orogenic tectonics is accommodated by top-to-the SE to ESE kinematics (Dn_{+2} deformation stage). Based on the similar zHe ages and exhumation history with the Santorini hanging wall (Schneider et al., 2018; Laskari et al., 2022a), the Amorgos top-SE to ESE kinematics could be associated to the Santorini detachment system (SDS), implying that the SDS was active at least during Early-Mid Miocene (19-17 Ma). High-angle normal faulting observed in the Amorgos Unit (Dn_{+3} deformation stage) is related to the Plio-Quaternary Aegean extensional and wrench-faulting (e.g., offshore Amorgos fault), leading to the modern morphology and controlling the southern coast of the island (Papadopoulos and Pavlides, 1992; Hooft et al., 2017; Tsampouraki-Kraounaki et al., 2021).

5. Conclusions

New field-based and (micro-)structural investigations from the low-grade HP rocks of Amorgos Unit allowed us to draw the following conclusions:

- The earliest Dna structures are synchronous with low-grade HP conditions and associated with an NW-SE stretching lineation Lna that took place in a compressional setting with top-NW kinematics. The dominant deformation mechanisms in calcite grains revealed low-temperature conditions not exceeding 400° C. Based on the preserved Fe-Mg carpholite, the HP event of Amorgos Unit took place during a short-lived SE-dipping intra-continental subduction zone under relatively warm geothermal gradients.
- The progressive Dnb structures are related to NW-verging folds and refolds, including an NE-SW intersection lineation Lnb. Map scale thrusts are consistent with top-to-the NW kinematics, compatible with an already formed retrobelt (e.g., Telendos thrust). The observed retroward top-NW

kinematics along with subordinate reverse top-SE shears and asymmetric fabrics in both lineation-parallel and lineation-normal sections, indicate a (monoclinic) general shear deformation pattern.

- The Dn+1 structures revealed an opposing transport direction with top-SE and SW fold vergence, overprinting the already formed composite foliation and still within a compressional setting. These top-SE kinematics, are probably associated with the southward nappe stacking in the advancing pro-wedge.
- The Dn+2 structures are related to localized deformation under ductile conditions, associated with a SE- plunging lineation and top-SE sense of shear. Asymmetric fabrics observed only in lineation-parallel sections indicate a monoclinic simple shear deformation pattern in the frame of an extensional deformation setting. Based on the similar kinematics, the Amorgos Pelagonian-derived Unit can be linked to the Santorini hanging wall, suggesting their common post-orogenic exhumation history.
- Dn+3 structures correspond to the final deformational phase recorded in the Amorgos Unit and are related to high-angle normal faulting.
- During the Latest Eocene-Oligocene collisional phase, the Hellenides were probably characterized by a composite double-vergent orogen with at least two subduction zones in combination with a retrobelt.
- Post-orogenic extension in the SE Cyclades was accommodated by the SDS that was active at least during Early-Mid Miocene.

Chapter IV

Structural Study and Detrital Zircon Provenance Analysis of the Cycladic Blueschist Unit Rocks from Iraklia Island: From the Paleozoic Basement Unroofing to the Cenozoic Exhumation.

Sofia Laskari [1], *, Konstantinos Soukis [1], Stylianos Lozios [1], Daniel F. Stockli [2], Eirini M. Poulaki [2] and Christina Stouraiti [1]

[1.] *Faculty of Geology and Geoenvironment, National and Kapodistrian University of Athens, Greece.*
[2.] *Department of Geological Sciences, Jackson School of Geosciences, University of Texas at Austin, USA.*

Abstract

Detailed mapping and structural observations on the Cycladic Blueschist Unit (CBU) on Iraklia Island integrated with detrital zircon (DZ) U-Pb ages elucidate the Mesozoic pre-subduction and the Cenozoic orogenic evolution. Iraklia tectonostratigraphy includes a heterogeneous Lower Schist Fm., juxtaposed against a Marble Fm. and an overlying Upper Schist Fm. The contact is an extensional ductile-to-brittle-ductile, top-to-N shear zone, kinematically associated with the Oligo-Miocene exhumation. The DZ spectra of the Lower Schist have Gondwanan/peri-Gondwanan provenance signatures and point to Late Triassic Maximum Depositional Ages (MDAs). A quartz-rich schist lens yielded Precambrian DZ ages exclusively and is interpreted as part of the pre-Variscan metasedimentary Cycladic Basement, equivalent to schists of the Ios Island core. The Upper Schist represents a distinctly different stratigraphic package with late Cretaceous MDAs and dominance of Late Paleozoic DZ ages, suggestive of a more internal Pelagonian source. The contrast in the DZ U-Pb record between Lower and Upper Schist likely reflects the difference between a Paleotethyan and Neotethyan geodynamic imprint. The Triassic DZ input from eroded volcanic material is related to the final Paleotethys closure and Pindos/CBU rift basin opening, while late Cretaceous metamorphic/magmatic zircons and ~48-56 Ma zircon rims constrain the onset of Neotethyan convergence and high-pressure subduction metamorphism.

1. Introduction

In most cases, poly-deformed and poly-metamorphosed high-grade rocks have lost their fossil record and much of the stratigraphic framework necessary for local and regional correlations. In ancient subduction complexes, this lack of a stratigraphic frame hinders the reconstruction of subduction and exhumation processes, hampers an understanding of these processes' overprint primary structures and lithostratigraphy and leads to the resulting tectonostratigraphy due to both subduction underplating and back-arc extension.

The recognition of Metamorphic Core Complexes (MCCs) (Lister et al., 1984) made the Attic-Cycladic Crystalline Complex (ACCC) (Fig. 1a, b) the subject for several studies (Bröcker et al., 1993; Gautier et al., 1993; Bröcker and Frantz 1998; Brichau et al., 2007; Jolivet and Brun 2010; Jolivet et al., 2010; Ring et al., 2010; Grasemann et al., 2012; Soukis and Stockli 2013; Huet et al., 2014; Malandri et al., 2017; Schneider et al., 2018; Flansburg et al., 2019; Poulaki et al., 2019) primarily focused on the Cenozoic structural and metamorphic evolution of the overlying Permian to Mesozoic Cycladic Blueschist Unit (CBU) and its Carboniferous Cycladic Basement (CB). These studies have offered insights into both the subduction processes and partly the back-arc extension and MCC-formation processes (Bröcker et al., 1993; Gautier et al., 1993; Bröcker and Frantz 1998; Brichau et al., 2007; Jolivet and Brun 2010; Jolivet et al., 2010; Ring et al., 2010; Grasemann et al., 2012; Soukis and Stockli 2013; Huet et al., 2014; Malandri et al., 2017; Schneider et al., 2018; Flansburg et al., 2019; Poulaki et al., 2019). However, despite a rare accumulation of constraints, several fundamental aspects of pre-orogenic configuration are still not fully understood. One of them is how the transition from the Paleozoic Paleotethys subduction cycle to Neotethys opening is imprinted into the CBU rock record.

The small island of Iraklia occupies a critical position between Ios and Naxos (Fig. 1c), two islands where pre-Alpine CB and the CBU rocks constitute the footwall of MCCs exhumed by sets of extensional detachments, including the Paros–Naxos detachment system. Although previous studies (Avdis and Triantaphyllis 1994; Behrmann and Seckel 2004) reported that Iraklia comprises CBU rocks mainly similar

to those of Naxos and Ios, the authors of (Papanikolaou 1987) suggested the existence of pre-alpine basement rocks. However, no detailed work has been carried out to investigate (a) the tectonostratigraphy of Iraklia, (b) the possible stratigraphic impact of the Paleotethyan and Neotethyan plate-tectonic cycles, and (c) the stratigraphic/metamorphic correlations with rocks in the footwalls of the Ios and Naxos MCCs.

Recently, detrital zircon (DZ) U-Pb studies in the ACCC have provided fundamental insights regarding the maximum depositional ages (MDAs), tectonic affinity and provenance of the CBU and CB rocks, and the age of metamorphism. A number of these studies have also shed light on the CBU stratigraphy and the pre-Eocene subduction paleogeographic organization (Henjes-Kunst & Kreuzer, 1982; Keay and Lister, 2002; Pe-piper and Piper 2002; Bröcker and Pidgeon 2007; Löwen et al., 2015; Bröcker et al., 2016; Hinsken et al., 2016; Seman et al., 2017; Grasemann et al., 2018; Flansburg et al., 2019; Poulaki et al., 2019).

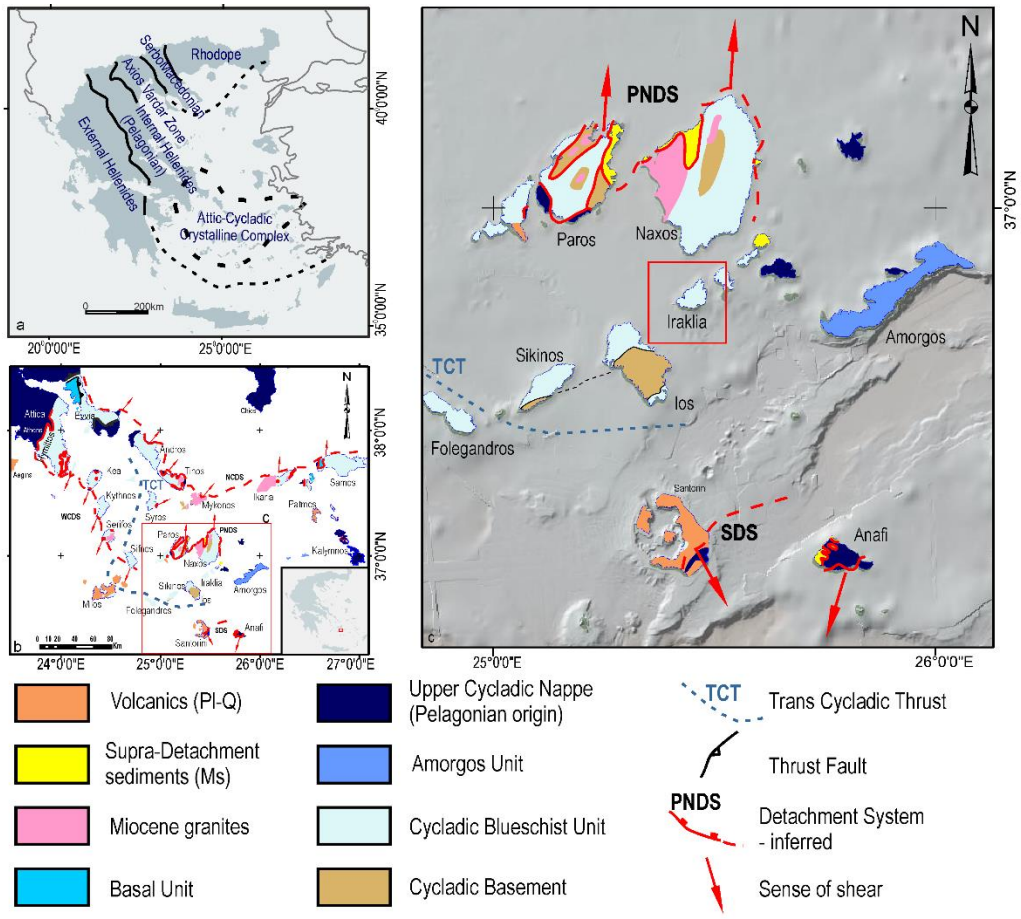

Figure 1. (**a**) Schematic map of major structures in Greece, (**b**) detailed map of the ACCC

illustrating the main units, the major structures, and (**c**) simplified geology of Iraklia and neighboring islands (base map made from GeoMapApp https://www.geomapapp.org accessed on 20th of December 2021). Trans Cycladic Thrust (TCT), North Cycladic Detachment System (NCDS), Paros-Naxos Detachment System (P-NDS) West Cycladic Detachment System (WCDS), and Santorini Detachment System (SDS) compiled from (Gautier and Brun, 1994; Pe-Piper and Piper 2002; Soukis and Papanikolaou 2004; Brichau et al., 2007; Ring et al., 2010; Jolivet et al., 2010; Lekkas et al., 2011; Soukis and Stockli 2013; Grasemann et al., 2012, 2018, 2021; Schneider et al., 2018).

This study combines detailed geological mapping, structural observations, and DZ U-Pb geochronology to (a) constrain the tectonostratigraphy of Iraklia CBU rocks, (b) establish tectonostratigraphic and metamorphic correlations with the neighboring Ios and Naxos, and (c) reconstruct the pre-subduction history of Iraklia, as part of the regional Paleotethyan to Neotethyan evolution.

2. Geological Setting

The ACCC exposes the deepest exhumed parts of the subducted and metamorphosed Hellenides as a result of Cenozoic back-arc extension due to accelerated slab roll-back of the subducting plate (Royden, 1993; Jolivet and Brun 2010; Ring et al., 2010). The tectonostratigraphy of the ACCC comprises the pre-alpine CB and the metasedimentary CBU cover sequence, which constitute the exhumed lower plate of regional low-angle detachment fault systems. The upper plate comprises the Upper Cycladic Nappe and the Late Miocene supra-detachment sediments (Jansen 1977; Dürr et al., 1978; Böger 1983, Papanikolaou 1987; Pe-Piper and Piper 2002; Jolivet and Brun 2010; Ring et al., 2010; Menant et al., 2016; Stouraiti et al., 2017; Mavrogonatos et al., 2021).

The CBU includes a Permo-Mesozoic sequence of marble, schists, and metavolcanic rocks metamorphosed under eclogite to blueschist metamorphic conditions in the Eocene, which are best preserved on Evvia, Syros, Sifnos, and the Tinos islands (Papanikolaou 1978; Blake et al., 1981; Bröcker 1990; Pe-Piper and Piper 2002; Keiter et al., 2011; Cisneros et al., 2021). While most classic CBU rocks experienced peak HP-LT metamorphism during the Eocene (~45-53Ma) (Bonneau and Kienast 1982; Wijbrans and McDougall 1988; Lagos et al., 2007), recent studies have documented

either prolonged or renewed early Eocene to Oligocene HP metamorphic event during ongoing subduction and underplating (Kotowski et al., 2020; Ring et al., 2020). During the Oligo-Miocene, the CBU and CB rocks have been reworked at a much lower pressure in various temperature conditions from greenschists to amphibolite facies and locally experienced partial melting conditions due to rapid syn-extensional decompression and migration of the Hellenic magmatic arc (e.g., Naxos, Paros, Ikaria and Mykonos, Jansen 1977; Keay et al.,2001; Denele et al., 2011; Laurent et al.,2015; Beaudoin et al., 2015; Laurent et al., 2015; Cao et al., 2017; Peillod et al., 2017; Ring et al., 2018).

An overall two-stage Cenozoic exhumation history has been documented in most CBU rocks. The earlier Eocene-Oligocene syn-orogenic exhumation stage occurred within the subduction zone, allowing for local preservation of the HP imprint (e.g., Evvia, Syros, Tinos, Sifnos) (Pe-Piper and Piper 2002; Keiter et al., 2011; Kotowski et al., 2020; Xypolias et al., 2003; Roche et al., 2016). The second stage included a late Cenozoic (mainly Miocene) post-orogenic exhumation, resulting in the formation of the MCCs bounded by low-angle detachment systems (Ring et al.,2003; Xypolias et al., 2003, 2012; Huet et al., 2009; Jolivet and Brun 2010; Jolivet et al., 2010; Ring et al.,2010; Bargnesi et al., 2013; Menant et al.,2016; Roche et al., 2016). The major detachment systems that have been identified juxtaposing the CBU against the Upper Cycladic Nappe are: i) the North Cycladic Detachment System (Andros, Tinos, Mykonos, Ikaria) and the Paros-Naxos Detachment System (Paros, Naxos, Ios) with top-to-the-N-NE kinematics, and ii) the West Cycladic Detachment System (Attica, Kea, Kythnos, Serifos) and the South Cycladic Shear Zone and the Santorini Detachment (Ios, Santorini) with top-to-the-S-SW kinematics, supporting the scenario of a symmetric pattern of extension in the Aegean Sea (Lister et al., 1984; Gautier et al., 1993; Bröcker and Franz 1998; Vandenberg and Lister 1999; Jolivet and Brun 2010; Jolivet et al., 2010; Ring et al., 2010; Lekkas et al., 2011; Philippon et al., 2011; Grasemann et al., 2012; Soukis and Stockli 2013; Mizera and Behrmann 2016; Schneider et al., 2018; Coleman et al., 2019, 2020). Emplacement of syn-tectonic Miocene I- and S-type granitic intrusions due to migration of the magmatic appears to temporally coincide with the late-stage activity of these detachment

systems (Altherr et al., 1994; Pe-Piper and Piper 2002; Brichau et al., 2007; Bolhar et al., 2010; Stouraiti et al., 2010, 2018; Denele et al., 2011; Laurent et al.,2015).

The structurally underlying CB is mainly exposed on the islands of Paros, Naxos, Ios, Sikinos and comprises Carboniferous (Variscan s.l.) granitoids related to the closure of the Paleotethys and intruded into late Proterozoic–early Paleozoic metasedimentary sequences of Gondwanan affinity (Jansen 1977, Papanikolaou 1977, 1980; Dürr et al., 1978; van der Maar 1981; Henjes-Kunst & Kreuzer, 1982; Andriessen et al., 1987; Engel and Reischmann 1998; Reisschmann 1998; Keay and Lister 2002; McGrath et al., 2017; Zlatkin et al., 2018; Flansburg et al., 2019). The contact between CB/CBU has been variably considered as either an extensional detachment fault, ductile shear zone (Forster and Lister 1999, 2009; Thomson et al., 2009; Augier et al., 2014), or thrust (Huet et al., 2009). While undoubtedly tectonically overprinted in a number of places, recent detrital zircon U-Pb studies have documented a deformed depositional CBU-CB contact with the CBU resting unconformably on the CB and representing continuous sedimentation from the late Permian to late Cretaceous (Keay, 1998; Bröcker et al., 2016; Seman et al., 2017; Poulaki et al., 2019, 2021). This suggests a parautochthonous nature for the contact between CB and CBU that is also supported by the similarity of DZ signatures of the basal CBU, closely resembling the underlying CB (Poulaki et al., 2019, 2021). The DZ signatures of the CB and CBU metasedimentary units throughout the Cyclades revealed a Gondwanan provenance (Keay and Lister 2002) that remained relatively unchanged until the CBU rocks approached the trench of the subduction zone, as indicated by significant late-stage input from the Internal Hellenides (Seman et al., 2017; Flansburg 2019; Poulaki et al., 2019).

Structurally, above the CBU lies the Upper Cycladic Nappe. This is a diverse group of low-grade to amphibolite-facies Permian to Mesozoic metasedimentary rocks, granitic orthogneiss, and metamorphosed ophiolitic rocks (the latter locally known as Upper Unit) (Dürr et al., 1978; Papanikolaou 1980, 2021; Reinecke et al., 1982; Bonneau 1984; Altherr et al., 1994; Bröcker and Franz 1998; Soukis and Papanikolaou 2004; Soukis and Stockli 2013; Huet et al., 2014; Menant et al., 2016; Mavrogonatos et al., 2021). The Upper Cycladic Nappe is intruded by sparse late

Cretaceous granitoids, and it is correlated with the Pelagonian domain of continental Greece (Dürr et al., 1978; Papanikolaou 1980; Reinecke et al., 1982; Bonneau 1984; Bröcker and Franz 1998; Soukis and Papanikolaou 2004; Huet et al., 2014; Menant et al., 2016). The Pelagonian-derived rocks of continental Greece exhibit a complete stratigraphy, consisting of Triassic to Jurassic carbonates underlying a wildflysch and ophiolites of late Jurassic to early Cretaceous age, covered by late Cretaceous transgressive carbonates and a late Cretaceous to Eocene flysch (Pe-Piper and Piper 2002; Papanikolaou 2021).

The geology of Iraklia island was first studied by the Greek Geological survey, which published a 1:50,000 scale geological map for the Iraklia and Schinoussa islands (Avdis and Triantaphyllis 1994). These workers reported the existence of a probable Triassic marble sequence, overlying schist and marble alternations, which they assigned to CBU. Subsequent structural and piezometric paleo-stress analyses were used to propose a four-stage deformation that includes an early D1 deformation attributed to the Eocene metamorphism, D2 shearing with top-to-the-north kinematics [17]. The syn-tectonic temperature conditions were constrained to 400–450 °C and differential stress approximately 29–62 MPa. In contrast, D3 and D4 deformation phases were attributed to E-W shortening, which resulted in isoclinal folding and reverse faulting. The same authors reported blueschists facies assemblages from the southwestern part of the island, suggesting that the main deformation phase occurred within the stability field of glaucophane.

Although the lithostratigraphy of Iraklia is quite well known, age constraints, the pre-subduction evolution, and the tectonostratigraphic relationships with the neighboring islands, especially of Naxos and Ios, where both the CB and CBU crop out, are still pending. In the following paragraphs, a new map and revised lithostratigraphy will be presented, based on new constraints on the structural evolution, DZ U-Pb sedimentary provenance, tectonic affinity and age of the CBU rocks of Iraklia.

3. A New Geological Map of Iraklia

3.1. Lithostratigraphic Subdivision

Based on the new geological mapping results, the lithostratigraphic column of CBU on Iraklia Island can be divided into two packages, juxtaposed by a ductile to brittle-ductile shear zone. The lower part includes the Lower Schist Formation, which is exposed mainly at the central and southern part of the island and a limited outcrop in the north-eastern region (Fig. 2). The Lower Schist Fm. is lithologically quite heterogeneous and includes light brown quartz-mica schists interlayered locally with isoclinally folded light gray to dark blue marble, paragneiss and quartz-rich schist lenses.

The upper part of the lithostratigraphic column includes a thick Marble Fm. and an overlying Upper Schist Fm. The Upper Schist Fm. comprises light green to light brown intensively quartz-chlorite mica-schist intercalated with thin marble layers (Fig. 2 and 3a). The thick Marble Fm. occupies the structural position between the Lower and Upper Schist Fm. and is a well-foliated calcite and dolomite marble sequence prominently outcropping over most of Iraklia, forming a single large-scale tectonic window at the central and southern part of Iraklia (Fig. 2 and 3b).

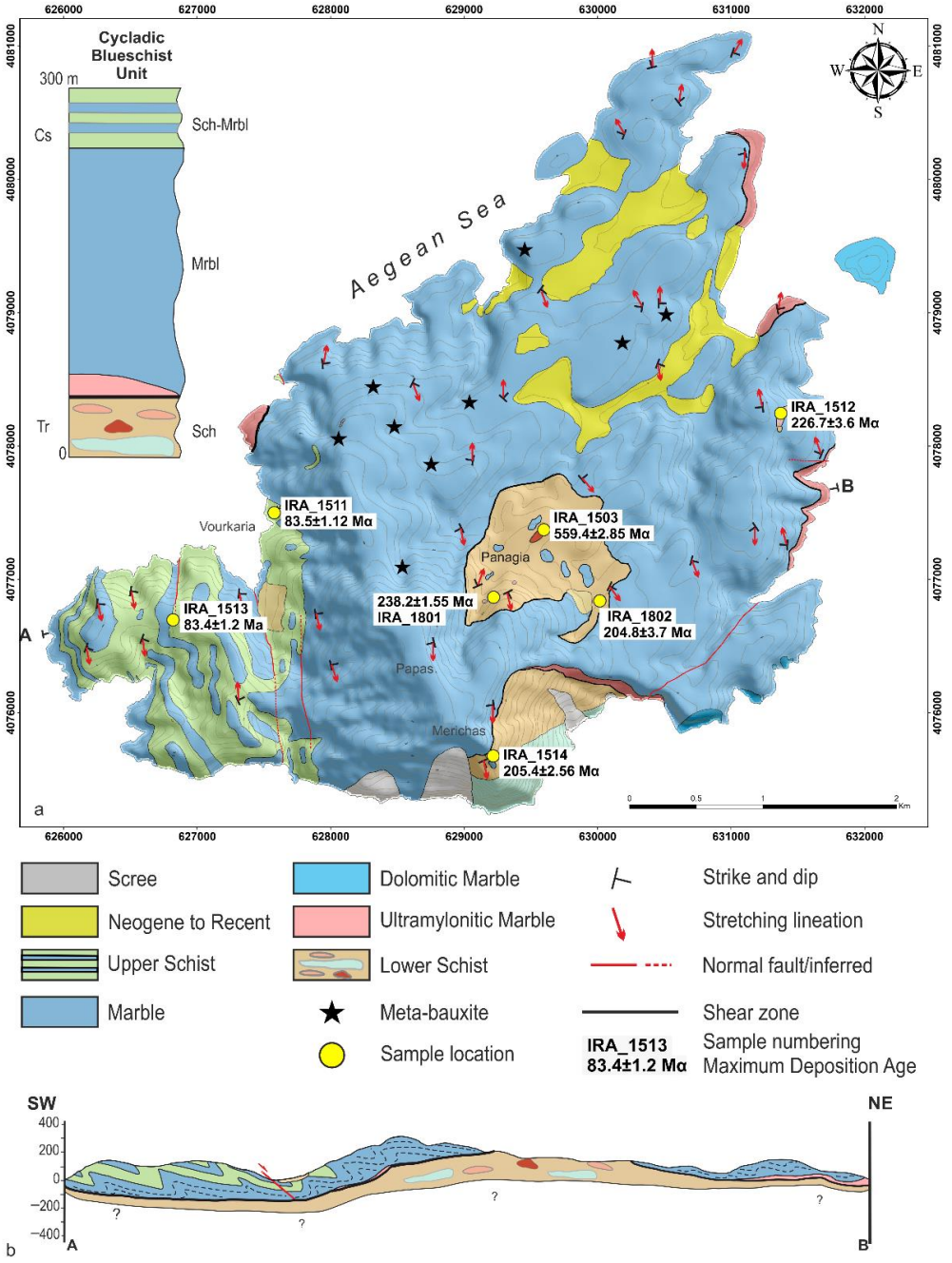

Figure 2. (**a**). Detailed geological map of Iraklia Island with metabauxite occurrences (Behrmann and Seckel 2007, this study) and locations of samples collected for U-Pb detrital zircon dating (yellow circles) and (**b**) cross-section A–B.

The Lower Schist Fm. is juxtaposed structurally against the Marble Fm. along a ductile to brittle-ductile shear zone marked by the presence of a calcitic, fine-grained ultramylonitic marble at its base. This ultramylonitic marble is exposed only in a few places along the coast (Supplementary Figure S1). At the structural top of this

Marble Fm., minor meta-bauxite occurrences are observed in north and north-western Iraklia (Berhmann and Seckel 2007; Brodhag et al., 2003), in this study.

In contrast, the contact between the Marble and Upper Schist Fm. appears to be gradational (depositional) and these two lithologies are folded together in large-scale N-S isoclinal folds.

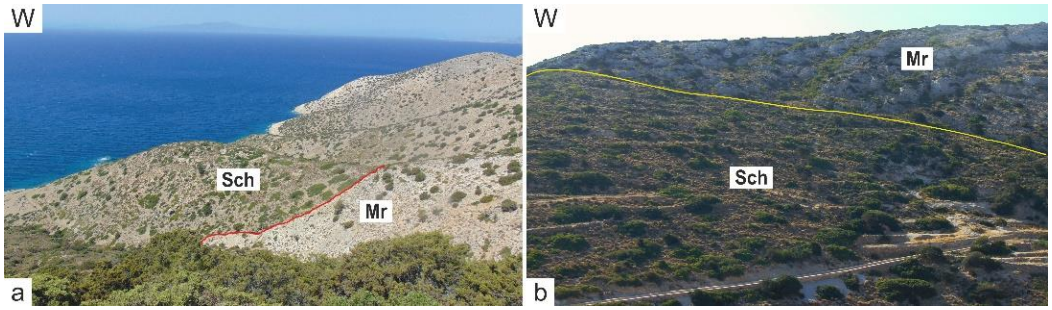

Figure 3. (**a**). View of the Upper Schist Fm. overlying the Marble Fm. (red line) in the SW part of the island (*36°50'11 " N, 25°26'14 " E*), (**b**). Main tectonic contact (yellow line) between the Lower Schist and the Marble Fm. from the central part of the island (*36°49'57" N, 25°27'2" E*).

3.2. Structures

Structural analysis on the CBU rocks on Iraklia revealed a three-stage deformation event (D1-D3), evolving from ductile to brittle conditions.

3.2.1. D1 Syn-Blueschist Facies Structures

The oldest D1 structure observed in thin sections represents a relic foliation S1 formed under blueschist-facies conditions, as revealed by the presence of blue amphibole. The HP-amphibole is preserved as inclusions within albite porphyroblasts that are syn-tectonic to the greenschist facies assemblages. In general, the albite is full of inclusions, usually forming an internal foliation (S1), sub-parallel to the main external S2 foliation. The growth of chlorite in between the boudinaged amphibole fragments strengthens the fact that the S2 foliation has been developed under greenschist-facies conditions (Fig. 4a, b). It should be noted that the blueschist minerals are observed mainly in the Upper Schist Fm. in southwest Iraklia.

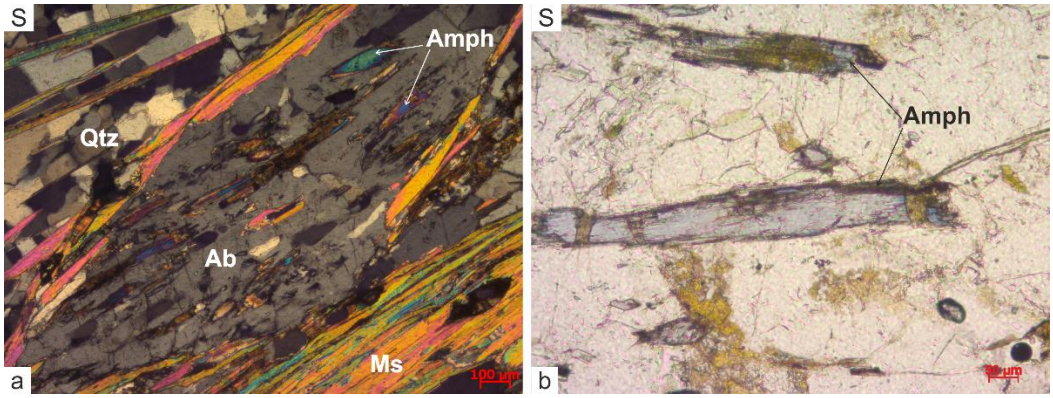

Figure 4. Microphotographs of glaucophane from the Upper Schist Fm. of SW Iraklia. (**a**). Albite porphyroblast with blue amphibole inclusions (crossed polars), and (**b**). elongated blue-amphibole grains boudinaged during the main D2 deformation stage. Note the chlorite grown in the interboudin area.

3.2.2. D2 Ductile to Brittle Deformation

The main D2 syn-metamorphic deformation stage is associated with the development of a dominant penetrative medium to fine-grained proto- to meso-mylonitic foliation (S2) that dips shallowly towards the east and west (Fig. 5a). An N-S stretching lineation (L2), parallel to isoclinal fold axes (B2), is formed on the S2 foliation planes, defined by the aligned and stretched calcite-quartz-micas aggregates (Fig. 5b, c). In thin sections, S2 foliation is formed by chlorite, epidote, actinolite, quartz, albite, white mica, and subordinate small garnet, attesting to greenschists-facies conditions. Dynamic recrystallization produced polygonal and non-equigranular quartz grains, which often exhibit subgrains. Undulose extinction of larger quartz grains indicates crystal–plastic deformation. Lensoid albite porphyroclasts bounded by chlorite and micas define a mylonitic foliation. Albite shows intense brittle deformation during D2 shearing, but despite the fracturing, it preserves D1 blue amphibole. In addition, small syn- and post-tectonic garnet grains are observed. Paragneissic rocks are mainly composed of quartz, albite, chlorite, actinolite, minor micas, calcite and garnet; the latter represents pre-tectonic porphyroblasts developed during the HP event. Kinematically, ubiquitous S-C' fabrics in most samples exhibit both top-to-the-N and S shearing, indicative of pure-shear deformation (Fig. 6a–c). Similarly, symmetric albite clasts are frequently observed, suggestive of a strong coaxial component. In stark contrast, the calcite-rich

ultramylonitic marbles record high-strain simple shear with the development of delta-clasts showing unambiguous top-to-the-N kinematics (Fig. 6d).

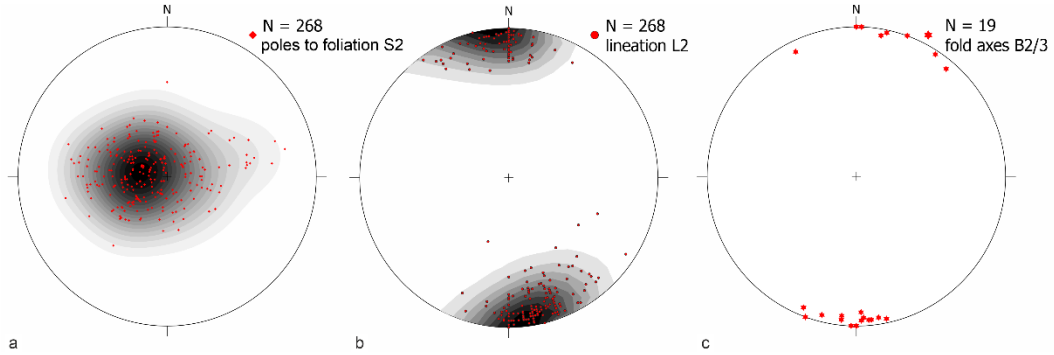

Figure 5. Stereoplots (lower hemisphere equal-area projection) (**a**). Poles to main foliation S2, (**b**). Stretching lineation L2 and (**c**) fold axes B2/3.

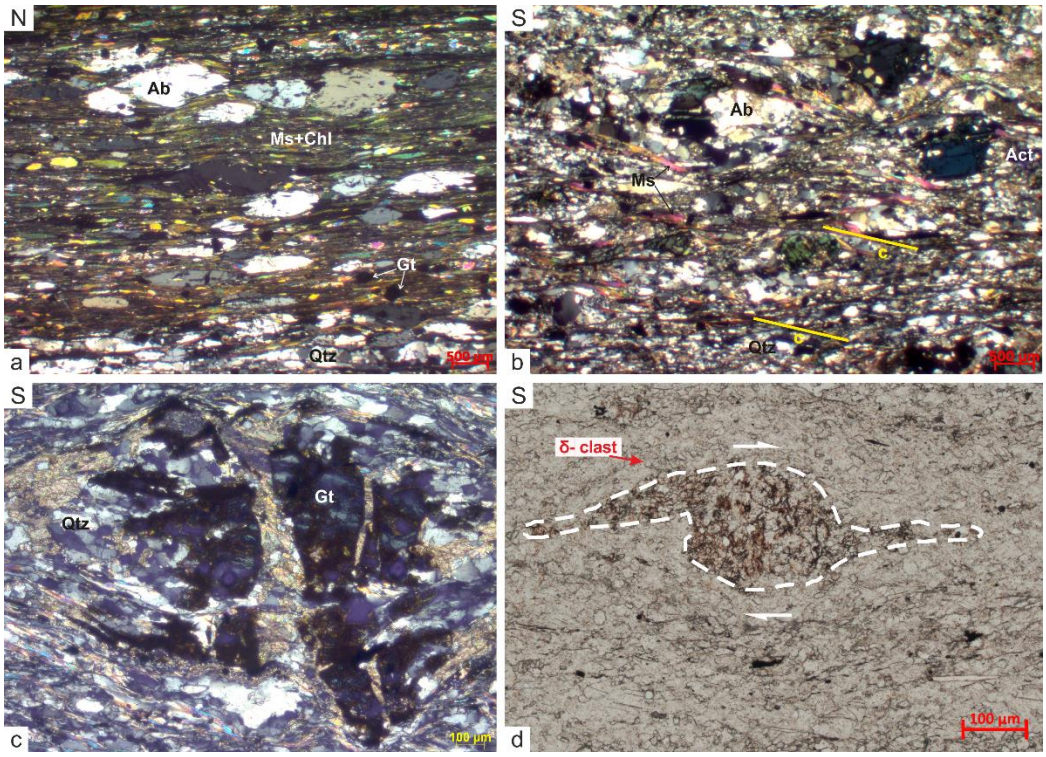

Figure 6. Thin sections (crossed polars) normal to the foliation and parallel to the stretching lineation (L2). (**a**) Upper Schist Fm. from the southwestern Iraklia (IRA_1509) comprising albite, quartz, chlorite, epidote, muscovite and rare post-tectonic garnet. S/C' shear bands indicate top-to-the-north shearing, (**b**) top-to-the-N S/C′ shear bands in the paragneissic rock of the Lower Schist Fm. (IRA_1507), (**c**) boudinaged and rotated pre-tectonic garnet towards the S, and (**d**) Delta-type calcite+siderite clast indicating top-to-the-N shearing (white arrows).

Similar simple-shear top-to-the-N kinematics are also observed in the marble mylonites along the contact between the Lower Schist Fm. and the overlying Marble Fm. defining a mylonitic shear. It should be noted that near this contact, a younger brittle overprint is observed, producing an up to 1.5 m thick cataclasitic fault zone (Fig. 7a). Progressively, the main S2 foliation is folded about N-S isoclinal folds and locally crenulated. An axial planar S3 cleavage is developed, associated with an N–S intersection lineation (L3) parallel to the main N–S fold axis (B2/3) observed in the southern part of the island (Fig. 5c, 7b).

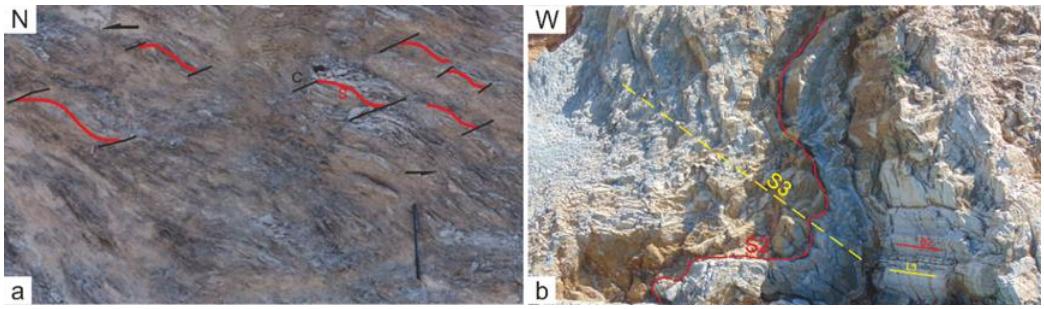

Figure 7. (**a**). S-C′ shear bands, developed in the Lower Schist Fm. with top-to-the-north kinematics (*36°49′57″ N, 25°27′5″ E*) and (**b**). Axial planar cleavage (S3) in the N–S isoclinal fold and an N–S intersection/stretching lineation L3 parallel to the B2/3 fold axes (southern part of the island) (*36°49′13″ N, 25°27′4″ E*).

3.2.3. D3 Late Brittle Deformation

D3 D3 structures are related to brittle high-angle normal faulting that cut through all previous structures. The most significant faults are the NW-trending Vourkaria and the NE-trending Merihas fault zones (Fig. 2). Kinematic indicators on the fault planes and the characteristic normal drag adjacent to the fault zones indicate a normal sense of slip.

4. Detrital Zircon U-Pb geochronology and results

4.1. Methodology

In this study, we performed detrital zircon (DZ) U-Pb dating on seven schist and paragneiss samples to constrain their provenance signature and maximum depositional ages (MDAs) in order to provide insights into the pre-subduction

evolution, tectonic affinity and regional tectonostratigraphic correlation of the metasedimentary CBU rocks of Iraklia.

Zircons were separated using standard separation techniques, including crushing and pulverizing, water table concentration, magnetic separation, and Bromoform and MEI heavy liquid separations at the UT Chron Laboratory at the University of Texas at Austin. Zircon grains were mounted on double-sided adhesive tape on 1-inch polycarbonate rounds. About 130 unpolished zircon grains were randomly selected from each sample for depth-profile Laser Ablation-Inductively Coupled Plasma-Mass Spectrometry (LA-ICP-MS) analysis, using a PhotonMachine Analyte G.2 excimer laser with a large-volume Helex cell connected to a Thermo Element2 ICP-MS, following the procedure outlined in Marsh and Stockli (2015) (Supplementary Figure S2). GJ1 was used as primary standard (601.7 ± 1.3 Ma; Jackson et al., 2004) and Plešovice as secondary standard (337.1 ± 0.4 Ma; Slama et al., 2008). The VisualAge Data Reduction Scheme was used in Iolite v3.7 for correction of the U-Pb zircon data (Paton et al., 2011; Petrus and Kamber, 2012). U-Pb ages of individual grains are reported with 2σ uncertainties. For dates >850 Ma, the $^{207}Pb/^{206}Pb$ date is reported, and for U-Pb dates <850 Ma, the $^{206}Pb/^{238}U$ dates are taken for the reported U-Pb age. A discordance filter 15% $^{206}Pb/^{238}U$ vs. $^{207}Pb/^{235}U$ and error filter 10% was applied to $^{206}Pb/^{238}U$ ages. A discordance filter 30% $^{206}Pb/^{238}U$ vs. $^{207}Pb/^{206}Pb$ was applied to $^{207}Pb/^{206}Pb$ ages. We used the detritalPy Python script (Sharman et al., 2018) for data visualization and plotting of sample data as Kernel Density Estimates (KDEs). The analytical data and calculated ages of all Iraklia samples are listed in Table S1 of the Supplementary Material.

4.2. U-Pb Results

Five samples were collected from the Lower Schist Fm., of which three were from the quartz-mica schist (IRA_1801, IRA_1802, IRA_1503) and two from the paragneisses (IRA_1514, IRA_1512) (Fig. 8, Supplementary Figure S3a-c). The quartz-rich schist IRA_1503 (*n* = 108) from the central part of the island close to Panagia village shows the youngest zircon U-Pb age mode at 559.4 ± 2.8 Ma (Ediacaran). This sample contains only Precambrian (100%) zircons with a prominent Neoproterozoic

(Tonian) peak at ~0.85 Ga, and a minor peak at the Paleoproterozoic/Archean boundary (~2.5 Ga). At the foot of Papas hill, the quartz-mica schist IRA_1801 (*n* = 130) reveals the youngest DZ age group at 238.2 ± 1.5 Ma (Carnian), with only a single zircon grain age at 220.1 ± 3.3 Ma, and zircon populations of Precambrian (*n* = 73, 52.6 %), Paleozoic (*n* = 50, 48%) and Mesozoic (*n* = 7, 5.4%) in age. The group of Paleozoic DZ ages shows a prominent Ordovician peak at 458.3 ± 6.5 Ma. Sample IRA_1802 (*n* = 118) reveals a similar age spectrum to sample IRA_1801 described above with DZ distributions of Precambrian (*n* = 54, 46%), Paleozoic (*n* = 42, 36%) and Mesozoic (*n* = 21, 18%) in age. However, for sample IRA_1802, the youngest DZ age component present is ~204.8 ± 2.9 Ma (Norian), with single zircon grain at 201.1 ± 5.2 Ma. Two prominent peaks are observed at ~243.2 ± 3.7 Ma (Anisian) and ~435.6 ± 7.4 Ma (Silurian). Depth-profile analysis from the two samples (IRA_1801, IRA_1802) from the Lower Schist Fm. revealed thin early Eocene metamorphic rims at about 48–49 Ma. Two zircons from each sample also yielded late Cretaceous metamorphic rims that experienced lead loss and hence were not included in the metamorphic age.

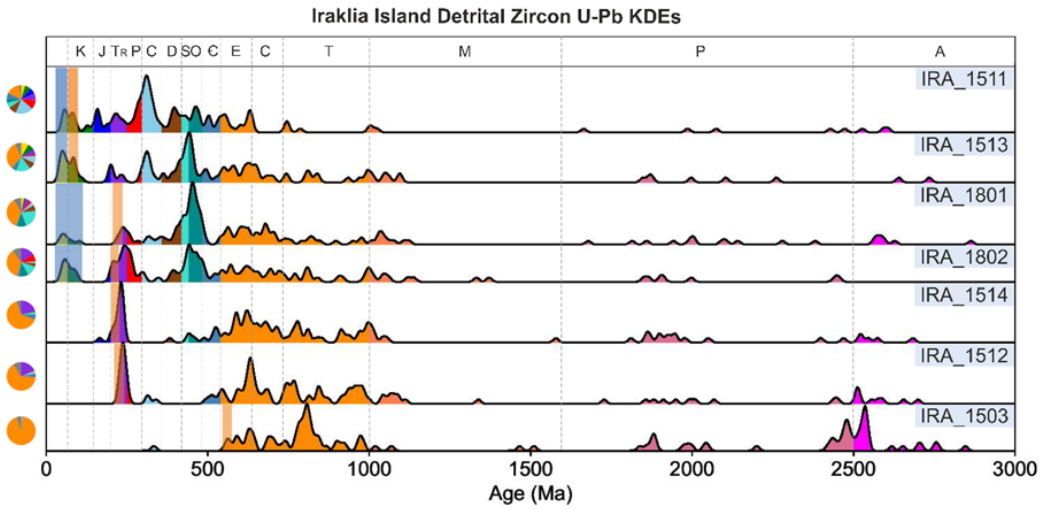

Figure 8. Detrital zircon U-Pb KDEs results. The diagrams show the compiled data from 3000-0 Ma for each sample. MDAs and metamorphic zircon rim ages are depicted in light-orange and blue, respectively. The pie diagrams show the proportions of core-age components.

Additionally, two paragneiss samples from the Lower Schist Fm. were analysed. IRA_1514 (*n* = 117) from the southern part of the island (Merihas) exhibits the youngest age mode at ~205.4 ± 2.6 Ma (Norian) with a single youngest zircon grain

at 165.4 ± 1.8 Ma. It is also contained Precambrian (*n* = 88, 75%), Paleozoic (*n* = 10, 8%), and Mesozoic (*n* = 20, 17%) DZ age modes without any prominent peak, except for a dominant Triassic component at ~233.8 ± 2.7 Ma. In sample IRA_1512 (*n* = 120), Triassic zircon ages of ~226.7 ± 3.6 Ma (Carnian) also make up the youngest age mode of this sample from the north-eastern part of the island. Precambrian zircons (*n* = 94, 78%) make up the majority of the older detrital age modes in this sample, while it possesses small amounts of lower Paleozoic (*n* = 9, 7%) and Mesozoic (*n* = 18, 15%) DZ age components. A prominent Triassic peak at 231.4 ± 1.1 Ma and a minor peak at the Ediacaran/Cryogenian boundary are also present. Despite the similar Triassic peaks in both samples (IRA_1514 and IRA_1512), these two paragneisses show marked differences in the Paleozoic DZ age spectra. More specifically, sample IRA_1514 contains a small group of early Paleozoic (Silurian, Ordovician, and Devonian) DZ age modes, not observed in the sample IRA_1512, which is characterized by late Paleozoic (Carboniferous-Permian) DZ age components.

From the Upper Schist Fm. two quartz-mica schists were collected from the southwestern and western parts of the island (Supplementary Figure S3d). Sample IRA_1513 (*n* = 105) shows the youngest DZ age mode at 83.4 ± 1.2 Ma (Campanian) with only one zircon grain at 76.1 ± 2.8 Ma, and a DZ spectrum composed of Precambrian (*n* = 49, 47%), Paleozoic (*n* = 42, 40%) and Mesozoic (*n* = 14, 13%) ages. A major peak is present at the Ordovician/Silurian boundary, while a minor late Carboniferous peak is observed at ~315.2 ± 6.1 Ma (Pennsylvanian). Sample IRA_1511 (*n* = 134) exhibits a similar DZ age mode at ~83.5 ± 1.1 Ma (Campanian) with two zircon grains at 71.4 ± 2.5 and 72.8 ± 1.1 Ma and containing DZ spectra characterized by Precambrian (*n* = 31, 23%), Paleozoic (*n* = 75, 56%) and Mesozoic (*n* = 28, 21%) DZ ages. Both samples also yielded thin early Cenozoic metamorphic rims with ages of 49-56 Ma (Early Eocene), similar to the rims obtained from the Lower Schist Fm. (Fig. 8, Supplementary Figure S4).

The Th/U in zircon grains from all Iraklia samples are useful to elucidate their origin. Most detrital zircons from the Lower and Upper Schist Fm. were derived from a felsic origin, as indicated by their elevated Th/U (>0.1, Fig. 9). In contrast, only a minor

component of zircons shows metamorphic (Th/U<0.1; Rubatto, 2002) and mafic-derived sources (Th/U>1.5, Linnemann et al., 2011). In addition, a small group of zircons is found in the transition zone between the felsic and mafic origin (1<Th/U<1.5, Hoskin and Schaltegger, 2003; Linnemann et al., 2011).

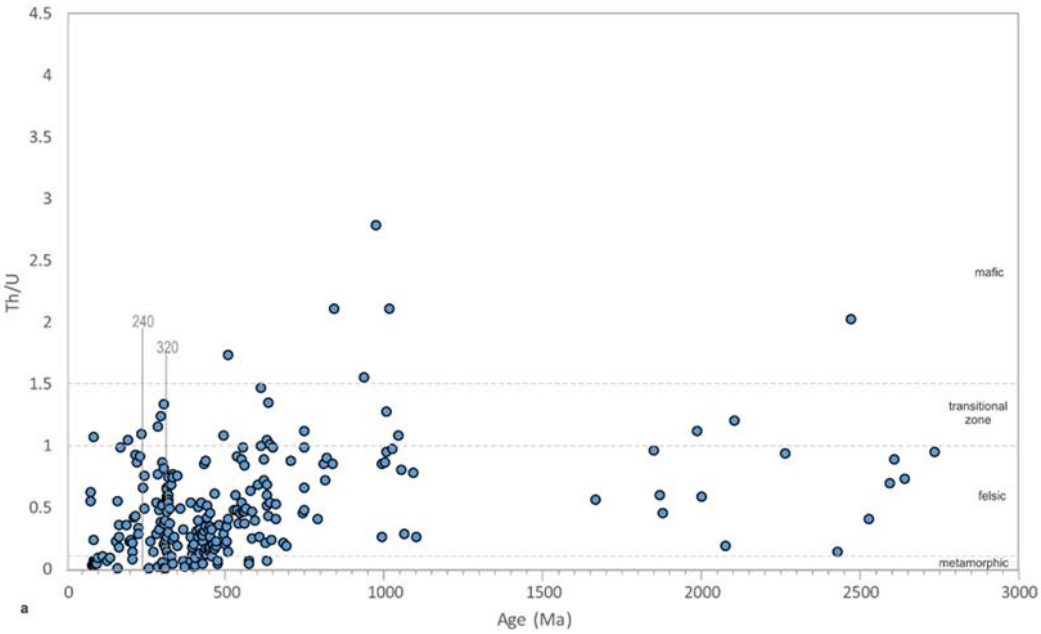

(**a**)

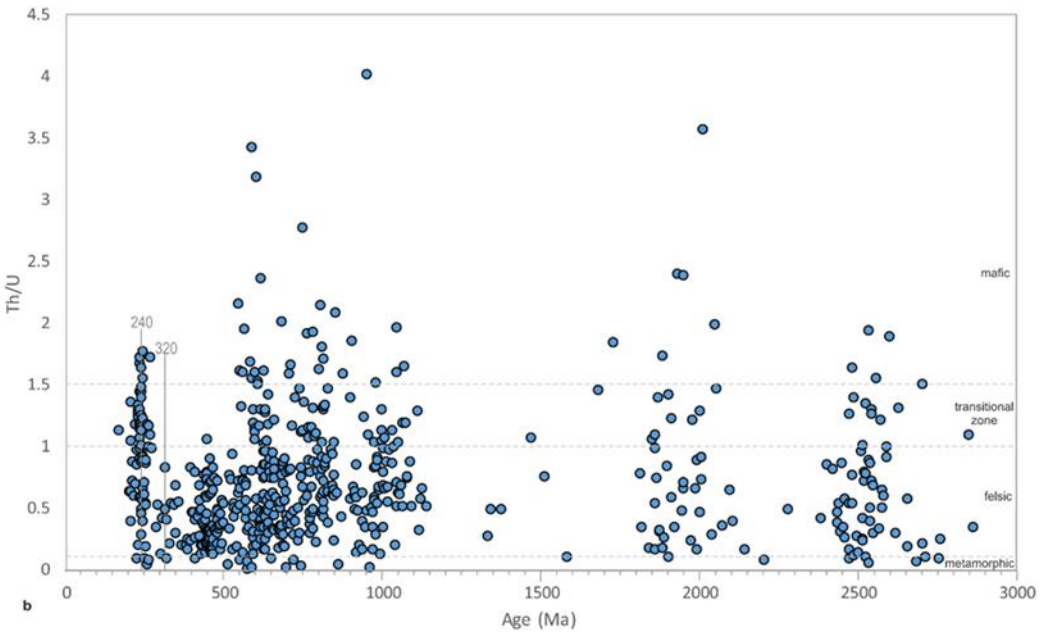

(**b**)

Figure 9. Zircon Th/U vs. age diagram from (**a**) the Upper Schist Fm. and (**b**) the Lower Schist Fm. of Iraklia island.

5. Discussion

5.1. Review of the Lithostratigraphy of Iraklia

The CBU rocks on Iraklia Island have been previously considered a Triassic sequence consisting of schist–marble alternations and an overlying marble (Avdis and Triantaphyllis 1994; Berhmann and Seckel 2007). However, our new DZ U-Pb data allow us to determine the MDAs and investigate the sedimentary provenance and, consequently, the tectonic affinity of the different rock units on Iraklia. Following the described method in Dickinson and Gehrels (2009), the youngest age modes (3+ grains) that overlap within 2-sigma error, excluding metamorphic rims, were used to calculate MDA in order to establish a new chronostratigraphic and refined lithostratigraphic framework for the Iraklia CBU section. On the basis of these data, the schists from the central and southwestern part of the island can be differentiated based on their MDAs, provenance, and lithology, as well as their structural position with respect to the intermediate Marble Fm.

The heterogeneous Lower Schist Fm. consists of various lithologies, including quartz-mica schists with lenses of paragneiss rocks and quartz-rich schist. The quartz-mica schist yielded late Triassic MDAs (Carnian-Rhaetian) ranging from 238.2 ± 1.5 to 204.8 ± 2.9 Ma. The paragneisses also gave late Triassic MDAs (Norian-Rhaetian) with ages of 226.7 ± 3.6 and 205.4 ± 2.6 Ma, while the quartz-rich schist yielded a Neoproterozoic (Ediacaran) MDA at about 559.4 ± 2.8 Ma. The contact with the overlying Marble Fm. is a ductile to brittle-ductile shear zone. Not surprisingly, given the highly strained marbles, no fossils have been reported from the carbonate rocks, implying that the obtained Carnian-Rhaetian MDAs for the underlying Lower Schist Fm. should be considered the upper age limit for the depositional age. The major age mode in the Lower Schist Fm. points to strong Triassic syn-rift, bimodal volcanic rocks and is indicative of a Triassic age for the Lower Schist Fm.

The Upper Schist Fm. mainly includes quartz-mica schists and surprisingly yielded late Cretaceous MDAs of 83.5 ± 1.12 and 83.4 ± 1.2 Ma (Campanian). The late Cretaceous MDAs and the early Eocene (Ypresian) U-Pb metamorphic rims bracket the true deposition age of the metasediments composing the Upper Schist Fm. as

latest Cretaceous to Paleocene. These schists are isoclinally folded with the underlying Marble Fm. Despite evidence for gradational stratigraphic contact, observed in a few places, an isoclinally folded early, prograde tectonic contact cannot be excluded. Interestingly, the metabauxite occurrences within the Marble Fm. in north-western Iraklia reflect a short emersion period and characterize shallow-water platform facies. Similar metabauxite lenses have also been observed on north-eastern Naxos (Jansen 1977) and Amorgos island (Minoux 1980; Dürr 1985). The occurrences of Amorgos were correlated with the Cretaceous bauxites of continental Greece (Laskou and Ekonomou 1990). Given the latest Cretaceous to Paleocene age of the overlying Upper Schist Fm., it seems plausible to posit a Cretaceous age for these metabauxites and the enveloping Marble Fm.

5.2. Structures and Metamorphism

Structural analysis on Iraklia island shows successive deformation events related mainly to syn-convergent prograde and back-arc extensional exhumation processes. Macro- and microstructures associated with the prograde path and the peak HP metamorphism are almost entirely obliterated.

This earlier HP event is only preserved as relic blueschist facies minerals, such as blue amphiboles and probably garnet in rocks of the Upper Schist Fm. and the paragneissic rocks, respectively. Additionally, strong evidence for the HP metamorphism is supported by thin, low Th/U zircon rims with U-Pb ages of ~48–56 Ma from both the Lower and Upper Schist Fm. These early Eocene metamorphic ages are in broad agreement with ages from HP/LT rocks in several Cycladic islands clustering between 55–40 Ma (Tomaschek et al., 2003; Ring and Layer, 2003; Forster and Lister, 2005; Putlitz et al., 2005; Lagos et al., 2007; Huet et al., 2014; Lister and Forster, 2016; Laurent et al., 2017; Cisneros et al., 2021). Isotopic dating on Ios and SE Naxos islands also revealed Eocene HP-LT metamorphism at ~55–40 Ma (van der Maar and Jansen 1983; Baldwin 1996; Poulaki et al., 2019) and 40 Ma, respectively (Avigad 1998; Ring et al., 2003), suggesting a prolonged or multi-stage HP-LT event in the Cyclades. Importantly, however, the Eocene zircon rims attest that the Iraklia

rocks are part of the same CBU HP-LT metamorphic assemblage documented on the CBU rocks regionally.

The main D2 deformation event produced N-S isoclinal folding with a penetrative S2 axial planar foliation and accompanied by the mineral/stretching lineation (L2). Based on the mineral assemblage, this metamorphic overprint of the Iraklia CBU rocks probably did not exceed the greenschist facies P-T conditions. In contrast, Naxos island was affected by high-grade post-HP-LT Barrovian-type metamorphism (Jansen and Schuiling, 1976; Buick and Holland, 1989; Duchene et al., 2006; Martin et al., 2006, 2008; Keiter et al., 2011; Grasemann et al., 2018).

Shear deformation was localized along the tectonic contact between the Lower Schist Fm. and the overlying Marble Fm. Ubiquitous shear bands along this contact display consistent top-to-the-north kinematics and advocate for internal deformation within lower-plate CBU rocks on Iraklia island. Given the kinematic similarities with extensional fabrics on Naxos, this intra-CBU contact likely represents a shear zone associated with exhumation and extensional crustal attenuation. This shear zone appears to account for the ductile lower-plate thinning of the CBU column in Iraklia. Similar ductile-brittle shear zones have been described within CBU from several Cycladic islands, all related to extensional shearing (Huet et al., 2009; Augier et al., 2014; Laurent et al., 2016).

5.3. Provenance of Detrital Zircons

The rocks of the CBU on Iraklia can be subdivided into Triassic and late Cretaceous lithostratigraphic packages on the basis of their MDA constraints. The DZ age spectra of the Lower and Upper Schist Fm. with their distinct ages thus record the sedimentary provenance evolution of two fundamentally different geodynamic environments. Hence, the DZ provenance evolution and changes have the potential to shed light on tectonic and palinspastic configuration during both late Triassic rift margin evolution associated with opening of the Neotethys and late Cretaceous–Paleocene convergence and subduction of the Neotethys.

In Lower Schist Fm., the DZ age spectra include a prominent signal of Early Paleozoic ages, a significant contribution of Neoproterozoic (Pan-African) ages, and a minor Late Paleozoic input. The combination of Neoproterozoic and Lower Paleozoic DZ input likely reflects eroded material from peri-Gondwanan terranes and points to uplift and erosion of the pre-Variscan crystalline basement, which served regionally as a source terrane. It should be noted that the abundant Neoproterozoic input might represent first-cycle basement derivation. However, it could just as likely be derived from the recycling of early Paleozoic Gondwanan strata in light of several cycles of the Gondwanan basement erosion, deposition, and recycling. Prominent early Paleozoic–Neoproterozoic ages have also ascertained from pre-Variscan CB rocks in the southern Cyclades (Keay and Lister 2002; Flansburg et al., 2019; Poulaki et al., 2019) and therefore likely represent a local source, especially during Permian-Triassic rifting. This is also supported by early exhumation of basement rocks described from both the southern Cyclades (e.g., Ios, Flansburg et al., 2019) and the Pelagonian domain (Vavassis et al., 2000). This is also reinforced by the results obtained from the quartz-rich schist layer within the Lower Schist Fm. However, the nearly unimodal Pan-African (Ediacaran) DZ age spectrum of the quartz-rich schist suggests either erosion of juvenile felsic crust from the East African orogeny or recycling of Late Neoproterozoic quartzites (Avigad et al., 2012; Meinhold et al., 2013). The high amount of Tonian DZ ages with a pronounced peak at 850 Ma points to the Minoan terranes, characteristic of the basement rocks exposed on the External Hellenides (Zulauf et al., 2015, 2018; Dörr et al., 2015; Xypolias et al., 2006, Kydonakis et al., 2014). On Ios island, Neoproterozoic metasedimentary sequences yielded similar MDAs and dominant Pan-African provenance and represent slivers of the pre-Carboniferous metasedimentary rocks of the CB intruded by voluminous Carboniferous granitoids (Flansburg et al., 2019). The minor late Paleozoic DZ input of the Lower Schist Fm. likely reflects eroded upper-crustal plutonic or volcano-sedimentary material associated with the active Eurasian convergent margin linked to Paleotethys closure. Late Carboniferous–early Permian magmatism characterizes the basement rocks in the Cyclades (Reischmann, 1998; Ring et al., 1999; Tomaschek et al., 2001; Xypolias et al., 2006; Lagos et al., 2007; Meinhold et al., 2013; Poulaki et al., 2019; Flansburg et al., 2019), the external Hellenides and Pelagonian domain

(Vavassis et al., 2000; Reischmann et al., 2001; Xypolias et al., 2006; Anders et al., 2007; Zulauf et al., 2015) .

Major Triassic DZ age input, associated with the Triassic magmatic activity, is significant in the paragneissic rocks and the quartz-mica schist of the Lower Schist Fm. The prominent Ladinian–Carnian peaks in the paragneisses reflect the long-lived bimodal syn-rift magmatic activity during Neotethyan opening. This is directly supported by the new Th/U data for the ~240 Ma Triassic detrital zircons, suggesting they originated from rocks with felsic and intermediate composition and a small number of mafic-derived zircons, attesting to bimodal syn-rift magmatism and opening of the Neotethyan oceanic basin (e.g., Pindos basin, southern Neotethys, Robertson, 2006; Robertson et al., 1991, 1996; Stampfli and Borel 2002; Zulauf et al., 2015, 2018). It is also striking that the DZ data from the Lower Schist Fm. exhibit remarkable similarities in terms of MDAs and provenance with the described Permian to Triassic CBU metasedimentary on Ios and Sikinos islands (Poulaki et al., 2019), implying a close spatial and genetic relationship.

The Upper Schist Fm. on Iraklia is characterized by late Cretaceous MDAs and exhibits DZ age spectra that show diminished Neoproterozoic, still significant early Paleozoic, and dominant late Paleozoic and Mesozoic DZ U-Pb age components. The abundant late Paleozoic–Mesozoic age modes probably reflect the input of recycled crystalline basement and metasedimentary rocks from the Pelagonian domain and/or more internal Hellenide domains as source rocks. Interestingly, the Th/U data for most Cretaceous detrital zircons point to a metamorphic origin with a limited contribution of zircons from felsic protoliths. These schists show similarities in provenance with the other late Cretaceous CBU schists from the Western Cyclades (Seman et al., 2017), northern Ios and Sikinos (Poulaki et al., 2019), and/or to the latest Cretaceous passive-margin sequence of Naxos island (Buick, 1991; Cao et al., 2017; Ring et al., 2018). This pronounced provenance shift suggests that the late Cretaceous Upper Schist Fm. of the CBU, as well as other similar late Cretaceous CBU rocks, received sediments from the upper-plate of the convergent margin and likely represents trench fill deposited shortly before subduction.

5.4. Regional Implications

Our provenance- and MDA-based correlation between age-equivalent CBU rocks of Iraklia and neighboring islands provides new insights into the paleogeography before the Cenozoic subduction and the related tectonometamorphic evolution. These data also illuminate the pre-subduction history of the island from the middle–late Triassic to late Cretaceous (Fig. 10) and establish a new stratigraphic column subdivided into two major diachronous packages.

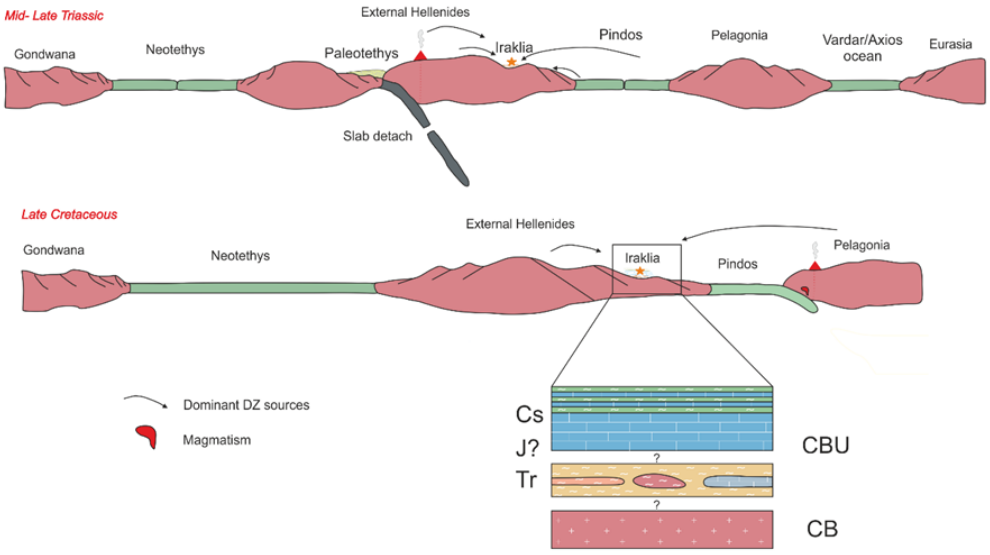

Figure 10. Schematic paleogeographic reconstruction of Iraklia island from middle–late Triassic to late Cretaceous time.

Our new data demonstrate that the lower portion CBU rocks in Iraklia were initially deposited in a locally sourced, isolated late Triassic syn-rift basin, receiving mainly recycled Gondwanan-affinity detrital zircons. This indicates that older, pre-Variscan basement rocks underwent uplift and erosion, supplying recycled sediment to the Lower Schist Fm. During this time, deposition was also accompanied by locally bimodal syn-rift volcanism, as evidenced by abundant Triassic zircons with felsic, intermediate, and mafic Th-U signatures. Overall Permian to Triassic magmatism was likely associated with both the final closure of southern Paleotethys that took place in Ladinian–early Carnian and early rifting and opening of Neotethyan basins (Aubouin et al., 1970; Fleury, 1980; Stampfli and Borel 2002; Reischmann 1998, Ring et al., 1999; Robertson, 2006; Robertson et al., 1991, 1996; Keay et al., 2001; Zulauf

et al., 2015, 2018; Poulaki et al., 2019; Flansburg et al., 2019). This late Triassic Lower Schist Fm. contains abundant Neoproterozoic Pan-African DZ ages, implying that sedimentation occurred in a proximal position to Ios island. This is also supported by the similarity of late Triassic metasedimentary rocks observed on both islands and the notion that these rocks are laterally equivalent lithological units, although sedimentation in northern Ios and Sikinos probably started in Permian times (Poulaki et al., 2019). However, no rocks structurally or stratigraphically lower than the Triassic Lower Schist Fm. are exposed in Iraklia. This lithostratigraphic correlation is also supported by the quartz-rich schist, characterized exclusively by unimodal Neoproterozoic DZ U-Pb ages that were probably sourced from pre-Variscan metasedimentary CB rocks on Ios. This also strengthens arguments for an early syn-rift unroofing and exhumation of crystalline basement rocks in a broader area. Sedimentation continued in a passive margin setting with deposition of shallow-water carbonates probably of (Jurassic?–)Cretaceous age, interrupted by short emersion episodes and bauxite deposits.

The Upper Schist Fm. on Iraklia, represents the final and fundamentally different episode of the depositional history of the CBU. It is marked by late Cretaceous quartz-mica schists that correlate well with CBU rocks in northern Ios (Poulaki et al., 2019) and Naxos (Buick 1991; Cao et al., 2017) islands, exhibiting a pronounced shift in DZ provenance dominated by Mesozoic and late Paleozoic and a dramatic reduction in Neoproterozoic age components. Sediments were likely derived from rocks exposed in the internal Hellenides, including the Pelagonian domain and Rhodope belt, and likely correspond to clastic sedimentation in the subduction trench with sediment sourced from the overriding plate and delivered to the convergent margin by fluvial systems from the hinterland.

Relic blue amphibole and ages of metamorphic zircon rims obtained from both CBU schist Fms., show that all the Iraklia rocks experienced Early Eocene HP subduction metamorphism, overprinted by a younger greenschist-facies metamorphism similar to Ios island (Baldwin and Lister, 1998; Forster and Lister, 2008; Thomson et al., 2009). However, they have not experienced the high-grade metamorphic conditions observed in the Naxos MCC associated with migmatitic dome formation (Jansen and

Schuiling, 1976; Buick and Holland 1989; Duchene et al., 2006 and references therein). Kinematic indicators demonstrate dominant top-to-the-N shearing during the main greenschist-facies deformation event. Top-to-the-S kinematics were also observed locally, but the lack of cross-cutting relationships does not allow a temporal differentiation between the different kinematics. However, it is also plausible that the opposing kinematics could be related to a general shear deformation pattern. Although no geochronological data could constrain the age of this intra-Cycladic Blueschists Unit shear zone of Iraklia, it presents kinematic similarities with the P-NDS. Similarly, the top-to-the-S kinematics is compatible with the South Cycladic Shear Zone (Vandenberg and Lister 1999; Thomson et al., 2009; Mizera and Behrmann 2016) and/or the Santorini Detachment System (Schneider et al., 2018) active concomitantly with the P-NDS. Although it is tempting to correlate the dominant top-to-the-N and subordinate top-to-the S-kinematics of Iraklia with the large-scale detachment faults, the latter juxtaposes either the Pelagonian-derived units against the CBU (P-NDS, SDS) or the CBU against the CB (SCSZ). Nonetheless, the intra-Cycladic Blueschists Unit shear zone of Iraklia has likely acted in a lower structural level, synchronous to the crustal-scale structures of the south Aegean domain, contributing to the attenuation of the CBU rocks probably in the footwall of P-NDS (Fig. 11).

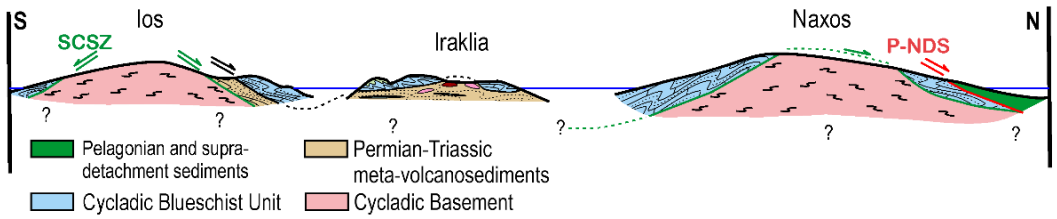

Figure 11. Simplified sketch illustrating the lithostratigraphic and structural correlations between Iraklia and the neighboring Ios and Naxos islands.

6. Conclusions

The island of Iraklia exposes a heterogeneous stratigraphic assemblage of CBU rocks. New DZ data show that this tectonostratigraphic column can be subdivided into distinct Lower and Upper Schist Fms., separated by a deformed marble horizon. The Lower Schist represents a middle to late Triassic meta-clastic sequence that likely

represents a locally sourced, syn-rift sequence that also received Triassic bimodal volcanic input. DZ U-Pb age spectra from the Lower Schist revealed a dominant Precambrian and a Lower Paleozoic signature supporting local sourcing and are similar to a pre-Variscan basement exposed on Ios.

The Lower Schist Fm. of the Iraklia CBU is structurally juxtaposed against an overlying Marble Fm. with bauxite lenses that exhibit abundant top-to-the-N ductile shear zone fabrics. Based on the regionally correlated occurrence of bauxite, the stratigraphic age of this formation is likely late Cretaceous—a notion supported by the MDAs from the overlying Upper Schist Fm. This age also suggests a significant intra-CBU depositional hiatus or structural omission—an omission would be compatible with the top-to-the-N shear zone that appears to have structurally attenuated the CBU in the footwall of the P-NDS.

The Upper Schist Fm. represents a late Cretaceous meta-clastic sequence with a distinctly different provenance signature, dominated by late Paleozoic and Mesozoic DZ U-Pb ages. This signals for a prominent sediment input from the internal Hellenides, including the Pelagonian domain, and appears to correspond to clastic sedimentation in the subduction trench with sediment sourced from the overriding plate prior to early Paleogene subduction, underplating, and metamorphism.

The zircon rim U-Pb ages from both CBU clastic formations on Iraklia revealed early Eocene HP-LT subduction metamorphism, similar to events documented in the neighboring islands of Ios, Sikinos, and Naxos, and is widespread throughout the Cyclades.

The Lower and Upper Schist Fms. of Iraklia bear significant similarities with Triassic and Cretaceous CBU schists, respectively, from the Ios and Sikinos islands, suggesting their close relationship during deposition and similar structural position during both Triassic rifting and during Cenozoic back-arc extension and detachment faulting in the attenuated footwall of the P-NDS.

Chapter V

Conclusions

Field-based observations, detailed structural analysis, detrital zircon U-Pb and zircon (U-Th)/He geochronological techniques were applied to the Amorgos metasedimentary sequences. Our results were compared to the neighboring Iraklia Island with the main focus on the differences in the paleogeography, subduction-related HP conditions, structural evolution, and exhumation processes. These combined data allow a better understanding of the Hellenic subduction zone orogen built-up from the Late Eocene- Oligocene collisional to Miocene post-orogenic extensional phase recorded in the Cycladic archipelago.

The Amorgos Unit presents a coherent Permo-Triassic to Mid-Eocene low-grade lithostratigraphy with lateral and vertical variations (Fig. 1), including shallow-water and pelagic carbonates bounded by siliciclastic sequences, which point to distinctly different provenance signatures. Based on the detrital zircon U-Pb provenance analysis, the basal metaconglomerate reveals a significant Precambrian and Variscan input, indicating its proximal position to the Pelagonian and Cycladic basement rocks. Interestingly, Iraklia island is composed of heterogeneous Mid- Late Triassic to Late Cretaceous CBU rocks, in which an isoclinally folded and locally ultramylonitic marble horizon separates the two distinct schist formations. DZ data from the lowermost schist show a dominant Precambrian and Lower Paleozoic signature similar to the pre-Variscan Cycladic basement, with the contribution of a Triassic bimodal volcanic input. Surprisingly, these schists contain minimal Carboniferous input compared to the basal metaconglomerate of the Amorgos Unit. However, the basal metaconglomerate entirely lacks Triassic input. Provenance differences reflect the different depositional environments, in which the Amorgos and Iraklia lowermost clastic sequences were formed, thus revealing their distinct paleogeographic position (Fig. 2). In this case, the Amorgos basal metaconglomerate is located in a proximal position to the southern Pelagonian margin that probably predated the syn-rift Triassic magmatism. Presumably, the ongoing subduction of the Paleotethys affected the basal metaconglomerate by supplying detritus during

the Permian. On the other hand, the Iraklia lowermost schists reflect the direct influence of the regional Triassic magmatic activity in response to the final closure of the Paleotethys and the early rifting/opening of the Pindos/CBU basin.

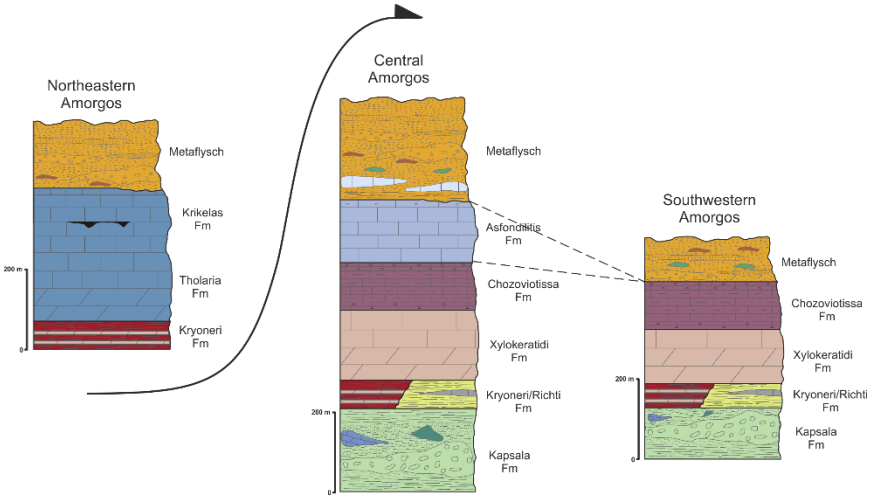

Figure 1. Differentiated lithostratigraphic columns based on the lateral variations on sedimentary facies and the overthrusted NE Amorgos onto central/SW Amorgos.

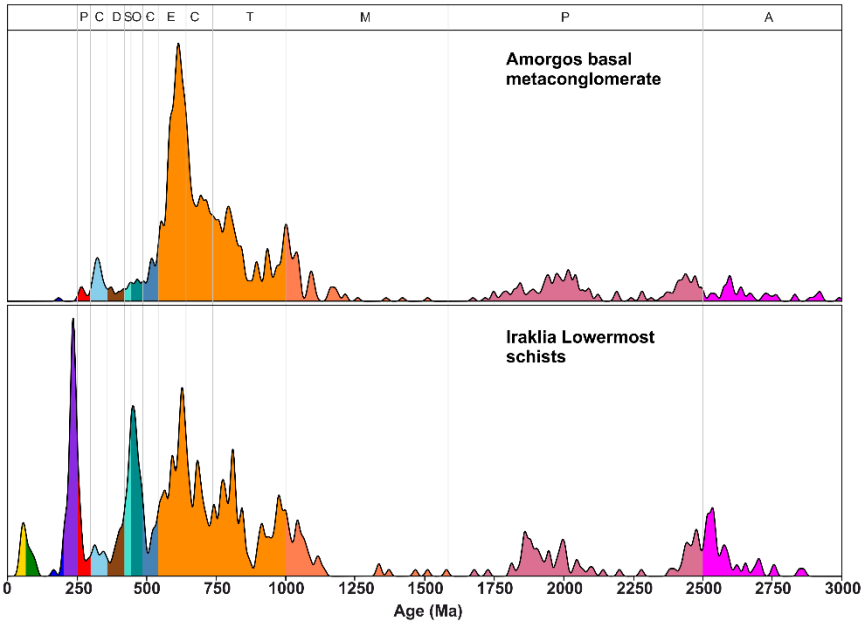

Figure 2. Multi-sample groups DZ KDEs from the lowermost clastic sequences between Amorgos and Iraklia islands.

Significant differences are also recorded in the DZ U-Pb ages from the Amorgos metaflysch and the Iraklia uppermost schists (Fig. 3). The Amorgos metaflysch shows a limited DZ Mesozoic age spectrum with the youngest age modes reaching the Jurassic, compared to the Iraklia uppermost schists that the Mesozoic age

components range from the Triassic to Late Cretaceous. These pronounced provenance differences correspond to depositional basins with distinct trench fill between the Amorgos and Iraklia top clastic sequences.

The presence of Fe-Mg carpholite is evidence of a subduction-related low-grade HP metamorphism for the Amorgos Unit. This HP event is incompatible with the P-T-t path recorded on the Iraklia metamorphic rocks. Based on the relic blue amphiboles and zircon U-Pb rims, the Iraklia metasedimentary rocks experienced prograde HP conditions at ~ 48-56 Ma. These Early Eocene ages suggest an attribution to the Upper-CBU HP nappe formed along the NE-directed subduction zone. On the contrary, no rims are obtained from the Amorgos Unit, but, since flysch sedimentation lasted up to Mid-Late Eocene, the HP metamorphism probably occurred in the latest Eocene.

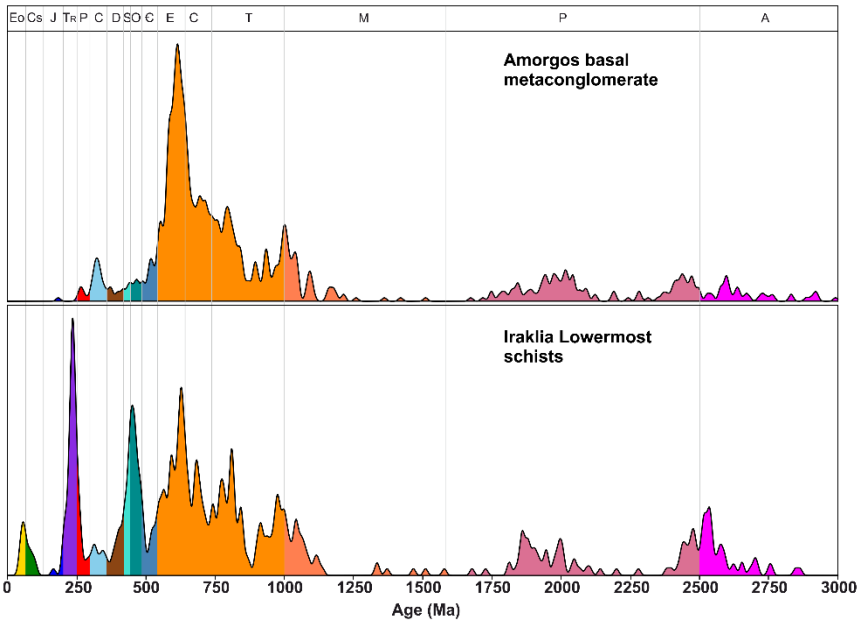

Figure 3. Multi-sample groups DZ KDEs from the uppermost clastic sequences between Amorgos and Iraklia islands.

The Amorgos HP event is consistent with top-NW retroward kinematics, indicating a short-lived SE-directed intracontinental subduction zone within the overriding plate, and further sustaining the distinctly different P-T path and position within the Hellenic orogen. This opposite subduction zone probably coexisted or evolved from the already formed retrobelt during the Late Eocene-Oligocene convergence and

collision system, causing a subsequent top-NW thrusting and duplication of the Amorgos stratigraphy. However, these top-NW kinematics, are affected by top-SE movements during a syn-orogenic compressional phase, reflecting the impact of the prolonged subduction and underplating of several nappes in the frontal wedge. The Iraklia metasedimentary rocks that are considered an integral part of the CBU, belonged to the frontal thrust sheets, while the underlying middle and bottom CBU HP nappes were accreted subsequently. This proves that the CBU- Pelagonian system was under a prolonged compressional phase throughout the Eocene-Oligocene. For a short period of time, the Hellenic orogen represented a composite double-verging compressive belt with two opposite dipping subduction zones.

The exhumation-related deformation of the Amorgos Unit is characterized by localized shear zones with a top-SE sense of shear. As evidenced by the zircon (U-Th)/He data, these must have formed during the Early –Mid Miocene, and they are temporally and kinematically linked to the Santorini Detachment System. On the contrary, the Iraklia CBU rocks exhibit top-N kinematics associated with a greenschist facies overprint, and are correlated with the Paros-Naxos Detachment System. In this case, the exhumation-related structures of Amorgos and Iraklia islands show that the extensional deformation was heterogeneously distributed in distinct structural levels.

Appendix A

Supplementary material for the Chapter II

Figure S1: MDA ages and MSWDs from the metaflysch calculated by the weighted mean of $^{206}Pb/^{238}U$ ages for concordance. IsoplotR was used for calculations (Vermeesch, 2018).

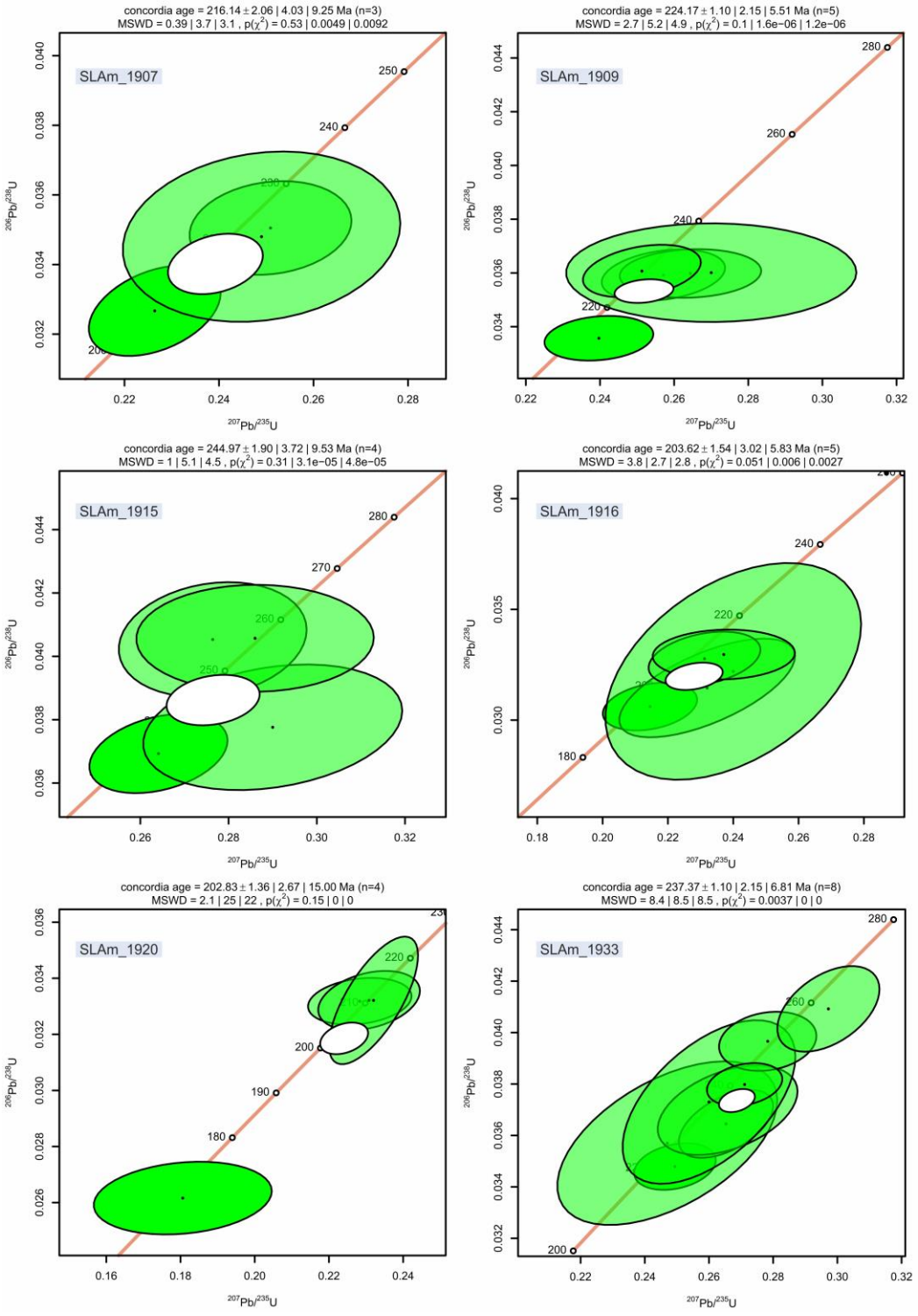

Figure S2: MDA ages and MSWDs from the Kapsala Fm. calculated by the weighted mean of $^{206}Pb/^{238}U$ ages for concordance. IsoplotR was used for calculations (Vermeesch, 2018).

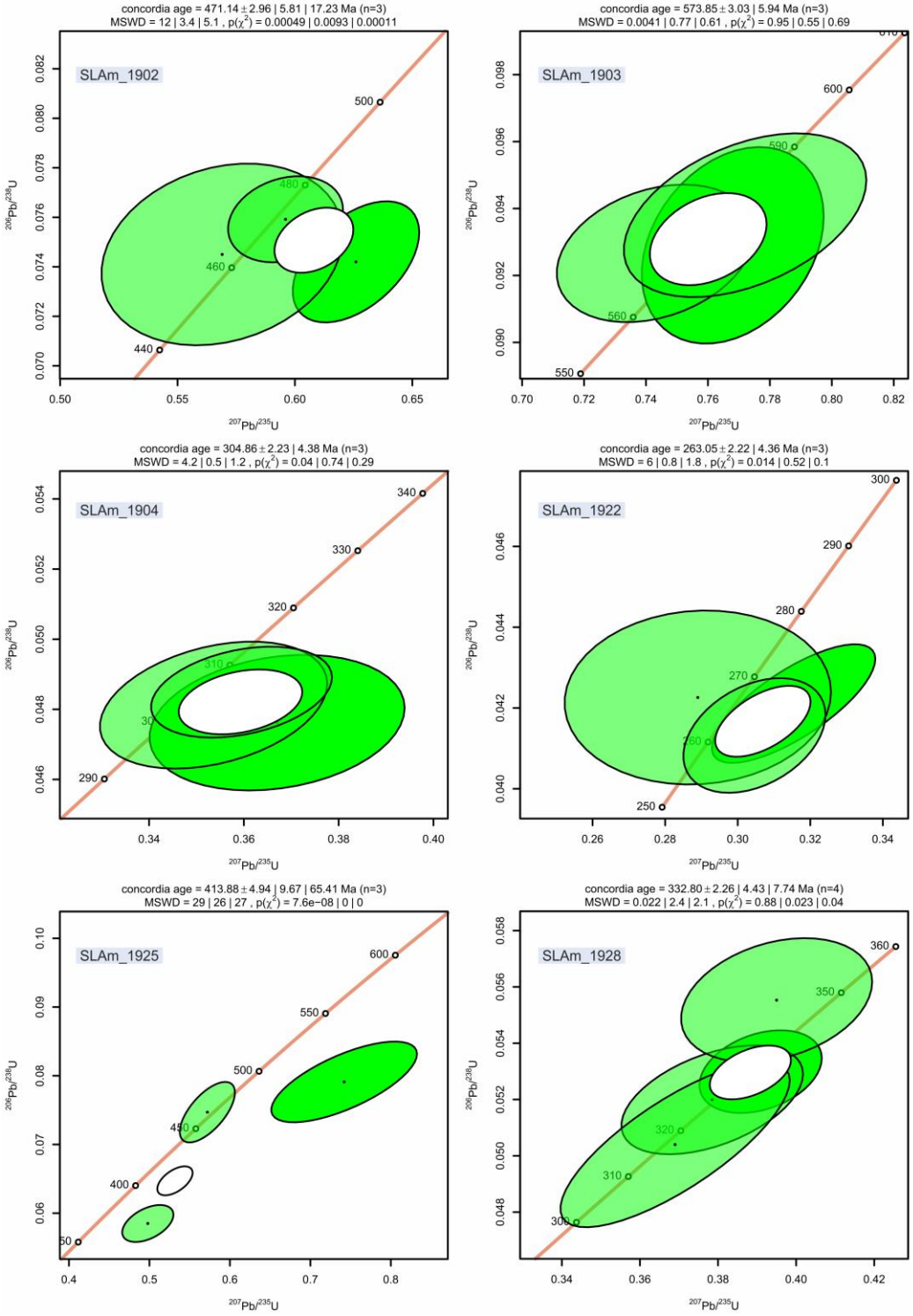

Table S1: U-Pb detrital zircon data from Amorgos Island, SE Cyclades, Greece

Sample Name:	SLAm1902							207/235		206/238		207/206		Best age			
Grain #	[U] ppm	U/Th	207/235	2σ error	206/238	2σ error	RHO	Age Ma	2σ error	Age (Ma)	2σ error	Age (Ma)	2σ error	(Ma)	2σ error	% Disc.	Rim/Core
SLAM1902_1.FIN2	395	3.24	1.254	0.028	0.1352	0.0027	0.617	823	12	817	15	839	36	817.0	15.0	0.7	
SLAM1902_2.FIN2	129.7	0.30	6.272	0.086	0.3625	0.0049	0.629	2013	12	1993	23	2024	22	2024.0	22.0	1.5	
SLAM1902_3.FIN2	57.9	1.21	1.333	0.044	0.1399	0.0026	0.331	860	20	844	15	895	71	844.0	15.0	1.9	
SLAM1902_4.FIN2	575	2.14	6.256	0.077	0.36	0.0049	0.547	2011	11	1981	23	2042	22	2042.0	22.0	3.0	
SLAM1902_5.FIN2	291	1.68	8.246	0.075	0.4061	0.0033	0.616	2257.5	8.3	2197	15	2314	13	2314.0	13.0	5.1	
SLAM1902_6.FIN2	233	1.83	0.569	0.021	0.0745	0.0015	0.212	457	13	462.9	9	405	84	462.9	9.0	1.3	
SLAM1902_7.FIN2	602	1.41	1.671	0.024	0.1717	0.0023	0.585	996.3	9.1	1021	13	948	25	948.0	25.0	7.7	
SLAM1902_8.FIN2	125.8	2.47	0.927	0.02	0.1077	0.0014	0.389	665	11	659.4	7.9	686	42	659.4	7.9	0.8	
SLAM1902_9.FIN2	319	3.35	1.535	0.023	0.1587	0.0021	0.547	943.2	9.1	950	11	929	28	929.0	28.0	2.3	
SLAM1902_10.FIN2	493	0.98	11	0.17	0.4976	0.0077	0.472	2522	15	2602	33	2453	27	2453.0	27.0	6.1	
SLAM1902_11.FIN2	96.3	0.41	0.876	0.028	0.1029	0.002	0.240	636	15	631	12	627	66	631.0	12.0	0.8	
SLAM1902_12.FIN2	1068	2.58	0.869	0.023	0.0957	0.0026	0.514	633	13	589	16	782	57	589.0	16.0	7.0	
SLAM1902_13.FIN2	231	1.62	1.143	0.021	0.1256	0.0018	0.446	772.5	9.8	763	10	778	39	763.0	10.0	1.2	
SLAM1902_14.FIN2	143.4	1.19	1.455	0.036	0.1516	0.0026	0.310	912	14	910	15	894	50	894.0	50.0	1.8	
SLAM1902_15.FIN2	321	0.92	1.63	0.023	0.1659	0.0016	0.400	981.1	8.9	989.2	9	940	28	940.0	28.0	5.2	
SLAM1902_16.FIN2	436	2.68	1.228	0.03	0.1204	0.0025	0.689	811	14	732	14	1008	37	732.0	14.0	9.7	
SLAM1902_17.FIN2	222	0.95	0.807	0.019	0.0978	0.0012	0.360	599	11	601.6	6.9	558	49	601.6	6.9	0.4	
SLAM1902_18.FIN2	135.7	0.93	1.044	0.028	0.1175	0.0024	0.478	723	14	715	14	723	56	715.0	14.0	1.1	
SLAM1902_19.FIN2	1064	4.53	0.895	0.054	0.0929	0.0058	0.600	646	29	571	34	900	110	571.0	34.0	11.6	
SLAM1902_20.FIN2	97.5	1.49	1.647	0.04	0.165	0.0035	0.661	985	16	984	19	995	38	995.0	38.0	1.1	
SLAM1902_21.FIN2	88.9	0.36	1.327	0.031	0.1418	0.0019	0.312	856	14	854	11	847	50	847.0	11.0	0.2	
SLAM1902_22.FIN2	176.5	0.58	1.621	0.03	0.1619	0.002	0.397	977	12	967	11	974	38	974.0	38.0	0.7	
SLAM1902_23.FIN2	294	2.05	0.845	0.018	0.1	0.0014	0.309	620.6	9.8	614.4	8.2	630	46	614.4	8.2	1.0	
SLAM1902_25.FIN2	466.3	1.35	10.64	0.1	0.4914	0.0053	0.616	2491.9	9.3	2575	23	2421	16	2421.0	16.0	6.4	
SLAM1902_26.FIN2	149.9	0.69	1.05	0.034	0.1062	0.0025	0.646	726	17	650	14	955	50	650.0	14.0	10.5	
SLAM1902_27.FIN2	131.5	0.80	1.363	0.026	0.1449	0.0016	0.234	871	11	872.3	8.9	858	39	858.0	39.0	1.7	
SLAM1902_28.FIN2	576	1.22	0.966	0.017	0.1045	0.0017	0.584	685.2	8.7	641	10	818	31	641.0	10.0	6.5	
SLAM1902_29.FIN2	881	1.61	0.778	0.041	0.0766	0.0044	0.614	583	24	476	26	1010	91	476.0	26.0	18.4	Rim
SLAM1902_29.FIN2	544.2	0.52	6.686	0.08	0.3881	0.0053	0.721	2070	11	2113	24	2015	17	2015.0	17.0	4.9	Core
SLAM1902_30.FIN2	159.1	1.34	0.846	0.021	0.1006	0.0015	0.073	621	12	617.9	8.6	616	57	617.9	8.6	0.5	
SLAM1902_31.FIN2	357.3	0.84	1.68	0.021	0.1635	0.0013	0.468	1002.9	8.7	976	7.1	1040	25	1040.0	25.0	6.2	
SLAM1902_32.FIN2	419.1	1.35	0.745	0.011	0.09156	0.00087	0.280	564.7	6.1	564.7	5.1	545	33	564.7	5.1	0.0	
SLAM1902_34.FIN2	494.2	3.55	11.24	0.12	0.5072	0.005	0.678	2542	10	2644	21	2455	14	2455.0	14.0	7.7	
SLAM1902_35.FIN2	98.1	1.14	0.823	0.023	0.0964	0.0019	0.394	607	13	593	11	657	60	593.0	11.0	2.3	
SLAM1902_36.FIN2	203.1	1.34	1.394	0.033	0.1429	0.0023	0.510	884	14	861	13	943	41	943.0	41.0	8.7	
SLAM1902_37.FIN2	527	1.84	0.947	0.015	0.1062	0.0012	0.616	676.6	8.1	650.4	6.9	770	26	650.4	6.9	3.9	
SLAM1902_38.FIN2	435.6	3.02	0.83	0.012	0.0992	0.0014	0.362	613	6.8	609.6	8	635	34	609.6	8.0	0.6	
SLAM1902_39.FIN2	167.9	1.40	1.07	0.02	0.1201	0.0013	0.073	737.7	9.7	731.1	7.5	770	45	731.1	7.5	0.9	
SLAM1902_40.FIN2	546	0.77	0.902	0.013	0.1085	0.0014	0.508	652.1	7.1	664.8	8	622	29	664.8	8.0	1.9	
SLAM1902_41.FIN2	91.5	1.28	0.809	0.025	0.0978	0.0017	0.229	601	15	601.6	9.8	573	68	601.6	9.8	0.1	
SLAM1902_43.FIN2	469	1.43	0.823	0.01	0.0987	0.0011	0.342	609.1	5.8	606.9	6.2	614	28	606.9	6.2	0.4	
SLAM1902_44.FIN2	1170	7.50	0.958	0.017	0.1082	0.0018	0.577	681.7	8.9	662	10	738	33	662.0	10.0	2.9	
SLAM1902_45.FIN2	71.9	1.30	1.405	0.036	0.1465	0.0018	0.415	888	15	881	10	901	43	901.0	43.0	2.2	
SLAM1902_46.FIN2	735	1.34	7.83	0.14	0.4392	0.007	0.802	2209	17	2345	31	2084	19	2084.0	19.0	12.5	
SLAM1902_47.FIN2	215.3	0.98	1.208	0.019	0.1329	0.0018	0.406	803.2	8.9	804	10	796	35	804.0	10.0	0.1	
SLAM1902_51.FIN2	136	1.78	14.95	0.33	0.508	0.011	0.819	2807	21	2646	45	2919	21	2919.0	21.0	9.4	
SLAM1902_52.FIN2	169.6	1.43	1.446	0.028	0.1508	0.0026	0.494	907	12	905	14	891	39	891.0	39.0	1.6	
SLAM1902_53.FIN2	250	2.80	1.029	0.019	0.1188	0.0013	0.390	716.8	9.6	723.7	7.4	673	40	723.7	7.4	1.0	
SLAM1902_54.FIN2	386	1.18	0.875	0.019	0.0999	0.0019	0.457	637	10	613	11	694	43	613.0	11.0	3.8	
SLAM1902_55.FIN2	159	0.52	0.896	0.02	0.105	0.0011	0.285	648	11	643.4	6.3	639	45	643.4	6.3	0.7	
SLAM1902_56.FIN2	413	0.63	0.866	0.016	0.1031	0.0013	0.157	632.5	8.9	632.3	7.8	620	46	632.3	7.8	0.0	
SLAM1902_57.FIN2	638	29.40	1.113	0.051	0.1207	0.0027	0.796	758	25	734	16	815	65	734.0	16.0	3.2	Rim
SLAM1902_57.FIN2	155.3	1.82	5.76	0.14	0.3524	0.0063	0.835	1942	20	1944	30	1933	24	1933.0	24.0	0.6	Core
SLAM1902_58.FIN2	235.7	1.51	0.751	0.015	0.0915	0.0014	0.387	569	8.8	564.4	8.4	585	44	564.4	8.4	0.8	
SLAM1902_59.FIN2	103.5	0.89	1.481	0.04	0.1529	0.0026	0.406	922	17	917	14	938	51	938.0	51.0	2.2	
SLAM1902_60.FIN2	505	2.70	1.573	0.021	0.155	0.0019	0.621	958.7	8.2	929	11	1036	23	1036.0	23.0	10.3	
SLAM1902_61.FIN2	54.9	4.98	1.068	0.033	0.1213	0.0019	0.166	736	16	738	11	730	69	738.0	11.0	0.3	

Table S1: U-Pb detrital zircon data from Amorgos Island, SE Cyclades, Greece.

SLAM1902_62.FIN2	78.6	0.70	1.042	0.037	0.119	0.0019	0.246	722	18	725	11	701	77	725.0	11.0	0.4	
SLAM1902_63.FIN2	219	1.60	0.928	0.015	0.1105	0.0011	0.221	665.8	7.9	675.4	6.6	620	39	675.4	6.6	1.4	
SLAM1902_64.FIN2	538	1.30	0.876	0.013	0.1032	0.0013	0.370	638	6.9	632.9	7.5	635	34	632.9	7.5	0.8	
SLAM1902_65.FIN2	425	0.60	0.906	0.014	0.1042	0.0013	0.238	654	7.4	638.9	7.8	695	35	638.9	7.8	2.3	
SLAM1902_66.FIN2	94.4	1.34	0.955	0.03	0.113	0.0021	0.232	678	15	690	12	596	65	690.0	12.0	1.8	
SLAM1902_67.FIN2	561	2.20	0.956	0.021	0.1098	0.0024	0.636	679	11	671	14	686	39	671.0	14.0	1.2	
SLAM1902_68.FIN2	236.4	0.78	0.96	0.019	0.1102	0.0018	0.412	682.4	9.9	674	10	692	43	674.0	10.0	1.2	
SLAM1902_70.FIN2	176.2	1.47	7.63	0.11	0.3993	0.0067	0.541	2188	14	2164	31	2191	27	2191.0	27.0	1.2	
SLAM1902_71.FIN2	575	0.78	0.626	0.011	0.0742	0.001	0.485	492.9	7.1	461.1	6.3	619	37	461.1	6.3	6.5	
SLAM1902_73.FIN2	283	4.16	1.158	0.019	0.1288	0.0016	0.430	780.8	9.2	781	9.2	754	36	781.0	9.2	0.0	
SLAM1902_74.FIN2	457	1.99	1.213	0.015	0.1331	0.0014	0.532	806.4	6.9	805.6	7.8	798	23	805.6	7.8	0.1	
SLAM1902_76.FIN2	107	0.74	4.63	0.11	0.3053	0.006	0.693	1751	20	1716	29	1788	31	1788.0	31.0	4.0	
SLAM1902_79.FIN2	513	7.60	1.034	0.02	0.1125	0.002	0.541	720	10	687	11	814	37	687.0	11.0	4.6	
SLAM1902_80.FIN2	307	1.12	11.04	0.13	0.487	0.0061	0.591	2526	11	2556	27	2490	19	2490.0	19.0	2.7	
SLAM1902_81.FIN2	485	3.39	0.897	0.012	0.1045	0.0012	0.338	650.5	6.7	640.8	6.8	673	31	640.8	6.8	1.5	
SLAM1902_83.FIN2	628	9.34	0.786	0.028	0.0885	0.0029	0.063	588	16	546	17	741	98	546.0	17.0	7.1	Rim
SLAM1902_83.FIN2	526	18.30	4.015	0.066	0.2605	0.004	0.516	1636	14	1492	20	1824	28	1824.0	28.0	18.2	Core
SLAM1902_84.FIN2	222	0.53	1.182	0.022	0.1296	0.0015	0.348	791	10	785.3	8.7	807	38	785.3	8.7	0.7	
SLAM1902_85.FIN2	279	2.10	0.894	0.023	0.106	0.0019	0.420	647	12	649	11	648	51	649.0	11.0	0.3	
SLAM1902_86.FIN2	347	0.78	1.236	0.023	0.1374	0.0021	0.451	815	10	830	12	787	41	830.0	12.0	1.8	
SLAM1902_87.FIN2	336	0.50	0.821	0.02	0.0982	0.0022	0.458	608	11	603	13	644	52	603.0	13.0	0.8	
SLAM1902_88.FIN2	409	1.04	0.87	0.014	0.1009	0.001	0.277	634.7	7.5	619.9	6.1	707	31	619.9	6.1	2.3	
SLAM1902_89.FIN2	505	2.11	1.074	0.018	0.1217	0.0018	0.572	739.8	8.8	740	10	743	30	740.0	10.0	0.0	
SLAM1902_90.FIN2	602	0.92	1.551	0.026	0.1522	0.003	0.603	952	11	913	17	1042	35	1042.0	35.0	12.4	
SLAM1902_91.FIN2	117	1.07	1.249	0.039	0.1349	0.0035	0.336	820	18	815	20	818	70	815.0	20.0	0.6	
SLAM1902_92.FIN2	154.1	1.61	1.209	0.024	0.1319	0.0016	0.369	803	11	798.3	8.8	788	40	798.3	8.8	0.6	
SLAM1902_93.FIN2	547	0.64	0.864	0.017	0.094	0.0017	0.348	631.7	9.2	579	10	797	47	579.0	10.0	8.3	
SLAM1902_94.FIN2	112.1	0.49	10.788	0.097	0.4741	0.0038	0.455	2504	8.3	2501	17	2480	15	2480.0	15.0	0.8	
SLAM1902_96.FIN2	128.9	1.28	0.884	0.017	0.10517	0.00099	0.261	641.8	9.1	644.5	5.7	609	43	644.5	5.7	0.4	
SLAM1902_97.FIN2	398.5	26.90	0.864	0.015	0.1011	0.0012	0.300	631.5	8.3	621	7.3	647	37	621.0	7.3	1.7	
SLAM1902_98.FIN2	408.9	0.72	0.924	0.011	0.1075	0.00099	0.294	664	5.7	658.1	5.7	671	27	658.1	5.7	0.9	
SLAM1902_99.FIN2	264.7	1.55	0.829	0.017	0.099	0.0012	0.429	612.1	9.4	608.4	7.2	618	39	608.4	7.2	0.6	
SLAM1902_100.FIN2	190	3.01	1.136	0.039	0.1274	0.0034	0.471	769	19	773	19	746	68	773.0	19.0	0.5	
SLAM1902_102.FIN2	244	2.34	0.968	0.02	0.1104	0.0014	0.397	687	11	675	7.9	719	41	675.0	7.9	1.7	
SLAM1902_104.FIN2	317	1.96	0.803	0.014	0.0945	0.0012	0.402	597.4	8	581.9	7.2	643	39	581.9	7.2	2.6	
SLAM1902_105.FIN2	438	0.69	1.344	0.019	0.144	0.0012	0.488	864.2	8.1	867	6.8	848	25	848.0	6.8	0.3	
SLAM1902_106.FIN2	326.3	2.86	0.839	0.017	0.1004	0.001	0.449	617.5	9.4	616.4	6.1	615	37	616.4	6.1	0.2	
SLAM1902_107.FIN2	601	0.94	5.252	0.056	0.3182	0.0032	0.648	1861.4	8.8	1780	15	1945	15	1945.0	15.0	8.5	
SLAM1902_108.FIN2	421	3.74	1.24	0.017	0.1307	0.0018	0.567	818.3	7.8	792	10	856	27	792.0	10.0	3.2	
SLAM1902_109.FIN2	532	0.99	0.853	0.014	0.0991	0.0014	0.105	625.5	7.7	609.1	8.2	676	32	609.1	8.2	2.6	
SLAM1902_110.FIN2	591	2.11	0.801	0.018	0.0791	0.0015	0.453	596	9.9	490.5	9.1	1028	42	490.5	9.1	17.7	
SLAM1902_111.FIN2	198	0.48	0.845	0.017	0.1022	0.0013	0.234	620.8	9.3	627.4	7.4	604	47	627.4	7.4	1.1	
SLAM1902_112.FIN2	276.3	0.71	1.115	0.02	0.1245	0.0016	0.514	761	9.8	756	9	783	35	756.0	9.0	0.7	
SLAM1902_114.FIN2	271	1.32	0.811	0.018	0.0972	0.0013	0.235	602	10	597.7	7.4	628	50	597.7	7.4	0.7	
SLAM1902_115.FIN2	902	1.74	0.828	0.016	0.0928	0.0016	0.695	613.7	8.4	571.9	9.7	777	30	571.9	9.7	6.8	
SLAM1902_116.FIN2	645	7.60	1.015	0.021	0.1182	0.0024	0.775	710	11	720	14	694	31	720.0	14.0	1.4	
SLAM1902_117.FIN2	68	-0.35	1.03	0.05	0.1172	0.003	0.393	709	26	714	18	679	95	714.0	18.0	0.7	
SLAM1902_119.FIN2	112.7	1.90	0.868	0.025	0.1007	0.0018	0.390	633	13	618	11	692	59	618.0	11.0	2.4	
SLAM1902_120.FIN2	949	2.36	1.021	0.011	0.1129	0.0013	0.531	714	5.5	689.6	7.3	800	24	689.6	7.3	3.4	
SLAM1902_121.FIN2	292.2	1.19	0.596	0.01	0.07592	0.00071	0.224	474.8	6.8	471.7	4.3	496	40	471.7	4.3	0.7	
SLAM1902_122.FIN2	1662	11.60	0.989	0.038	0.1081	0.0049	0.709	697	20	661	28	835	65	661.0	28.0	5.2	
SLAM1902_123.FIN2	192	2.54	1.763	0.03	0.177	0.0019	0.487	1030	11	1051	10	1003	30	1003.0	30.0	4.8	
SLAM1902_124.FIN2	145	1.04	0.874	0.022	0.1028	0.0014	0.023	636	12	630.8	8.1	648	61	630.8	8.1	0.8	
SLAM1902_125.FIN2	87.2	0.70	0.839	0.02	0.0996	0.0011	0.223	617	11	612	6.4	618	53	612.0	6.4	0.8	
SLAM1902_126.FIN2	752	2.18	0.907	0.013	0.1034	0.0011	0.603	655.2	6.8	634.3	6.7	721	24	634.3	6.7	3.2	
SLAM1902_127.FIN2	147	0.95	1.082	0.045	0.1063	0.0029	0.393	743	22	651	17	1014	87	651.0	17.0	12.4	
SLAM1902_128.FIN2	306	0.87	1.013	0.02	0.1168	0.0016	0.415	708.8	9.9	711.8	9.3	674	39	711.8	9.3	0.4	
SLAM1902_129.FIN2	312	0.82	1.279	0.021	0.1384	0.0016	0.476	835.1	9.1	835.5	8.8	819	29	835.5	8.8	0.0	
SLAM1902_130.FIN2	192.2	3.11	0.874	0.016	0.10063	0.00096	0.124	636.6	9	618	5.7	685	42	618.0	5.7	2.9	
SLAM1902_131.FIN2	907	3.35	11.36	0.19	0.507	0.017	0.341	2552	16	2638	76	2470	55	2470.0	55.0	6.8	

Sample Name: Grain #	SLAm1903 [U] ppm	U/Th	207/235	2σ error	206/238	2σ error	RHO	207/235 Age Ma	2σ error	206/238 Age (Ma)	2σ error	207/206 Age (Ma)	2σ error	Best age (Ma)	2σ error	% Disc.	Rim/Core
SLAM1903_1.FIN2	179	2.29	0.878	0.014	0.09922	0.00084	0.335	639.2	7.8	609.8	4.9	734	33	609.8	4.9	4.6	
SLAM1903_2.FIN2	124.6	18.60	0.913	0.022	0.108	0.0016	0.402	657	12	661	9.3	634	49	661.0	9.3	0.6	
SLAM1903_3.FIN2	407	2.22	1.635	0.041	0.1683	0.0042	0.856	982	16	1001	23	934	33	934.0	33.0	7.2	
SLAM1903_4.FIN2	172	0.79	0.982	0.031	0.105	0.0024	0.440	692	16	643	14	831	55	643.0	14.0	7.1	
SLAM1903_5.FIN2	86.3	0.96	1.157	0.021	0.1274	0.0015	0.341	778	10	772.5	8.4	791	37	772.5	8.4	0.7	
SLAM1903_6.FIN2	51.2	1.34	1.567	0.061	0.1539	0.0046	0.495	951	24	921	26	1008	73	1008.0	73.0	8.6	
SLAM1903_7.FIN2	682	3.15	1.164	0.032	0.1224	0.0035	0.692	780	15	743	20	884	46	743.0	20.0	4.7	
SLAM1903_8.FIN2	359.6	1.54	0.819	0.017	0.0981	0.0017	0.492	606.4	9.2	603	9.8	626	39	603.0	9.8	0.6	
SLAM1903_9.FIN2	253.3	0.70	1.497	0.019	0.154	0.0015	0.449	928	7.8	923.4	8.5	938	25	938.0	25.0	1.6	
SLAM1903_10.FIN2	243.8	0.77	0.786	0.012	0.09571	0.00092	0.345	588	7	589.1	5.4	583	35	589.1	5.4	0.2	
SLAM1903_11.FIN2	147.8	2.29	7.625	0.08	0.404	0.0036	0.589	2186.6	9.4	2187	16	2186	17	2186.0	17.0	0.0	
SLAM1903_12.FIN2	274	2.56	0.839	0.023	0.0975	0.0022	0.505	616	12	599	13	666	53	599.0	13.0	2.8	
SLAM1903_13.FIN2	226	1.86	1.231	0.022	0.1343	0.0015	0.537	814	9.8	812.5	8.5	808	33	812.5	8.5	0.2	
SLAM1903_14.FIN2	238	1.43	0.82	0.013	0.1006	0.001	0.432	607.3	7.2	618.1	5.9	562	36	618.1	5.9	1.8	
SLAM1903_16.FIN2	520	2.78	0.901	0.018	0.1022	0.0023	0.609	651.6	9.6	627	13	740	40	627.0	13.0	3.8	
SLAM1903_17.FIN2	614	2.31	1.15	0.02	0.12	0.0018	0.525	776.8	9.5	731	10	920	35	731.0	10.0	5.9	
SLAM1903_18.FIN2	159.5	0.71	0.772	0.016	0.0938	0.001	0.426	579.3	9	578.7	6.1	573	40	578.7	6.1	0.1	
SLAM1903_19.FIN2	205	0.56	0.896	0.016	0.1062	0.0012	0.356	649	8.7	650.6	7.2	648	37	650.6	7.2	0.2	
SLAM1903_20.FIN2	518	3.18	5.94	0.11	0.3511	0.0053	0.641	1965	17	1939	25	1993	28	1993.0	28.0	2.7	Rim
SLAM1903_20.FIN2	71.1	1.90	9.55	0.22	0.4508	0.0069	0.589	2389	22	2398	31	2385	33	2385.0	33.0	0.5	Core
SLAM1903_21.FIN2	217	1.49	0.986	0.019	0.1129	0.0015	0.243	695.5	9.5	689.5	8.4	710	40	689.5	8.4	0.9	
SLAM1903_22.FIN2	102.7	2.34	1.071	0.034	0.1212	0.0027	0.483	737	17	737	16	731	59	737.0	16.0	0.0	Rim
SLAM1903_22.FIN2	47.73	0.85	1.353	0.049	0.1429	0.0028	0.243	865	21	861	16	884	74	884.0	74.0	2.6	Core
SLAM1903_23.FIN2	476	22.70	0.848	0.034	0.0976	0.0027	0.788	621	18	600	16	697	52	600.0	16.0	3.4	Rim
SLAM1903_23.FIN2	370	1.35	4.069	0.095	0.2534	0.0053	0.868	1646	19	1456	27	1904	20	1904.0	20.0	23.5	Core
SLAM1903_24.FIN2	88	2.41	1.471	0.04	0.1575	0.0028	0.558	916	17	942	16	848	49	848.0	16.0	2.8	
SLAM1903_25.FIN2	512	3.72	0.991	0.021	0.1148	0.0023	0.681	697	11	700	13	690	36	700.0	13.0	0.4	
SLAM1903_26.FIN2	315	1.22	1.203	0.02	0.12655	0.00095	0.355	800.4	9	768	5.4	890	33	768.0	5.4	4.0	
SLAM1903_27.FIN2	285	0.92	0.871	0.02	0.1029	0.0019	0.577	634	11	631	11	648	43	631.0	11.0	0.5	
SLAM1903_28.FIN2	88.4	2.34	0.864	0.022	0.1042	0.0014	0.263	630	12	638.9	8.3	586	57	638.9	8.3	1.4	
SLAM1903_29.FIN2	227.9	0.81	1.109	0.022	0.122	0.0016	0.502	756	10	742.1	9.2	793	37	742.1	9.2	1.8	
SLAM1903_30.FIN2	325	2.60	5.22	0.12	0.2988	0.0065	0.635	1851	19	1683	32	2044	35	2044.0	35.0	17.7	
SLAM1903_31.FIN2	392	1.93	5.415	0.072	0.3531	0.0046	0.756	1886	11	1948	22	1820	17	1820.0	17.0	7.0	
SLAM1903_32.FIN2	507	1.10	0.825	0.023	0.0981	0.0021	0.607	610	12	603	12	645	50	603.0	12.0	1.1	
SLAM1903_33.FIN2	239	1.36	1.693	0.034	0.1671	0.0026	0.683	1007	12	996	14	1046	33	1046.0	33.0	4.8	
SLAM1903_34.FIN2	413	1.43	0.812	0.011	0.0966	0.001	0.334	602.7	6.1	594.1	6	635	29	594.1	6.0	1.4	
SLAM1903_35.FIN2	323.1	0.38	0.849	0.015	0.098	0.001	0.268	623.4	8.3	602.4	6.1	699	38	602.4	6.1	3.4	
SLAM1903_36.FIN2	301.7	2.38	0.768	0.012	0.0929	0.0012	0.294	577.5	6.9	572.4	7	600	36	572.4	7.0	0.9	
SLAM1903_37.FIN2	275.4	1.42	0.828	0.015	0.0978	0.0012	0.378	611.4	8	601.6	6.9	647	37	601.6	6.9	1.6	
SLAM1903_38.FIN2	388	1.42	0.869	0.011	0.1014	0.0011	0.442	634.6	6	622.6	6.2	677	27	622.6	6.2	1.9	
SLAM1903_39.FIN2	221	2.37	1.416	0.039	0.1503	0.0035	0.660	891	16	902	20	871	47	871.0	47.0	3.6	
SLAM1903_40.FIN2	291	2.27	0.888	0.013	0.105	0.0011	0.171	644.9	7.2	643.8	6.4	646	32	643.8	6.4	0.2	
SLAM1903_41.FIN2	295	1.03	0.917	0.014	0.1042	0.001	0.379	659.9	7.4	639	5.9	730	30	639.0	5.9	3.2	
SLAM1903_42.FIN2	373	1.16	0.867	0.027	0.1018	0.0024	0.517	633	15	625	14	660	57	625.0	14.0	1.3	
SLAM1903_43.FIN2	362.2	0.89	0.819	0.011	0.09943	0.00095	0.349	607.2	5.9	611	5.6	591	28	611.0	5.6	0.6	
SLAM1903_44.FIN2	164.2	0.87	1.634	0.026	0.1617	0.0017	0.509	982	10	965.8	9.4	1009	31	1009.0	31.0	4.3	
SLAM1903_45.FIN2	550	3.35	0.936	0.017	0.1122	0.0019	0.574	671.7	9	686	11	624	34	686.0	11.0	2.1	
SLAM1903_46.FIN2	184.2	1.60	1.25	0.022	0.1329	0.0015	0.317	822.1	9.8	804.2	8.4	868	36	804.2	8.4	2.2	
SLAM1903_47.FIN2	182.3	1.14	0.849	0.018	0.101	0.0018	0.455	622	10	620	10	638	45	620.0	10.0	0.3	
SLAM1903_48.FIN2	136	2.02	0.849	0.023	0.1013	0.0023	0.393	621	13	622	13	614	59	622.0	13.0	0.2	
SLAM1903_49.FIN2	100.4	1.37	0.82	0.023	0.096	0.0015	0.219	606	13	590.9	9	665	66	590.9	9.0	2.5	
SLAM1903_50.FIN2	269.6	6.80	5.915	0.067	0.3516	0.0034	0.570	1962.4	9.9	1942	16	1986	17	1986.0	17.0	2.2	Rim
SLAM1903_50.FIN2	101.2	3.35	11.34	0.24	0.4635	0.0066	0.435	2549	20	2454	29	2628	33	2628.0	33.0	6.6	Core
SLAM1903_51.FIN2	74.7	2.06	12.86	0.27	0.514	0.011	0.616	2672	18	2672	49	2669	31	2669.0	31.0	0.1	
SLAM1903_52.FIN2	240	0.98	1.627	0.031	0.1595	0.0023	0.560	979	12	954	13	1039	31	1039.0	31.0	8.2	
SLAM1903_53.FIN2	375	5.38	1.4	0.044	0.1456	0.0045	0.590	888	19	875	25	930	59	930.0	59.0	5.9	
SLAM1903_54.FIN2	459	2.29	0.841	0.019	0.0986	0.002	0.570	617	11	606	12	661	44	606.0	12.0	1.8	
SLAM1903_55.FIN2	74.8	1.37	15.49	0.2	0.5606	0.0059	0.783	2843	13	2867	25	2830	18	2830.0	18.0	1.3	
SLAM1903_56.FIN2	107.3	1.43	1.18	0.026	0.1312	0.0017	0.219	791	13	794.7	9.7	781	50	794.7	9.7	0.5	
SLAM1903_57.FIN2	169.2	1.04	5.543	0.082	0.3363	0.0045	0.687	1906	13	1868	21	1953	20	1953.0	20.0	4.4	
SLAM1903_58.FIN2	49.7	1.66	1.1	0.054	0.1178	0.0029	0.359	747	26	718	17	836	93	718.0	17.0	3.9	
SLAM1903_59.FIN2	114.7	0.64	1.701	0.023	0.1682	0.0017	0.270	1008.6	8.5	1002.2	9.5	1031	29	1031.0	29.0	2.8	
SLAM1903_60.FIN2	144	1.52	1.702	0.033	0.1711	0.002	0.475	1009	13	1018	11	995	35	995.0	35.0	2.3	
SLAM1903_61.FIN2	165.1	1.54	0.862	0.018	0.0997	0.0012	0.372	631	10	612.8	6.8	693	44	612.8	6.8	2.9	
SLAM1903_62.FIN2	258.2	0.42	1.194	0.026	0.1309	0.0021	0.662	795	12	793	12	812	33	793.0	12.0	0.3	
SLAM1903_63.FIN2	199	1.10	1.119	0.022	0.1272	0.0014	0.270	761	11	771.8	8.2	740	40	771.8	8.2	1.4	

SLAM1903_64.FIN2	93.3	0.76	13.58	0.16	0.5144	0.0053	0.591	2719	11	2674	23	2760	16	2760.0	16.0	3.1	
SLAM1903_65.FIN2	375	2.23	0.865	0.016	0.1058	0.0011	0.383	632	8.6	648.3	6.6	584	38	648.3	6.6	2.6	
SLAM1903_66.FIN2	109	1.20	1.196	0.025	0.13	0.0018	0.310	796	12	787	10	825	47	787.0	10.0	1.1	
SLAM1903_67.FIN2	269.3	3.17	0.743	0.013	0.09266	0.00084	0.288	563.1	7.4	571.2	5	529	38	571.2	5.0	1.4	
SLAM1903_68.FIN2	208.9	2.18	0.849	0.017	0.09884	0.0009	0.156	622.7	9.3	607.5	5.3	673	45	607.5	5.3	2.4	
SLAM1903_69.FIN2	100.3	1.90	12.87	0.23	0.5161	0.0085	0.856	2669	18	2680	37	2665	16	2665.0	16.0	0.6	
SLAM1903_70.FIN2	125	0.78	0.838	0.021	0.1005	0.001	0.134	617	11	617.5	5.9	606	55	617.5	5.9	0.1	
SLAM1903_71.FIN2	179.9	9.76	13.93	0.14	0.5374	0.0052	0.768	2743	10	2771	22	2731	13	2731.0	13.0	1.5	
SLAM1903_72.FIN2	252	0.63	0.768	0.015	0.0944	0.0011	0.179	577.6	8.6	581.7	6.7	563	46	581.7	6.7	0.7	
SLAM1903_73.FIN2	213	1.47	0.968	0.017	0.1147	0.0013	0.457	686	8.8	700.1	7.2	640	35	700.1	7.2	2.1	
SLAM1903_74.FIN2	211	2.84	1.461	0.024	0.1534	0.0018	0.564	913	10	919.9	9.8	900	29	900.0	29.0	2.2	
SLAM1903_75.FIN2	153	1.55	5.907	0.095	0.3541	0.0051	0.689	1959	14	1953	24	1973	24	1973.0	24.0	1.0	
SLAM1903_76.FIN2	309	4.53	1.04	0.018	0.1197	0.0014	0.585	722.2	9	728.6	7.9	707	29	728.6	7.9	0.9	
SLAM1903_77.FIN2	262	1.37	0.918	0.018	0.10879	0.00094	0.338	659.8	9.5	665.7	5.4	633	40	665.7	5.4	0.9	
SLAM1903_78.FIN2	594	5.46	0.81	0.013	0.0983	0.0011	0.646	602.8	7.1	604.1	6.4	607	29	604.1	6.4	0.2	
SLAM1903_79.FIN2	214	1.05	1.075	0.024	0.1191	0.0013	0.197	739	12	725.2	7.6	770	48	725.2	7.6	1.9	
SLAM1903_80.FIN2	275.9	1.67	1.002	0.017	0.1158	0.0011	0.277	703.6	8.4	706.5	6.5	688	36	706.5	6.5	0.4	
SLAM1903_81.FIN2	146.8	1.12	0.854	0.019	0.1018	0.0013	0.360	625	10	625.6	7.6	617	46	625.6	7.6	0.1	
SLAM1903_82.FIN2	534	1.90	0.914	0.022	0.1039	0.0019	0.551	658	12	637	11	717	40	637.0	11.0	3.2	
SLAM1903_83.FIN2	246	1.52	0.883	0.015	0.10354	0.00094	0.308	641.1	8.3	635	5.5	652	37	635.0	5.5	1.0	
SLAM1903_84.FIN2	166.7	2.86	6.508	0.074	0.3746	0.0033	0.613	2045	10	2051	16	2041	16	2041.0	16.0	0.5	
SLAM1903_85.FIN2	612	5.02	6.36	0.13	0.3686	0.007	0.827	2025	19	2022	33	2025	21	2025.0	21.0	0.1	Rim
SLAM1903_85.FIN2	113	0.90	10.6	0.12	0.4761	0.0061	0.496	2488	11	2510	26	2469	21	2469.0	21.0	1.7	Core
SLAM1903_86.FIN2	253.1	9.20	0.995	0.015	0.1148	0.00089	0.148	700.4	7.6	700.5	5.1	687	34	700.5	5.1	0.0	
SLAM1903_87.FIN2	142	0.83	0.826	0.016	0.1002	0.0011	0.172	610.2	8.9	615.5	6.3	574	45	615.5	6.3	0.9	
SLAM1903_88.FIN2	76.5	1.58	0.853	0.025	0.1004	0.0013	0.195	623	14	616.8	7.4	616	65	616.8	7.4	1.0	
SLAM1903_89.FIN2	252	1.84	1.762	0.048	0.1716	0.0028	0.651	1031	17	1021	16	1050	40	1050.0	40.0	2.8	
SLAM1903_90.FIN2	382	6.70	0.942	0.015	0.1111	0.0013	0.411	672.5	7.9	678.8	7.3	646	32	678.8	7.3	0.9	
SLAM1903_91.FIN2	1408	23.10	0.911	0.04	0.1036	0.0035	0.741	657	21	635	20	715	60	635.0	20.0	3.3	Rim
SLAM1903_91.FIN2	85.8	0.85	1.894	0.055	0.1883	0.0028	0.312	1078	20	1112	15	993	57	993.0	57.0	12.0	Core
SLAM1903_92.FIN2	153.1	2.19	5.97	0.19	0.3264	0.0077	0.861	1968	28	1820	37	2121	29	2121.0	29.0	14.2	
SLAM1903_93.FIN2	218.7	5.53	10	0.28	0.459	0.011	0.725	2428	27	2428	48	2423	31	2423.0	31.0	0.2	
SLAM1903_94.FIN2	471	1.23	0.925	0.02	0.1045	0.002	0.413	663	11	641	12	729	50	641.0	12.0	3.3	
SLAM1903_95.FIN2	116.3	0.58	1.705	0.04	0.168	0.0027	0.418	1008	15	1001	15	1006	46	1006.0	46.0	0.5	
SLAM1903_96.FIN2	358	1.49	0.899	0.015	0.1068	0.0013	0.540	650	8.2	653.8	7.9	620	32	653.8	7.9	0.6	
SLAM1903_97.FIN2	16.8	2.25	6.59	0.18	0.376	0.0081	0.501	2058	24	2054	38	2054	44	2054.0	44.0	0.0	
SLAM1903_98.FIN2	333.2	1.76	0.819	0.014	0.0992	0.0011	0.322	606.9	7.8	609.6	6.4	583	38	609.6	6.4	0.4	
SLAM1903_100.FIN2	190	2.67	1.504	0.038	0.1493	0.0039	0.660	928	15	896	22	1007	42	1007.0	42.0	11.0	
SLAM1903_101.FIN2	31.9	0.89	9.8	0.2	0.4475	0.0069	0.520	2411	19	2387	29	2422	31	2422.0	31.0	1.4	
SLAM1903_102.FIN2	322.3	9.31	16.3	0.35	0.53	0.011	0.764	2897	19	2740	48	2991	23	2991.0	23.0	8.4	
SLAM1903_103.FIN2	433	3.53	6.95	0.14	0.3857	0.0071	0.602	2099	18	2100	33	2094	29	2094.0	29.0	0.3	
SLAM1903_104.FIN2	65.8	2.78	16.22	0.34	0.549	0.011	0.671	2884	20	2822	46	2926	28	2926.0	28.0	3.6	
SLAM1903_105.FIN2	668	8.39	1.065	0.028	0.1193	0.0024	0.716	735	14	726	14	747	34	726.0	14.0	1.2	
SLAM1903_106.FIN2	144.2	1.24	6.289	0.091	0.3752	0.0047	0.641	2014	13	2053	22	1968	20	1968.0	20.0	4.3	
SLAM1903_107.FIN2	97.4	2.10	0.818	0.021	0.0993	0.0013	0.085	605	12	609.9	7.8	555	62	609.9	7.8	0.8	
SLAM1903_110.FIN2	171.9	1.18	0.835	0.023	0.0978	0.0018	0.418	614	13	601	11	636	58	601.0	11.0	2.1	
SLAM1903_111.FIN2	338	1.34	1.175	0.026	0.1282	0.0022	0.655	788	12	777	12	788	35	777.0	12.0	1.4	
SLAM1903_112.FIN2	26	2.51	0.888	0.05	0.1012	0.0025	0.011	635	27	621	15	640	120	621.0	15.0	2.2	
SLAM1903_113.FIN2	224	1.05	0.792	0.018	0.0956	0.0016	0.445	592	10	588.2	9.2	586	44	588.2	9.2	0.6	
SLAM1903_114.FIN2	125.3	2.61	0.879	0.023	0.1013	0.0013	0.302	639	12	621.6	7.6	677	54	621.6	7.6	2.7	
SLAM1903_115.FIN2	445	1.88	0.853	0.019	0.0998	0.0022	0.619	624	10	613	13	656	45	613.0	13.0	1.8	
SLAM1903_116.FIN2	417	5.89	1.491	0.019	0.1534	0.0015	0.415	925.9	7.7	920.1	8.4	931	27	931.0	27.0	1.2	
SLAM1903_117.FIN2	158.8	1.79	6.03	0.066	0.3637	0.0029	0.453	1978.6	9.6	1999	14	1951	19	1951.0	19.0	2.5	
SLAM1903_118.FIN2	1015	51.00	0.867	0.055	0.1001	0.0079	0.700	633	31	614	47	700	120	614.0	47.0	3.0	Rim
SLAM1903_118.FIN2	65.6	1.15	5.91	0.12	0.345	0.0061	0.616	1963	18	1908	29	2009	32	2009.0	32.0	5.0	Core
SLAM1903_119.FIN2	200	1.87	0.871	0.019	0.1029	0.0011	0.306	635	10	631.3	6.3	632	46	631.3	6.3	0.6	
SLAM1903_120.FIN2	20.1	1.09	6.25	0.28	0.357	0.011	0.559	2006	40	1964	50	2019	61	2019.0	61.0	2.7	Rim
SLAM1903_120.FIN2	48.66	0.86	15.11	0.27	0.5487	0.0099	0.365	2821	17	2819	41	2832	30	2832.0	30.0	0.5	Core
SLAM1903_121.FIN2	106.8	1.20	0.849	0.023	0.1019	0.0015	0.133	622	13	625.5	8.9	589	62	625.5	8.9	0.6	
SLAM1903_122.FIN2	210.4	1.93	0.859	0.029	0.0996	0.0019	0.152	629	16	612	11	680	75	612.0	11.0	2.7	
SLAM1903_123.FIN2	293.2	6.85	0.92	0.014	0.1075	0.0011	0.438	661.5	7.3	657.9	6.4	663	29	657.9	6.4	0.5	
SLAM1903_124.FIN2	79	1.02	0.906	0.026	0.105	0.0018	0.242	652	14	643	11	666	64	643.0	11.0	1.4	
SLAM1903_125.FIN2	170.8	1.41	4.461	0.077	0.2882	0.0042	0.678	1723	14	1632	21	1832	24	1832.0	24.0	10.9	
SLAM1903_126.FIN2	396	2.29	2.299	0.04	0.2086	0.0032	0.643	1212	12	1221	17	1190	29	1190.0	29.0	2.6	
SLAM1903_127.FIN2	40.27	1.30	1.121	0.036	0.1287	0.0018	0.259	760	18	780	10	676	69	780.0	10.0	2.6	
SLAM1903_128.FIN2	96.8	1.74	1.043	0.028	0.1168	0.0018	0.389	722	14	712	10	738	56	712.0	10.0	1.4	
SLAM1903_129.FIN2	314.9	1.64	0.907	0.019	0.1049	0.0019	0.473	655	9.6	643	11	701	43	643.0	11.0	1.8	
SLAM1903_130.FIN2	788	1.07	0.869	0.011	0.0973	0.0011	0.557	634.7	6	598.4	6.3	768	24	598.4	6.3	5.7	

Sample Name:	SLAm1904							207/235		206/238		207/206		Best age			
Grain #	[U] ppm	U/Th	207/235	2σ error	206/238	2σ error	RHO	Age Ma	2σ error	Age (Ma)	2σ error	Age (Ma)	2σ error	(Ma)	2σ error	% Disc.	Rim/Core
SLAM1904_1.FIN2	234.9	1.25	1.16	0.017	0.1292	0.0011	0.247	780.9	8.2	783.3	6.5	767	33	783.3	6.5	0.3	
SLAM1904_2.FIN2	186.1	1.29	12.51	0.16	0.5068	0.0062	0.756	2641	12	2641	26	2638	14	2638.0	14.0	0.1	
SLAM1904_3.FIN2	151.4	1.59	1.221	0.036	0.1322	0.0024	0.676	807	16	800	14	828	47	800.0	14.0	0.9	
SLAM1904_4.FIN2	503	1.55	0.3595	0.0078	0.04849	0.00053	0.325	312	6	305.2	3.2	363	48	305.2	3.2	2.2	
SLAM1904_5.FIN2	244.4	3.96	0.993	0.017	0.1172	0.0014	0.323	699.3	8.5	714.2	8.1	643	37	714.2	8.1	2.1	
SLAM1904_6.FIN2	197	4.32	6.31	0.13	0.37	0.0066	0.882	2016	18	2027	31	2009	18	2009.0	18.0	0.9	
SLAM1904_7.FIN2	635	3.48	0.3827	0.0093	0.05315	0.00062	0.388	328.5	6.8	333.8	3.8	284	49	333.8	3.8	1.6	
SLAM1904_8.FIN2	258.6	2.56	0.873	0.016	0.1047	0.0014	0.498	637.4	9.1	641.5	8.3	617	37	641.5	8.3	0.6	
SLAM1904_9.FIN2	280	3.94	0.927	0.018	0.1106	0.0016	0.381	664.6	9.4	675.9	9.4	620	42	675.9	9.4	1.7	
SLAM1904_10.FIN2	234	1.46	0.856	0.019	0.1026	0.0012	0.217	626	10	629.3	7.2	605	49	629.3	7.2	0.5	
SLAM1904_11.FIN2	59.7	2.44	0.386	0.025	0.0501	0.001	0.106	329	19	315.1	6.3	390	140	315.1	6.3	4.2	
SLAM1904_12.FIN2	661	1.38	0.594	0.012	0.072	0.0013	0.702	472.7	7.7	448	7.8	596	33	448.0	7.8	5.2	
SLAM1904_13.FIN2	261	3.05	0.546	0.032	0.0631	0.0024	0.538	440	21	394	15	670	110	394.0	15.0	10.5	Rim
SLAM1904_13.FIN2	75.4	0.74	1.516	0.049	0.1499	0.0028	0.388	934	20	900	15	997	64	997.0	64.0	9.7	Core
SLAM1904_14.FIN2	334.7	0.34	1.103	0.024	0.1207	0.0021	0.607	752	11	734	12	803	36	734.0	12.0	2.4	
SLAM1904_15.FIN2	458	1.95	3.56	0.1	0.2412	0.0079	0.731	1539	23	1392	41	1749	42	1749.0	42.0	20.4	Rim
SLAM1904_15.FIN2	304	1.20	5.19	0.13	0.3027	0.005	0.631	1849	21	1704	25	2014	34	2014.0	34.0	15.4	Core
SLAM1904_16.FIN2	219	3.85	5.261	0.057	0.3428	0.0033	0.568	1861.1	9.3	1899	16	1818	18	1818.0	18.0	4.5	
SLAM1904_17.FIN2	334	3.69	1.138	0.019	0.1259	0.0011	0.367	770	9	764.2	6.6	782	32	764.2	6.6	0.8	
SLAM1904_18.FIN2	529	6.90	0.459	0.036	0.0504	0.0018	0.411	381	25	320.1	9.4	750	150	320.1	9.4	16.0	Rim
SLAM1904_19.FIN2	287	1.31	0.832	0.026	0.0997	0.0028	0.577	616	16	612	16	621	65	612.0	16.0	0.6	
SLAM1904_21.FIN2	134.4	1.98	1.165	0.038	0.1288	0.0031	0.212	783	18	781	18	780	77	781.0	18.0	0.3	
SLAM1904_22.FIN2	149	10.60	1.397	0.036	0.1497	0.0025	0.598	884	15	899	14	841	40	841.0	14.0	1.7	
SLAM1904_23.FIN2	35.4	2.36	1.374	0.072	0.1432	0.0049	0.547	864	32	860	28	860	100	860.0	100.0	0.0	
SLAM1904_24.FIN2	79.2	19.50	1.68	0.12	0.1592	0.0092	0.682	994	46	951	51	1080	110	1080.0	110.0	11.9	Rim
SLAM1904_24.FIN2	74.9	0.62	5.82	0.13	0.3466	0.0049	0.389	1946	19	1918	23	1978	39	1978.0	39.0	3.0	Core
SLAM1904_25.FIN2	130.9	2.17	1.126	0.043	0.1231	0.0036	0.648	761	21	748	21	792	61	748.0	21.0	1.7	
SLAM1904_26.FIN2	275	1.35	0.367	0.011	0.04762	0.00079	0.217	316.4	8.5	299.8	4.9	414	67	299.8	4.9	5.2	
SLAM1904_28.FIN2	166	0.92	1.568	0.032	0.1582	0.0021	0.485	956	13	947	12	969	38	969.0	38.0	2.3	
SLAM1904_29.FIN2	212	3.48	0.728	0.021	0.0883	0.0018	0.299	555	13	545	10	584	63	545.0	10.0	1.8	
SLAM1904_30.FIN2	342	3.21	0.3706	0.0099	0.05159	0.00071	0.269	319.3	7.3	324.2	4.3	272	57	324.2	4.3	1.5	
SLAM1904_31.FIN2	142.1	1.54	1.758	0.036	0.1713	0.0023	0.403	1028	13	1019	13	1045	37	1045.0	37.0	2.5	
SLAM1904_32.FIN2	197.1	0.73	1.517	0.026	0.1538	0.002	0.329	936	11	922	11	961	37	961.0	37.0	4.1	
SLAM1904_33.FIN2	168	2.94	0.567	0.029	0.0696	0.0022	0.469	452	18	433	13	521	98	433.0	13.0	4.2	
SLAM1904_34.FIN2	707	4.69	1.691	0.061	0.1714	0.0059	0.815	996	23	1017	33	953	45	953.0	45.0	6.7	
SLAM1904_35.FIN2	234	2.12	1.225	0.047	0.1299	0.0034	0.683	807	21	787	19	838	57	787.0	19.0	2.5	
SLAM1904_36.FIN2	206	1.01	0.754	0.032	0.089	0.003	0.716	567	18	549	18	626	64	549.0	18.0	3.2	
SLAM1904_37.FIN2	354	5.97	0.3616	0.0075	0.05104	0.0006	0.376	312.9	5.6	320.9	3.7	248	44	320.9	3.7	2.6	
SLAM1904_38.FIN2	193.5	2.15	0.372	0.021	0.0499	0.0017	0.289	320	16	314	11	350	120	314.0	11.0	1.9	
SLAM1904_39.FIN2	281	1.97	0.3536	0.0098	0.04812	0.00074	0.337	306.5	7.3	302.9	4.5	316	57	302.9	4.5	1.2	
SLAM1904_40.FIN2	572	1.07	13.97	0.22	0.5633	0.009	0.428	2745	15	2878	37	2646	28	2646.0	28.0	8.8	
SLAM1904_41.FIN2	61.6	2.88	0.891	0.028	0.0992	0.0017	0.207	644	15	609	10	738	69	609.0	10.0	5.4	
SLAM1904_42.FIN2	363	1.13	0.82	0.032	0.0963	0.004	0.650	604	18	592	24	641	71	592.0	24.0	2.0	
SLAM1904_43.FIN2	314	2.79	0.3659	0.0085	0.04941	0.00068	0.179	316.7	6.5	310.9	4.2	339	54	310.9	4.2	1.8	
SLAM1904_44.FIN2	769	14.60	0.607	0.092	0.0635	0.0077	0.381	477	57	397	46	860	330	397.0	46.0	16.8	Rim
SLAM1904_44.FIN2	51.5	1.35	4.8	0.16	0.3036	0.0078	0.523	1777	27	1707	38	1848	55	1848.0	55.0	7.6	Core
SLAM1904_45.FIN2	133	1.51	0.741	0.03	0.0933	0.0028	0.632	559	17	575	16	481	69	575.0	16.0	2.9	
SLAM1904_46.FIN2	537	4.54	0.3882	0.0074	0.05304	0.00059	0.215	332.5	5.3	333.1	3.6	314	40	333.1	3.6	0.2	
SLAM1904_47.FIN2	101.1	1.22	1.277	0.054	0.1307	0.0044	0.720	825	24	790	25	883	60	790.0	25.0	4.2	
SLAM1904_48.FIN2	175.8	1.56	0.431	0.017	0.0574	0.0013	0.348	363	12	360.6	8.3	358	78	360.6	8.3	0.7	
SLAM1904_49.FIN2	338	1.69	0.573	0.015	0.0707	0.0012	0.223	458.7	9.5	440.5	7.1	531	55	440.5	7.1	4.0	
SLAM1904_50.FIN2	69.2	0.50	1.665	0.063	0.1679	0.005	0.773	985	25	998	28	979	49	979.0	49.0	1.9	
SLAM1904_51.FIN2	528	2.11	11.23	0.22	0.479	0.01	0.863	2539	18	2520	44	2547	19	2547.0	19.0	1.1	
SLAM1904_52.FIN2	443	28.50	0.565	0.02	0.0719	0.002	0.516	454	13	448	12	477	68	448.0	12.0	1.3	Rim
SLAM1904_52.FIN2	127.6	2.77	1.633	0.064	0.162	0.0038	0.489	979	25	967	21	1005	67	1005.0	67.0	3.8	Core
SLAM1904_53.FIN2	422	10.39	6.32	0.24	0.365	0.013	0.940	2006	35	1999	62	2025	23	2025.0	23.0	1.3	
SLAM1904_54.FIN2	206	1.32	0.733	0.026	0.0896	0.0028	0.748	554	15	552	16	564	48	552.0	16.0	0.4	
SLAM1904_55.FIN2	967	3.10	0.654	0.019	0.0786	0.002	0.819	510	12	488	12	601	36	488.0	12.0	4.3	
SLAM1904_56.FIN2	233.9	1.19	0.769	0.023	0.0876	0.0025	0.641	577	13	541	15	727	54	541.0	15.0	6.2	
SLAM1904_57.FIN2	118	1.37	1.175	0.038	0.1337	0.0034	0.628	783	18	810	20	714	54	810.0	20.0	3.4	
SLAM1904_58.FIN2	63.2	2.41	0.8	0.027	0.0939	0.0019	0.269	593	15	578	11	622	74	578.0	11.0	2.5	
SLAM1904_59.FIN2	459	0.87	10.26	0.2	0.4565	0.0092	0.957	2458	18	2427	39	2472	18	2472.0	18.0	1.8	
SLAM1904_60.FIN2	60.7	1.45	0.79	0.032	0.0897	0.0021	0.396	586	18	553	12	688	82	553.0	12.0	5.6	
SLAM1904_61.FIN2	478	2.53	0.881	0.025	0.0989	0.0021	0.571	641	13	608	12	751	51	608.0	12.0	5.1	
SLAM1904_63.FIN2	307	1.43	0.81	0.036	0.0971	0.0037	0.852	595	20	596	22	588	52	596.0	22.0	0.2	
SLAM1904_64.FIN2	153.2	1.60	0.569	0.021	0.0723	0.0024	0.481	454	14	450	14	462	78	450.0	14.0	0.9	
SLAM1904_65.FIN2	133.4	1.46	0.544	0.015	0.0672	0.0012	0.292	439.7	9.6	419.4	7.1	516	63	419.4	7.1	4.6	

SLAM1904_66.FIN2	174.8	0.87	5.339	0.086	0.3357	0.0046	0.573	1872	14	1864	22	1875	24	1875.0	24.0	0.6	
SLAM1904_67.FIN2	67.8	2.06	0.862	0.033	0.1029	0.0031	0.516	630	18	631	18	627	74	631.0	18.0	0.2	
SLAM1904_68.FIN2	314.6	1.53	1.017	0.02	0.118	0.0019	0.673	711.6	9.8	719	11	683	32	719.0	11.0	1.0	
SLAM1904_69.FIN2	387	1.09	0.751	0.017	0.0872	0.0017	0.494	567.2	9.7	539	10	677	46	539.0	10.0	5.0	
SLAM1904_70.FIN2	154.4	2.11	0.747	0.022	0.0896	0.0012	0.268	564	13	552.9	7.1	590	62	552.9	7.1	2.0	
SLAM1904_71.FIN2	319	3.35	0.944	0.028	0.1106	0.0026	0.691	671	15	676	15	663	45	676.0	15.0	0.7	
SLAM1904_72.FIN2	80.9	0.83	1.392	0.051	0.1423	0.0045	0.534	878	21	856	26	928	72	928.0	72.0	7.8	
SLAM1904_73.FIN2	401	5.70	0.795	0.035	0.0921	0.0035	0.732	588	20	567	21	673	69	567.0	21.0	3.6	
SLAM1904_74.FIN2	107.2	1.29	1.163	0.044	0.1229	0.0031	0.596	780	21	746	18	866	66	746.0	18.0	4.4	
SLAM1904_75.FIN2	190.3	1.88	0.86	0.025	0.1011	0.0024	0.547	627	14	621	14	650	56	621.0	14.0	1.0	
SLAM1904_76.FIN2	36.77	1.29	1.619	0.051	0.1601	0.0027	0.160	970	20	957	15	987	62	987.0	62.0	3.0	
SLAM1904_77.FIN2	419	3.07	0.927	0.052	0.1015	0.0039	0.729	666	29	623	23	800	85	623.0	23.0	6.5	Rim
SLAM1904_77.FIN2	244.1	1.42	3.79	0.14	0.2546	0.0078	0.806	1585	30	1460	40	1750	39	1750.0	39.0	16.6	Core
SLAM1904_78.FIN2	365	2.05	1.795	0.036	0.1714	0.003	0.486	1044	12	1019	17	1089	39	1089.0	39.0	6.4	
SLAM1904_79.FIN2	463	2.39	0.379	0.012	0.0531	0.0015	0.581	325	8.7	333.4	9.1	271	59	333.4	9.1	2.6	
SLAM1904_80.FIN2	217	17.80	1.163	0.072	0.1283	0.006	0.378	780	34	778	34	780	130	778.0	34.0	0.3	Rim
SLAM1904_80.FIN2	102.5	1.99	9.79	0.29	0.438	0.012	0.744	2407	28	2348	56	2469	35	2469.0	35.0	4.9	Core
SLAM1904_81.FIN2	46.8	2.54	1.146	0.058	0.1243	0.0035	0.310	767	28	755	20	770	110	755.0	20.0	1.6	
SLAM1904_82.FIN2	507	1.58	0.808	0.02	0.0964	0.0019	0.858	600	11	593	11	632	42	593.0	11.0	1.2	
SLAM1904_83.FIN2	1010	4.25	0.24	0.023	0.0289	0.003	0.650	218	19	183	19	550	190	183.0	19.0	16.1	Rim
SLAM1904_83.FIN2	209	2.29	0.536	0.019	0.0701	0.002	0.523	434	12	437	12	410	68	437.0	12.0	0.7	Core
SLAM1904_85.FIN2	219	2.15	0.928	0.025	0.1008	0.002	0.500	665	13	621	12	807	54	621.0	12.0	6.6	
SLAM1904_86.FIN2	91.8	1.05	0.765	0.026	0.0917	0.0013	0.261	575	15	565.5	8	604	74	565.5	8.0	1.7	
SLAM1904_87.FIN2	256	2.38	0.952	0.026	0.1112	0.0025	0.535	678	14	679	15	687	53	679.0	15.0	0.1	
SLAM1904_88.FIN2	296	1.31	1.111	0.021	0.1206	0.0018	0.539	757	10	734	10	835	33	734.0	10.0	3.0	
SLAM1904_89.FIN2	140	2.01	0.653	0.019	0.0844	0.0015	0.369	508	12	522.2	9.2	439	60	522.2	9.2	2.8	
SLAM1904_90.FIN2	1080	6.65	6.25	0.11	0.3675	0.0065	0.822	2010	15	2017	31	2010	19	2010.0	19.0	0.3	
SLAM1904_91.FIN2	108.5	0.71	1.022	0.027	0.1179	0.0016	0.327	712	13	719.2	9.4	694	54	719.2	9.4	1.0	
SLAM1904_92.FIN2	209.5	4.67	1.635	0.046	0.1734	0.0055	0.824	978	18	1028	30	891	38	891.0	38.0	15.4	
SLAM1904_93.FIN2	214	1.50	0.981	0.018	0.1143	0.0013	0.282	692.7	9.3	697.6	7.6	686	42	697.6	7.6	0.7	
SLAM1904_94.FIN2	288.4	1.48	0.859	0.016	0.1032	0.0011	0.335	628.3	8.6	633.2	6.6	614	37	633.2	6.6	0.8	
SLAM1904_95.FIN2	246.4	1.69	0.766	0.024	0.0995	0.003	0.778	574	14	610	18	441	45	610.0	18.0	6.3	
SLAM1904_96.FIN2	291	13.00	0.468	0.06	0.065	0.0096	0.849	387	42	405	58	320	180	405.0	58.0	4.7	Rim
SLAM1904_96.FIN2	45.6	1.11	1.272	0.05	0.1391	0.0045	0.441	830	23	838	25	807	81	838.0	25.0	1.0	Core
SLAM1904_97.FIN2	138.3	1.53	3.671	0.077	0.2452	0.0046	0.759	1561	17	1412	23	1773	26	1773.0	26.0	20.4	
SLAM1904_98.FIN2	746	6.96	0.359	0.028	0.0429	0.0029	0.787	311	21	271	18	620	110	271.0	18.0	12.9	Rim
SLAM1904_98.FIN2	256	4.01	1.683	0.029	0.1716	0.0024	0.445	1000	11	1021	13	962	34	962.0	34.0	6.1	Core
SLAM1904_99.FIN2	65.7	2.02	1.131	0.041	0.126	0.0028	0.387	766	20	764	16	762	74	764.0	16.0	0.3	
SLAM1904_100.FIN2	558	5.89	5.52	0.17	0.3245	0.0096	0.841	1903	28	1806	46	2004	31	2004.0	31.0	9.9	
SLAM1904_101.FIN2	142.8	2.33	0.717	0.025	0.0901	0.0019	0.511	547	15	556	11	507	65	556.0	11.0	1.6	
SLAM1904_102.FIN2	505	36.40	0.428	0.02	0.0557	0.0015	0.555	361	14	349.4	9.4	424	85	349.4	9.4	3.2	Rim
SLAM1904_102.FIN2	306	1.35	0.942	0.039	0.0979	0.0038	0.475	672	21	602	22	923	78	602.0	22.0	10.4	Core
SLAM1904_103.FIN2	420	1.57	0.996	0.035	0.1149	0.0039	0.743	698	18	699	23	692	57	699.0	23.0	0.1	
SLAM1904_104.FIN2	71.1	7.90	3.91	0.14	0.2576	0.0072	0.686	1608	28	1476	37	1797	45	1797.0	45.0	17.9	
SLAM1904_105.FIN2	283	2.10	0.839	0.022	0.1015	0.0019	0.505	617	12	623	11	604	46	623.0	11.0	1.0	
SLAM1904_106.FIN2	330.8	1.37	4.982	0.061	0.309	0.0034	0.695	1815	10	1735	17	1912	17	1912.0	17.0	9.3	
SLAM1904_107.FIN2	113.7	0.99	0.814	0.032	0.0968	0.0028	0.647	600	18	595	16	612	66	595.0	16.0	0.8	
SLAM1904_108.FIN2	403.3	13.16	0.881	0.024	0.104	0.0025	0.706	639	13	638	15	636	48	638.0	15.0	0.2	
SLAM1904_109.FIN2	319.1	1.51	0.924	0.02	0.1094	0.0018	0.633	663	11	669	11	645	37	669.0	11.0	0.9	
SLAM1904_110.FIN2	313	3.78	0.853	0.015	0.0997	0.0011	0.294	625.3	7.9	612.5	6.5	687	36	612.5	6.5	2.0	
SLAM1904_111.FIN2	121.7	2.11	0.821	0.03	0.0858	0.0022	0.451	605	17	530	13	897	75	530.0	13.0	12.4	
SLAM1904_112.FIN2	495	8.76	0.937	0.028	0.1126	0.0033	0.761	671	15	687	19	631	43	687.0	19.0	2.4	
SLAM1904_113.FIN2	71.8	2.82	1.133	0.047	0.1261	0.0048	0.542	764	22	765	27	769	79	765.0	27.0	0.1	
SLAM1904_114.FIN2	313	1.33	1.092	0.025	0.1214	0.0017	0.431	747	12	738.4	9.6	768	41	738.4	9.6	1.2	
SLAM1904_115.FIN2	681	1.59	0.3839	0.0091	0.05106	0.00062	0.311	329.4	6.7	321	3.8	384	51	321.0	3.8	2.6	
SLAM1904_116.FIN2	34.7	1.58	1.285	0.06	0.1312	0.0027	0.305	829	27	794	15	897	97	794.0	15.0	4.2	
SLAM1904_117.FIN2	277	0.86	1.28	0.037	0.1365	0.0032	0.729	835	17	824	18	862	42	824.0	18.0	1.3	
SLAM1904_118.FIN2	417	3.99	0.796	0.016	0.0938	0.0013	0.669	592.8	9.2	578.9	7.5	656	35	578.9	7.5	2.3	
SLAM1904_119.FIN2	246	1.12	6.18	0.1	0.3603	0.0057	0.785	1998	14	1982	27	2017	20	2017.0	20.0	1.7	
SLAM1904_120.FIN2	361	1.13	0.898	0.02	0.1083	0.0015	0.477	649	10	662.9	8.8	595	43	662.9	8.8	2.1	Rim
SLAM1904_121.FIN2	125.4	1.80	6.55	0.11	0.3699	0.0045	0.585	2051	15	2028	21	2072	25	2072.0	25.0	2.1	Core
SLAM1904_122.FIN2	284	1.86	0.377	0.012	0.0517	0.0013	0.487	323.1	8.7	325	8	324	63	325.0	8.0	0.6	
SLAM1904_123.FIN2	212	0.85	1.086	0.028	0.1212	0.0024	0.623	744	14	737	14	769	42	737.0	14.0	0.9	
SLAM1904_124.FIN2	429	2.15	0.37	0.011	0.04959	0.0008	0.322	319.2	7.8	312	4.9	364	60	312.0	4.9	2.3	
SLAM1904_125.FIN2	56.7	0.78	1.166	0.031	0.1334	0.0017	0.147	783	15	806.8	9.6	698	61	806.8	9.6	3.0	
SLAM1904_126.FIN2	433	1.96	0.896	0.014	0.10684	0.00099	0.466	648.5	7.4	654.3	5.8	628	29	654.3	5.8	0.9	
SLAM1904_127.FIN2	370	9.45	6.56	0.3	0.385	0.014	0.893	2022	44	2087	65	1973	41	1973.0	41.0	5.8	
SLAM1904_128.FIN2	168.2	3.25	0.817	0.021	0.096	0.0015	0.394	605	12	591	9.1	659	47	591.0	9.1	2.3	
SLAM1904_129.FIN2	190.5	1.52	1.26	0.031	0.1341	0.0023	0.341	826	14	811	13	852	50	811.0	13.0	1.8	
SLAM1904_130.FIN2	88.6	0.41	0.897	0.041	0.1027	0.002	0.098	647	22	630	12	670	100	630.0	12.0	2.6	

Sample Name:	SLAm1907							207/235		206/238		207/206		Best age			
Grain #	[U] ppm	U/Th	207/235	2σ error	206/238	2σ error	RHO	Age Ma	2σ error	Age (Ma)	2σ error	Age (Ma)	2σ error	(Ma)	2σ error	% Disc.	Rim/Core
SLAM1907_1.FIN2	447	1.05	0.4428	0.009	0.05838	0.00089	0.390	371.5	6.3	365.7	5.4	402	45	365.7	5.4	1.6	
SLAM1907_2.FIN2	67.9	2.14	0.399	0.02	0.0543	0.00097	0.028	338	15	340.8	5.9	290	110	340.8	5.9	0.8	
SLAM1907_3.FIN2	518	1.46	0.3921	0.008	0.0535	0.00063	0.428	335.2	5.8	335.9	3.8	324	41	335.9	3.8	0.2	
SLAM1907_5.FIN2	300	1.29	0.2509	0.007	0.03505	0.00055	0.154	226.7	5.7	222	3.4	283	63	222.0	3.4	2.1	
SLAM1907_6.FIN2	298	6.04	0.875	0.047	0.1026	0.0062	0.447	636	25	629	36	710	130	629.0	36.0	1.1	Rim
SLAM1907_6.FIN2	68.7	0.96	1.726	0.069	0.1634	0.0035	0.430	1014	25	975	20	1090	75	1090.0	75.0	10.6	Core
SLAM1907_7.FIN2	592	2.33	0.4178	0.0081	0.05139	0.00058	0.355	353.8	5.8	323	3.5	548	41	323.0	3.5	8.7	
SLAM1907_8.FIN2	157.8	2.00	0.293	0.01	0.03899	0.00091	0.247	259.9	8	246.5	5.6	389	79	246.5	5.6	5.2	
SLAM1907_9.FIN2	163.7	0.93	0.503	0.019	0.0629	0.002	0.399	411	13	393	12	513	81	393.0	12.0	4.4	
SLAM1907_11.FIN2	258	1.85	0.385	0.012	0.0512	0.0011	0.355	330.1	8.7	321.9	6.4	371	68	321.9	6.4	2.5	
SLAM1907_12.FIN2	719	13.18	0.3952	0.0095	0.052	0.001	0.462	337.3	6.9	326.8	6.1	399	50	326.8	6.1	3.1	
SLAM1907_13.FIN2	773	2.40	0.314	0.018	0.041	0.0021	0.698	278	15	259	13	463	94	259.0	13.0	6.8	
SLAM1907_14.FIN2	679	1.66	0.411	0.014	0.0559	0.0017	0.712	348	10	351	10	335	54	351.0	10.0	0.9	
SLAM1907_15.FIN2	389.2	1.94	0.541	0.016	0.0707	0.0019	0.603	437	11	440	11	423	55	440.0	11.0	0.7	
SLAM1907_16.FIN2	886	3.33	0.855	0.016	0.1023	0.0017	0.517	626.2	8.9	627.4	9.8	610	37	627.4	9.8	0.2	
SLAM1907_17.FIN2	312	10.72	0.466	0.022	0.0607	0.0021	0.354	386	15	379	13	400	83	379.0	13.0	1.8	
SLAM1907_18.FIN2	413	2.05	0.872	0.04	0.1003	0.0056	0.771	629	21	613	33	731	75	613.0	33.0	2.5	
SLAM1907_19.FIN2	738	1.49	0.4111	0.0075	0.05448	0.00084	0.300	349.1	5.4	341.9	5.1	394	44	341.9	5.1	2.1	
SLAM1907_21.FIN2	474	2.45	0.4815	0.0085	0.06375	0.00072	0.363	398.6	5.8	398.3	4.3	392	36	398.3	4.3	0.1	
SLAM1907_22.FIN2	1280	13.00	0.3783	0.0065	0.05179	0.00057	0.384	325.5	4.8	325.5	3.5	321	38	325.5	3.5	0.0	
SLAM1907_23.FIN2	1214	1.77	0.3066	0.0076	0.04352	0.00092	0.655	272.2	6.2	274.6	5.7	244	46	274.6	5.7	0.9	
SLAM1907_24.FIN2	361	1.80	0.386	0.013	0.0495	0.0012	0.400	330.1	9.3	311.6	7.4	445	66	311.6	7.4	5.6	
SLAM1907_25.FIN2	874	12.97	0.989	0.015	0.1159	0.0018	0.561	697.4	7.6	706	10	663	33	706.0	10.0	1.2	
SLAM1907_26.FIN2	254.5	12.00	0.787	0.021	0.0944	0.0022	0.457	588	12	581	13	605	57	581.0	13.0	1.2	
SLAM1907_27.FIN2	281.8	1.45	0.441	0.015	0.053	0.0011	0.426	370	10	332.7	6.8	582	64	332.7	6.8	10.1	
SLAM1907_29.FIN2	408	1.47	0.2264	0.0057	0.03267	0.00053	0.392	206.8	4.7	207.2	3.3	217	51	207.2	3.3	0.2	
SLAM1907_30.FIN2	643	25.00	0.548	0.035	0.0681	0.0029	0.746	442	23	425	18	520	88	425.0	18.0	3.8	
SLAM1907_31.FIN2	449.6	2.05	0.4026	0.0091	0.05341	0.00092	0.461	342.7	6.5	335.3	5.7	392	45	335.3	5.7	2.2	
SLAM1907_32.FIN2	216	1.91	0.412	0.014	0.05076	0.00059	0.235	348.4	9.7	319.2	3.6	539	68	319.2	3.6	8.4	
SLAM1907_33.FIN2	353	11.22	0.603	0.01	0.07821	0.00068	0.232	478.1	6.4	485.4	4	434	37	485.4	4.0	1.5	
SLAM1907_34.FIN2	193.7	1.53	0.381	0.012	0.0508	0.0011	0.319	326.3	8.9	319.3	6.8	362	69	319.3	6.8	2.1	
SLAM1907_35.FIN2	149	0.89	5.05	0.14	0.3233	0.0071	0.632	1824	23	1805	35	1839	40	1839.0	40.0	1.8	
SLAM1907_36.FIN2	466	6.00	0.581	0.012	0.0744	0.0013	0.614	464.8	7.4	462.5	7.6	479	38	462.5	7.6	0.5	
SLAM1907_37.FIN2	1450	28.80	0.504	0.03	0.0665	0.0032	0.869	413	20	415	19	402	65	415.0	19.0	0.5	Rim
SLAM1907_37.FIN2	272.7	1.49	5.08	0.12	0.3019	0.0057	0.717	1830	21	1700	28	1983	29	1983.0	29.0	14.3	Core
SLAM1907_38.FIN2	296	1.58	1.804	0.024	0.1768	0.0016	0.533	1045.3	8.9	1049.2	8.8	1036	24	1036.0	24.0	1.3	
SLAM1907_39.FIN2	358	3.46	0.616	0.015	0.0786	0.0016	0.594	485.7	9.4	487.6	9.3	474	46	487.6	9.3	0.4	
SLAM1907_40.FIN2	239.9	2.64	0.602	0.013	0.0757	0.0011	0.340	477.4	8.3	470.5	6.7	503	47	470.5	6.7	1.4	
SLAM1907_41.FIN2	557	1.04	0.3678	0.0084	0.0495	0.00081	0.444	317.3	6.2	312	5.1	351	48	312.0	5.1	1.7	
SLAM1907_42.FIN2	587	0.55	0.2226	0.0049	0.03058	0.00051	0.392	203.8	4.1	194.1	3.2	330	48	194.1	3.2	4.8	
SLAM1907_43.FIN2	616	37.00	0.429	0.047	0.0552	0.002	0.639	361	34	346	12	440	220	346.0	12.0	4.2	Rim
SLAM1907_43.FIN2	613	11.50	6.52	0.13	0.3821	0.007	0.754	2046	17	2085	33	2009	24	2009.0	24.0	3.8	Core
SLAM1907_44.FIN2	706	2.18	0.5411	0.0071	0.07189	0.00057	0.262	438.8	4.7	447.5	3.4	393	29	447.5	3.4	2.0	
SLAM1907_45.FIN2	520	3.67	11.17	0.13	0.4967	0.0049	0.674	2538	11	2599	21	2490	16	2490.0	16.0	4.4	
SLAM1907_46.FIN2	329	0.68	5.256	0.077	0.3373	0.0045	0.637	1860	12	1873	22	1848	22	1848.0	22.0	1.4	
SLAM1907_47.FIN2	526	3.31	0.3805	0.0077	0.05146	0.00071	0.475	327.8	5.8	323.4	4.4	348	43	323.4	4.4	1.3	
SLAM1907_48.FIN2	242	0.71	0.874	0.023	0.1035	0.0016	0.499	636	12	634.8	9.5	631	50	634.8	9.5	0.2	
SLAM1907_49.FIN2	283.3	7.10	3.432	0.067	0.2601	0.005	0.704	1509	16	1489	25	1535	29	1535.0	29.0	3.0	
SLAM1907_50.FIN2	347	1.63	0.404	0.01	0.05459	0.00072	0.312	343.8	7.3	342.6	4.4	344	52	342.6	4.4	0.3	
SLAM1907_51.FIN2	278	1.51	0.615	0.013	0.07622	0.00083	0.289	485.5	8.3	473.5	5	528	47	473.5	5.0	2.5	
SLAM1907_52.FIN2	294	3.41	0.3668	0.0087	0.05195	0.0008	0.289	316.5	6.5	326.4	4.9	245	52	326.4	4.9	3.1	
SLAM1907_53.FIN2	310	2.30	0.968	0.024	0.1117	0.0025	0.628	685	12	682	14	693	43	682.0	14.0	0.4	
SLAM1907_54.FIN2	65.2	1.15	4.58	0.064	0.3081	0.003	0.338	1743	12	1731	15	1756	26	1756.0	26.0	1.4	
SLAM1907_56.FIN2	182	1.20	0.381	0.012	0.05157	0.00089	0.229	326.3	8.8	324.1	5.5	323	68	324.1	5.5	0.7	
SLAM1907_57.FIN2	206	1.23	0.249	0.012	0.0348	0.001	0.154	224.8	9.4	220.4	6.2	290	100	220.4	6.2	2.0	
SLAM1907_58.FIN2	418	1.46	0.3654	0.0089	0.04941	0.00085	0.511	315.4	6.6	310.8	5.2	343	46	310.8	5.2	1.5	
SLAM1907_59.FIN2	486	1.63	0.3968	0.0071	0.05404	0.00047	0.313	338.8	5.2	339.3	2.9	329	38	339.3	2.9	0.1	
SLAM1907_60.FIN2	343	1.91	4.74	0.056	0.3089	0.0029	0.752	1773	10	1735	14	1818	14	1818.0	14.0	4.6	
SLAM1907_61.FIN2	68.4	1.85	5.62	0.22	0.341	0.013	0.713	1911	34	1888	61	1949	39	1949.0	39.0	3.1	
SLAM1907_62.FIN2	269	0.78	0.556	0.012	0.06967	0.00078	0.060	449.1	7.4	434.1	4.7	508	50	434.1	4.7	3.3	
SLAM1907_63.FIN2	220.9	1.85	0.439	0.011	0.0577	0.00089	0.429	369.1	8	361.5	5.4	404	51	361.5	5.4	2.1	
SLAM1907_64.FIN2	172.4	0.95	0.432	0.013	0.05676	0.0009	0.176	363.3	9	355.8	5.5	393	65	355.8	5.5	2.1	
SLAM1907_65.FIN2	144.3	0.72	1.605	0.031	0.1623	0.0019	0.367	969	12	969	11	968	37	968.0	37.0	0.1	
SLAM1907_66.FIN2	306	1.06	0.3167	0.0077	0.04385	0.00053	0.205	278.7	6	276.7	3.2	287	53	276.7	3.2	0.7	
SLAM1907_67.FIN2	88	1.40	0.265	0.012	0.03784	0.00055	0.054	236.9	9.4	239.4	3.4	210	89	239.4	3.4	1.1	
SLAM1907_68.FIN2	334.1	1.20	0.3767	0.009	0.05144	0.00067	0.272	323.9	6.6	323.3	4.1	321	52	323.3	4.1	0.2	
SLAM1907_69.FIN2	578	1.41	0.3611	0.0065	0.04915	0.00059	0.255	312.6	4.9	309.3	3.6	333	42	309.3	3.6	1.1	

Sample Name:	SLAm1909							207/235		206/238		207/206		Best age			
Grain #	[U] ppm	U/Th	207/235	2σ error	206/238	2σ error	RHO	Age Ma	2σ error	Age (Ma)	2σ error	Age (Ma)	2σ error	(Ma)	2σ error	% Disc.	Rim/Core
SLAM1909_1.FIN2	355	1.53	0.425	0.011	0.05235	0.00059	0.391	358.9	7.5	328.9	3.6	542	44	328.9	3.6	8.4	
SLAM1909_2.FIN2	204	1.33	0.398	0.011	0.05257	0.00072	0.159	339.5	7.7	330.3	4.4	407	62	330.3	4.4	2.7	
SLAM1909_3.FIN2	2440	83.30	0.923	0.038	0.115	0.0044	0.506	664	20	701	26	542	88	701.0	26.0	5.6	Rim
SLAM1909_3.FIN2	533	9.80	1.78	0.02	0.1806	0.0019	0.591	1037.3	7.4	1070	10	984	20	984.0	20.0	8.7	Core
SLAM1909_4.FIN2	398	5.70	1.431	0.029	0.1523	0.0021	0.680	901	12	913	12	882	34	882.0	34.0	3.5	
SLAM1909_5.FIN2	329	1.35	0.2756	0.0071	0.03908	0.00047	0.246	246.7	5.6	247.1	2.9	250	54	247.1	2.9	0.2	
SLAM1909_6.FIN2	329	1.15	0.2686	0.0065	0.03757	0.00035	0.044	241.2	5.2	237.8	2.2	278	57	237.8	2.2	1.4	
SLAM1909_7.FIN2	910	54.00	0.383	0.01	0.05223	0.00079	0.254	329.5	7.6	328.2	4.9	330	77	328.2	4.9	0.4	Rim
SLAM1909_7.FIN2	119	1.15	3.989	0.061	0.2749	0.0031	0.436	1630	12	1565	16	1720	26	1720.0	26.0	9.0	Core
SLAM1909_8.FIN2	393	3.68	0.5276	0.0088	0.06864	0.00069	0.357	429.7	5.8	427.9	4.2	437	36	427.9	4.2	0.4	
SLAM1909_9.FIN2	582	1.40	0.3382	0.0059	0.04729	0.00053	0.490	295.5	4.5	297.9	3.3	275	34	297.9	3.3	0.8	
SLAM1909_10.FIN2	298.1	0.44	0.873	0.012	0.10337	0.00084	0.248	636.7	6.3	634.1	4.9	653	31	634.1	4.9	0.4	
SLAM1909_11.FIN2	248.5	1.79	0.4105	0.0098	0.05673	0.00073	0.225	348.6	7.1	355.7	4.5	308	53	355.7	4.5	2.0	
SLAM1909_12.FIN2	208.5	2.44	0.4171	0.0095	0.0538	0.00061	0.273	353.2	6.8	337.8	3.7	461	51	337.8	3.7	4.4	
SLAM1909_14.FIN2	779	0.72	0.2845	0.0048	0.04035	0.00033	0.232	254.1	3.8	255	2.1	257	38	255.0	2.1	0.4	
SLAM1909_15.FIN2	587	1.17	0.669	0.023	0.06611	0.00085	0.415	519	14	412.6	5.2	1023	61	412.6	5.2	20.5	
SLAM1909_16.FIN2	399	1.72	0.898	0.02	0.1002	0.0011	0.449	649	11	615.3	6.2	774	42	615.3	6.2	5.2	
SLAM1909_17.FIN2	138	1.41	10.65	0.36	0.4704	0.009	0.944	2477	35	2481	40	2481	34	2481.0	34.0	0.0	
SLAM1909_18.FIN2	700	2.46	0.3908	0.0065	0.0537	0.00052	0.353	334.6	4.7	337.2	3.2	308	36	337.2	3.2	0.8	
SLAM1909_19.FIN2	723	1.72	0.3915	0.0052	0.05361	0.00048	0.294	335.2	3.8	336.6	2.9	323	31	336.6	2.9	0.4	
SLAM1909_20.FIN2	340	1.57	0.3808	0.0077	0.05131	0.00055	0.321	327.1	5.6	322.6	3.4	343	43	322.6	3.4	1.4	
SLAM1909_21.FIN2	1240	1.41	0.5743	0.0068	0.07406	0.00083	0.528	460.5	4.4	460.5	5	439	25	460.5	5.0	0.0	
SLAM1909_22.FIN2	346	3.03	0.3911	0.0068	0.05258	0.00055	0.295	334.8	4.9	330.3	3.4	337	39	330.3	3.4	1.3	
SLAM1909_23.FIN2	192.3	0.99	15.28	0.28	0.5473	0.0099	0.807	2830	17	2811	41	2828	18	2828.0	18.0	0.6	
SLAM1909_24.FIN2	416	1.13	0.362	0.0065	0.04848	0.00056	0.211	313.4	4.8	305.2	3.4	351	43	305.2	3.4	2.6	
SLAM1909_25.FIN2	281	1.28	0.795	0.012	0.09556	0.00074	0.246	593.5	6.8	588.3	4.4	593	34	588.3	4.4	0.9	
SLAM1909_26.FIN2	382	0.85	0.2652	0.0059	0.03822	0.00046	0.130	238.5	4.7	241.8	2.8	197	51	241.8	2.8	1.4	
SLAM1909_27.FIN2	818	0.76	0.4107	0.0067	0.05656	0.00071	0.396	349.1	4.8	354.6	4.3	298	36	354.6	4.3	1.6	
SLAM1909_28.FIN2	603	2.82	0.2631	0.0056	0.03782	0.00046	0.384	236.8	4.5	239.3	2.9	199	41	239.3	2.9	1.1	
SLAM1909_29.FIN2	333	1.13	0.2863	0.0063	0.03921	0.00046	0.324	255.3	4.9	247.9	2.9	302	46	247.9	2.9	2.9	
SLAM1909_30.FIN2	891	24.70	0.418	0.014	0.05162	0.00066	0.055	354.3	9.7	324.5	4	547	83	324.5	4.0	8.4	
SLAM1909_31.FIN2	1105	1.40	0.38	0.01	0.04022	0.00039	0.464	327.5	7.9	254.2	2.4	877	54	254.2	2.4	22.4	
SLAM1909_32.FIN2	230.9	0.90	0.2644	0.0078	0.03598	0.00037	0.106	237.6	6.2	227.9	2.3	321	63	227.9	2.3	4.1	
SLAM1909_33.FIN2	583	8.20	3.79	0.21	0.2216	0.0097	0.951	1566	44	1285	51	1985	31	DISC	DISC	35.3	
SLAM1909_34.FIN2	304	0.94	1.596	0.022	0.1589	0.0015	0.331	967.6	8.5	950.4	8.4	1002	28	1002.0	28.0	5.1	
SLAM1909_35.FIN2	183	2.06	10.88	0.33	0.451	0.012	0.964	2501	30	2393	54	2595	15	2595.0	15.0	7.8	
SLAM1909_36.FIN2	523	7.26	0.5523	0.0079	0.07101	0.00075	0.361	446.1	5.2	442.2	4.5	453	32	442.2	4.5	0.9	
SLAM1909_37.FIN2	325	1.95	0.3894	0.007	0.05233	0.00054	0.231	333.5	5.1	328.8	3.3	359	41	328.8	3.3	1.4	
SLAM1909_38.FIN2	547	1.78	0.5525	0.0088	0.07152	0.00098	0.506	446.1	5.8	445.3	5.9	450	34	445.3	5.9	0.2	
SLAM1909_39.FIN2	475	0.92	0.2397	0.006	0.03357	0.00034	0.184	218.4	5	212.8	2.1	259	53	212.8	2.1	2.6	
SLAM1909_40.FIN2	871	1.19	0.5192	0.0071	0.06824	0.0006	0.448	424.3	4.8	425.5	3.6	409	29	425.5	3.6	0.3	
SLAM1909_41.FIN2	827	2.40	0.3693	0.0058	0.04987	0.00045	0.050	318.9	4.3	313.7	2.7	353	40	313.7	2.7	1.6	
SLAM1909_42.FIN2	81	0.62	1.285	0.032	0.1363	0.0021	0.129	836	14	823	12	866	62	823.0	12.0	1.6	
SLAM1909_43.FIN2	338	2.28	6.81	0.11	0.3613	0.0067	0.606	2085	14	1987	32	2186	27	2186.0	27.0	9.1	
SLAM1909_44.FIN2	463	2.39	4.482	0.043	0.3177	0.0028	0.383	1727.2	7.9	1778	13	1668	19	1668.0	19.0	6.6	
SLAM1909_45.FIN2	462.8	1.48	1.138	0.02	0.1284	0.0023	0.532	770.6	9.7	778	13	746	35	778.0	13.0	1.0	
SLAM1909_46.FIN2	237.7	2.00	0.534	0.011	0.07045	0.00071	0.130	433.6	7.2	438.8	4.2	410	48	438.8	4.2	1.2	
SLAM1909_47.FIN2	195.6	0.84	0.2629	0.0076	0.03643	0.00045	0.117	236.4	6.2	230.7	2.8	289	63	230.7	2.8	2.4	
SLAM1909_48.FIN2	171.1	2.42	2.964	0.043	0.241	0.0026	0.532	1397	11	1391	13	1415	24	1415.0	24.0	1.7	
SLAM1909_49.FIN2	214.6	5.01	1.293	0.026	0.1355	0.002	0.547	842	12	819	11	914	35	819.0	11.0	2.7	
SLAM1909_50.FIN2	587	1.73	0.3794	0.006	0.05254	0.00054	0.298	326.3	4.4	330	3.3	314	36	330.0	3.3	1.1	
SLAM1909_51.FIN2	760	2.82	0.2962	0.0067	0.04207	0.00037	0.262	263	5.3	265.6	2.3	250	47	265.6	2.3	1.0	
SLAM1909_52.FIN2	755	2.03	0.3621	0.0057	0.04939	0.00051	0.318	313.5	4.3	310.8	3.1	343	36	310.8	3.1	0.9	
SLAM1909_53.FIN2	348.1	1.25	0.795	0.011	0.09756	0.00075	0.278	593.6	6.1	600.1	4.4	581	31	600.1	4.4	1.1	
SLAM1909_54.FIN2	405	2.24	0.3809	0.0076	0.05232	0.00058	0.217	327.3	5.6	328.7	3.5	321	46	328.7	3.5	0.4	
SLAM1909_55.FIN2	113.2	1.29	1.684	0.029	0.1665	0.0017	0.206	1003	11	992.6	9.2	1019	38	1019.0	38.0	2.6	
SLAM1909_56.FIN2	142	1.69	11.79	0.19	0.5044	0.0068	0.745	2586	15	2631	29	2554	18	2554.0	18.0	3.0	
SLAM1909_57.FIN2	155.6	0.95	3.428	0.039	0.2685	0.0026	0.396	1509.7	9	1533	13	1479	22	1479.0	22.0	3.7	
SLAM1909_58.FIN2	57.15	0.88	0.27	0.016	0.03601	0.00075	0.004	240	12	228	4.7	340	120	228.0	4.7	5.0	
SLAM1909_59.FIN2	384	0.59	0.833	0.012	0.10151	0.00097	0.402	614.7	6.8	623.2	5.7	579	30	623.2	5.7	1.4	
SLAM1909_60.FIN2	476	1.88	0.3827	0.0068	0.05355	0.00045	0.307	328.7	5	336.2	2.8	268	39	336.2	2.8	2.3	
SLAM1909_61.FIN2	274	1.48	0.261	0.012	0.03222	0.00085	0.333	235	9.4	204.4	5.3	512	83	204.4	5.3	13.0	
SLAM1909_62.FIN2	601	3.83	0.3658	0.0064	0.05057	0.0007	0.481	316.2	4.8	318	4.3	288	37	318.0	4.3	0.6	
SLAM1909_63.FIN2	418	5.63	0.6391	0.009	0.08287	0.00085	0.408	501.3	5.6	513.2	5.1	443	31	513.2	5.1	2.4	
SLAM1909_64.FIN2	342	0.85	0.953	0.012	0.11045	0.00095	0.268	679.2	6	675.3	5.5	688	27	675.3	5.5	0.6	

SLAM1909_65.FIN2	115.3	0.68	0.842	0.018	0.101	0.0011	0.267	619	10	620.2	6.5	603	47	620.2	6.5	0.2	
SLAM1909_66.FIN2	1770	88.00	0.426	0.012	0.0569	0.0016	0.743	359.8	8.8	356.7	9.5	391	55	356.7	9.5	0.9	Rim
SLAM1909_66.FIN2	237.2	3.04	0.907	0.016	0.1094	0.0012	0.495	656.2	8.9	669.4	7.1	604	40	669.4	7.1	2.0	Core
SLAM1909_67.FIN2	534	0.76	0.2544	0.0049	0.03632	0.00045	0.208	229.9	3.9	230	2.8	228	44	230.0	2.8	0.0	
SLAM1909_68.FIN2	696	2.23	0.302	0.0066	0.04111	0.00054	0.335	267.7	5.1	259.7	3.3	325	47	259.7	3.3	3.0	
SLAM1909_69.FIN2	467.4	0.70	0.4013	0.0081	0.05194	0.00054	0.118	342	5.9	326.4	3.3	417	49	326.4	3.3	4.6	
SLAM1909_71.FIN2	359	1.01	0.794	0.013	0.09175	0.00098	0.392	594.2	7.3	565.8	5.8	684	34	565.8	5.8	4.8	
SLAM1909_72.FIN2	141.6	1.56	0.39	0.011	0.05366	0.00065	0.083	333.5	8.2	336.9	4	293	62	336.9	4.0	1.0	
SLAM1909_73.FIN2	1387	2.01	0.4113	0.0063	0.05388	0.00048	0.246	349.4	4.5	338.3	2.9	409	34	338.3	2.9	3.2	
SLAM1909_75.FIN2	975	3.37	0.4821	0.0055	0.06477	0.00047	0.204	399.3	3.8	404.6	2.8	368	27	404.6	2.8	1.3	
SLAM1909_76.FIN2	308	1.05	0.2571	0.0068	0.03592	0.00039	0.278	231.9	5.5	227.5	2.4	278	52	227.5	2.4	1.9	
SLAM1909_77.FIN2	66.9	0.75	0.303	0.014	0.03661	0.00061	0.020	267	11	231.8	3.8	540	100	231.8	3.8	13.2	
SLAM1909_78.FIN2	887	1.71	0.4244	0.0054	0.05703	0.0005	0.462	359	3.9	357.5	3	365	27	357.5	3.0	0.4	
SLAM1909_79.FIN2	384	4.64	0.7	0.014	0.0862	0.0018	0.648	538.1	8.2	533	10	548	43	533.0	10.0	0.9	
SLAM1909_80.FIN2	539	0.66	1.88	0.019	0.1844	0.0014	0.513	1073.4	6.6	1090.6	7.5	1036	18	1036.0	18.0	5.3	
SLAM1909_81.FIN2	356	2.07	0.3816	0.008	0.05221	0.00055	0.279	327.7	5.9	328	3.4	313	45	328.0	3.4	0.1	
SLAM1909_82.FIN2	1360	83.00	0.3703	0.0095	0.04951	0.00089	0.530	319.6	7	311.5	5.5	354	45	311.5	5.5	2.5	
SLAM1909_83.FIN2	398	1.74	0.78	0.014	0.0941	0.0012	0.346	584.6	8	579.7	6.9	591	39	579.7	6.9	0.8	
SLAM1909_84.FIN2	116	1.35	0.376	0.013	0.05119	0.00061	0.152	322.5	9.3	321.8	3.7	305	71	321.8	3.7	0.2	
SLAM1909_85.FIN2	1415	0.80	0.5517	0.0061	0.07188	0.00064	0.473	446.3	4.1	447.5	3.8	429	23	447.5	3.8	0.3	
SLAM1909_86.FIN2	68.9	1.17	0.861	0.023	0.1028	0.0012	0.240	628	13	630.8	7.3	593	58	630.8	7.3	0.4	
SLAM1909_87.FIN2	538	3.87	5.561	0.087	0.329	0.0035	0.688	1907	14	1833	17	1987	20	1987.0	20.0	7.8	
SLAM1909_88.FIN2	644	1.61	0.3822	0.0057	0.05158	0.00049	0.433	328.8	4.3	324.2	3	336	32	324.2	3.0	1.4	
SLAM1909_89.FIN2	409	1.72	0.2933	0.0055	0.04167	0.00044	0.227	260.8	4.3	263.2	2.7	226	44	263.2	2.7	0.9	
SLAM1909_90.FIN2	213.3	1.77	0.71	0.014	0.08774	0.00079	0.289	543.5	8.6	542.1	4.7	522	44	542.1	4.7	0.3	
SLAM1909_91.FIN2	420	1.18	0.2736	0.0064	0.03849	0.00065	0.464	245.8	5.3	243.4	4.1	250	46	243.4	4.1	1.0	
SLAM1909_92.FIN2	1041	1.47	0.3873	0.005	0.05351	0.00039	0.217	332.2	3.7	336	2.4	287	31	336.0	2.4	1.1	
SLAM1909_93.FIN2	590	2.17	0.4097	0.0091	0.05402	0.00074	0.183	348.2	6.6	339.1	4.5	411	51	339.1	4.5	2.6	
SLAM1909_94.FIN2	373	1.25	0.3029	0.0083	0.03811	0.00068	0.428	268.1	6.5	241	4.2	496	57	241.0	4.2	10.1	
SLAM1909_95.FIN2	1024	2.36	1.355	0.021	0.1478	0.0019	0.879	868.1	9.2	889	11	828	17	828.0	11.0	2.4	
SLAM1909_96.FIN2	83	0.70	0.294	0.013	0.03909	0.00057	0.194	260	10	247.2	3.5	360	91	247.2	3.5	4.9	
SLAM1909_97.FIN2	894	19.27	0.998	0.014	0.1181	0.0017	0.581	702.4	7.3	719.5	9.7	669	29	719.5	9.7	2.4	
SLAM1909_98.FIN2	278	0.90	0.2674	0.007	0.03776	0.00056	0.308	240	5.6	238.9	3.5	273	55	238.9	3.5	0.5	
SLAM1909_99.FIN2	384	0.94	0.3961	0.008	0.05579	0.00067	0.288	338.3	5.8	349.9	4.1	286	42	349.9	4.1	3.4	
SLAM1909_100.FIN2	1229	15.40	0.3738	0.0097	0.0519	0.0014	0.648	322	7.2	326.1	8.6	321	49	326.1	8.6	1.3	
SLAM1909_101.FIN2	515	8.40	0.567	0.022	0.0734	0.0021	0.604	454	15	456	13	461	68	456.0	13.0	0.4	
SLAM1909_102.FIN2	185.5	1.61	0.758	0.017	0.0935	0.0017	0.458	571.8	9.8	575.9	9.7	574	47	575.9	9.7	0.7	
SLAM1909_103.FIN2	295.5	1.25	0.2866	0.0072	0.04148	0.00064	0.465	255.3	5.6	262	4	222	48	262.0	4.0	2.6	
SLAM1909_104.FIN2	535	2.28	0.867	0.016	0.1041	0.0013	0.436	633.1	8.5	638.6	7.5	627	37	638.6	7.5	0.9	
SLAM1909_105.FIN2	150	0.41	5.151	0.085	0.3304	0.0046	0.672	1842	14	1839	22	1856	22	1856.0	22.0	0.9	
SLAM1909_106.FIN2	919	2.03	0.284	0.0091	0.0399	0.0012	0.395	253.4	7.3	252.1	7.6	259	75	252.1	7.6	0.5	
SLAM1909_107.FIN2	234	1.22	0.387	0.012	0.05216	0.00077	0.369	331.4	8.8	328.5	4.5	356	65	328.5	4.5	0.9	
SLAM1909_108.FIN2	857	1.53	0.5726	0.0091	0.07333	0.00077	0.228	459.4	5.9	456.2	4.6	471	37	456.2	4.6	0.7	
SLAM1909_109.FIN2	558	1.78	0.3979	0.0063	0.05489	0.00054	0.251	340.3	4.5	344.5	3.3	310	37	344.5	3.3	1.2	
SLAM1909_110.FIN2	698	1.88	0.489	0.014	0.0538	0.0013	0.669	403.1	9.4	337.7	7.7	782	45	337.7	7.7	16.2	
SLAM1909_111.FIN2	1243	1.74	0.67	0.014	0.0851	0.0018	0.744	520	8.5	528	10	500	34	528.0	10.0	1.5	
SLAM1909_112.FIN2	725	1.38	0.3847	0.0073	0.05039	0.00058	0.305	330	5.4	316.9	3.5	421	42	316.9	3.5	4.0	
SLAM1909_113.FIN2	431	0.86	0.28	0.014	0.0376	0.0017	0.066	251	11	238	11	370	150	238.0	11.0	5.2	
SLAM1909_114.FIN2	741	1.11	0.2859	0.0057	0.0402	0.00054	0.418	254.9	4.5	254.1	3.4	276	41	254.1	3.4	0.3	
SLAM1909_115.FIN2	803	1.97	0.4097	0.0075	0.05507	0.00071	0.520	348.3	5.4	345.5	4.3	366	37	345.5	4.3	0.8	
SLAM1909_116.FIN2	469	1.43	0.4308	0.0073	0.05884	0.0008	0.429	363.3	5.2	368.5	4.9	336	38	368.5	4.9	1.4	
SLAM1909_117.FIN2	292	1.66	0.387	0.015	0.0514	0.0014	0.457	331	11	323.3	8.6	385	77	323.3	8.6	2.3	
SLAM1909_118.FIN2	337	1.67	0.3512	0.007	0.04839	0.00044	0.147	305.1	5.3	304.6	2.7	307	46	304.6	2.7	0.2	
SLAM1909_119.FIN2	388	2.39	0.3976	0.0084	0.05442	0.00054	0.284	339.3	6.1	341.6	3.3	313	45	341.6	3.3	0.7	
SLAM1909_120.FIN2	584	1.66	0.784	0.018	0.0956	0.0016	0.576	587	11	588.6	9.4	581	40	588.6	9.4	0.3	
SLAM1909_121.FIN2	85.9	0.40	6.63	0.11	0.3744	0.0044	0.510	2061	14	2049	21	2077	23	2077.0	23.0	1.3	
SLAM1909_122.FIN2	596	1.52	0.3783	0.0066	0.05213	0.00073	0.443	325.4	4.8	327.6	4.4	308	37	327.6	4.4	0.7	
SLAM1909_123.FIN2	329	1.57	0.2513	0.0065	0.03607	0.0004	0.334	227.1	5.3	228.4	2.5	209	52	228.4	2.5	0.6	
SLAM1909_124.FIN2	267.6	1.12	0.2631	0.0081	0.03754	0.00056	0.245	236.5	6.4	237.5	3.5	236	64	237.5	3.5	0.4	
SLAM1909_125.FIN2	1070	2.01	0.466	0.01	0.0622	0.0014	0.564	387.9	7.2	388.6	8.7	393	42	388.6	8.7	0.2	
SLAM1909_126.FIN2	682	1.35	0.3787	0.006	0.05282	0.00053	0.430	326.3	4.3	331.8	3.2	287	32	331.8	3.2	1.7	
SLAM1909_127.FIN2	435	3.52	0.5	0.016	0.0647	0.0015	0.465	411	11	404	9.2	429	72	404.0	9.2	1.7	
SLAM1909_128.FIN2	651	2.52	0.3923	0.0079	0.05355	0.00093	0.449	335.4	5.8	336.2	5.7	334	44	336.2	5.7	0.2	
SLAM1909_129.FIN2	151.4	1.57	1.426	0.044	0.1482	0.0033	0.627	896	18	890	18	910	50	910.0	50.0	2.2	
SLAM1909_130.FIN2	385	4.38	1.503	0.03	0.1556	0.0026	0.499	930	12	934	15	918	38	918.0	38.0	1.7	
SLAM1909_131.FIN2	1201	149.00	0.956	0.017	0.1133	0.0021	0.685	683.3	9.5	691	12	655	30	691.0	12.0	1.1	
SLAM1909_132.FIN2	329	7.80	0.813	0.016	0.1002	0.0014	0.463	603	9.2	615.3	8.1	545	41	615.3	8.1	2.0	

Sample Name:	SLAm1915							207/235		206/238		207/206		Best age			
Grain #	[U] ppm	U/Th	207/235	2σ error	206/238	2σ error	RHO	Age Ma	2σ error	Age (Ma)	2σ error	Age (Ma)	2σ error	(Ma)	2σ error	% Disc.	Rim/Core
SLAM1915_1.FIN2	123	3.10	7.549	0.089	0.4	0.0037	0.494	2178	11	2168	17	2181	18	2181.0	18.0	0.6	
SLAM1915_2.FIN2	498	1.20	0.2641	0.0064	0.03693	0.00051	0.329	237.5	5.1	233.8	3.1	266	50	233.8	3.1	1.6	
SLAM1915_3.FIN2	729	1.67	0.3808	0.0068	0.0534	0.00058	0.351	327.2	5	335.3	3.6	263	38	335.3	3.6	2.5	
SLAM1915_4.FIN2	127	2.30	0.908	0.025	0.1053	0.002	0.447	654	14	645	12	675	58	645.0	12.0	1.4	
SLAM1915_5.FIN2	227	1.82	16.5	0.48	0.524	0.011	0.556	2896	28	2714	46	3039	38	3039.0	38.0	10.7	
SLAM1915_6.FIN2	768	2.26	0.4115	0.0078	0.05547	0.00092	0.554	349.4	5.6	347.9	5.6	357	38	347.9	5.6	0.4	
SLAM1915_7.FIN2	263	1.37	0.398	0.012	0.0529	0.001	0.377	340.1	9.1	332.4	6.3	374	62	332.4	6.3	2.3	
SLAM1915_8.FIN2	1160	4.06	0.3695	0.008	0.04964	0.00075	0.494	318.6	5.9	312.2	4.6	353	43	312.2	4.6	2.0	
SLAM1915_9.FIN2	396	3.44	0.3877	0.008	0.05146	0.00061	0.274	332.9	5.7	323.5	3.8	395	45	323.5	3.8	2.8	
SLAM1915_10.FIN2	168.5	0.57	1.069	0.02	0.1201	0.0016	0.430	737	10	731.1	9	748	39	731.1	9.0	0.8	
SLAM1915_11.FIN2	166.2	1.95	1.141	0.036	0.1288	0.0034	0.776	770	17	780	20	726	45	780.0	20.0	1.3	
SLAM1915_12.FIN2	159.6	1.11	0.142	0.0093	0.01616	0.00042	0.365	133.7	8.2	103.3	2.6	650	130	103.3	2.6	22.7	
SLAM1915_13.FIN2	176.7	2.08	0.362	0.01	0.05092	0.00077	0.209	312.9	7.4	320.1	4.7	256	60	320.1	4.7	2.3	
SLAM1915_15.FIN2	123.2	0.79	0.29	0.012	0.03776	0.00081	0.263	257.1	9.7	238.9	5	401	85	238.9	5.0	7.1	
SLAM1915_16.FIN2	189.3	1.85	1.232	0.028	0.1298	0.0025	0.537	815	13	786	14	890	44	786.0	14.0	3.6	
SLAM1915_17.FIN2	312	1.70	0.3941	0.0091	0.05352	0.00068	0.105	336.5	6.6	336	4.1	338	55	336.0	4.1	0.1	
SLAM1915_18.FIN2	228	1.30	1.793	0.027	0.1759	0.0016	0.422	1041.3	9.8	1044.5	8.7	1032	28	1032.0	28.0	1.2	
SLAM1915_19.FIN2	236.3	1.76	0.37	0.014	0.0496	0.0013	0.445	318	11	312.2	8.3	361	78	312.2	8.3	1.8	
SLAM1915_20.FIN2	204.7	1.97	0.385	0.011	0.05294	0.00097	0.360	330.5	8.1	332.4	5.9	313	60	332.4	5.9	0.6	
SLAM1915_21.FIN2	286	1.10	0.864	0.014	0.10402	0.00098	0.297	631.3	7.6	637.8	5.7	602	35	637.8	5.7	1.0	
SLAM1915_22.FIN2	432	1.29	1.692	0.024	0.1679	0.002	0.554	1004.5	9	1000	11	1012	26	1012.0	26.0	1.2	
SLAM1915_23.FIN2	110.6	1.25	0.371	0.013	0.05037	0.00089	0.133	318.4	9.5	316.7	5.4	317	75	316.7	5.4	0.5	
SLAM1915_24.FIN2	203	2.61	0.554	0.015	0.0718	0.0011	0.368	448	10	446.7	6.7	445	58	446.7	6.7	0.3	
SLAM1915_25.FIN2	580	1.65	0.845	0.011	0.1002	0.001	0.382	621.8	6.2	615.3	6	649	30	615.3	6.0	1.0	
SLAM1915_26.FIN2	366	2.39	0.381	0.012	0.05172	0.00077	0.219	326.9	9.1	325	4.7	321	72	325.0	4.7	0.6	
SLAM1915_27.FIN2	217.4	1.93	0.835	0.02	0.1017	0.0013	0.446	615	11	624.1	7.4	577	47	624.1	7.4	1.5	
SLAM1915_28.FIN2	189.9	0.71	0.2764	0.0087	0.04053	0.00074	0.170	246.9	6.9	256.1	4.6	171	65	256.1	4.6	3.7	
SLAM1915_29.FIN2	190	0.66	0.837	0.016	0.10281	0.00093	0.164	615.8	8.8	630.7	5.4	551	43	630.7	5.4	2.4	
SLAM1915_30.FIN2	570	1.73	0.55	0.012	0.07184	0.00081	0.405	444.4	7.8	447.2	4.9	422	45	447.2	4.9	0.6	
SLAM1915_31.FIN2	249	0.83	1.224	0.035	0.1295	0.0025	0.579	807	16	785	14	864	49	785.0	14.0	2.7	
SLAM1915_33.FIN2	709	2.61	0.5128	0.0079	0.06781	0.00054	0.341	420.6	5.4	422.9	3.2	393	32	422.9	3.2	0.5	
SLAM1915_34.FIN2	478.8	1.93	5.347	0.073	0.3405	0.005	0.734	1874	12	1888	24	1859	22	1859.0	22.0	1.6	
SLAM1915_35.FIN2	92.9	1.23	0.379	0.015	0.0523	0.0011	0.133	324	11	328.5	6.6	314	88	328.5	6.6	1.4	
SLAM1915_36.FIN2	114	1.38	0.286	0.011	0.04057	0.00069	0.012	253.9	8.6	256.3	4.3	237	83	256.3	4.3	0.9	
SLAM1915_37.FIN2	134.1	0.54	1.017	0.025	0.117	0.0017	0.415	710	13	713.2	9.5	709	50	713.2	9.5	0.5	
SLAM1915_38.FIN2	750	4.44	0.5	0.028	0.0651	0.0021	0.662	411	19	407	13	432	90	407.0	13.0	1.0	Rim
SLAM1915_38.FIN2	141.3	1.11	0.957	0.028	0.1117	0.0013	0.391	679	14	682.2	7.6	631	58	682.2	7.6	0.5	Core
SLAM1915_40.FIN2	275	1.54	17.38	0.32	0.603	0.011	0.758	2954	18	3039	42	2899	20	2899.0	20.0	4.8	
SLAM1915_41.FIN2	305	0.87	0.709	0.02	0.0884	0.0017	0.234	543	12	546	9.8	525	65	546.0	9.8	0.6	Rim
SLAM1915_41.FIN2	62.4	0.98	1.66	0.063	0.168	0.0035	0.147	990	24	1005	18	957	83	957.0	83.0	5.0	Core
SLAM1915_42.FIN2	597	6.09	0.3684	0.0089	0.04829	0.00079	0.351	318.1	6.7	304	4.8	418	55	304.0	4.8	4.4	
SLAM1915_43.FIN2	236	1.53	0.3727	0.009	0.05166	0.00065	0.001	320.8	6.7	324.7	4	296	58	324.7	4.0	1.2	
SLAM1915_44.FIN2	171.5	1.35	0.565	0.018	0.0727	0.0015	0.097	453	12	452.4	9.2	451	75	452.4	9.2	0.1	
SLAM1915_46.FIN2	338	1.00	0.848	0.016	0.1017	0.0013	0.474	622.6	8.7	624.2	7.7	616	36	624.2	7.7	0.3	
SLAM1915_47.FIN2	496	4.74	0.815	0.014	0.09662	0.00085	0.299	604.2	7.7	594.5	5	635	36	594.5	5.0	1.6	
SLAM1915_48.FIN2	409	2.25	0.549	0.014	0.0714	0.0011	0.408	443.4	9.4	444.7	6.9	429	54	444.7	6.9	0.3	
SLAM1915_49.FIN2	1435	6.52	0.488	0.021	0.0609	0.0015	0.808	403	14	381.1	8.9	520	57	381.1	8.9	5.4	
SLAM1915_50.FIN2	701	2.20	0.5157	0.0078	0.06693	0.00057	0.261	421.9	5.2	417.6	3.5	434	35	417.6	3.5	1.0	
SLAM1915_53.FIN2	735	1.81	0.3867	0.008	0.05242	0.00063	0.139	331.6	5.9	329.3	3.8	346	39	329.3	3.8	0.7	
SLAM1915_55.FIN2	475	3.81	0.812	0.021	0.0954	0.0027	0.491	602	12	587	16	661	58	587.0	16.0	2.5	

Sample Name:	SLAm1916							207/235		206/238		207/206		Best age			
Grain #	[U] ppm	U/Th	207/235	2σ error	206/238	2σ error	RHO	Age Ma	2σ error	Age (Ma)	2σ error	Age (Ma)	2σ error	(Ma)	2σ error	% Disc.	Rim/Core
SLAM1916_1.FIN2	141	0.99	0.387	0.014	0.0527	0.0012	0.384	331	10	331.1	7.1	321	71	331.1	7.1	0.0	
SLAM1916_2.FIN2	823	2.69	0.3577	0.0063	0.05034	0.00064	0.511	310.1	4.7	317.1	4	250	35	317.1	4.0	2.3	
SLAM1916_3.FIN2	1005	28.50	0.4321	0.0092	0.0582	0.0011	0.535	365.9	7	364.6	6.9	369	47	364.6	6.9	0.4	Rim
SLAM1916_3.FIN2	151.5	2.35	0.617	0.025	0.0776	0.0015	0.350	485	16	481.6	8.7	478	84	481.6	8.7	0.7	Core
SLAM1916_4.FIN2	114.6	1.27	1.174	0.026	0.126	0.0022	0.505	786	12	765	13	817	45	765.0	13.0	2.7	
SLAM1916_5.FIN2	195.8	11.68	0.91	0.019	0.1039	0.0014	0.296	656	10	637	8.3	709	46	637.0	8.3	2.9	
SLAM1916_6.FIN2	383	10.13	0.39	0.024	0.0521	0.0014	0.517	333	18	327.4	8.8	360	120	327.4	8.8	1.7	Rim
SLAM1916_6.FIN2	468.5	11.70	0.957	0.015	0.106	0.0012	0.354	681.1	7.5	649.7	7.1	780	34	649.7	7.1	4.6	Core
SLAM1916_7.FIN2	208	1.13	5.03	0.12	0.3031	0.0067	0.783	1819	20	1704	33	1950	25	1950.0	25.0	12.6	
SLAM1916_8.FIN2	1047	1.72	0.3738	0.0069	0.05094	0.00075	0.475	322.1	5.1	320.2	4.6	315	38	320.2	4.6	0.6	
SLAM1916_9.FIN2	264.6	0.95	0.454	0.015	0.049	0.0011	0.658	378	10	308.4	6.7	798	51	308.4	6.7	18.4	
SLAM1916_10.FIN2	484.7	1.77	0.2268	0.005	0.03385	0.00037	0.206	208.3	4.3	214.6	2.3	135	48	214.6	2.3	3.0	
SLAM1916_11.FIN2	230.7	1.89	0.584	0.016	0.0722	0.0011	0.128	466	10	449.3	6.4	531	66	449.3	6.4	3.6	
SLAM1916_12.FIN2	74.9	1.31	7.59	0.12	0.4008	0.006	0.574	2181	14	2171	27	2180	24	2180.0	24.0	0.4	
SLAM1916_13.FIN2	247	2.14	5.341	0.059	0.3369	0.0033	0.635	1873.9	9.4	1871	16	1870	15	1870.0	15.0	0.1	
SLAM1916_14.FIN2	2950	6.40	0.371	0.055	0.0478	0.0079	0.813	318	41	300	48	460	230	300.0	48.0	5.7	Rim
SLAM1916_14.FIN2	301.8	12.60	3.475	0.095	0.2332	0.0058	0.652	1517	22	1350	30	1750	40	1750.0	40.0	22.9	Core
SLAM1916_15.FIN2	1070	18.10	1.072	0.029	0.118	0.0031	0.787	738	14	719	18	779	37	719.0	18.0	2.6	
SLAM1916_16.FIN2	128.3	2.54	0.69	0.02	0.0813	0.0013	0.239	531	12	503.5	7.5	618	64	503.5	7.5	5.2	
SLAM1916_17.FIN2	263.1	1.74	0.2312	0.007	0.03277	0.0005	0.334	210.6	5.7	207.8	3.1	233	61	207.8	3.1	1.3	
SLAM1916_18.FIN2	389	1.17	0.277	0.037	0.0382	0.0021	0.370	245	27	242	13	250	190	242.0	13.0	1.2	
SLAM1916_19.FIN2	759	59.60	0.44	0.019	0.0591	0.0019	0.509	369	13	370	11	349	84	370.0	11.0	0.3	
SLAM1916_20.FIN2	5040	4.83	0.281	0.021	0.0365	0.0023	0.537	251	16	231	14	430	150	231.0	14.0	8.0	Rim
SLAM1916_20.FIN2	216.2	2.54	1.336	0.04	0.1207	0.0026	0.620	858	18	734	15	1173	49	734.0	15.0	14.5	Core
SLAM1916_21.FIN2	194	1.35	0.682	0.019	0.0838	0.0016	0.394	527	11	518.7	9.3	551	60	518.7	9.3	1.6	
SLAM1916_22.FIN2	240	0.88	0.801	0.016	0.097	0.00092	0.194	595.9	9	596.7	5.4	567	44	596.7	5.4	0.1	
SLAM1916_23.FIN2	207.4	1.90	0.3368	0.0098	0.04642	0.00074	0.242	293.7	7.4	292.4	4.6	286	61	292.4	4.6	0.4	
SLAM1916_24.FIN2	257	6.34	11.95	0.47	0.463	0.017	0.835	2582	35	2436	74	2710	39	2710.0	39.0	10.1	
SLAM1916_25.FIN2	210	0.80	6.643	0.084	0.3791	0.0046	0.786	2063	11	2071	21	2043	14	2043.0	14.0	1.4	
SLAM1916_26.FIN2	317.3	1.41	0.2831	0.0099	0.03744	0.0009	0.411	252.9	7.9	236.8	5.6	360	70	236.8	5.6	6.4	
SLAM1916_27.FIN2	248	1.84	0.3684	0.0097	0.05079	0.00063	0.349	317.5	7.2	319.3	3.9	288	53	319.3	3.9	0.6	
SLAM1916_28.FIN2	436	1.77	0.4232	0.008	0.0581	0.00055	0.189	357.7	5.7	364	3.4	292	43	364.0	3.4	1.8	
SLAM1916_29.FIN2	243	1.82	0.404	0.01	0.0546	0.00072	0.476	343.6	7.2	342.6	4.4	315	49	342.6	4.4	0.3	
SLAM1916_30.FIN2	153.7	1.13	0.98	0.031	0.1107	0.002	0.204	692	16	677	12	730	71	677.0	12.0	2.2	
SLAM1916_31.FIN2	331	1.51	1.181	0.018	0.1299	0.0016	0.300	791.2	8.5	786.9	9.1	785	36	786.9	9.1	0.5	
SLAM1916_32.FIN2	118.3	0.70	0.559	0.017	0.07	0.0011	0.119	448	11	435.7	6.4	485	67	435.7	6.4	2.7	
SLAM1916_33.FIN2	234.8	1.96	9.582	0.088	0.4284	0.0042	0.783	2394.1	8.6	2298	19	2464	13	2464.0	13.0	6.7	
SLAM1916_34.FIN2	293	2.04	0.267	0.014	0.0337	0.0011	0.534	238	11	213.8	6.8	442	89	213.8	6.8	10.2	
SLAM1916_35.FIN2	251.4	1.90	0.476	0.015	0.0637	0.0018	0.493	396	11	398	11	369	66	398.0	11.0	0.5	
SLAM1916_36.FIN2	87.6	3.58	5.6	0.23	0.3107	0.0089	0.839	1901	37	1755	48	2069	40	2069.0	40.0	15.2	
SLAM1916_37.FIN2	1139	164.00	0.4193	0.0074	0.0567	0.00067	0.274	355.3	5.3	355.5	4.1	333	40	355.5	4.1	0.1	Rim
SLAM1916_37.FIN2	363.8	4.15	1.07	0.025	0.1182	0.0014	0.272	738	13	720.2	8	772	51	720.2	8.0	2.4	Core
SLAM1916_38.FIN2	576	2.37	0.5998	0.0084	0.07645	0.00074	0.125	477.4	5.5	474.9	4.4	477	37	474.9	4.4	0.5	
SLAM1916_39.FIN2	804	1.86	0.3519	0.0053	0.04887	0.00061	0.489	305.8	4	307.5	3.8	278	32	307.5	3.8	0.6	
SLAM1916_40.FIN2	254.6	2.38	0.2666	0.0079	0.03778	0.00044	0.265	239.2	6.3	239.1	2.7	223	59	239.1	2.7	0.0	
SLAM1916_41.FIN2	217	13.50	0.46	0.022	0.0592	0.0024	0.572	385	16	370	15	444	92	370.0	15.0	3.9	
SLAM1916_42.FIN2	961	2.91	0.3574	0.0061	0.04949	0.00071	0.530	309.9	4.6	311.4	4.4	288	35	311.4	4.4	0.5	
SLAM1916_43.FIN2	83.9	1.59	0.846	0.023	0.0928	0.0014	0.152	620	12	571.8	8.3	767	61	571.8	8.3	7.8	
SLAM1916_44.FIN2	232	1.77	0.24	0.016	0.0322	0.002	0.432	216	13	204	12	390	120	204.0	12.0	5.6	
SLAM1916_45.FIN2	555	2.48	0.2719	0.005	0.03858	0.00036	0.233	243.9	4	244	2.2	241	42	244.0	2.2	0.0	
SLAM1916_46.FIN2	116.1	1.38	0.708	0.023	0.0825	0.0012	0.388	545	14	510.8	7.3	650	66	510.8	7.3	6.3	
SLAM1916_47.FIN2	445	3.55	0.375	0.012	0.0509	0.0013	0.581	323.2	9.1	320	7.8	335	58	320.0	7.8	1.0	
SLAM1916_48.FIN2	264	2.00	0.2514	0.0074	0.03605	0.00045	0.084	227	6	228.3	2.8	201	63	228.3	2.8	0.6	
SLAM1916_49.FIN2	848	31.00	5.315	0.074	0.3562	0.0056	0.794	1869	12	1963	26	1763	17	1763.0	17.0	11.3	
SLAM1916_50.FIN2	283.1	0.83	0.3636	0.0093	0.04982	0.00091	0.403	316.2	6.9	313.3	5.6	326	55	313.3	5.6	0.9	
SLAM1916_51.FIN2	514	24.70	0.373	0.026	0.0501	0.0027	0.827	320	20	315	17	345	89	315.0	17.0	1.6	Rim
SLAM1916_51.FIN2	447	14.80	0.792	0.025	0.0947	0.0029	0.637	591	14	583	17	625	59	583.0	17.0	1.4	Core
SLAM1916_52.FIN2	152	3.00	0.556	0.016	0.071	0.0011	0.252	447	10	442.1	6.6	454	61	442.1	6.6	1.1	
SLAM1916_53.FIN2	415.9	20.70	0.947	0.042	0.1026	0.0019	0.643	672	19	630	11	786	55	630.0	11.0	6.3	
SLAM1916_54.FIN2	430	2.37	0.3816	0.0082	0.0523	0.00073	0.368	327.6	6	328.6	4.4	316	46	328.6	4.4	0.3	
SLAM1916_55.FIN2	105.7	1.50	0.264	0.012	0.03671	0.00062	0.020	236.4	9.7	232.4	3.8	282	98	232.4	3.8	1.7	
SLAM1916_56.FIN2	543	2.41	12	0.18	0.4991	0.0069	0.626	2601	14	2608	30	2599	20	2599.0	20.0	0.3	
SLAM1916_57.FIN2	376.6	2.23	0.387	0.012	0.0519	0.0014	0.583	330.3	9.1	325.7	8.6	359	59	325.7	8.6	1.4	
SLAM1916_58.FIN2	578	1.70	0.251	0.0061	0.03666	0.00065	0.462	226.9	5	232	4	195	48	232.0	4.0	2.2	
SLAM1916_59.FIN2	501	3.06	6.8	0.13	0.3828	0.0066	0.794	2084	17	2087	31	2090	21	2090.0	21.0	0.1	
SLAM1916_60.FIN2	236	10.80	0.37	0.015	0.05	0.0012	0.490	319	11	314.5	7.6	342	76	314.5	7.6	1.4	
SLAM1916_61.FIN2	159.1	1.36	0.363	0.013	0.04874	0.00083	0.285	312.5	9.9	306.7	5.1	334	73	306.7	5.1	1.9	
SLAM1916_62.FIN2	158.3	1.67	1.242	0.025	0.1312	0.0018	0.415	818	11	794	10	882	40	794.0	10.0	2.9	
SLAM1916_63.FIN2	214	1.49	0.3085	0.0098	0.04168	0.00065	0.230	272.2	7.7	263.2	4	344	70	263.2	4.0	3.3	

SLAM1916_64.FIN2	117	0.56	0.364	0.014	0.0502	0.0011	0.391	314	10	315.9	6.9	293	73	315.9	6.9	0.6	
SLAM1916_65.FIN2	396	1.16	0.2597	0.0065	0.0368	0.00054	0.303	233.9	5.2	232.9	3.3	252	53	232.9	3.3	0.4	
SLAM1916_66.FIN2	1020	49.40	0.561	0.011	0.0752	0.0011	0.686	451.6	7.1	467.1	6.5	384	30	467.1	6.5	3.4	
SLAM1916_67.FIN2	719	2.27	0.3709	0.0057	0.05016	0.00062	0.174	320	4.2	315.4	3.8	353	39	315.4	3.8	1.4	
SLAM1916_68.FIN2	182.3	0.98	0.305	0.027	0.0416	0.0015	0.445	263	18	262.6	9.1	250	110	262.6	9.1	0.2	
SLAM1916_69.FIN2	1188	52.00	0.3939	0.0099	0.0544	0.0012	0.716	336.3	7.2	341.2	7.1	299	38	341.2	7.1	1.5	
SLAM1916_70.FIN2	2420	61.40	0.649	0.044	0.0843	0.0043	0.843	506	27	522	25	442	76	522.0	25.0	3.2	Rim
SLAM1916_70.FIN2	159.4	1.14	4.74	0.16	0.2809	0.0087	0.729	1769	28	1594	44	1988	41	1988.0	41.0	19.8	Core
SLAM1916_71.FIN2	107	0.89	0.838	0.033	0.0928	0.0022	0.492	616	18	572	13	769	76	572.0	13.0	7.1	
SLAM1916_72.FIN2	1340	52.00	0.416	0.021	0.054	0.003	0.643	353	15	339	18	457	95	339.0	18.0	4.0	Rim
SLAM1916_72.FIN2	157.8	1.07	1.691	0.033	0.1639	0.0025	0.445	1003	12	978	14	1053	38	1053.0	38.0	7.1	Core
SLAM1916_73.FIN2	471	1.31	0.2907	0.0075	0.03955	0.0007	0.620	258.5	5.9	250	4.3	330	45	250.0	4.3	3.3	
SLAM1916_74.FIN2	194	0.72	0.841	0.026	0.0979	0.0024	0.737	617	14	601	14	683	45	601.0	14.0	2.6	
SLAM1916_75.FIN2	118.3	1.04	0.85	0.026	0.0996	0.0018	0.227	622	14	612	11	651	67	612.0	11.0	1.6	
SLAM1916_76.FIN2	66.6	1.76	1.403	0.042	0.1425	0.0025	0.276	887	17	859	14	961	64	961.0	64.0	10.6	
SLAM1916_77.FIN2	311	2.22	0.2746	0.0078	0.03926	0.00055	0.249	245.6	6.2	248.2	3.4	222	59	248.2	3.4	1.1	
SLAM1916_78.FIN2	574	2.48	0.3902	0.0098	0.05042	0.0008	0.520	333.5	7.1	317	4.9	452	49	317.0	4.9	4.9	
SLAM1916_79.FIN2	182	1.58	1.056	0.023	0.119	0.0016	0.361	730	11	724.4	9.1	755	43	724.4	9.1	0.8	
SLAM1916_80.FIN2	544	1.24	0.3025	0.0089	0.03898	0.00063	0.494	268.5	6.7	246.5	3.9	455	56	246.5	3.9	8.2	
SLAM1916_81.FIN2	563.9	1.44	0.374	0.0065	0.05074	0.00049	0.361	322.8	4.7	319	3	338	36	319.0	3.0	1.2	
SLAM1916_82.FIN2	325	1.19	0.2584	0.0077	0.03701	0.00073	0.423	232.7	6.1	234.2	4.6	228	59	234.2	4.6	0.6	
SLAM1916_83.FIN2	798	22.26	0.3303	0.0056	0.04706	0.00057	0.311	289.5	4.3	296.4	3.5	241	39	296.4	3.5	2.4	
SLAM1916_84.FIN2	224	1.65	0.423	0.012	0.05158	0.00071	0.257	358.7	8	324.2	4.3	575	58	324.2	4.3	9.6	
SLAM1916_85.FIN2	554	1.15	0.2804	0.0089	0.03903	0.00099	0.578	250.1	7	246.7	6.2	288	57	246.7	6.2	1.4	
SLAM1916_86.FIN2	348	2.08	0.3844	0.0091	0.05236	0.00088	0.392	330.5	6.9	328.9	5.4	350	50	328.9	5.4	0.5	
SLAM1916_87.FIN2	351.8	1.44	0.2688	0.0069	0.03876	0.00066	0.293	241.2	5.5	245.1	4.1	212	54	245.1	4.1	1.6	
SLAM1916_88.FIN2	225.4	2.06	0.2829	0.0084	0.03878	0.00048	0.189	252.1	6.6	245.3	3	317	63	245.3	3.0	2.7	
SLAM1916_89.FIN2	543	0.51	0.232	0.011	0.03145	0.00091	0.648	210.8	8.7	199.5	5.7	338	77	199.5	5.7	5.4	
SLAM1916_90.FIN2	136.3	1.21	5.38	0.16	0.3216	0.0062	0.720	1871	26	1795	30	1963	37	1963.0	37.0	8.6	
SLAM1916_91.FIN2	631	1.74	0.3257	0.0069	0.04592	0.00074	0.494	285.8	5.3	289.4	4.5	266	43	289.4	4.5	1.3	
SLAM1916_92.FIN2	324	2.71	0.987	0.027	0.1108	0.0023	0.492	694	14	677	13	750	54	677.0	13.0	2.4	
SLAM1916_93.FIN2	441	4.37	0.867	0.022	0.1076	0.0024	0.658	631	12	658	14	528	44	658.0	14.0	4.3	
SLAM1916_94.FIN2	112.3	0.92	0.2371	0.0089	0.03296	0.00046	0.068	216	7.4	209	2.9	283	79	209.0	2.9	3.2	
SLAM1916_95.FIN2	190.7	1.10	0.571	0.016	0.0673	0.0011	0.271	457	10	419.8	6.7	639	60	419.8	6.7	8.1	
SLAM1916_96.FIN2	141.6	2.19	0.285	0.011	0.0429	0.0011	0.239	254.3	9	270.8	6.8	157	82	270.8	6.8	6.5	
SLAM1916_97.FIN2	247	2.13	5.89	0.15	0.341	0.007	0.670	1954	22	1889	34	2026	33	2026.0	33.0	6.8	
SLAM1916_98.FIN2	446	1.89	0.3406	0.0073	0.04812	0.00076	0.465	297.1	5.5	302.9	4.6	263	44	302.9	4.6	2.0	
SLAM1916_99.FIN2	411	2.35	0.375	0.011	0.0538	0.0011	0.424	322.7	8.4	337.8	6.8	229	60	337.8	6.8	4.7	
SLAM1916_100.FIN2	259	1.19	0.2759	0.009	0.03794	0.00061	0.435	246.4	7.1	240	3.8	301	63	240.0	3.8	2.6	
SLAM1916_101.FIN2	251	1.05	0.2145	0.0059	0.03061	0.00044	0.294	196.9	4.9	194.4	2.7	229	56	194.4	2.7	1.3	
SLAM1916_102.FIN2	309.3	2.00	0.626	0.013	0.0786	0.0011	0.426	492.8	8	487.6	6.6	513	43	487.6	6.6	1.1	
SLAM1916_103.FIN2	342.1	2.01	1.024	0.017	0.1157	0.0016	0.566	715.8	8.4	706.4	9.3	751	30	706.4	9.3	1.3	
SLAM1916_104.FIN2	11.77	1.15	0.655	0.053	0.0828	0.0028	0.214	496	32	512	17	380	150	512.0	17.0	3.2	
SLAM1916_105.FIN2	2230	4.16	0.289	0.017	0.0381	0.0028	0.703	257	14	241	17	420	110	241.0	17.0	6.2	Rim
SLAM1916_105.FIN2	616	1.74	0.359	0.0061	0.04958	0.0005	0.411	311.2	4.5	311.9	3.1	303	35	311.9	3.1	0.2	Core
SLAM1916_106.FIN2	550	4.51	0.3619	0.0076	0.04904	0.00082	0.473	313.1	5.7	308.6	5.1	353	44	308.6	5.1	1.4	
SLAM1916_107.FIN2	1900	3.39	0.3406	0.0061	0.0443	0.00073	0.664	297.2	4.6	279.4	4.5	440	31	279.4	4.5	6.0	
SLAM1916_108.FIN2	205.5	2.58	0.2602	0.0072	0.03693	0.00053	0.124	235	6	233.8	3.3	249	63	233.8	3.3	0.5	
SLAM1916_109.FIN2	202.1	1.69	0.371	0.01	0.05126	0.00068	0.369	320.2	7.6	322.2	4.2	296	54	322.2	4.2	0.6	
SLAM1916_110.FIN2	441	2.49	0.347	0.045	0.0372	0.003	0.683	296	33	235	19	690	180	235.0	19.0	20.6	
SLAM1916_112.FIN2	325	6.00	0.436	0.014	0.0543	0.0012	0.456	366	10	340.6	7	531	73	340.6	7.0	6.9	
SLAM1916_113.FIN2	1122	2.73	0.795	0.01	0.0954	0.001	0.611	593.5	5.7	587.6	6.1	621	24	587.6	6.1	1.0	
SLAM1916_114.FIN2	444	2.30	0.351	0.02	0.0449	0.0017	0.258	304	15	283	10	460	130	283.0	10.0	6.9	Rim
SLAM1916_114.FIN2	416	1.50	0.457	0.011	0.0571	0.001	0.294	381.8	7.8	357.7	6.2	532	55	357.7	6.2	6.3	Core
SLAM1916_115.FIN2	620	2.18	0.29	0.0064	0.0393	0.00051	0.499	258.1	5	248.4	3.2	347	45	248.4	3.2	3.8	
SLAM1916_116.FIN2	265	0.78	0.2408	0.0061	0.03543	0.00044	0.135	219.2	5.1	224.4	2.7	173	55	224.4	2.7	2.4	
SLAM1916_117.FIN2	177.3	1.22	1.598	0.049	0.1575	0.0038	0.791	966	19	941	21	1022	40	1022.0	40.0	7.9	
SLAM1916_118.FIN2	167.5	1.04	0.372	0.011	0.04973	0.00081	0.424	319.7	8	312.8	5	371	56	312.8	5.0	2.2	
SLAM1916_119.FIN2	72.8	3.79	1.124	0.072	0.1187	0.0051	0.656	758	34	722	29	850	100	722.0	29.0	4.7	
SLAM1916_120.FIN2	298	1.83	0.3778	0.009	0.05179	0.00069	0.437	324.6	6.6	325.4	4.2	307	47	325.4	4.2	0.2	
SLAM1916_121.FIN2	99.6	0.73	2.347	0.046	0.2074	0.0035	0.546	1226	14	1214	19	1249	35	1249.0	35.0	2.8	
SLAM1916_122.FIN2	931	3.16	0.3619	0.0077	0.04984	0.00075	0.436	313.3	5.7	313.5	4.6	313	42	313.5	4.6	0.1	
SLAM1916_123.FIN2	878	163.00	0.518	0.02	0.0674	0.0023	0.724	423	14	420	14	445	62	420.0	14.0	0.7	Rim
SLAM1916_123.FIN2	245	1.79	1.251	0.026	0.1332	0.0016	0.474	822	12	805.9	9.1	867	38	805.9	9.1	2.0	Core
SLAM1916_124.FIN2	119.1	1.51	0.331	0.012	0.04273	0.00079	0.257	288.9	9.2	269.6	4.9	429	75	269.6	4.9	6.7	
SLAM1916_125.FIN2	490	1.78	0.2604	0.0069	0.03674	0.00061	0.522	234.4	5.6	232.5	3.8	250	49	232.5	3.8	0.8	
SLAM1916_126.FIN2	268	1.57	0.25	0.01	0.03616	0.00095	0.616	225	8.2	228.9	5.9	200	65	228.9	5.9	1.7	
SLAM1916_127.FIN2	236	1.81	0.3245	0.0089	0.04488	0.00082	0.426	284.5	6.8	283	5.1	289	53	283.0	5.1	0.5	
SLAM1916_128.FIN2	241	3.26	0.96	0.024	0.116	0.0025	0.556	680	12	707	14	596	50	707.0	14.0	4.0	
SLAM1916_129.FIN2	315	1.57	0.2819	0.0072	0.04026	0.00064	0.542	251.5	5.7	254.4	4	232	49	254.4	4.0	1.2	
SLAM1916_130.FIN2	406	2.05	0.554	0.017	0.07	0.0013	0.596	445	11	436.7	7.5	481	54	436.7	7.5	1.9	

Sample Name:	SLAm1920							207/235		206/238		207/206		Best age			
Grain #	[U] ppm	U/Th	207/235	2σ error	206/238	2σ error	RHO	Age Ma	2σ error	Age (Ma)	2σ error	Age (Ma)	2σ error	(Ma)	2σ error	% Disc.	Rim/Core
SLAM1920_1.FIN2	129.7	1.10	0.388	0.014	0.05215	0.00075	0.158	331.3	9.8	327.7	4.6	352	76	327.7	4.6	1.1	
SLAM1920_2.FIN2	830	0.85	0.2713	0.0047	0.03875	0.00035	0.298	243.5	3.7	245.1	2.2	234	38	245.1	2.2	0.7	
SLAM1920_3.FIN2	69.5	0.62	5.77	0.12	0.3452	0.0054	0.186	1940	18	1911	26	1975	42	1975.0	42.0	3.2	
SLAM1920_4.FIN2	5720	2.84	0.232	0.0049	0.03321	0.00093	0.704	211.9	4.1	210.6	5.8	235	47	210.6	5.8	0.6	Rim
SLAM1920_4.FIN2	1370	2.32	0.3528	0.0046	0.04914	0.00044	0.526	306.6	3.5	309.2	2.7	282	26	309.2	2.7	0.8	Core
SLAM1920_6.FIN2	196.3	2.97	2.222	0.029	0.2003	0.0025	0.479	1186.9	9.1	1177	13	1207	26	1207.0	26.0	2.5	
SLAM1920_7.FIN2	631	1.89	0.3766	0.0072	0.05203	0.00047	0.277	324.2	5.3	326.9	2.9	297	42	326.9	2.9	0.8	
SLAM1920_8.FIN2	90.1	1.22	2.357	0.062	0.2079	0.0035	0.667	1225	19	1217	19	1245	40	1245.0	40.0	2.2	
SLAM1920_9.FIN2	542	1.27	0.3666	0.0067	0.05075	0.00048	0.292	317.4	4.8	319.1	2.9	293	40	319.1	2.9	0.5	
SLAM1920_10.FIN2	233	1.14	0.958	0.015	0.1104	0.001	0.322	682.3	7.5	675.1	5.9	698	33	675.1	5.9	1.1	
SLAM1920_11.FIN2	40.3	0.90	0.364	0.022	0.048	0.0013	0.086	311	16	301.9	7.8	360	130	301.9	7.8	2.9	
SLAM1920_12.FIN2	482	2.82	0.3792	0.0072	0.05081	0.00074	0.356	326	5.3	319.4	4.5	380	45	319.4	4.5	2.0	
SLAM1920_13.FIN2	141.4	1.97	0.855	0.017	0.1039	0.001	0.236	627.7	9	637.2	5.8	581	45	637.2	5.8	1.5	
SLAM1920_14.FIN2	704	2.53	0.797	0.019	0.096	0.0019	0.665	594	11	591	11	605	40	591.0	11.0	0.5	
SLAM1920_15.FIN2	1200	1.50	0.4757	0.0091	0.06308	0.00093	0.361	394.6	6.3	394.2	5.7	387	41	394.2	5.7	0.1	
SLAM1920_16.FIN2	32.8	0.86	0.832	0.033	0.0988	0.0016	0.069	611	18	607.3	9.6	583	92	607.3	9.6	0.6	
SLAM1920_17.FIN2	256	28.60	0.826	0.012	0.1002	0.0011	0.397	610.6	6.8	615.8	6.2	582	33	615.8	6.2	0.9	
SLAM1920_18.FIN2	571	1.74	0.785	0.016	0.0959	0.0012	0.481	587.5	8.9	590.2	7.3	561	41	590.2	7.3	0.5	
SLAM1920_19.FIN2	512	1.66	0.4956	0.0079	0.06532	0.00062	0.507	408.3	5.4	407.9	3.7	402	35	407.9	3.7	0.1	
SLAM1920_20.FIN2	334.3	3.29	0.555	0.013	0.07234	0.00086	0.363	447.6	8.2	450.2	5.2	416	48	450.2	5.2	0.6	
SLAM1920_21.FIN2	65.3	5.22	0.66	0.03	0.0769	0.0016	0.106	511	18	477.5	9.7	630	100	477.5	9.7	6.6	
SLAM1920_22.FIN2	97.7	0.56	3.261	0.064	0.2548	0.0046	0.576	1471	16	1462	24	1474	34	1474.0	34.0	0.8	
SLAM1920_23.FIN2	62.7	1.77	1.844	0.05	0.1783	0.0036	0.509	1060	18	1057	19	1056	52	1056.0	52.0	0.1	
SLAM1920_24.FIN2	77.4	2.23	0.742	0.026	0.0893	0.0014	0.004	564	16	551.4	8.3	566	80	551.4	8.3	2.2	
SLAM1920_25.FIN2	143	1.63	0.402	0.013	0.0533	0.0011	0.208	341.5	9.2	334.4	6.7	387	69	334.4	6.7	2.1	
SLAM1920_26.FIN2	379	2.16	0.602	0.015	0.0785	0.0013	0.446	478.1	9.7	487.1	7.5	423	52	487.1	7.5	1.9	
SLAM1920_27.FIN2	406	1.23	0.2308	0.0056	0.03321	0.00043	0.323	211	4.7	210.6	2.7	204	50	210.6	2.7	0.2	
SLAM1920_28.FIN2	261	1.43	1.789	0.027	0.1755	0.0017	0.341	1040.6	9.7	1042.1	9.1	1026	29	1026.0	29.0	1.6	
SLAM1920_29.FIN2	860	0.91	0.2761	0.0057	0.03884	0.00038	0.194	247.3	4.6	245.6	2.4	252	47	245.6	2.4	0.7	
SLAM1920_30.FIN2	232.7	1.00	0.3286	0.0076	0.04524	0.00055	0.003	288.7	5.7	285.2	3.4	303	57	285.2	3.4	1.2	
SLAM1920_31.FIN2	699	1.28	0.3571	0.0052	0.04905	0.00036	0.274	310.2	3.9	308.7	2.2	311	31	308.7	2.2	0.5	
SLAM1920_32.FIN2	213.9	0.91	0.2527	0.0076	0.03504	0.00061	0.394	228.9	6.2	222	3.8	275	62	222.0	3.8	3.0	
SLAM1920_33.FIN2	380	1.39	0.301	0.019	0.02979	0.00082	0.181	266	15	189.2	5.1	1020	140	189.2	5.1	28.9	
SLAM1920_34.FIN2	389.1	1.59	0.2962	0.007	0.0416	0.00052	0.381	263.6	5.3	262.7	3.2	251	46	262.7	3.2	0.3	
SLAM1920_35.FIN2	771	3.04	0.3999	0.0059	0.0541	0.00048	0.452	341.2	4.3	339.6	2.9	349	31	339.6	2.9	0.5	
SLAM1920_36.FIN2	360	4.18	0.618	0.013	0.07907	0.00095	0.457	488.1	8.2	490.5	5.7	472	43	490.5	5.7	0.5	
SLAM1920_37.FIN2	133.5	1.49	0.1806	0.0098	0.02616	0.00053	0.192	167.8	8.4	166.4	3.3	180	100	166.4	3.3	0.8	
SLAM1920_38.FIN2	146.4	1.92	3.529	0.08	0.2718	0.0063	0.648	1533	20	1547	32	1502	34	1502.0	34.0	3.0	
SLAM1920_39.FIN2	1004	3.61	0.3798	0.0059	0.05132	0.00053	0.391	326.6	4.3	322.6	3.3	332	33	322.6	3.3	1.2	
SLAM1920_40.FIN2	237	1.25	0.344	0.011	0.0444	0.00072	0.188	299.2	8.7	280	4.4	426	74	280.0	4.4	6.4	
SLAM1920_41.FIN2	668	2.48	0.4104	0.0063	0.05577	0.00054	0.342	349.3	4.4	349.8	3.3	326	33	349.8	3.3	0.1	
SLAM1920_42.FIN2	484	1.57	0.3807	0.0063	0.05189	0.00059	0.362	327.2	4.6	326.6	3.7	325	39	326.6	3.7	0.2	
SLAM1920_43.FIN2	250	1.27	1.684	0.024	0.1678	0.0015	0.411	1001.5	9.1	999.7	8.2	1003	26	1003.0	26.0	0.3	
SLAM1920_44.FIN2	965	3.38	0.4318	0.0088	0.0577	0.0012	0.490	364.1	6.2	361.4	7.5	374	54	361.4	7.5	0.7	
SLAM1920_45.FIN2	306	1.32	0.4036	0.0091	0.05463	0.00064	0.235	343.6	6.5	342.8	3.9	333	50	342.8	3.9	0.2	
SLAM1920_46.FIN2	705	1.21	0.4443	0.007	0.06019	0.00057	0.345	372.9	4.9	376.7	3.5	342	35	376.7	3.5	1.0	
SLAM1920_47.FIN2	319	1.97	0.2773	0.0081	0.03866	0.00052	0.256	248	6.5	244.5	3.2	268	62	244.5	3.2	1.4	
SLAM1920_48.FIN2	550	1.38	0.2734	0.0053	0.0382	0.00049	0.217	245.1	4.2	241.6	3	262	45	241.6	3.0	1.4	
SLAM1920_50.FIN2	242	1.31	0.329	0.012	0.04355	0.00069	0.275	287.9	8.9	274.8	4.3	382	71	274.8	4.3	4.6	
SLAM1920_51.FIN2	303.3	1.53	1.534	0.038	0.1522	0.0029	0.533	943	15	913	16	1010	45	1010.0	45.0	9.6	
SLAM1920_52.FIN2	290	1.63	0.851	0.014	0.1019	0.001	0.121	624.5	7.7	625.7	5.9	611	40	625.7	5.9	0.2	
SLAM1920_53.FIN2	267.1	1.32	0.624	0.016	0.0741	0.0011	0.427	491	10	460.6	6.4	626	53	460.6	6.4	6.2	
SLAM1920_56.FIN2	2030	40.70	0.36	0.019	0.0508	0.0022	0.698	311	14	319	13	251	87	319.0	13.0	2.6	
SLAM1920_57.FIN2	264	1.71	0.377	0.01	0.05074	0.00072	0.365	323.6	7.5	319	4.4	339	56	319.0	4.4	1.4	
SLAM1920_58.FIN2	704	2.17	0.3829	0.0055	0.05289	0.00053	0.380	328.9	4	332.2	3.2	301	32	332.2	3.2	1.0	
SLAM1920_59.FIN2	358.4	3.72	0.598	0.011	0.07725	0.00071	0.352	475.1	7.2	479.6	4.2	443	40	479.6	4.2	0.9	
SLAM1920_60.FIN2	162.9	1.40	0.761	0.021	0.0935	0.0011	0.151	573	12	576	6.7	547	63	576.0	6.7	0.5	
SLAM1920_61.FIN2	610	0.70	0.5277	0.0096	0.06795	0.00087	0.496	429.8	6.4	423.7	5.2	452	36	423.7	5.2	1.4	

SLAM1920_62.FIN2	160.2	1.94	0.383	0.011	0.0525	0.0011	0.352	328.6	8.5	330	6.8	309	64	330.0	6.8	0.4	
SLAM1920_63.FIN2	680	1.90	0.589	0.012	0.0766	0.001	0.574	469.4	7.6	476	6	427	38	476.0	6.0	1.4	
SLAM1920_64.FIN2	31.5	1.67	0.225	0.021	0.0248	0.0013	0.267	204	17	158	8	610	180	158.0	8.0	22.5	
SLAM1920_65.FIN2	64.5	0.91	2.84	0.061	0.2374	0.0049	0.412	1364	16	1371	26	1339	45	1339.0	45.0	2.4	
SLAM1920_66.FIN2	297	1.29	0.2387	0.0057	0.03486	0.00041	0.193	217	4.7	220.9	2.6	180	52	220.9	2.6	1.8	
SLAM1920_67.FIN2	989	28.60	0.403	0.029	0.0551	0.0032	0.659	342	21	346	20	310	110	346.0	20.0	1.2	Rim
SLAM1920_67.FIN2	421	8.85	0.601	0.02	0.0782	0.0021	0.458	477	12	485	13	416	73	485.0	13.0	1.7	Core
SLAM1920_68.FIN2	107.5	0.82	0.853	0.022	0.1021	0.0013	0.233	624	12	626.6	7.5	596	56	626.6	7.5	0.4	
SLAM1920_69.FIN2	258.3	1.53	0.569	0.01	0.07338	0.00066	0.172	456.5	6.6	456.5	4	452	41	456.5	4.0	0.0	
SLAM1920_70.FIN2	240	0.94	0.366	0.0092	0.04929	0.00049	0.008	316	6.9	310.2	3	343	58	310.2	3.0	1.8	
SLAM1920_71.FIN2	331.8	1.68	0.416	0.01	0.05301	0.00079	0.220	352.5	7.2	333.6	4.7	466	56	333.6	4.7	5.4	
SLAM1920_72.FIN2	23.8	2.09	0.714	0.054	0.0866	0.0024	0.124	539	31	535	14	500	160	535.0	14.0	0.7	
SLAM1920_73.FIN2	200.3	1.27	6.585	0.072	0.3795	0.0046	0.696	2057.3	9.8	2073	21	2038	16	2038.0	16.0	1.7	
SLAM1920_74.FIN2	122.6	0.43	1.465	0.029	0.1534	0.0019	0.186	914	12	920	11	890	44	890.0	44.0	3.4	
SLAM1920_75.FIN2	240	1.87	0.385	0.011	0.05323	0.00089	0.262	329.8	7.9	334.2	5.4	301	61	334.2	5.4	1.3	
SLAM1920_76.FIN2	565	2.06	0.3777	0.0054	0.05169	0.00056	0.241	325.1	4	324.8	3.4	313	36	324.8	3.4	0.1	
SLAM1920_77.FIN2	1040	2.51	0.3655	0.0087	0.0501	0.0011	0.595	316.4	6.6	315.3	6.6	319	45	315.3	6.6	0.3	
SLAM1920_78.FIN2	297	1.59	1.018	0.018	0.1181	0.0014	0.470	711.6	8.9	719.2	7.8	675	34	719.2	7.8	1.1	
SLAM1920_79.FIN2	271.1	1.46	4.811	0.073	0.2921	0.004	0.640	1784	13	1651	20	1935	23	1935.0	23.0	14.7	
SLAM1920_80.FIN2	246.2	1.01	0.281	0.011	0.03165	0.00072	0.142	250.8	8.7	200.8	4.5	702	91	200.8	4.5	19.9	
SLAM1920_81.FIN2	352	1.89	0.3744	0.0082	0.05066	0.00073	0.299	323.4	6.3	318.5	4.5	346	52	318.5	4.5	1.5	
SLAM1920_82.FIN2	65.3	1.36	21.61	0.22	0.6351	0.0064	0.654	3165.8	9.7	3168	25	3155	13	3155.0	13.0	0.4	
SLAM1920_83.FIN2	267.5	2.09	10.79	0.16	0.4584	0.0059	0.717	2504	13	2431	26	2550	17	2550.0	17.0	4.7	
SLAM1920_84.FIN2	158.3	2.06	0.366	0.011	0.05028	0.0009	0.298	316.3	7.9	316.8	5.6	288	63	316.8	5.6	0.2	
SLAM1920_85.FIN2	67.6	0.64	8.94	0.28	0.395	0.013	0.641	2322	29	2149	61	2480	44	2480.0	44.0	13.3	
SLAM1920_86.FIN2	212	3.14	0.873	0.026	0.1049	0.0028	0.624	639	15	643	16	614	58	643.0	16.0	0.6	
SLAM1920_87.FIN2	293.7	0.84	0.286	0.011	0.0353	0.001	0.449	254.8	8.6	223.5	6.4	529	76	223.5	6.4	12.3	
SLAM1920_88.FIN2	552	1.15	0.261	0.0091	0.03701	0.00095	0.225	235.2	7.3	234.3	5.9	232	81	234.3	5.9	0.4	
SLAM1920_89.FIN2	372	1.51	0.452	0.011	0.05596	0.00098	0.335	377.6	7.6	350.9	6	531	56	350.9	6.0	7.1	
SLAM1920_90.FIN2	161.6	8.84	0.39	0.02	0.0527	0.0022	0.086	332	15	331	14	320	120	331.0	14.0	0.3	
SLAM1920_91.FIN2	954	3.98	0.4042	0.0058	0.05378	0.00069	0.421	344.9	4.3	337.7	4.2	383	34	337.7	4.2	2.1	
SLAM1920_92.FIN2	133.3	1.52	4.74	0.099	0.3191	0.0062	0.506	1771	17	1784	30	1755	34	1755.0	34.0	1.7	
SLAM1920_93.FIN2	773	1.86	0.402	0.012	0.0539	0.0017	0.567	341.8	8.9	338	10	374	62	338.0	10.0	1.1	
SLAM1920_94.FIN2	608	1.68	0.3917	0.0065	0.05226	0.00042	0.302	335.2	4.7	328.4	2.6	361	36	328.4	2.6	2.0	
SLAM1920_95.FIN2	606	1.11	0.375	0.006	0.0513	0.0004	0.299	323	4.5	322.5	2.5	307	36	322.5	2.5	0.2	
SLAM1920_96.FIN2	51.67	0.35	5.81	0.17	0.3567	0.0082	0.234	1944	25	1965	39	1914	58	1914.0	58.0	2.7	
SLAM1920_97.FIN2	308	1.28	0.2283	0.0057	0.03318	0.00034	0.223	208.3	4.7	210.4	2.1	170	50	210.4	2.1	1.0	
SLAM1920_98.FIN2	490	58.00	0.3931	0.0086	0.05363	0.00069	0.440	336.3	6.3	336.7	4.2	315	44	336.7	4.2	0.1	Rim
SLAM1920_98.FIN2	215.2	2.03	0.92	0.023	0.107	0.0017	0.120	662	12	655	10	669	59	655.0	10.0	1.1	Core
SLAM1920_100.FIN2	0.63	0.21	148	39	1.24	0.35	0.990	5080	280	5400	1100	5120	110	5120.0	110.0	5.5	

Sample Name:	SLAm1922							207/235		206/238		207/206		Best age			
Grain #	[U] ppm	U/Th	207/235	2σ error	206/238	2σ error	RHO	Age Ma	2σ error	Age (Ma)	2σ error	Age (Ma)	2σ error	(Ma)	2σ error	% Disc.	Rim/Core
SLAM1922_1.FIN2	71.7	0.78	0.828	0.035	0.0979	0.0028	0.278	608	20	602	16	621	92	602.0	16.0	1.0	
SLAM1922_2.FIN2	536	10.40	0.812	0.082	0.089	0.012	0.864	602	47	549	74	840	150	549.0	74.0	8.8	Rim
SLAM1922_2.FIN2	389	0.92	10.22	0.28	0.3956	0.0076	0.696	2447	25	2146	35	2715	31	2715.0	31.0	21.0	Core
SLAM1922_3.FIN2	292.6	3.68	2.001	0.084	0.1882	0.0078	0.280	1113	29	1111	42	1100	110	1100.0	110.0	1.0	Rim
SLAM1922_3.FIN2	202	3.59	4.95	0.17	0.2914	0.0077	0.635	1803	29	1647	39	1995	48	1995.0	48.0	17.4	Core
SLAM1922_4.FIN2	70.8	1.74	1.697	0.036	0.1657	0.0019	0.405	1005	14	988	11	1048	39	1048.0	39.0	5.7	
SLAM1922_5.FIN2	144	2.10	0.776	0.018	0.0938	0.0012	0.282	581	10	578.1	6.9	587	51	578.1	6.9	0.5	
SLAM1922_6.FIN2	53.5	1.02	1.693	0.049	0.1684	0.0026	0.222	1001	18	1003	14	996	64	996.0	64.0	0.7	
SLAM1922_7.FIN2	145.2	1.69	6.89	0.14	0.3784	0.0059	0.748	2092	19	2067	28	2124	25	2124.0	25.0	2.7	
SLAM1922_8.FIN2	210	1.39	1.708	0.033	0.1627	0.0026	0.618	1009	12	971	14	1096	32	1096.0	32.0	11.4	
SLAM1922_9.FIN2	604	12.25	0.7	0.037	0.0855	0.002	0.325	538	22	529	12	590	110	529.0	12.0	1.7	Rim
SLAM1922_9.FIN2	40.1	0.83	8.87	0.19	0.4027	0.0067	0.704	2323	20	2180	31	2451	26	2451.0	26.0	11.1	Core
SLAM1922_10.FIN2	117.5	3.23	1.212	0.022	0.131	0.0016	0.316	804.1	9.9	793.2	9.1	836	36	793.2	9.1	1.4	
SLAM1922_11.FIN2	235.6	1.15	0.3154	0.0092	0.04211	0.0006	0.752	277.7	7.1	265.9	3.7	374	65	265.9	3.7	4.2	
SLAM1922_12.FIN2	22.44	1.87	0.88	0.042	0.1037	0.002	0.035	633	23	637	12	590	110	637.0	12.0	0.6	
SLAM1922_13.FIN2	105.8	1.35	9.01	0.19	0.4183	0.0072	0.882	2331	21	2250	33	2416	20	2416.0	20.0	6.9	
SLAM1922_14.FIN2	20.24	1.04	1.059	0.048	0.1171	0.0026	0.128	729	25	713	15	750	100	713.0	15.0	2.2	
SLAM1922_15.FIN2	107.5	1.22	0.882	0.021	0.1029	0.0015	0.354	643	11	631	8.9	674	49	631.0	8.9	1.9	
SLAM1922_16.FIN2	134.5	0.79	1.645	0.031	0.1636	0.0022	0.398	987	12	976	12	1014	37	1014.0	37.0	3.7	
SLAM1922_17.FIN2	274	2.16	0.905	0.023	0.1094	0.0022	0.648	652	12	669	13	600	44	669.0	13.0	2.6	
SLAM1922_18.FIN2	75.5	1.41	1.703	0.04	0.1682	0.0021	0.305	1007	15	1002	12	1017	46	1017.0	46.0	1.5	
SLAM1922_19.FIN2	72.1	1.36	1.691	0.04	0.1654	0.0023	0.168	1002	15	986	13	1046	53	1046.0	53.0	5.7	
SLAM1922_20.FIN2	395	5.61	0.879	0.024	0.1105	0.0027	0.616	639	13	677	16	515	50	677.0	16.0	5.9	
SLAM1922_21.FIN2	120.3	1.55	0.397	0.012	0.05407	0.00083	0.186	338	8.9	339.4	5.1	308	68	339.4	5.1	0.4	
SLAM1922_22.FIN2	256	5.20	0.781	0.054	0.0845	0.005	0.433	585	30	523	30	840	140	523.0	30.0	10.6	Rim
SLAM1922_22.FIN2	443	0.82	4.353	0.08	0.3021	0.0058	0.823	1704	16	1700	29	1717	21	1717.0	21.0	1.0	Core
SLAM1922_23.FIN2	167	2.03	1.639	0.032	0.1628	0.0019	0.375	982	12	972	11	1007	38	1007.0	38.0	3.5	
SLAM1922_24.FIN2	249	32.00	1.12	0.025	0.1175	0.0021	0.047	761	12	716	12	897	58	716.0	12.0	5.9	
SLAM1922_25.FIN2	777	6.76	0.783	0.012	0.0934	0.0013	0.603	586.4	6.7	575.6	7.4	633	27	575.6	7.4	1.8	
SLAM1922_26.FIN2	130.7	0.94	1.659	0.031	0.1638	0.0025	0.580	994	12	977	14	1029	33	1029.0	33.0	5.1	
SLAM1922_27.FIN2	927	19.90	0.799	0.061	0.1008	0.008	0.732	591	33	617	46	530	120	617.0	46.0	4.4	Rim
SLAM1922_27.FIN2	535	1.62	4.69	0.21	0.309	0.014	0.777	1750	39	1728	70	1799	54	1799.0	54.0	3.9	Core
SLAM1922_28.FIN2	110.6	1.06	4.099	0.078	0.2608	0.0048	0.663	1652	15	1492	25	1859	29	1859.0	29.0	19.7	
SLAM1922_29.FIN2	104.6	0.50	0.745	0.018	0.0881	0.0012	0.337	563	11	544.4	6.9	630	52	544.4	6.9	3.3	
SLAM1922_30.FIN2	126.4	1.57	0.882	0.017	0.1067	0.0011	0.223	640.7	8.9	653.3	6.3	594	43	653.3	6.3	2.0	
SLAM1922_31.FIN2	113	1.75	1.498	0.045	0.1427	0.0042	0.712	926	18	859	23	1096	43	1096.0	43.0	21.6	
SLAM1922_32.FIN2	45.5	1.21	0.289	0.015	0.04226	0.00088	0.063	255	12	266.8	5.4	180	110	266.8	5.4	4.6	
SLAM1922_33.FIN2	50.1	0.77	5.61	0.097	0.3314	0.0044	0.470	1914	15	1847	22	1994	29	1994.0	29.0	7.4	
SLAM1922_34.FIN2	72.7	1.90	0.863	0.025	0.1038	0.0016	0.227	629	14	636.3	9.2	584	64	636.3	9.2	1.2	
SLAM1922_35.FIN2	147.2	1.57	0.74	0.016	0.08999	0.00091	0.176	561.7	9.2	555.4	5.4	570	49	555.4	5.4	1.1	
SLAM1922_36.FIN2	212	4.70	1.214	0.028	0.1311	0.0023	0.541	805	13	794	13	836	40	794.0	13.0	1.4	
SLAM1922_37.FIN2	401	6.45	1.041	0.034	0.1165	0.0033	0.645	719	17	709	19	753	54	709.0	19.0	1.4	
SLAM1922_38.FIN2	322	2.70	0.644	0.012	0.08097	0.00078	0.205	505.3	7.1	501.8	4.7	507	40	501.8	4.7	0.7	
SLAM1922_39.FIN2	477	1.94	4.42	0.11	0.2828	0.0057	0.826	1711	20	1604	29	1844	24	1844.0	24.0	13.0	Core
SLAM1922_40.FIN2	66.2	0.47	5.375	0.096	0.3249	0.0054	0.630	1876	16	1811	26	1963	27	1963.0	27.0	7.7	
SLAM1922_41.FIN2	657	4.17	0.484	0.02	0.0702	0.0031	0.609	402	14	437	19	229	80	437.0	19.0	8.7	
SLAM1922_42.FIN2	571	5.94	7.02	0.14	0.404	0.0052	0.801	2113	18	2186	24	2042	23	2042.0	23.0	7.1	
SLAM1922_43.FIN2	333.6	23.20	0.872	0.015	0.1008	0.0011	0.454	635.6	8.2	618.7	6.6	695	35	618.7	6.6	2.7	
SLAM1922_44.FIN2	136.8	2.57	0.831	0.018	0.0992	0.0013	0.346	612	10	609.7	7.5	611	47	609.7	7.5	0.4	
SLAM1922_45.FIN2	104.6	1.09	0.913	0.02	0.107	0.0011	0.210	656	11	655.1	6.5	647	48	655.1	6.5	0.1	
SLAM1922_46.FIN2	292	1.53	0.3046	0.008	0.04132	0.00058	0.361	269.3	6.2	261.5	3.7	334	54	261.5	3.7	2.9	
SLAM1922_47.FIN2	353	1.91	0.958	0.013	0.1127	0.0011	0.444	681.6	6.9	688.4	6.6	656	28	688.4	6.6	1.0	
SLAM1922_48.FIN2	81.4	1.64	10.92	0.27	0.4577	0.0096	0.892	2507	23	2424	43	2578	19	2578.0	19.0	6.0	
SLAM1922_49.FIN2	136	3.25	0.835	0.027	0.0937	0.0021	0.393	616	16	577	12	750	72	577.0	12.0	6.3	
SLAM1922_50.FIN2	111.3	3.04	1.981	0.096	0.1818	0.0067	0.493	1093	33	1078	37	1097	91	1097.0	91.0	1.7	
SLAM1922_51.FIN2	412	1.92	0.771	0.015	0.0941	0.0013	0.489	578.8	8.5	579.4	7.9	565	38	579.4	7.9	0.1	
SLAM1922_52.FIN2	112	2.26	1.007	0.023	0.1158	0.0017	0.406	705	11	706	10	692	46	706.0	10.0	0.1	
SLAM1922_53.FIN2	127.1	2.71	1.798	0.043	0.1688	0.0036	0.574	1042	16	1005	20	1108	43	1108.0	43.0	9.3	
SLAM1922_54.FIN2	315	6.91	13.57	0.38	0.516	0.014	0.697	2713	26	2675	60	2744	34	2744.0	34.0	2.5	
SLAM1922_55.FIN2	167.6	1.35	0.309	0.013	0.0448	0.0013	0.664	271.7	9.7	282.6	8.1	187	69	282.6	8.1	4.0	
SLAM1922_56.FIN2	121.1	1.26	1.136	0.045	0.1229	0.0035	0.607	765	21	750	21	801	65	750.0	21.0	2.0	
SLAM1922_57.FIN2	751	3.27	1.733	0.029	0.1753	0.002	0.720	1019	11	1041	11	965	22	965.0	22.0	7.9	
SLAM1922_58.FIN2	408	10.49	11.44	0.18	0.4904	0.0074	0.781	2558	15	2570	32	2542	19	2542.0	19.0	1.1	
SLAM1922_59.FIN2	69.1	0.73	1.618	0.037	0.1606	0.0026	0.341	976	15	959	14	1011	49	1011.0	49.0	5.1	

SLAM1922_60.FIN2	563	0.98	3.02	0.14	0.2134	0.0099	0.749	1409	35	1246	52	1673	59	1673.0	59.0	25.5	Rim
SLAM1922_60.FIN2	168.6	0.85	5.091	0.084	0.3382	0.0044	0.665	1834	15	1877	21	1782	26	1782.0	26.0	5.3	Core
SLAM1922_61.FIN2	220.1	2.61	1.389	0.058	0.1553	0.0052	0.777	876	25	928	29	741	57	741.0	29.0	5.9	
SLAM1922_62.FIN2	134.8	1.25	1.926	0.072	0.1774	0.0059	0.709	1079	25	1050	32	1155	55	1155.0	55.0	9.1	
SLAM1922_63.FIN2	201	3.91	0.823	0.023	0.093	0.0023	0.519	607	13	573	13	728	55	573.0	13.0	5.6	
SLAM1922_64.FIN2	91.7	2.22	1.62	0.034	0.158	0.0024	0.560	977	13	947	14	1040	36	1040.0	36.0	8.9	
SLAM1922_65.FIN2	343.6	1.40	0.925	0.033	0.1054	0.0025	0.618	661	17	645	15	699	61	645.0	15.0	2.4	
SLAM1922_66.FIN2	120.8	4.57	0.905	0.047	0.1083	0.0052	0.482	644	25	661	30	590	100	661.0	30.0	2.6	
SLAM1922_67.FIN2	594	13.31	1.682	0.05	0.1693	0.0044	0.660	995	20	1006	24	975	47	975.0	47.0	3.2	
SLAM1922_68.FIN2	311	23.80	1.026	0.024	0.1153	0.0021	0.512	714	12	703	12	761	43	703.0	12.0	1.5	
SLAM1922_69.FIN2	34.2	1.04	1.829	0.059	0.1872	0.0057	0.463	1050	21	1104	31	939	69	939.0	69.0	17.6	
SLAM1922_70.FIN2	294.6	1.64	0.987	0.016	0.113	0.0014	0.555	696.1	8.3	690	8.3	710	32	690.0	8.3	0.9	
SLAM1922_71.FIN2	124.6	1.59	6.287	0.078	0.3618	0.0036	0.549	2015	11	1990	17	2040	19	2040.0	19.0	2.5	
SLAM1922_72.FIN2	111	0.93	0.83	0.036	0.0876	0.0022	0.487	609	21	541	13	847	80	541.0	13.0	11.2	
SLAM1922_73.FIN2	83.5	1.62	5.38	0.17	0.339	0.011	0.743	1868	28	1874	52	1875	42	1875.0	42.0	0.1	
SLAM1922_74.FIN2	235.3	10.69	0.962	0.021	0.111	0.0019	0.531	682	11	678	11	687	43	678.0	11.0	0.6	
SLAM1922_75.FIN2	183	1.54	1.015	0.033	0.1147	0.0029	0.506	708	16	699	16	718	63	699.0	16.0	1.3	
SLAM1922_76.FIN2	275.1	1.14	1.208	0.044	0.128	0.003	0.652	797	20	776	17	846	54	776.0	17.0	2.6	
SLAM1922_77.FIN2	324	3.03	1.153	0.02	0.1246	0.0021	0.525	778.1	9.4	756	12	832	37	756.0	12.0	2.8	
SLAM1922_78.FIN2	219	1.63	1.59	0.076	0.1435	0.005	0.740	959	29	864	28	1179	62	1179.0	62.0	26.7	
SLAM1922_79.FIN2	411	2.53	1.396	0.025	0.1439	0.0022	0.658	885	10	866	12	926	28	926.0	28.0	6.5	
SLAM1922_80.FIN2	304	1.63	1.162	0.022	0.1257	0.0022	0.662	782	10	763	12	832	34	763.0	12.0	2.4	
SLAM1922_81.FIN2	124	1.46	0.759	0.028	0.0985	0.0023	0.502	569	16	605	13	421	65	605.0	13.0	6.3	
SLAM1922_82.FIN2	92	2.46	0.841	0.023	0.0986	0.0014	0.281	618	13	606.1	8.5	668	57	606.1	8.5	1.9	
SLAM1922_84.FIN2	234	1.10	4.47	0.12	0.3023	0.0077	0.779	1720	21	1700	38	1744	31	1744.0	31.0	2.5	
SLAM1922_85.FIN2	179.2	1.98	0.895	0.016	0.1046	0.0011	0.363	647.8	8.3	641.2	6.3	664	34	641.2	6.3	1.0	
SLAM1922_86.FIN2	209.9	1.08	6.268	0.079	0.3643	0.0045	0.670	2013	11	2001	21	2019	18	2019.0	18.0	0.9	
SLAM1922_87.FIN2	108.8	1.31	0.931	0.021	0.1094	0.0015	0.312	666	11	669.2	9	639	51	669.2	9.0	0.5	
SLAM1922_88.FIN2	77.7	1.32	1.593	0.068	0.1605	0.0049	0.515	960	27	962	27	978	75	978.0	75.0	1.6	
SLAM1922_89.FIN2	34.8	2.44	0.867	0.035	0.0991	0.0018	0.112	629	19	609	11	666	89	609.0	11.0	3.2	
SLAM1922_90.FIN2	342	3.02	1.821	0.039	0.1784	0.0045	0.687	1049	14	1060	25	1029	40	1029.0	40.0	3.0	
SLAM1922_91.FIN2	42.5	0.57	1.302	0.048	0.1396	0.0025	0.257	842	22	842	14	827	77	842.0	14.0	0.0	
SLAM1922_92.FIN2	368	2.42	1.447	0.069	0.1423	0.0064	0.660	909	30	858	37	1035	81	1035.0	81.0	17.1	
SLAM1922_93.FIN2	548	37.50	0.675	0.012	0.0939	0.0019	0.590	522.8	7.2	578	11	290	38	578.0	11.0	10.6	
SLAM1922_94.FIN2	115.4	1.22	1.521	0.04	0.1573	0.0029	0.510	934	16	941	16	906	47	906.0	47.0	3.9	
SLAM1922_95.FIN2	119.1	0.54	1.676	0.033	0.1673	0.0022	0.312	998	12	997	12	991	38	991.0	38.0	0.6	
SLAM1922_96.FIN2	236.3	1.52	0.873	0.015	0.1031	0.001	0.305	636.3	8.3	632.3	6.1	639	38	632.3	6.1	0.6	
SLAM1922_98.FIN2	78.5	0.71	0.826	0.025	0.1006	0.002	0.291	608	14	617	12	567	69	617.0	12.0	1.5	
SLAM1922_99.FIN2	234	1.78	1.851	0.026	0.1815	0.0018	0.434	1063.2	9.1	1075	9.6	1038	26	1038.0	26.0	3.6	
SLAM1922_100.FIN2	228.3	1.77	0.923	0.015	0.10694	0.00088	0.219	662.9	7.7	654.9	5.1	678	34	654.9	5.1	1.2	
SLAM1922_101.FIN2	168.9	2.15	1.402	0.051	0.1471	0.0051	0.529	882	22	883	29	892	67	892.0	67.0	1.0	
SLAM1922_102.FIN2	236.2	2.29	11	0.13	0.4529	0.0043	0.656	2521	11	2407	19	2608	14	2608.0	14.0	7.7	
SLAM1922_103.FIN2	94.2	0.89	1.216	0.028	0.1328	0.0017	0.334	805	13	803.6	9.6	800	45	803.6	9.6	0.2	
SLAM1922_104.FIN2	212.7	1.92	11.281	0.098	0.4726	0.0042	0.633	2545.7	8.1	2494	18	2579	12	2579.0	12.0	3.3	
SLAM1922_105.FIN2	225.4	0.78	1.371	0.031	0.1469	0.0024	0.329	875	13	884	13	841	48	841.0	13.0	1.0	
SLAM1922_106.FIN2	427	1.39	0.776	0.013	0.0942	0.0013	0.615	582.3	7.6	580.3	7.5	583	31	580.3	7.5	0.3	
SLAM1922_107.FIN2	693	13.10	5.77	0.15	0.3618	0.0072	0.782	1941	22	1990	34	1887	29	1887.0	29.0	5.5	Rim
SLAM1922_107.FIN2	217	1.76	7.142	0.08	0.3988	0.0035	0.650	2128	10	2163	16	2089	14	2089.0	14.0	3.5	Core
SLAM1922_108.FIN2	335	2.71	1.233	0.027	0.1321	0.0021	0.556	814	12	800	12	840	41	800.0	12.0	1.7	
SLAM1922_109.FIN2	135.6	0.41	5.81	0.12	0.3562	0.0067	0.687	1944	18	1961	32	1926	29	1926.0	29.0	1.8	
SLAM1922_110.FIN2	265	0.99	6.23	0.19	0.371	0.0098	0.925	1996	26	2028	46	1967	21	1967.0	21.0	3.1	
SLAM1922_111.FIN2	178.7	1.62	1.808	0.032	0.1727	0.0024	0.513	1047	12	1028	13	1082	33	1082.0	33.0	5.0	
SLAM1922_112.FIN2	116.7	1.49	0.844	0.018	0.101	0.0012	0.234	619.3	9.8	620.1	6.8	591	47	620.1	6.8	0.1	
SLAM1922_113.FIN2	284	1.61	6.899	0.089	0.3839	0.0042	0.629	2097	11	2093	20	2092	17	2092.0	17.0	0.0	
SLAM1922_114.FIN2	112	2.37	17.7	0.24	0.568	0.0084	0.739	2970	13	2896	35	3017	17	3017.0	17.0	4.0	
SLAM1922_115.FIN2	296.6	0.99	2.148	0.035	0.1727	0.0025	0.650	1165	12	1027	14	1420	25	1420.0	25.0	27.7	
SLAM1922_116.FIN2	273.8	1.22	0.788	0.011	0.09635	0.00088	0.257	589.5	6.4	593.5	5.3	557	33	593.5	5.3	0.7	
SLAM1922_117.FIN2	92.9	2.32	1.788	0.049	0.1735	0.0034	0.624	1037	18	1030	19	1046	42	1046.0	42.0	1.5	
SLAM1922_118.FIN2	126.5	3.93	0.874	0.018	0.1045	0.0013	0.334	637.1	9.2	640.8	7.4	595	43	640.8	7.4	0.6	
SLAM1922_119.FIN2	800	37.50	0.879	0.019	0.1054	0.0022	0.751	641	10	646	13	615	35	646.0	13.0	0.8	
SLAM1922_120.FIN2	188	9.10	14.39	0.22	0.5394	0.0082	0.705	2774	15	2782	34	2766	18	2766.0	18.0	0.6	
SLAM1922_121.FIN2	80.6	0.61	0.756	0.026	0.0926	0.0023	0.442	569	16	570	14	529	71	570.0	14.0	0.2	
SLAM1922_122.FIN2	227	0.97	1.676	0.027	0.1666	0.0021	0.558	999	10	993	12	994	30	994.0	30.0	0.1	
SLAM1922_123.FIN2	227.4	1.18	10.51	0.23	0.4328	0.0093	0.728	2481	19	2314	42	2611	28	2611.0	28.0	11.4	
SLAM1922_124.FIN2	472	3.19	12.21	0.22	0.526	0.01	0.664	2619	17	2721	42	2529	26	2529.0	26.0	7.6	
SLAM1922_125.FIN2	314	75.00	0.88	0.035	0.1029	0.0034	0.336	640	19	631	20	630	100	631.0	20.0	1.4	Rim
SLAM1922_125.FIN2	128.1	1.42	1.794	0.036	0.1765	0.0026	0.183	1041	13	1047	14	1010	46	1010.0	46.0	3.7	Core
SLAM1922_126.FIN2	103.6	0.98	0.78	0.022	0.0957	0.0013	0.249	583	12	588.9	7.9	526	61	588.9	7.9	1.0	
SLAM1922_127.FIN2	167.5	0.82	0.811	0.016	0.098	0.001	0.258	601.3	8.8	602.6	5.9	571	43	602.6	5.9	0.2	
SLAM1922_128.FIN2	268	1.30	13.19	0.17	0.519	0.0066	0.810	2692	12	2696	27	2680	15	2680.0	15.0	0.6	
SLAM1922_129.FIN2	470	8.00	10.09	0.16	0.4696	0.0064	0.761	2442	15	2480	28	2398	19	2398.0	19.0	3.4	
SLAM1922_130.FIN2	377.5	10.47	9.53	0.13	0.4567	0.0074	0.651	2389	13	2426	34	2349	23	2349.0	23.0	3.3	

Sample Name:	SLAm1925							207/235		206/238		207/206		Best age			
Grain #	[U] ppm	U/Th	207/235	2σ error	206/238	2σ error	RHO	Age Ma	2σ error	Age (Ma)	2σ error	Age (Ma)	2σ error	(Ma)	2σ error	% Disc.	Rim/Core
SLAM1925_1.FIN2	427	2.97	2.078	0.081	0.1796	0.0048	0.831	1135	29	1064	26	1259	49	1259.0	49.0	15.5	
SLAM1925_2.FIN2	970	1.60	1.106	0.019	0.1162	0.0022	0.549	755.6	9.1	708	13	878	36	708.0	13.0	6.3	
SLAM1925_3.FIN2	45.7	0.97	1.055	0.032	0.1201	0.0016	0.184	730	15	730.9	9.2	707	65	730.9	9.2	0.1	
SLAM1925_4.FIN2	206	1.76	1.425	0.038	0.1484	0.0032	0.484	896	16	891	18	895	52	895.0	52.0	0.4	
SLAM1925_5.FIN2	777	5.15	0.943	0.012	0.10985	0.00093	0.241	674	6	671.8	5.4	666	28	671.8	5.4	0.3	
SLAM1925_6.FIN2	93.3	0.38	11.78	0.16	0.4896	0.0065	0.662	2585	13	2568	28	2589	19	2589.0	19.0	0.8	
SLAM1925_7.FIN2	224	2.24	1.036	0.02	0.1191	0.0015	0.373	721.2	9.8	725.5	8.7	703	36	725.5	8.7	0.6	
SLAM1925_8.FIN2	150.2	1.39	0.955	0.034	0.1024	0.0021	0.090	679	18	629	12	825	82	629.0	12.0	7.4	
SLAM1925_9.FIN2	92.5	3.31	0.938	0.031	0.1089	0.0019	0.165	672	17	666	11	660	79	666.0	11.0	0.9	
SLAM1925_10.FIN2	143.1	1.76	0.768	0.02	0.0945	0.0011	0.236	577	11	582.3	6.6	528	56	582.3	6.6	0.9	
SLAM1925_11.FIN2	223	1.61	0.861	0.016	0.1025	0.001	0.293	629.8	8.6	628.9	6	609	40	628.9	6.0	0.1	
SLAM1925_12.FIN2	548	1.93	0.931	0.017	0.1075	0.0018	0.433	667.5	9.2	658	11	678	44	658.0	11.0	1.4	
SLAM1925_13.FIN2	257	1.26	0.814	0.021	0.0949	0.0015	0.417	603	12	584.5	8.7	654	50	584.5	8.7	3.1	
SLAM1925_14.FIN2	115.9	0.93	16.47	0.13	0.5612	0.0041	0.472	2903.9	7.3	2873	16	2917	12	2917.0	12.0	1.5	
SLAM1925_15.FIN2	78.2	0.62	13.59	0.25	0.5206	0.008	0.746	2719	17	2700	34	2726	21	2726.0	21.0	1.0	
SLAM1925_16.FIN2	389	1.25	1.426	0.038	0.1416	0.0022	0.559	898	16	854	12	993	45	993.0	45.0	14.0	
SLAM1925_17.FIN2	479	1.16	0.893	0.013	0.10478	0.00096	0.389	648.5	7.3	642.3	5.6	651	31	642.3	5.6	1.0	
SLAM1925_18.FIN2	78.1	1.76	0.99	0.03	0.1136	0.0017	0.237	699	15	694	10	703	68	694.0	10.0	0.7	
SLAM1925_19.FIN2	188	2.48	0.955	0.02	0.1126	0.0013	0.173	681	11	687.9	7.7	635	49	687.9	7.7	1.0	
SLAM1925_20.FIN2	550	1.95	11.55	0.26	0.4982	0.0082	0.760	2560	21	2602	36	2526	26	2526.0	26.0	3.0	
SLAM1925_21.FIN2	340	4.57	0.852	0.013	0.1025	0.0011	0.473	625	7.3	628.9	6.6	593	31	628.9	6.6	0.6	
SLAM1925_22.FIN2	176.6	7.25	0.893	0.021	0.1057	0.0021	0.378	646	11	647	12	626	54	647.0	12.0	0.2	
SLAM1925_23.FIN2	114.6	0.68	0.715	0.032	0.0845	0.003	0.528	543	19	522	18	613	83	522.0	18.0	3.9	
SLAM1925_24.FIN2	140.2	0.64	9.49	0.15	0.4475	0.006	0.567	2385	14	2383	27	2380	23	2380.0	23.0	0.1	
SLAM1925_25.FIN2	79.8	1.54	0.886	0.038	0.0993	0.0026	0.342	640	21	610	15	723	91	610.0	15.0	4.7	
SLAM1925_27.FIN2	373	0.80	2.023	0.053	0.1665	0.0035	0.638	1120	18	992	19	1361	42	1361.0	42.0	27.1	
SLAM1925_28.FIN2	600	15.20	0.71	0.11	0.089	0.013	0.850	545	65	548	77	520	440	548.0	77.0	0.6	Rim
SLAM1925_28.FIN2	216.8	1.40	7.77	0.12	0.409	0.0076	0.658	2203	14	2208	34	2193	24	2193.0	24.0	0.7	Core
SLAM1925_29.FIN2	299	3.87	27.45	0.26	0.7224	0.0067	0.657	3398.3	9.2	3507	26	3332	13	3332.0	13.0	5.3	
SLAM1925_30.FIN2	86.7	0.41	10.91	0.19	0.4799	0.0078	0.554	2513	16	2525	34	2499	26	2499.0	26.0	1.0	
SLAM1925_31.FIN2	113.5	0.30	0.808	0.022	0.095	0.0015	0.338	599	13	584.8	8.7	634	58	584.8	8.7	2.4	
SLAM1925_32.FIN2	200	0.82	0.742	0.037	0.0791	0.0024	0.694	559	22	490	14	861	75	490.0	14.0	12.3	
SLAM1925_33.FIN2	138	1.96	2.531	0.057	0.1935	0.0029	0.551	1278	16	1140	16	1510	36	1510.0	36.0	24.5	
SLAM1925_34.FIN2	384	3.49	8.75	0.33	0.435	0.013	0.805	2295	36	2328	57	2278	41	2278.0	41.0	2.2	
SLAM1925_35.FIN2	358.7	0.66	0.801	0.012	0.0953	0.0011	0.291	596.7	7	586.8	6.3	630	36	586.8	6.3	1.7	
SLAM1925_36.FIN2	492.5	2.34	1.076	0.022	0.1157	0.0018	0.472	742	11	706	10	852	42	706.0	10.0	4.9	
SLAM1925_37.FIN2	997	20.80	0.954	0.016	0.1129	0.0016	0.652	679.9	8.2	689.5	9.5	651	26	689.5	9.5	1.4	
SLAM1925_39.FIN2	91.2	-1.00	17.39	0.43	0.599	0.014	0.649	2951	24	3021	58	2903	34	2903.0	34.0	4.1	
SLAM1925_40.FIN2	129.9	0.65	0.875	0.022	0.1062	0.0019	0.323	636	12	650	11	568	56	650.0	11.0	2.2	
SLAM1925_42.FIN2	28.8	0.95	0.823	0.041	0.0983	0.0029	0.275	603	23	604	17	570	110	604.0	17.0	0.2	
SLAM1925_43.FIN2	754	6.80	9.97	0.19	0.455	0.01	0.483	2428	18	2412	46	2437	37	2437.0	37.0	1.0	
SLAM1925_44.FIN2	223.5	1.10	1.36	0.033	0.1476	0.0031	0.480	869	14	887	17	821	49	821.0	17.0	2.1	
SLAM1925_45.FIN2	251	1.04	1.686	0.035	0.168	0.0026	0.485	1003	14	1000	15	1008	38	1008.0	38.0	0.8	
SLAM1925_46.FIN2	94.7	0.60	0.781	0.027	0.0913	0.0021	0.396	583	15	563	13	647	71	563.0	13.0	3.4	
SLAM1925_47.FIN2	417	3.76	1.215	0.018	0.1337	0.0017	0.457	806.2	8.1	808.9	9.5	789	31	808.9	9.5	0.3	
SLAM1925_48.FIN2	211	1.32	0.98	0.028	0.1118	0.002	0.624	692	15	683	11	714	49	683.0	11.0	1.3	
SLAM1925_49.FIN2	195	2.12	0.843	0.019	0.0989	0.0016	0.184	619	11	607.8	9.4	649	55	607.8	9.4	1.8	
SLAM1925_50.FIN2	157.8	1.08	1.875	0.042	0.189	0.0043	0.515	1070	15	1114	23	991	47	991.0	47.0	12.4	
SLAM1925_51.FIN2	88.5	1.71	17	0.25	0.5947	0.0087	0.664	2932	14	3011	36	2885	19	2885.0	19.0	4.4	
SLAM1925_52.FIN2	88.2	1.68	1.695	0.055	0.1558	0.005	0.681	1003	21	932	28	1166	58	1166.0	58.0	20.1	
SLAM1925_53.FIN2	448	10.24	1.221	0.023	0.1312	0.0021	0.452	809	10	795	12	845	39	795.0	12.0	1.7	
SLAM1925_54.FIN2	50.8	3.11	0.942	0.031	0.1118	0.002	0.226	672	17	683	11	621	76	683.0	11.0	1.6	
SLAM1925_55.FIN2	392	18.59	0.961	0.015	0.1141	0.0018	0.459	682.8	7.7	696	10	642	36	696.0	10.0	1.9	
SLAM1925_56.FIN2	526	1.78	0.95	0.015	0.109	0.0018	0.504	677.2	8	667	10	719	32	667.0	10.0	1.5	
SLAM1925_57.FIN2	53	0.95	1.659	0.041	0.1655	0.0026	0.322	989	15	987	14	997	53	997.0	53.0	1.0	
SLAM1925_58.FIN2	129.5	1.61	4.97	0.19	0.32	0.011	0.792	1803	33	1785	56	1839	46	1839.0	46.0	2.9	
SLAM1925_59.FIN2	900	11.60	0.382	0.026	0.0404	0.003	0.493	328	19	255	19	900	150	255.0	19.0	22.3	Rim
SLAM1925_59.FIN2	246	1.85	5.242	0.089	0.3223	0.0062	0.636	1858	15	1799	30	1929	27	1929.0	27.0	6.7	Core
SLAM1925_60.FIN2	94.7	3.43	0.846	0.025	0.1013	0.0031	0.416	619	14	623	19	625	68	623.0	19.0	0.6	
SLAM1925_61.FIN2	160.7	1.21	1.618	0.048	0.1644	0.0039	0.617	972	19	984	22	942	53	942.0	53.0	4.5	
SLAM1925_62.FIN2	173.7	1.11	1.626	0.033	0.1626	0.0027	0.341	979	13	971	15	1001	44	1001.0	44.0	3.0	
SLAM1925_63.FIN2	270	2.15	0.832	0.021	0.0995	0.0023	0.434	613	12	611	14	630	55	611.0	14.0	0.3	

SLAM1925_66.FIN2	82.7	0.81	0.813	0.026	0.0982	0.0017	0.096	602	15	603.7	9.7	587	76	603.7	9.7	0.3	
SLAM1925_67.FIN2	0.46	0.01	190	150	1.7	1.4	0.996	5000	1000	5700	3500	5160	300	5160.0	300.0	10.5	
SLAM1925_69.FIN2	418	2.22	0.877	0.034	0.1011	0.0037	0.656	635	18	620	21	682	61	620.0	21.0	2.4	
SLAM1925_70.FIN2	357	1.25	0.498	0.013	0.0585	0.0011	0.478	409.6	8.8	366.7	6.7	654	51	366.7	6.7	10.5	
SLAM1925_71.FIN2	163.3	2.72	1.36	0.056	0.1404	0.005	0.613	863	23	845	28	904	72	845.0	28.0	2.1	
SLAM1925_72.FIN2	299	0.99	0.816	0.021	0.0996	0.0024	0.595	603	12	612	14	568	50	612.0	14.0	1.5	
SLAM1925_73.FIN2	334	2.82	0.824	0.02	0.0973	0.002	0.589	608	11	598	12	643	44	598.0	12.0	1.6	
SLAM1925_74.FIN2	336	2.42	1.475	0.056	0.1518	0.006	0.690	913	23	912	34	930	66	930.0	66.0	1.9	
SLAM1925_75.FIN2	222	1.17	0.789	0.017	0.0965	0.0017	0.467	588.9	9.5	593.4	9.7	575	38	593.4	9.7	0.8	
SLAM1925_76.FIN2	233	0.52	0.827	0.016	0.0989	0.0013	0.464	610.3	8.8	607.6	7.6	621	39	607.6	7.6	0.4	
SLAM1925_77.FIN2	37.7	3.00	0.702	0.051	0.087	0.0044	0.321	534	31	536	26	550	150	536.0	26.0	0.4	
SLAM1925_78.FIN2	210	5.55	1.413	0.042	0.1468	0.0035	0.777	891	18	882	20	914	38	914.0	38.0	3.5	
SLAM1925_79.FIN2	602	2.98	1.634	0.019	0.1658	0.0016	0.477	982.4	7.2	988.5	8.7	973	22	973.0	22.0	1.6	
SLAM1925_80.FIN2	79	3.03	0.52	0.1	0.0599	0.0071	0.723	420	70	375	43	650	380	375.0	43.0	10.7	Rim
SLAM1925_80.FIN2	149.7	0.17	5.426	0.088	0.3299	0.0051	0.641	1886	14	1836	25	1945	22	1945.0	22.0	5.6	Core
SLAM1925_81.FIN2	73.6	2.48	10.55	0.16	0.4708	0.0064	0.626	2481	14	2489	29	2476	21	2476.0	21.0	0.5	
SLAM1925_82.FIN2	147	16.40	1.093	0.028	0.1194	0.0023	0.353	748	13	727	13	824	54	727.0	13.0	2.8	
SLAM1925_83.FIN2	62.6	2.44	10.33	0.15	0.4625	0.0061	0.722	2463	14	2452	26	2476	18	2476.0	18.0	1.0	
SLAM1925_84.FIN2	159	2.22	0.999	0.022	0.1135	0.002	0.383	701	11	693	11	716	48	693.0	11.0	1.1	
SLAM1925_85.FIN2	242	1.30	1.206	0.021	0.1326	0.0016	0.366	802.4	9.5	802.8	9	781	32	802.8	9.0	0.0	
SLAM1925_86.FIN2	125.4	1.68	0.944	0.022	0.1049	0.0015	0.346	674	11	643.1	8.6	761	48	643.1	8.6	4.6	
SLAM1925_87.FIN2	71.9	6.80	0.905	0.042	0.1043	0.0031	0.595	648	23	639	18	669	82	639.0	18.0	1.4	
SLAM1925_88.FIN2	445.4	1.59	1.12	0.018	0.1257	0.0017	0.560	762.1	8.4	763.3	9.9	753	30	763.3	9.9	0.2	
SLAM1925_89.FIN2	19.5	2.35	8.02	0.22	0.3617	0.0089	0.527	2224	25	1987	42	2439	45	2439.0	45.0	18.5	
SLAM1925_90.FIN2	80.3	0.71	1.715	0.042	0.1657	0.0028	0.225	1014	15	988	15	1046	56	1046.0	56.0	5.5	
SLAM1925_91.FIN2	126.7	0.80	1.381	0.027	0.1482	0.0017	0.293	880	12	890.8	9.6	853	41	853.0	41.0	4.4	
SLAM1925_92.FIN2	101.9	0.55	1.023	0.034	0.1141	0.0024	0.066	716	18	696	14	759	86	696.0	14.0	2.8	
SLAM1925_93.FIN2	548	2.82	0.858	0.011	0.10252	0.00091	0.407	628.4	5.9	629.1	5.3	615	26	629.1	5.3	0.1	
SLAM1925_94.FIN2	124.2	0.78	0.992	0.033	0.1118	0.0025	0.558	697	17	683	14	727	59	683.0	14.0	2.0	
SLAM1925_95.FIN2	146.7	0.97	0.821	0.017	0.0971	0.001	0.212	606.9	9.3	597.3	6	627	45	597.3	6.0	1.6	
SLAM1925_96.FIN2	218	2.07	0.916	0.03	0.1069	0.0027	0.239	660	16	654	16	656	78	654.0	16.0	0.9	
SLAM1925_97.FIN2	246	0.67	0.805	0.016	0.095	0.0016	0.522	598.5	8.8	585	9.5	643	38	585.0	9.5	2.3	
SLAM1925_98.FIN2	117	1.17	1.35	0.032	0.1433	0.0022	0.387	866	14	863	13	845	50	845.0	13.0	0.3	
SLAM1925_99.FIN2	348	3.27	7.12	0.19	0.362	0.0097	0.672	2116	23	1991	46	2242	37	2242.0	37.0	11.2	
SLAM1925_100.FIN2	210.6	1.38	0.968	0.019	0.1099	0.0013	0.359	685.9	9.9	671.8	7.5	713	41	671.8	7.5	2.1	
SLAM1925_101.FIN2	259	1.07	0.879	0.033	0.0953	0.0029	0.347	638	18	586	17	805	78	586.0	17.0	8.2	
SLAM1925_102.FIN2	163.2	0.85	0.966	0.018	0.1139	0.0016	0.276	685	9.4	695.1	9.4	639	44	695.1	9.4	1.5	
SLAM1925_103.FIN2	313	2.31	1.174	0.034	0.1261	0.0034	0.443	791	16	765	20	834	58	765.0	20.0	3.3	
SLAM1925_104.FIN2	43.28	1.65	1.285	0.04	0.1361	0.0033	0.271	836	18	822	18	848	78	822.0	18.0	1.7	
SLAM1925_105.FIN2	451	1.34	0.572	0.014	0.0747	0.0018	0.649	459.1	9.3	464	11	423	45	464.0	11.0	1.1	
SLAM1925_106.FIN2	467	1.19	0.846	0.01	0.1009	0.00083	0.378	622	5.7	619.6	4.9	614	26	619.6	4.9	0.4	
SLAM1925_107.FIN2	170.8	1.18	1.684	0.029	0.1675	0.0023	0.515	1001	11	998	13	993	32	993.0	32.0	0.5	
SLAM1925_108.FIN2	247	2.37	0.791	0.029	0.096	0.0018	0.351	591	16	591	11	567	75	591.0	11.0	0.0	
SLAM1925_109.FIN2	555	1.21	0.832	0.015	0.0942	0.0012	0.211	614.1	8.3	580.2	7.2	723	43	580.2	7.2	5.5	
SLAM1925_110.FIN2	91.2	0.60	0.793	0.025	0.0956	0.0017	0.416	594	13	588	10	587	58	588.0	10.0	1.0	
SLAM1925_112.FIN2	84	0.77	1.252	0.034	0.138	0.0024	0.313	823	16	833	14	773	59	833.0	14.0	1.2	
SLAM1925_113.FIN2	228.8	0.98	1.547	0.028	0.1536	0.0034	0.518	949	12	920	19	1003	40	1003.0	40.0	8.3	
SLAM1925_114.FIN2	404	1.00	0.853	0.017	0.1029	0.0019	0.654	625	9.5	631	11	596	34	631.0	11.0	1.0	
SLAM1925_115.FIN2	502	3.34	1.134	0.02	0.1237	0.0021	0.515	768	9.5	751	12	812	35	751.0	12.0	2.2	
SLAM1925_116.FIN2	636	2.22	1.537	0.02	0.1574	0.0019	0.583	944.9	8.2	942	11	943	22	943.0	22.0	0.1	
SLAM1925_117.FIN2	192.1	2.00	0.945	0.017	0.1082	0.0013	0.297	674.2	8.8	662.1	7.3	703	41	662.1	7.3	1.8	
SLAM1925_119.FIN2	814	11.04	1.034	0.021	0.1177	0.0024	0.664	720	11	717	14	730	36	717.0	14.0	0.4	
SLAM1925_120.FIN2	83	1.33	0.748	0.027	0.083	0.0021	0.516	563	15	514	13	745	65	514.0	13.0	8.7	
SLAM1925_121.FIN2	173.5	1.11	0.801	0.023	0.0954	0.0024	0.402	595	13	587	14	625	64	587.0	14.0	1.3	
SLAM1925_122.FIN2	454	2.61	0.745	0.016	0.0897	0.0019	0.571	563.9	9.4	554	11	610	44	554.0	11.0	1.8	
SLAM1925_123.FIN2	688	1.15	1.626	0.043	0.165	0.0049	0.722	978	16	983	27	967	43	967.0	43.0	1.7	
SLAM1925_124.FIN2	80.2	1.47	1.212	0.031	0.1387	0.0028	0.423	805	15	837	16	716	56	837.0	16.0	4.0	
SLAM1925_125.FIN2	937	30.30	0.87	0.062	0.1038	0.0063	0.792	632	33	636	36	620	110	636.0	36.0	0.6	
SLAM1925_126.FIN2	300	2.19	9.78	0.28	0.44	0.013	0.589	2412	26	2345	59	2466	45	2466.0	45.0	4.9	
SLAM1925_127.FIN2	72.5	1.22	1.079	0.04	0.1187	0.0035	0.478	737	20	722	20	774	72	722.0	20.0	2.0	
SLAM1925_128.FIN2	135.6	1.13	5.607	0.09	0.3452	0.0058	0.531	1916	14	1911	28	1925	29	1925.0	29.0	0.7	
SLAM1925_129.FIN2	58.1	1.48	0.836	0.026	0.0997	0.0015	0.170	614	14	612.7	9	611	67	612.7	9.0	0.2	
SLAM1925_130.FIN2	778	7.06	0.862	0.017	0.1017	0.002	0.665	629.5	9.5	624	12	659	37	624.0	12.0	0.9	

Sample Name:	SLAm1928							207/235		206/238		207/206		Best age			
Grain #	[U] ppm	U/Th	207/235	2σ error	206/238	2σ error	RHO	Age Ma	2σ error	Age (Ma)	2σ error	Age (Ma)	2σ error	(Ma)	2σ error	% Disc.	Rim/Core
SLAM1928_1.FIN2	511	1.52	0.693	0.021	0.0848	0.002	0.719	532	13	524	12	561	46	524.0	12.0	1.5	
SLAM1928_14.FIN2	132	6.67	1.477	0.049	0.1275	0.0024	0.947	795	14	760	13	903	21	760.0	13.0	4.4	
SLAM1928_3.FIN2	190	2.72	0.906	0.031	0.1061	0.0027	0.671	653	17	649	16	663	57	649.0	16.0	0.6	
SLAM1928_4.FIN2	702	7.14	0.828	0.012	0.1003	0.0013	0.500	611.6	6.7	616	7.5	604	32	616.0	7.5	0.7	
SLAM1928_5.FIN2	105.3	1.09	1.271	0.048	0.1336	0.0034	0.357	828	21	808	20	876	77	808.0	20.0	2.4	
SLAM1928_6.FIN2	173.6	2.34	1.017	0.027	0.1172	0.0022	0.482	710	14	714	12	699	52	714.0	12.0	0.6	
SLAM1928_7.FIN2	106	0.72	0.846	0.026	0.1014	0.0017	0.332	620	14	622	10	600	63	622.0	10.0	0.3	
SLAM1928_8.FIN2	238.7	1.66	0.774	0.023	0.0943	0.0022	0.605	580	13	581	13	578	56	581.0	13.0	0.2	
SLAM1928_9.FIN2	375	1.09	1.274	0.036	0.1301	0.002	0.255	830	16	788	11	924	61	788.0	11.0	5.1	
SLAM1928_10.FIN2	137	0.77	0.776	0.026	0.095	0.0015	0.348	579	15	584.8	8.6	532	69	584.8	8.6	1.0	
SLAM1928_11.FIN2	216.4	0.59	5.37	0.13	0.335	0.0064	0.614	1877	21	1861	31	1892	35	1892.0	35.0	1.6	
SLAM1928_12.FIN2	82	2.35	0.989	0.03	0.114	0.0016	0.186	695	15	696	9.3	670	64	696.0	9.3	0.1	
SLAM1928_13.FIN2	673	5.88	5.03	0.11	0.306	0.0073	0.759	1821	19	1722	37	1944	27	1944.0	27.0	11.4	
SLAM1928_14.FIN2	233	1.35	0.606	0.018	0.0785	0.0017	0.539	479	11	487	10	439	57	487.0	10.0	1.7	
SLAM1928_15.FIN2	624.2	0.68	0.3909	0.0064	0.05299	0.0006	0.326	335.2	4.7	332.8	3.7	344	37	332.8	3.7	0.7	
SLAM1928_16.FIN2	272.1	1.82	12.23	0.14	0.5084	0.0058	0.691	2620	11	2648	25	2598	16	2598.0	16.0	1.9	
SLAM1928_17.FIN2	365	0.46	0.704	0.031	0.0894	0.0034	0.739	538	19	551	20	496	65	551.0	20.0	2.4	
SLAM1928_18.FIN2	48.2	0.94	0.953	0.08	0.1121	0.0062	0.294	672	41	684	36	630	170	684.0	36.0	1.8	
SLAM1928_19.FIN2	143	1.30	6.35	0.12	0.3609	0.0064	0.609	2021	17	1985	31	2066	27	2066.0	27.0	3.9	
SLAM1928_20.FIN2	216	1.03	1.201	0.03	0.132	0.0031	0.570	799	14	798	18	786	49	798.0	18.0	0.1	
SLAM1928_21.FIN2	524	3.00	1.5	0.028	0.1563	0.0022	0.683	930	12	936	12	910	30	910.0	30.0	2.9	
SLAM1928_22.FIN2	40.3	1.03	0.92	0.039	0.1102	0.0019	0.082	659	20	674	11	562	94	674.0	11.0	2.3	
SLAM1928_23.FIN2	156.7	2.66	1.184	0.028	0.1337	0.0019	0.487	791	13	809	11	719	46	809.0	11.0	2.3	
SLAM1928_24.FIN2	118.8	1.50	0.807	0.025	0.0939	0.0017	0.463	597	14	578	10	647	57	578.0	10.0	3.2	
SLAM1928_26.FIN2	350	2.92	0.896	0.016	0.1054	0.0015	0.539	648.2	8.7	645.6	8.6	651	31	645.6	8.6	0.4	
SLAM1928_27.FIN2	440	0.82	1.016	0.043	0.1051	0.0029	0.655	703	21	643	17	874	71	643.0	17.0	8.5	
SLAM1928_28.FIN2	63.2	1.00	1.228	0.043	0.1316	0.0025	0.189	808	19	796	14	818	77	796.0	14.0	1.5	
SLAM1928_29.FIN2	223	0.57	0.678	0.022	0.0832	0.0017	0.632	522	13	515	10	549	53	515.0	10.0	1.3	
SLAM1928_30.FIN2	453	1.69	1.182	0.046	0.1244	0.0033	0.598	786	21	755	19	873	67	755.0	19.0	3.9	
SLAM1928_31.FIN2	276	1.80	0.77	0.025	0.0971	0.0032	0.713	579	14	596	19	534	52	596.0	19.0	2.9	
SLAM1928_32.FIN2	264	1.12	1.141	0.031	0.1297	0.0022	0.710	769	15	786	13	725	41	786.0	13.0	2.2	
SLAM1928_33.FIN2	146.7	2.24	0.848	0.02	0.1009	0.0012	0.168	621	11	619.7	7.1	616	52	619.7	7.1	0.2	
SLAM1928_34.FIN2	504	4.93	6.5	0.11	0.3874	0.0063	0.769	2046	15	2109	30	1985	19	1985.0	19.0	6.2	
SLAM1928_35.FIN2	321.5	1.74	1.137	0.028	0.1288	0.0022	0.490	768	13	781	13	723	47	781.0	13.0	1.7	
SLAM1928_36.FIN2	752	17.10	0.771	0.024	0.082	0.0022	0.802	578	13	507	13	868	38	507.0	13.0	12.3	
SLAM1928_37.FIN2	656	1.20	1.746	0.05	0.1708	0.0036	0.456	1022	18	1016	20	1019	56	1019.0	56.0	0.3	
SLAM1928_38.FIN2	238.9	0.81	0.838	0.02	0.1035	0.0016	0.380	616	11	634.9	9.4	537	53	634.9	9.4	3.1	
SLAM1928_39.FIN2	42.4	1.53	11.84	0.27	0.4819	0.0095	0.715	2588	22	2530	41	2636	29	2636.0	29.0	4.0	
SLAM1928_40.FIN2	450.1	4.09	1.053	0.026	0.1129	0.0022	0.637	728	13	692	12	825	45	692.0	12.0	4.9	
SLAM1928_41.FIN2	136.6	1.30	1.197	0.028	0.1292	0.0019	0.483	797	13	783	11	834	43	783.0	11.0	1.8	
SLAM1928_42.FIN2	118.2	0.53	1.644	0.038	0.1705	0.0026	0.535	984	15	1014	14	933	41	933.0	41.0	8.7	
SLAM1928_43.FIN2	231.6	2.70	6.56	0.26	0.327	0.011	0.774	2039	34	1818	55	2283	47	2283.0	47.0	20.4	
SLAM1928_44.FIN2	42.1	1.33	0.88	0.044	0.0995	0.0027	0.416	634	25	611	16	690	100	611.0	16.0	3.6	
SLAM1928_45.FIN2	63.8	1.13	9.9	0.22	0.475	0.011	0.711	2418	21	2501	47	2368	29	2368.0	29.0	5.6	
SLAM1928_46.FIN2	306	1.54	0.3785	0.0095	0.05199	0.00079	0.474	325	7	326.6	4.8	314	48	326.6	4.8	0.5	
SLAM1928_47.FIN2	210	0.83	1.494	0.03	0.1572	0.0018	0.443	927	12	940.8	9.9	892	37	892.0	37.0	5.5	
SLAM1928_48.FIN2	305	1.58	1.528	0.075	0.149	0.0044	0.678	936	30	894	25	1030	75	1030.0	75.0	13.2	
SLAM1928_49.FIN2	159.1	1.24	10.86	0.17	0.4801	0.0079	0.709	2509	14	2526	35	2497	21	2497.0	21.0	1.2	
SLAM1928_50.FIN2	680	4.96	1.806	0.09	0.1636	0.0061	0.640	1035	32	975	34	1161	79	1161.0	79.0	16.0	
SLAM1928_51.FIN2	185	20.20	1.04	0.035	0.1172	0.0033	0.482	725	18	714	19	748	72	714.0	19.0	1.5	
SLAM1928_52.FIN2	284	0.51	0.827	0.018	0.1004	0.0012	0.457	610.1	9.8	616.6	7.2	568	39	616.6	7.2	1.1	
SLAM1928_53.FIN2	152.6	3.25	1.984	0.055	0.18	0.0036	0.510	1107	19	1066	20	1177	50	1177.0	50.0	9.4	
SLAM1928_54.FIN2	289	1.14	0.937	0.022	0.1069	0.0017	0.475	670	12	654	10	707	46	654.0	10.0	2.4	
SLAM1928_55.FIN2	62.2	2.69	0.779	0.038	0.0981	0.0031	0.339	580	22	602	18	470	100	602.0	18.0	3.8	
SLAM1928_56.FIN2	400	1.14	5.662	0.075	0.3369	0.0043	0.539	1924	11	1871	21	1974	21	1974.0	21.0	5.2	
SLAM1928_57.FIN2	641	1.04	0.738	0.024	0.0952	0.003	0.732	559	14	586	18	456	53	586.0	18.0	4.8	
SLAM1928_58.FIN2	445	1.72	0.719	0.017	0.088	0.0016	0.540	548.2	9.9	543.2	9.3	565	44	543.2	9.3	0.9	
SLAM1928_59.FIN2	467	2.87	1.645	0.047	0.1662	0.0049	0.765	984	19	989	27	997	40	997.0	40.0	0.8	
SLAM1928_60.FIN2	84.8	2.11	1.638	0.037	0.1663	0.0024	0.225	982	14	991	13	964	50	964.0	50.0	2.8	
SLAM1928_61.FIN2	221.9	0.96	0.873	0.019	0.1035	0.0017	0.434	636	11	635	10	647	47	635.0	10.0	0.2	
SLAM1928_62.FIN2	38.01	1.44	11.9	0.21	0.4965	0.0077	0.329	2593	16	2597	33	2597	32	2597.0	32.0	0.0	
SLAM1928_63.FIN2	517	2.77	1.109	0.035	0.1253	0.0025	0.538	761	18	761	14	751	59	761.0	14.0	0.0	
SLAM1928_64.FIN2	1370	5.59	0.669	0.028	0.083	0.0022	0.539	518	17	514	13	519	75	514.0	13.0	0.8	

SLAM1928_65.FIN2	216	1.98	0.622	0.017	0.0753	0.0014	0.389	489	11	467.8	8.3	579	61	467.8	8.3	4.3
SLAM1928_66.FIN2	1056	8.96	0.782	0.029	0.0945	0.0036	0.668	583	16	581	21	583	68	581.0	21.0	0.3
SLAM1928_67.FIN2	615	1.16	0.744	0.024	0.0834	0.0021	0.486	564	14	516	12	756	66	516.0	12.0	8.5
SLAM1928_68.FIN2	697	6.30	1.202	0.034	0.1355	0.0033	0.768	799	16	819	19	731	40	819.0	19.0	2.5
SLAM1928_69.FIN2	95.2	1.09	0.777	0.026	0.0938	0.0024	0.408	580	15	578	14	549	75	578.0	14.0	0.3
SLAM1928_70.FIN2	1059	7.10	1.803	0.029	0.1856	0.0029	0.659	1046	10	1097	15	931	27	931.0	27.0	17.8
SLAM1928_71.FIN2	577	5.19	1.323	0.023	0.1388	0.0022	0.572	854.5	9.8	837	12	893	32	837.0	12.0	2.0
SLAM1928_72.FIN2	778	6.84	1.101	0.058	0.1093	0.0029	0.747	740	27	668	17	913	78	668.0	17.0	9.7
SLAM1928_73.FIN2	48.4	1.37	0.842	0.043	0.1036	0.003	0.160	613	24	638	18	520	110	638.0	18.0	4.1
SLAM1928_74.FIN2	308.6	0.59	0.728	0.018	0.0908	0.0017	0.644	553	11	559.7	9.8	536	44	559.7	9.8	1.2
SLAM1928_75.FIN2	249	0.85	1.756	0.037	0.1738	0.0021	0.536	1027	14	1033	12	1024	37	1024.0	37.0	0.9
SLAM1928_76.FIN2	258	1.39	0.395	0.01	0.05553	0.0009	0.296	337.5	7.3	348.3	5.5	279	55	348.3	5.5	3.2
SLAM1928_77.FIN2	617	0.52	10.28	0.28	0.4782	0.009	0.701	2456	26	2518	40	2411	36	2411.0	36.0	4.4
SLAM1928_78.FIN2	564	1.39	0.369	0.012	0.0504	0.0012	0.776	317.4	8.9	317.1	7.2	356	46	317.1	7.2	0.1
SLAM1928_79.FIN2	261	1.03	0.775	0.028	0.0905	0.0026	0.487	579	16	558	15	660	70	558.0	15.0	3.6
SLAM1928_80.FIN2	234	0.85	1.596	0.075	0.1574	0.0055	0.549	960	29	941	31	1001	85	1001.0	85.0	6.0
SLAM1928_81.FIN2	68.4	1.35	1.211	0.04	0.1238	0.0026	0.167	807	17	752	15	921	83	752.0	15.0	6.8
SLAM1928_82.FIN2	482	1.38	0.834	0.017	0.1006	0.0015	0.659	614.4	9.2	617.7	9	599	34	617.7	9.0	0.5
SLAM1928_83.FIN2	628	3.10	0.811	0.022	0.0984	0.0027	0.758	600	12	604	16	583	43	604.0	16.0	0.7
SLAM1928_84.FIN2	269.6	1.65	0.893	0.028	0.1025	0.0021	0.584	645	15	629	12	701	52	629.0	12.0	2.5
SLAM1928_85.FIN2	184.1	2.79	1.003	0.035	0.102	0.0019	0.453	699	18	626	11	908	72	626.0	11.0	10.4
SLAM1928_86.FIN2	195	2.24	1.041	0.044	0.1154	0.0036	0.582	722	21	703	21	784	67	703.0	21.0	2.6
SLAM1928_87.FIN2	451	0.94	1.068	0.022	0.1225	0.0021	0.560	736	11	745	12	694	38	745.0	12.0	1.2
SLAM1928_88.FIN2	696	6.93	0.587	0.019	0.0668	0.0016	0.532	468	12	417	9.6	714	61	417.0	9.6	10.9
SLAM1928_89.FIN2	116.7	3.11	0.762	0.039	0.0965	0.0027	0.109	572	22	594	16	470	120	594.0	16.0	3.8
SLAM1928_90.FIN2	191.2	1.02	1.715	0.041	0.17	0.0026	0.535	1012	15	1012	14	1012	42	1012.0	42.0	0.0
SLAM1928_91.FIN2	348	1.57	5.636	0.096	0.3451	0.0062	0.785	1918	15	1909	30	1939	21	1939.0	21.0	1.5
SLAM1928_92.FIN2	202	1.15	2.145	0.052	0.1926	0.0038	0.568	1160	17	1135	20	1214	41	1214.0	41.0	6.5
SLAM1928_93.FIN2	561	2.65	1.419	0.034	0.1509	0.0029	0.605	894	14	906	16	875	38	875.0	38.0	3.5
SLAM1928_94.FIN2	358	0.78	1.553	0.039	0.1564	0.0025	0.621	949	15	936	14	982	41	982.0	41.0	4.7
SLAM1928_95.FIN2	144.1	1.66	1.452	0.038	0.1538	0.0023	0.556	907	15	922	13	868	43	868.0	43.0	6.2
SLAM1928_96.FIN2	715	3.53	10.19	0.25	0.466	0.01	0.794	2448	23	2463	46	2436	25	2436.0	25.0	1.1
SLAM1928_97.FIN2	188.2	1.92	0.789	0.028	0.1	0.0031	0.668	587	16	613	18	508	55	613.0	18.0	4.4
SLAM1928_98.FIN2	255.3	3.43	11.15	0.21	0.508	0.01	0.836	2534	17	2645	45	2446	19	2446.0	19.0	8.1
SLAM1928_99.FIN2	438	1.32	1.48	0.035	0.1557	0.0026	0.623	921	14	933	14	897	39	897.0	39.0	4.0
SLAM1928_100.FIN2	58.6	0.84	0.983	0.033	0.1176	0.0021	0.359	691	17	716	12	606	70	716.0	12.0	3.6
SLAM1928_101.FIN2	115.1	1.68	6.711	0.098	0.3882	0.0047	0.545	2073	13	2116	21	2042	22	2042.0	22.0	3.6
SLAM1928_102.FIN2	64.1	0.63	0.753	0.027	0.095	0.0017	0.203	568	16	584.9	9.9	495	79	584.9	9.9	3.0
SLAM1928_103.FIN2	269	1.61	8.46	0.17	0.3577	0.0068	0.733	2281	18	1975	33	2574	23	2574.0	23.0	23.3
SLAM1928_104.FIN2	4.63	0.20	10.5	0.59	0.475	0.024	0.958	2430	52	2459	90	2434	63	2434.0	63.0	1.0
SLAM1928_105.FIN2	144.4	1.69	1.055	0.03	0.1143	0.0027	0.507	730	14	697	16	825	54	697.0	16.0	4.5
SLAM1928_106.FIN2	417	1.56	0.738	0.014	0.0899	0.0013	0.453	560.3	8.3	556.1	7.8	565	40	556.1	7.8	0.7
SLAM1928_107.FIN2	251.6	2.92	0.967	0.037	0.1066	0.0022	0.377	688	20	653	13	742	73	653.0	13.0	5.1
SLAM1928_108.FIN2	242.1	1.23	1.687	0.04	0.1603	0.0032	0.571	1003	16	958	18	1092	44	1092.0	44.0	12.3
SLAM1928_109.FIN2	502	10.35	1.125	0.022	0.1263	0.002	0.694	763	11	766	12	749	31	766.0	12.0	0.4
SLAM1928_110.FIN2	561	2.91	0.786	0.014	0.0965	0.0012	0.546	587.9	8.1	593.9	7.1	558	34	593.9	7.1	1.0
SLAM1928_112.FIN2	1188	5.74	0.769	0.011	0.0949	0.0014	0.593	578.6	6.5	584.2	8	549	29	584.2	8.0	1.0
SLAM1928_113.FIN2	191.9	1.66	1.328	0.031	0.1359	0.0021	0.561	855	13	821	12	931	40	821.0	12.0	4.0
SLAM1928_114.FIN2	356	6.70	0.713	0.014	0.0889	0.0015	0.554	545	8.2	548.7	9	518	38	548.7	9.0	0.7
SLAM1928_115.FIN2	158.7	2.02	10.19	0.13	0.4723	0.0063	0.644	2450	12	2492	27	2405	20	2405.0	20.0	3.6
SLAM1928_116.FIN2	376	0.92	1.354	0.037	0.1516	0.0035	0.868	866	16	909	20	741	34	741.0	20.0	5.0
SLAM1928_117.FIN2	399	1.43	10.11	0.17	0.4193	0.0078	0.825	2445	16	2255	35	2596	18	2596.0	18.0	13.1
SLAM1928_118.FIN2	716	3.78	0.711	0.021	0.0952	0.0027	0.732	543	13	586	16	354	46	586.0	16.0	7.9
SLAM1928_119.FIN2	452	8.08	0.88	0.028	0.0981	0.0018	0.581	642	15	603	11	758	57	603.0	11.0	6.1
SLAM1928_120.FIN2	212	1.15	1.264	0.024	0.1379	0.0022	0.407	828	11	832	12	814	39	832.0	12.0	0.5
SLAM1928_121.FIN2	174.4	1.08	1.221	0.04	0.1367	0.003	0.649	806	18	825	17	737	53	825.0	17.0	2.4
SLAM1928_122.FIN2	269.4	0.70	5.444	0.063	0.3494	0.0034	0.663	1891	10	1931	16	1844	17	1844.0	17.0	4.7
SLAM1928_123.FIN2	347	1.10	1.111	0.023	0.1241	0.0018	0.483	757	11	754	11	762	38	754.0	11.0	0.4
SLAM1928_124.FIN2	221	1.35	1.164	0.053	0.1221	0.0036	0.762	779	25	742	21	904	60	742.0	21.0	4.7
SLAM1928_125.FIN2	220.6	1.23	1.208	0.071	0.1162	0.0041	0.525	793	32	708	23	1020	110	708.0	23.0	10.7
SLAM1928_126.FIN2	83.4	0.98	1.057	0.03	0.1195	0.0015	0.035	729	15	727.6	8.7	720	64	727.6	8.7	0.2
SLAM1928_127.FIN2	520	2.01	1.64	0.041	0.1805	0.005	0.759	983	16	1068	27	817	42	817.0	27.0	8.6
SLAM1928_128.FIN2	304	1.59	0.574	0.024	0.0598	0.0017	0.666	458	15	374	10	922	70	374.0	10.0	18.3
SLAM1928_129.FIN2	111.2	5.45	1.25	0.085	0.1316	0.0049	0.747	815	38	796	28	870	100	796.0	28.0	2.3
SLAM1928_130.FIN2	114.6	0.74	2.154	0.042	0.209	0.0025	0.392	1164	13	1223	13	1087	37	1087.0	37.0	12.5

Sample Name: Grain #	SLAm1933 [U] ppm	U/Th	207/235	2σ error	206/238	2σ error	RHO	207/235 Age Ma	2σ error	206/238 Age (Ma)	2σ error	207/206 Age (Ma)	2σ error	Best age (Ma)	2σ error	% Disc.	Rim/Core
SLAM1933_1.FIN2	603	1.65	0.3899	0.008	0.04976	0.00052	0.462	333.7	5.7	313.5	3.3	459	42	313.5	3.3	6.1	
SLAM1933_2.FIN2	249	1.88	0.3652	0.008	0.04901	0.00056	0.108	316.2	6.1	308.4	3.4	354	52	308.4	3.4	2.5	
SLAM1933_3.FIN2	386	1.79	1.7	0.023	0.1649	0.0021	0.662	1008.8	8.3	984	12	1056	22	1056.0	22.0	6.8	
SLAM1933_4.FIN2	392	1.93	0.3785	0.008	0.05163	0.00081	0.505	325.3	5.8	324.5	5	323	42	324.5	5.0	0.2	
SLAM1933_5.FIN2	273	1.85	0.3798	0.0081	0.05237	0.00059	0.425	326.2	6	329	3.6	299	45	329.0	3.6	0.9	
SLAM1933_6.FIN2	344	2.66	0.606	0.016	0.0748	0.0013	0.679	479	10	464.7	7.7	538	44	464.7	7.7	3.0	
SLAM1933_7.FIN2	221	2.69	0.3439	0.0093	0.05	0.001	0.327	300.4	7.2	314.5	6.4	208	60	314.5	6.4	4.7	
SLAM1933_8.FIN2	752	1.15	0.2884	0.0086	0.043	0.0012	0.719	256.4	6.7	271.5	7.4	147	45	271.5	7.4	5.9	
SLAM1933_9.FIN2	1213	4.01	2.165	0.066	0.1972	0.0052	0.735	1169	22	1159	28	1197	45	1197.0	45.0	3.2	
SLAM1933_10.FIN2	220	1.18	0.506	0.012	0.06707	0.00084	0.322	414.5	8.2	418.4	5	391	51	418.4	5.0	0.9	
SLAM1933_11.FIN2	135.5	1.80	0.567	0.017	0.0717	0.0014	0.535	454	11	446.3	8.7	480	58	446.3	8.7	1.7	
SLAM1933_12.FIN2	389	7.92	0.567	0.014	0.0716	0.001	0.305	453.2	8	445.5	6	488	42	445.5	6.0	1.7	
SLAM1933_13.FIN2	525	1.07	0.3562	0.0063	0.05024	0.00059	0.466	309.6	4.8	315.9	3.6	256	36	315.9	3.6	2.0	
SLAM1933_14.FIN2	188	2.09	0.3549	0.0093	0.04932	0.00057	0.182	307.5	7	310.3	3.5	275	56	310.3	3.5	0.9	
SLAM1933_15.FIN2	861	1.41	0.3535	0.0055	0.0492	0.0004	0.216	307	4.1	309.6	2.5	270	34	309.6	2.5	0.8	
SLAM1933_16.FIN2	296.9	6.13	1.033	0.03	0.1103	0.0025	0.626	719	15	675	15	850	50	675.0	15.0	6.1	
SLAM1933_17.FIN2	356	3.96	7.5	0.29	0.405	0.015	0.793	2151	34	2188	69	2135	43	2135.0	43.0	2.5	
SLAM1933_18.FIN2	161.3	2.25	1.527	0.029	0.1534	0.0017	0.460	939	12	919.9	9.7	976	35	976.0	35.0	5.7	
SLAM1933_19.FIN2	116	1.39	16.43	0.48	0.551	0.015	0.801	2899	26	2828	59	2959	32	2959.0	32.0	4.4	
SLAM1933_20.FIN2	2120	110.00	0.3907	0.0082	0.0535	0.00098	0.730	334.7	6	335.9	6	328	42	335.9	6.0	0.4	Rim
SLAM1933_20.FIN2	455.7	3.98	1.569	0.02	0.1586	0.0017	0.632	957.2	8	948.9	9.6	975	22	975.0	22.0	2.7	Core
SLAM1933_21.FIN2	173	0.86	1.599	0.035	0.1646	0.0031	0.587	969	14	981	17	940	40	940.0	40.0	4.4	
SLAM1933_22.FIN2	715	157.00	0.497	0.024	0.0633	0.0021	0.779	408	16	396	13	470	67	396.0	13.0	2.9	
SLAM1933_39.FIN2	169.1	10.81	0.677	0.017	0.07343	0.00088	0.952	470.2	5.5	452.3	5.1	638	16	452.3	5.1	3.8	
SLAM1933_23.FIN2	242.9	2.37	0.76	0.021	0.0835	0.0015	0.678	572	12	516.6	8.8	772	49	516.6	8.8	9.7	
SLAM1933_24.FIN2	305	39.50	0.885	0.02	0.1015	0.0016	0.669	642	11	623.1	9.4	698	36	623.1	9.4	2.9	
SLAM1933_25.FIN2	412	1.52	0.392	0.012	0.0532	0.0015	0.707	334.7	8.5	334.1	9	327	53	334.1	9.0	0.2	
SLAM1933_26.FIN2	89.3	0.69	0.756	0.022	0.0915	0.002	0.305	569	13	564	12	569	62	564.0	12.0	0.9	
SLAM1933_27.FIN2	659	1.77	0.363	0.0062	0.04974	0.00055	0.442	314.6	4.5	312.9	3.4	317	35	312.9	3.4	0.5	
SLAM1933_28.FIN2	304	1.21	0.3769	0.0077	0.05074	0.00046	0.256	324.2	5.7	319	2.8	343	45	319.0	2.8	1.6	
SLAM1933_29.FIN2	212.1	1.77	0.612	0.013	0.07774	0.00089	0.407	483.5	7.9	482.5	5.3	484	41	482.5	5.3	0.2	
SLAM1933_30.FIN2	139.6	1.87	0.403	0.014	0.05247	0.00079	0.063	342.7	9.9	329.6	4.8	413	77	329.6	4.8	3.8	
SLAM1933_31.FIN2	95.8	2.26	0.455	0.014	0.0589	0.00089	0.214	379.1	9.5	368.8	5.4	423	66	368.8	5.4	2.7	
SLAM1933_32.FIN2	114.4	2.51	0.549	0.018	0.0719	0.0013	0.006	443	12	447.5	7.5	401	79	447.5	7.5	1.0	
SLAM1933_33.FIN2	57.2	0.96	1.095	0.052	0.1189	0.0026	0.422	747	25	724	15	811	86	724.0	15.0	3.1	
SLAM1933_34.FIN2	849	0.83	0.3906	0.0054	0.05209	0.00044	0.299	334.5	4	327.3	2.7	365	32	327.3	2.7	2.2	
SLAM1933_35.FIN2	232	1.57	0.491	0.022	0.063	0.0019	0.533	404	15	394	12	446	85	394.0	12.0	2.5	
SLAM1933_36.FIN2	774	7.30	0.569	0.024	0.0716	0.0027	0.877	458	15	445	16	505	44	445.0	16.0	2.8	
SLAM1933_37.FIN2	108.7	0.78	0.878	0.02	0.1078	0.0014	0.214	638	11	659.5	8	547	51	659.5	8.0	3.4	
SLAM1933_38.FIN2	142.8	1.16	12.14	0.26	0.4983	0.0086	0.897	2611	20	2603	38	2628	19	2628.0	19.0	1.0	
SLAM1933_40.FIN2	99.6	1.56	0.403	0.016	0.0535	0.0013	0.303	343	12	335.6	7.7	385	83	335.6	7.7	2.2	
SLAM1933_41.FIN2	779	2.18	0.2972	0.0065	0.04092	0.00068	0.460	263.7	5.1	258.5	4.2	305	45	258.5	4.2	2.0	
SLAM1933_42.FIN2	558	6.85	0.958	0.02	0.1119	0.0023	0.780	680	11	683	13	682	30	683.0	13.0	0.4	
SLAM1933_43.FIN2	744	1.30	0.2653	0.006	0.03645	0.00054	0.522	238.5	4.8	230.7	3.4	307	43	230.7	3.4	3.3	
SLAM1933_44.FIN2	384	2.69	0.386	0.01	0.0522	0.0011	0.739	331	7.8	328.1	6.5	342	41	328.1	6.5	0.9	
SLAM1933_45.FIN2	778	2.01	0.3824	0.0066	0.05223	0.00071	0.523	328.4	4.8	328.2	4.4	319	33	328.2	4.4	0.1	
SLAM1933_47.FIN2	645	1.03	0.2494	0.0052	0.03479	0.00037	0.277	225.7	4.2	220.4	2.3	269	45	220.4	2.3	2.3	
SLAM1933_48.FIN2	93	1.22	1.043	0.036	0.1168	0.0029	0.506	721	18	712	17	741	71	712.0	17.0	1.2	
SLAM1933_49.FIN2	1265	1.36	0.432	0.028	0.0519	0.002	0.765	361	19	326	12	605	91	326.0	12.0	9.7	
SLAM1933_50.FIN2	736	2.16	0.3352	0.0054	0.0453	0.00062	0.429	293.3	4.1	285.6	3.8	340	38	285.6	3.8	2.6	
SLAM1933_51.FIN2	619	41.00	0.468	0.011	0.06348	0.0009	0.480	389.6	7.3	396.7	5.4	353	47	396.7	5.4	1.8	
SLAM1933_52.FIN2	290	1.68	0.247	0.014	0.0357	0.0013	0.523	223	11	225.9	8	203	95	225.9	8.0	1.3	
SLAM1933_53.FIN2	216.7	2.02	0.381	0.01	0.05255	0.00055	0.165	326.9	7.3	330.1	3.4	299	56	330.1	3.4	1.0	
SLAM1933_54.FIN2	399	5.36	0.557	0.011	0.07254	0.0009	0.409	448.9	7.3	451.4	5.4	430	41	451.4	5.4	0.6	
SLAM1933_55.FIN2	1890	6.10	0.403	0.016	0.0553	0.0021	0.635	343	12	347	13	323	72	347.0	13.0	1.2	
SLAM1933_56.FIN2	470	1.86	0.2658	0.0089	0.03698	0.00071	0.421	238.8	7.1	234	4.4	277	67	234.0	4.4	2.0	
SLAM1933_58.FIN2	430	2.66	0.585	0.017	0.0739	0.0018	0.656	468	11	459	11	523	52	459.0	11.0	1.9	
SLAM1933_59.FIN2	342.7	0.98	0.498	0.014	0.05602	0.0007	0.297	409.3	9.7	351.3	4.3	733	61	351.3	4.3	14.2	
SLAM1933_60.FIN2	26.17	1.69	0.381	0.028	0.0506	0.0011	0.089	322	21	317.8	7.1	320	140	317.8	7.1	1.3	
SLAM1933_61.FIN2	399	1.68	0.26	0.011	0.0373	0.0013	0.551	233.6	8.7	235.9	8	217	73	235.9	8.0	1.0	
SLAM1933_62.FIN2	92.8	1.19	0.403	0.022	0.049	0.0011	0.094	342	16	308.1	6.9	540	120	308.1	6.9	9.9	
SLAM1933_63.FIN2	128.7	1.82	0.372	0.014	0.04995	0.00078	0.311	319	10	314.2	4.8	337	74	314.2	4.8	1.5	
SLAM1933_64.FIN2	561	1.50	0.2783	0.0062	0.03966	0.00047	0.180	248.9	4.9	250.7	2.9	221	48	250.7	2.9	0.7	
SLAM1933_65.FIN2	696	1.46	0.2711	0.0048	0.03798	0.00034	0.258	243.3	3.8	240.3	2.1	262	39	240.3	2.1	1.2	
SLAM1933_66.FIN2	1700	3.36	0.3701	0.0053	0.0505	0.00069	0.718	320	4	317.5	4.3	331	25	317.5	4.3	0.8	
SLAM1933_67.FIN2	300	3.98	0.632	0.014	0.07973	0.00094	0.393	495.8	8.5	494.4	5.6	485	45	494.4	5.6	0.3	
SLAM1933_69.FIN2	59.9	1.34	0.724	0.033	0.0839	0.0021	0.467	548	20	519	13	647	96	519.0	13.0	5.3	
SLAM1933_70.FIN2	322.2	2.10	0.381	0.014	0.0508	0.0014	0.580	326	10	319.5	8.3	381	64	319.5	8.3	2.0	
SLAM1933_71.FIN2	91.7	1.47	0.592	0.027	0.0728	0.0021	0.475	471	18	453	13	543	85	453.0	13.0	3.8	
SLAM1933_72.FIN2	543	2.78	0.994	0.026	0.1136	0.0021	0.624	699	13	693	12	722	40	693.0	12.0	0.9	
SLAM1933_73.FIN2	240	5.27	0.433	0.011	0.05798	0.00071	0.293	364.9	7.8	363.3	4.3	364	54	363.3	4.3	0.4	
SLAM1933_74.FIN2	115.3	1.87	1.017	0.025	0.1148	0.0016	0.275	710	13	700.5	9.2	720	53	700.5	9.2	1.3	

Table S2: Zircon (U-Th)/He data from Amorgos Island, SE Cyclades, Greece.

Table S2: Zircon (U-Th)/He data ages from Amorgos Island, SE Cyclades, Greece

Lithology	Sample	Age, Ma	err., Ma	U (ppm)	Th (ppm)	147Sm (ppm)	[U]e	Th/U	He (nmol/g)	mass (ug)	Ft	ESR
quartzite/clast	zSLAM-1902-1	17.0	1.36	161.3	50.1	23.7	172.9	0.31	12.0	4.62	0.75	47.20
"	zSLAM-1902-2	16.2	1.29	209.6	53.8	15.2	222.1	0.26	15.0	5.38	0.77	51.21
"	zSLAM-1902-3	5.2	0.42	169.4	149.8	23.0	204.0	0.88	4.2	4.75	0.74	44.99
"	zSLAM-1902-4	47.2	3.78	73.0	35.3	14.4	81.2	0.48	15.4	3.79	0.74	45.07
quartz-mica/clast	zSLAM-1903-1	15.0	1.20	116.6	99.3	34.4	139.6	0.85	7.8	2.38	0.69	37.03
"	zSLAM-1903-2	17.8	1.42	98.2	63.7	7.7	112.9	0.65	8.4	7.10	0.78	53.18
"	zSLAM-1903-3	14.9	1.20	518.1	230.1	35.9	571.3	0.44	32.1	2.28	0.70	37.53
"	zSLAM-1903-4	15.2	1.22	322.7	41.2	21.4	332.3	0.13	19.3	2.55	0.71	38.04
metaconglomerate	zSLAM-1904-1	17.9	1.43	176.3	51.7	8.9	188.3	0.29	14.1	6.16	0.77	51.20
"	zSLAM-1904-2	100.7	8.06	34.4	16.9	14.2	38.4	0.49	15.5	3.86	0.74	44.22
"	zSLAM-1904-3	22.1	1.77	53.6	46.8	35.9	64.6	0.87	5.1	1.52	0.66	33.81
"	zSLAM-1904-4	12.6	1.01	60.4	25.4	15.4	66.3	0.42	3.3	3.54	0.74	44.18
metaflysch	zSLAM-1909-1	19.2	1.54	115.9	72.6	10.0	132.6	0.63	9.7	2.72	0.70	38.67
"	zSLAM-1909-3	29.7	2.37	768.0	114.0	4.8	794.2	0.15	98.8	5.64	0.78	51.45
"	zSLAM-1909-4	36.4	2.91	618.2	289.1	14.2	684.8	0.47	92.7	1.93	0.69	36.44
"	zSLAM-1916-2	12.5	1.00	384.3	56.3	14.3	397.3	0.15	18.5	1.91	0.69	35.84
"	zSLAM-1916-3	15.0	1.20	132.0	79.6	25.3	150.5	0.60	8.9	3.24	0.73	43.07
"	zSLAM-1916-4	16.5	1.32	532.6	238.3	8.6	587.5	0.45	40.5	6.38	0.77	51.02
"	zSLAM-1920-1	17.8	1.42	86.8	25.0	4.4	92.6	0.29	6.9	6.18	0.78	52.03
"	zSLAM-1920-2	24.8	1.98	133.7	62.2	11.7	148.1	0.46	13.8	2.34	0.70	37.70
"	zSLAM-1920-3	33.2	2.66	549.8	193.6	10.4	594.4	0.35	76.0	2.62	0.71	39.68
"	zSLAM-1920-4	44.9	3.59	270.6	175.8	9.5	311.1	0.65	54.4	2.88	0.72	41.31
metaconglomerate/matrix	zSLAM-1922-1	17.2	1.38	130.4	49.6	12.9	141.9	0.38	9.9	4.23	0.75	46.53
"	zSLAM-1922-2	13.2	1.06	264.9	44.9	22.8	275.3	0.17	13.9	2.40	0.71	38.63
"	zSLAM-1922-3	23.1	1.85	119.3	121.5	8.8	147.4	1.02	13.4	3.10	0.72	42.84
"	zSLAM-1922-4	17.8	1.42	218.1	163.0	10.7	255.7	0.75	17.4	2.55	0.71	39.67
"	zSLAM-1925-1	14.8	1.18	87.7	55.6	13.1	100.5	0.63	6.0	4.18	0.74	45.59
"	zSLAM-1925-2	14.2	1.13	122.7	52.2	20.1	134.8	0.43	7.3	2.72	0.71	39.39
"	zSLAM-1925-3	12.7	1.02	121.2	45.6	0.0	131.8	0.38	6.3	2.53	0.70	37.89
"	zSLAM-1925-4	6.3	0.50	226.6	56.6	-14.4	239.5	0.25	5.6	1.89	0.69	36.45
metaflysch	zSLAM-1931-1	17.5	1.40	367.9	99.1	0.0	390.7	0.27	28.2	4.82	0.76	49.19
"	zSLAM-1931-2	19.4	1.55	452.0	214.1	18.5	501.4	0.47	37.8	2.96	0.72	41.06
"	zSLAM-1931-3	18.2	1.45	233.2	120.1	5.2	260.9	0.51	19.6	5.22	0.76	49.81
"	zSLAM-1931-4	32.5	2.60	207.3	77.6	11.2	225.2	0.37	30.2	4.87	0.76	49.19

Appendix B

Supplementary material for the Chapter IV

Figure S1: a) View of the contacts between the ultramylonitic marble and the underlying Lower Schists (yellow dashed line) and the overlying Marble Fm. (orange dashed line) (*36°49'41.43" N 25°27'40.13" E*), b) S-trending stretching lineation from the ultramylonitic marble (*36°49'22.70"N 25°27'9.53"E*) and c) Panoramic view of the contact between the ultramylonitic marble and the Marble Fm. (red dashed line), observed along the southern coastline of Iraklia (*36°49'35.84" N 25°28'29.85" E*).

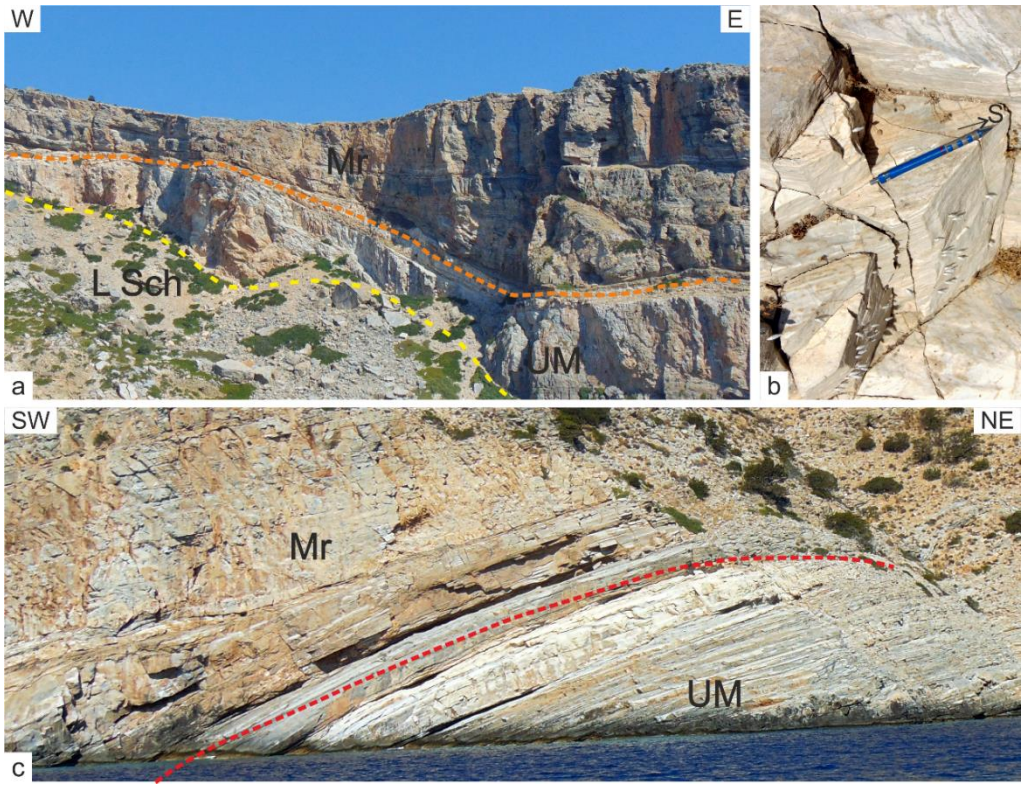

Figure S2: Mosaic photos of detrital zircon grains from the collected samples from Iraklia Island: a) IRA_1512, b) IRA_1802 and c) IRA_1511.

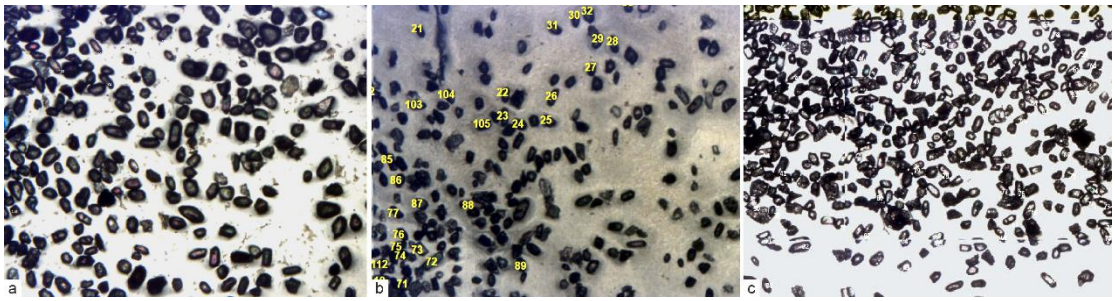

Figure S3: Representative photos of collected samples from Iraklia island: a) Precambrian quartz-mica schist (*36°50'14.50" N 25°27'22.24" E*), b) Middle-Late Triassic quartz-mica schist (*36°50'1.62" N 25°27'42.06" E*), c) Middle-Late Triassic paragneiss (*36°49'22.71" N 25°27'6.58" E*), and d) Late Cretaceous quartz-mica schist (*36°49'54.59" N 25°25'51.07" E*)

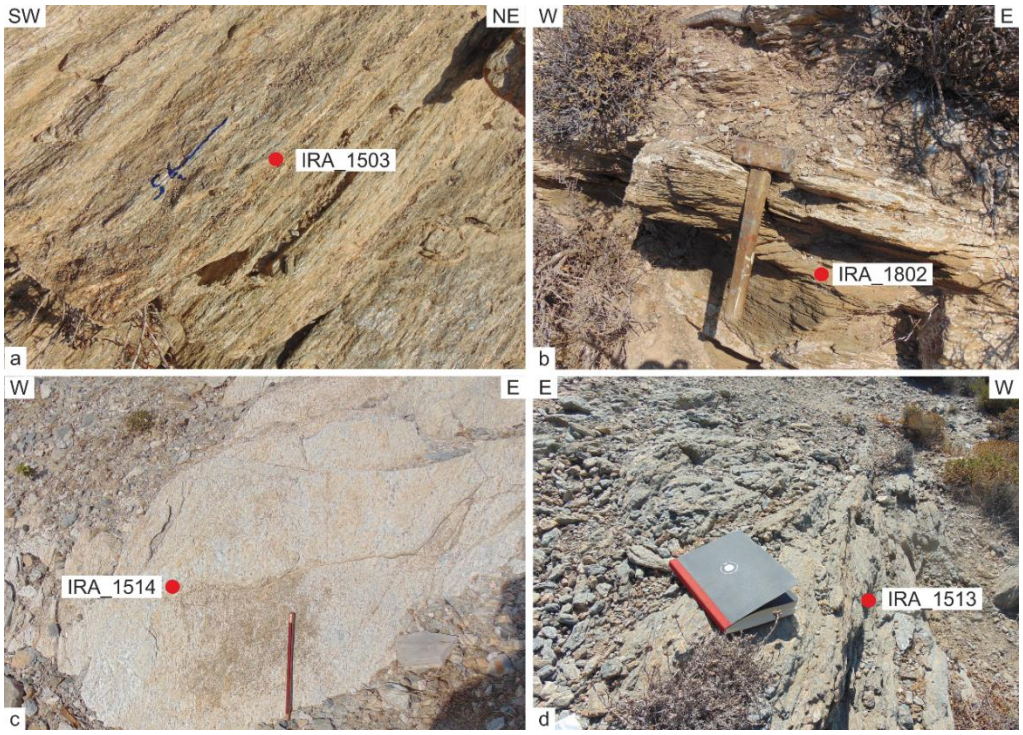

Figure S4: Rim ages and MSWDs calculated by the weighted mean of $^{206}Pb/^{238}U$ ages for concordance. IsoplotR was used for calculations [136]

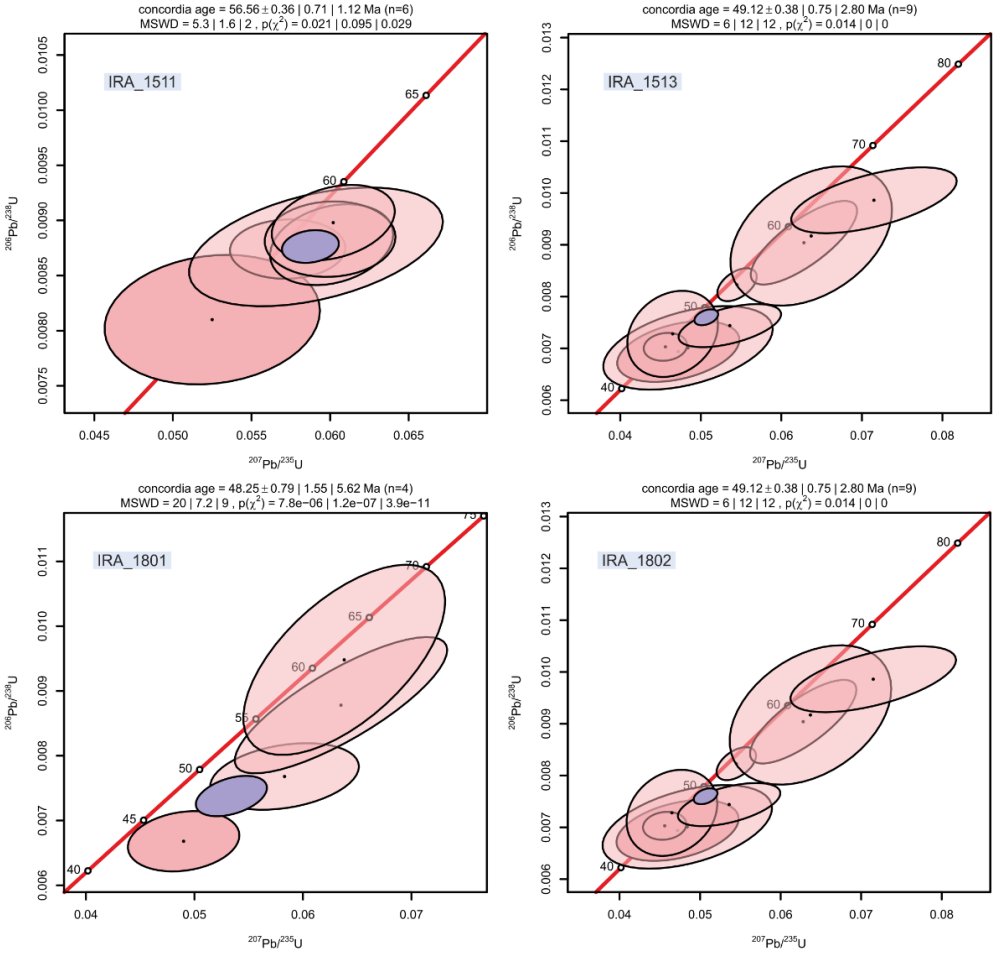

Table S1: U-Pb detrital zircon analyses from Iraklia Island, central Cyclades, Greece

Sample Name:	IRA1503							207/235		206/238		207/206		Best age			
Grain	[U] ppm	U/Th	207/235	2σ error	206/238	2σ error	RHO	Age (Ma)	2σ error	Age (Ma)	2σ error	Age (Ma)	2σ error	(Ma)	2σ error	Th/U	Rim
IRA1503_76.FIN2	364	1.86	0.435	0.026	0.053	0.0024	0.82468	365	18	333	15	592	78	333	15	0.537634	
IRA1503_106.FIN2	490	0.624	0.7378	0.008	0.08997	0.00071	0.33489	561.3	4.7	555.3	4.2	584	26	555.3	4.2	1.602564	
IRA1503_119.FIN2	295.4	0.5125	0.759	0.012	0.0913	0.00069	0.25195	573	6.8	563.2	4	1999	33	563.2	4	1.95122	
IRA1503_68.FIN2	238	1.464	0.762	0.014	0.0921	0.0011	0.4409	574.3	8.1	567.7	6.5	599	36	567.7	6.5	0.68306	
IRA1503_89.FIN2	336	0.643	0.798	0.017	0.0955	0.0013	0.41419	594.3	9.5	587.7	7.6	618	40	587.7	7.6	1.55521	
IRA1503_114.FIN2	195	0.292	0.782	0.018	0.0955	0.0012	0.012496	586	10	587.8	7.2	569	56	587.8	7.2	3.424658	
IRA1503_59.FIN2	280	0.875	0.796	0.012	0.0964	0.0011	0.41738	594.5	6.5	593.2	6.2	582	32	593.2	6.2	1.142857	
IRA1503_81.FIN2	86.3	0.665	0.791	0.021	0.0982	0.0012	0.14376	595	12	603.8	6.9	560	62	603.8	6.9	1.503759	
IRA1503_17.FIN2	173.3	1.172	0.843	0.015	0.10137	0.00097	0.17151	621.2	8.2	623.5	5.7	597	37	623.5	5.7	0.853242	
IRA1503_58.FIN2	1590	1.034	0.852	0.014	0.1017	0.0017	0.054391	625.4	7.9	624.3	9.8	595	31	624.3	9.8	0.967118	
IRA1503_94.FIN2	148	1.34	0.864	0.02	0.1017	0.0015	0.31631	634	11	625.4	9.1	654	49	625.4	9.1	0.746269	
IRA1503_78.FIN2	102.2	2.3	0.897	0.036	0.1027	0.0026	0.049392	649	19	630	15	731	96	630	15	0.434783	
IRA1503_20.FIN2	88.4	0.702	0.873	0.021	0.1042	0.0013	0.25692	638	12	638.8	7.5	639	47	638.8	7.5	1.424501	
IRA1503_24.FIN2	418	1.182	0.87	0.014	0.1042	0.0011	0.65647	635	7.8	639.7	6.3	620	26	639.7	6.3	0.846024	
IRA1503_69.FIN2	141.3	1.256	0.876	0.017	0.1051	0.0011	0.27081	639.6	8.8	644	6.5	623	35	644	6.5	0.796178	
IRA1503_113.FIN2	466	0.496	1.002	0.021	0.1115	0.0019	0.85239	704	10	682	11	785	37	682	11	2.016129	
IRA1503_82.FIN2	108.9	1.114	1.039	0.03	0.1128	0.002	0.53161	723	14	689	12	845	50	689	12	0.897666	
IRA1503_73.FIN2	204	1.58	1.013	0.028	0.1133	0.0023	0.63584	708	14	692	14	774	46	692	14	0.632911	
IRA1503_110.FIN2	227	1.25	0.997	0.015	0.1152	0.0011	0.17652	701.5	7.6	702.9	6.2	705	33	702.9	6.2	0.8	
IRA1503_46.FIN2	88.9	0.602	1	0.023	0.1157	0.0017	0.4769	703	12	706	10	682	43	706	10	1.66113	
IRA1503_120.FIN2	98.8	0.714	1.04	0.029	0.119	0.0017	0.38434	724	15	724.4	9.6	594	57	724.4	9.6	1.40056	
IRA1503_8.FIN2	67.6	1.314	1.147	0.039	0.1218	0.0022	0.30744	776	18	741	12	870	67	741	12	0.761035	
IRA1503_25.FIN2	50.6	1.209	1.131	0.04	0.1221	0.0023	0.11621	769	18	742	13	833	82	742	13	0.82713	
IRA1503_16.FIN2	564	2.132	1.138	0.014	0.1266	0.0011	0.72557	771.4	6.4	768.6	6.3	782	20	768.6	6.3	0.469043	
IRA1503_101.FIN2	76	0.5174	1.185	0.036	0.1281	0.002	0.41856	794	16	777	11	832	57	777	11	1.932741	
IRA1503_38.FIN2	196.8	0.765	1.167	0.019	0.1283	0.0014	0.51246	784.4	8.8	778.1	8.2	798	29	778.1	8.2	1.30719	
IRA1503_49.FIN2	110.9	0.911	1.158	0.032	0.1289	0.0017	0.27973	781	15	783	9.3	749	59	783	9.3	1.097695	
IRA1503_56.FIN2	168	0.919	1.182	0.024	0.1295	0.0015	0.43321	792	11	785.1	8.5	803	40	785.1	8.5	1.088139	
IRA1503_92.FIN2	271	0.9003	1.191	0.02	0.1297	0.0013	0.6245	795.6	9.3	786.2	7.6	805	30	786.2	7.6	1.110741	
IRA1503_47.FIN2	311	1.02	1.198	0.021	0.1306	0.0014	0.32383	799.1	9.6	791.2	8.2	807	36	791.2	8.2	0.980392	
IRA1503_71.FIN2	85.5	1.158	1.224	0.024	0.1312	0.0016	0.12852	810	11	794.6	9.2	874	46	794.6	9.2	0.863558	
IRA1503_61.FIN2	104.3	0.616	1.227	0.024	0.1318	0.0014	0.36326	811	11	797.7	8.1	841	39	797.7	8.1	1.623377	
IRA1503_53.FIN2	174.6	0.465	1.249	0.023	0.1327	0.0017	0.24092	821	10	804.1	9.8	837	39	804.1	9.8	2.150538	
IRA1503_10.FIN2	193	1.319	1.226	0.018	0.1329	0.0013	0.26239	812.7	8	804.3	7.4	847	32	804.3	7.4	0.75815	
IRA1503_12.FIN2	405	1.632	1.226	0.015	0.13302	0.00095	0.68859	811.8	6.8	805	5.4	837	22	805	5.4	0.612745	
IRA1503_90.FIN2	129.4	1.219	1.219	0.03	0.1331	0.0016	0.2895	809	14	805.5	9.1	797	46	805.5	9.1	0.820345	
IRA1503_50.FIN2	221.5	0.962	1.216	0.019	0.1333	0.0017	0.44719	806.9	8.5	808	10	799	30	808	10	1.039501	
IRA1503_44.FIN2	345	1.097	1.22	0.019	0.1335	0.0013	0.3788	808.9	8.4	808.4	7.4	810	36	808.4	7.4	0.911577	
IRA1503_67.FIN2	241.6	1.577	1.206	0.016	0.1341	0.0012	0.18648	803.6	7.4	811	6.8	776	32	811	6.8	0.634115	
IRA1503_45.FIN2	494	0.768	1.217	0.014	0.13415	0.00098	0.37697	808.5	6.2	812.1	5.7	799	22	812.1	5.7	1.302083	
IRA1503_43.FIN2	656	1.184	1.225	0.012	0.1348	0.001	0.44924	811.7	5.6	815.2	5.7	791	19	815.2	5.7	0.844595	
IRA1503_33.FIN2	163	0.748	1.23	0.021	0.1353	0.0013	0.17941	813.5	9.7	817.8	7.3	809	40	817.8	7.3	1.336898	
IRA1503_91.FIN2	905	1.563	1.263	0.012	0.1364	0.001	0.5395	829.1	5.3	824.2	5.7	833	16	824.2	5.7	0.639795	
IRA1503_87.FIN2	120.8	0.682	1.237	0.027	0.1371	0.0013	0.11002	816	12	828.1	7.3	783	43	828.1	7.3	1.466276	
IRA1503_105.FIN2	335	1.07	1.343	0.021	0.1387	0.0017	0.57875	863.7	9.1	838	10	945	27	838	10	0.934579	
IRA1503_54.FIN2	276	0.969	1.304	0.017	0.14	0.0012	0.29618	846.6	7.7	844.4	6.5	817	29	844.4	6.5	1.031992	
IRA1503_99.FIN2	140	1.302	1.305	0.02	0.14	0.0011	0.084995	848.1	8.4	844.7	6.2	850	35	844.7	6.2	0.768049	
IRA1503_3.FIN2	158	2.345	1.431	0.026	0.1524	0.002	0.35439	902	11	914	11	867	38	867	38	0.426439	

IRA1503_104.FIN2	143.9	0.715	1.367	0.023	0.1435	0.0012	0.26849	875.6	9.5	864.2	6.5	897	31	897	31	1.398601
IRA1503_21.FIN2	77.6	0.538	1.381	0.03	0.1458	0.0018	0.38691	879	13	877	10	902	45	902	45	1.858736
IRA1503_26.FIN2	176	1.172	1.466	0.021	0.1519	0.0013	0.28275	915.3	8.9	911.6	7.2	916	31	916	31	0.853242
IRA1503_84.FIN2	271	4.823	1.554	0.02	0.161	0.0011	0.34202	952.9	8.2	963.1	6	926	28	926	28	0.20734
IRA1503_40.FIN2	453	5.9	1.71	0.02	0.1735	0.0016	0.39105	1011.6	7.7	1031	9	968	23	968	23	0.169492
IRA1503_34.FIN2	339	0.97	1.596	0.026	0.1622	0.0018	0.66794	969.3	9.9	969	10	970	26	970	26	1.030928
IRA1503_57.FIN2	332.2	3.561	1.647	0.021	0.1645	0.0013	0.38496	989.6	8.2	981.7	7.1	976	26	976	26	0.28082
IRA1503_31.FIN2	287.1	1.84	1.685	0.019	0.1688	0.0014	0.53223	1002.3	7.2	1005.4	7.8	983	21	983	21	0.543478
IRA1503_30.FIN2	387	1.029	1.76	0.019	0.1742	0.0015	0.4226	1030.5	6.9	1035.3	8.5	1019	23	1019	23	0.971817
IRA1503_1.FIN2	71.4	0.836	1.786	0.036	0.1734	0.0024	0.40497	1040	13	1031	13	1069	35	1069	35	1.196172
IRA1503_65.FIN2	251	0.937	2.682	0.053	0.2119	0.0031	0.60218	1324	14	1239	17	1466	30	1466	30	1.067236
IRA1503_62.FIN2	42.41	1.325	2.691	0.081	0.2113	0.0041	0.27357	1333	22	1235	22	1510	62	1510	62	0.754717
IRA1503_19.FIN2	235	5.79	5.371	0.038	0.346	0.0023	0.53112	1879.8	6	1916	11	1837	13	1837	13	0.172712
IRA1503_79.FIN2	552	6.03	5.25	0.047	0.3356	0.0029	0.60773	1860.5	7.6	1865	14	1858	15	1858	15	0.165837
IRA1503_4.FIN2	346	3.108	5.008	0.068	0.3188	0.0046	0.61844	1820	11	1783	22	1874	21	1874	21	0.32175
IRA1503_22.FIN2	245.3	5.82	5.734	0.059	0.3588	0.0029	0.54854	1935.8	9	1978	13	1881	18	1881	18	0.171821
IRA1503_112.FIN2	296	5.47	5.463	0.045	0.3465	0.0032	0.54713	1894.2	7.1	1917	15	1882	14	1882	14	0.182815
IRA1503_37.FIN2	493	3.8	5.569	0.042	0.3516	0.0024	0.61868	1912.1	6.6	1943	11	1886	12	1886	12	0.263158
IRA1503_111.FIN2	143.2	4.151	6.166	0.056	0.3711	0.0028	0.53637	1998.8	7.9	2034	13	1972	14	1972	14	0.240906
IRA1503_86.FIN2	128.3	1.503	4.613	0.092	0.2706	0.0032	0.41474	1749	17	1544	16	1986	33	1986	33	0.665336
IRA1503_118.FIN2	244.1	2.15	6.23	0.1	0.3666	0.0044	0.70358	2007	14	2013	21	904	20	1999	20	0.465116
IRA1503_88.FIN2	430	3.43	6.395	0.097	0.3683	0.0039	0.6732	2030	13	2021	18	2038	18	2038	18	0.291545
IRA1503_98.FIN2	74.6	0.5035	6.3	0.11	0.3622	0.005	0.57919	2019	16	1996	24	2048	28	2048	28	1.986097
IRA1503_4.FIN2	596	11.6	6.988	0.092	0.3674	0.0032	0.62124	2114	12	2017	15	2200	19	2200	19	0.086207
IRA1503_6.FIN2	41.84	1.223	10.13	0.21	0.4666	0.0087	0.74327	2442	19	2470	39	2420	24	2420	24	0.817661
IRA1503_102.FIN2	30	2.13	9.46	0.19	0.435	0.007	0.66823	2389	19	2326	31	2434	25	2434	25	0.469484
IRA1503_60.FIN2	586	2.65	9.686	0.099	0.4411	0.0029	0.58532	2405.2	9.5	2355	13	2434	13	2434	13	0.377358
IRA1503_63.FIN2	130.4	1.157	8.33	0.1	0.3768	0.0038	0.54835	2268	11	2061	18	2445	19	2445	19	0.864304
IRA1503_28.FIN2	281.1	3.856	8.34	0.13	0.376	0.0065	0.8038	2268	14	2057	30	2457	18	2457	18	0.259336
IRA1503_36.FIN2	430	6.23	8.319	0.087	0.374	0.0044	0.50034	2266.1	9.5	2048	21	2469	20	2469	20	0.160514
IRA1503_5.FIN2	89.5	0.794	10.36	0.14	0.4675	0.0047	0.71185	2465	12	2472	20	2469	18	2469	18	1.259446
IRA1503_75.FIN2	119.9	1.856	9.411	0.093	0.4247	0.0039	0.60344	2378.2	9.1	2281	17	2472	16	2472	16	0.538793
IRA1503_13.FIN2	226	1.87	9.157	0.096	0.4087	0.0036	0.71719	2354.4	9.3	2211	16	2479	13	2479	13	0.534759
IRA1503_51.FIN2	135.7	0.6081	10.881	0.085	0.4815	0.0036	0.59952	2512.3	7.3	2533	16	2480	12	2480	12	1.644466
IRA1503_39.FIN2	627.5	1.304	9.94	0.11	0.4453	0.0046	0.58167	2430.5	9.4	2374	20	2481	15	2481	15	0.766871
IRA1503_96.FIN2	23.03	8.4	10.47	0.35	0.466	0.016	0.77819	2475	30	2459	71	2483	41	2483	41	0.119048
IRA1503_41.FIN2	159.1	0.714	9.7	0.12	0.4331	0.0045	0.34635	2405	11	2319	20	2484	16	2484	16	1.40056
IRA1503_83.FIN2	278	3.64	9.29	0.15	0.4106	0.0048	0.75039	2366	15	2217	22	2496	17	2496	17	0.274725
IRA1503_48.FIN2	684	7.21	10.15	0.11	0.4442	0.005	0.77091	2448	10	2369	22	2498	15	2498	15	0.138696
IRA1503_70.FIN2	311.4	0.992	10.372	0.078	0.457	0.0042	0.59252	2469.6	7.4	2426	19	2511	13	2511	13	1.008065
IRA1503_27.FIN2	285	4.25	10.86	0.12	0.4729	0.0046	0.79467	2511	10	2496	20	2515	12	2515	12	0.235294
IRA1503_77.FIN2	1262	9.2	9.84	0.07	0.4292	0.0031	0.5643	2419.7	6.6	2302	14	2520	12	2520	12	0.108696
IRA1503_7.FIN2	100.8	0.74	11.43	0.12	0.497	0.0046	0.22348	2557.6	9.6	2600	20	2523	15	2523	15	1.351351
IRA1503_85.FIN2	64.3	0.516	11.15	0.11	0.4798	0.0045	0.62098	2535.7	9.6	2526	20	2530	15	2530	15	1.937984
IRA1503_55.FIN2	541	1.123	10.776	0.068	0.4641	0.0032	0.53944	2503.6	5.9	2457	14	2531	11	2531	11	0.890472
IRA1503_29.FIN2	858	16.99	11.204	0.08	0.4853	0.0043	0.72478	2540.5	6.7	2552	19	2533.7	9.8	2533.7	9.8	0.058858
IRA1503_80.FIN2	220	1.98	11.15	0.17	0.4819	0.0064	0.77491	2533	14	2534	28	2534	17	2534	17	0.505051
IRA1503_66.FIN2	280.6	2.55	11.349	0.081	0.4887	0.0035	0.66726	2551.6	6.7	2565	15	2535	10	2535	10	0.392157
IRA1503_15.FIN2	529	1.153	11.703	0.081	0.5069	0.0041	0.81404	2581.1	6.4	2643	17	2538.5	8.9	2538.5	8.9	0.867303
IRA1503_100.FIN2	72.8	0.769	11.06	0.13	0.4798	0.0047	0.60234	2530	11	2525	21	2539	15	2539	15	1.30039
IRA1503_107.FIN2	141.6	0.792	10.98	0.11	0.4733	0.005	0.59823	2522.9	9.7	2497	22	2540	15	2540	15	1.262626
IRA1503_23.FIN2	152.5	1.379	11.78	0.1	0.5075	0.004	0.65915	2588.8	8.1	2646	17	2540	11	2540	11	0.725163
IRA1503_11.FIN2	164	1.46	10.94	0.15	0.4693	0.0059	0.80896	2517	13	2479	26	2544	14	2544	14	0.684932
IRA1503_93.FIN2	301	3.35	12.16	0.19	0.5	0.01	0.588	2615	15	2613	44	2618	27	2618	27	0.298507
IRA1503_14.FIN2	1229	5.33	12.824	0.099	0.5155	0.0035	0.21985	2666.1	7.3	2680	15	2652	13	2652	13	0.187617
IRA1503_42.FIN2	35.6	0.663	13.39	0.23	0.5214	0.0099	0.77014	2707	16	2702	42	2700	21	2700	21	1.508296
IRA1503_64.FIN2	198	9.6	13.52	0.16	0.5251	0.0074	0.7929	2718	12	2719	31	2709	14	2709	14	0.104167
IRA1503_32.FIN2	793	10.15	13.861	0.094	0.5243	0.0041	0.59898	2741	6.4	2717	17	2752	11	2752	11	0.098522
IRA1503_109.FIN2	877	4.07	13.09	0.11	0.4934	0.0034	0.62329	2685.9	7.7	2585	15	2760	10	2760	10	0.2457
IRA1503_116.FIN2	275.7	0.91	15.76	0.13	0.5661	0.0044	0.71284	2861.6	7.7	2891	18	2846	11	2846	11	1.098901

Sample Name:	IRA1511							207/235		206/238		207/206		Best age			
Grain	[U] ppm	U/Th	207/235	2σ error	206/238	2σ error	RHO	Age (Ma)	2σ error	Age (Ma)	2σ error	Age (Ma)	2σ error	(Ma)	2σ error	Th/U	Rim
IRA_1511_1.FIN71	284	2.27	0.0525	0.0028	0.0081	0.00024	0.13789	51.9	2.7	52	1.6	110	120	52	1.6	0.440529	rim
IRA_1511_1.FIN114	631	1.323	0.0573	0.0015	0.00874	0.00011	0.042912	56.5	1.4	56.1	0.69	47	52	56.1	0.69	0.755858	rim
IRA_1511_1.FIN125	528	1.126	0.0591	0.0033	0.00876	0.00022	0.42444	58.3	3.2	56.2	1.4	170	120	56.2	1.4	0.888099	rim
IRA_1511_1.FIN113	744	1.21	0.0601	0.0016	0.00878	0.00015	0.25746	59.2	1.5	56.36	0.99	143	58	56.36	0.99	0.826446	rim
IRA_1511_1.FIN161	653	1.014	0.06	0.0017	0.00883	0.00014	0.0584	59.1	1.7	56.64	0.87	160	75	56.64	0.87	0.986193	rim
IRA_1511_1.FIN150	684	1.07	0.0602	0.0016	0.00898	0.00014	0.30016	59.3	1.5	57.62	0.9	115	55	57.62	0.9	0.934579	rim
IRA_1511_1.FIN14	278.7	1.829	0.0774	0.0033	0.01115	0.0004	0.067286	75.7	3.1	71.4	2.5	180	110	71.4	2.5	0.546747	
IRA_1511_1.FIN75	335	1.595	0.074	0.0024	0.01143	0.00021	0.025088	72.4	2.3	73.2	1.3	48	76	73.2	1.3	0.626959	
IRA_1511_1.FIN135	732	14.86	0.086	0.0045	0.0126	0.0005	0.64537	83.7	4.2	80.7	3.2	227	98	80.7	3.2	0.067295	
IRA_1511_1.FIN77	1122	4.1	0.0881	0.0089	0.01297	0.00057	0.85745	85.7	8.3	83	3.6	140	150	83	3.6	0.243902	
IRA_1511_1.FIN94	680	0.937	0.0914	0.0026	0.01303	0.00022	0.2166	88.8	2.4	83.5	1.4	217	66	83.5	1.4	1.067236	
IRA_1511_1.FIN131	1003	19.7	0.0852	0.0073	0.01324	0.0006	0.13904	82.9	6.8	84.8	3.8	50	190	84.8	3.8	0.050761	
IRA_1511_1.FIN142	1120	10.3	0.1007	0.0083	0.0147	0.0012	0.64178	97.4	7.6	94.2	7.5	100	150	94.2	7.5	0.097087	
IRA_1511_1.FIN96	677	13.9	0.1373	0.007	0.0195	0.0012	0.48043	130.6	6.2	124.3	7.5	240	130	124.3	7.5	0.071942	
IRA_1511_1.FIN36	1188	11.5	0.147	0.012	0.02049	0.0008	0.64923	139	10	130.8	5.1	270	240	130.8	5.1	0.086957	
IRA_1511_1.FIN101	802	4.48	0.176	0.015	0.0236	0.0012	0.61229	165	13	150.2	7.5	370	200	150.2	7.5	0.223214	
IRA_1511_1.FIN90	801	81	0.17	0.014	0.0246	0.0018	0.86082	160	12	156	11	240	110	156	11	0.012346	
IRA_1511_1.FIN22	304	1.809	0.174	0.0039	0.02458	0.00044	0.24654	162.8	3.4	156.5	2.8	267	56	156.5	2.8	0.552792	
IRA_1511_1.FIN26	906	2.75	0.1694	0.0099	0.02497	0.00059	0.56948	158.8	8.6	159	3.7	174	97	159	3.7	0.363636	
IRA_1511_1.FIN88	527	3.89	0.1813	0.0084	0.0252	0.001	0.14779	169.1	7.3	160.3	6.5	250	130	160.3	6.5	0.257069	
IRA_1511_1.FIN132	474	5.77	0.177	0.0042	0.02532	0.00041	0.385	166	3.8	161.2	2.6	251	61	161.2	2.6	0.17331	
IRA_1511_1.FIN78	179	1.015	0.1836	0.0056	0.02577	0.00037	0.20454	171	4.8	164	2.3	272	73	164	2.3	0.985222	
IRA_1511_1.FIN29	315	2.78	0.219	0.013	0.0292	0.0014	0.67111	201	11	185.8	9	380	110	185.8	9	0.359712	
IRA_1511_1.FIN55	907.7	0.954	0.2006	0.0053	0.02994	0.00052	0.27417	185.6	4.5	190.2	3.3	123	58	190.2	3.3	1.048218	
IRA_1511_1.FIN41	1010	13.19	0.2427	0.0083	0.03197	0.00063	0.53937	220.5	6.8	202.9	4	394	72	202.9	4	0.075815	
IRA_1511_1.FIN126	2870	2.39	0.251	0.013	0.0327	0.002	0.94511	227	10	208	12	424	46	208	12	0.41841	
IRA_1511_1.FIN51	361	2.298	0.2436	0.0066	0.03363	0.00087	0.66208	221.2	5.4	213.2	5.4	314	52	213.2	5.4	0.435161	
IRA_1511_1.FIN143	471	1.084	0.2457	0.0053	0.03367	0.00065	0.47128	222.9	4.3	213.5	4	292	48	213.5	4	0.922509	
IRA_1511_1.FIN104	101.4	1.161	0.2371	0.0082	0.03425	0.00063	0.07428	215.7	6.7	217.1	4	221	79	217.1	4	0.861326	
IRA_1511_1.FIN102	840	3.02	0.272	0.011	0.03527	0.00068	0.42731	244.5	9	223.4	4.2	399	65	223.4	4.2	0.331126	
IRA_1511_1.FIN162	371	3.44	0.2647	0.0063	0.03543	0.00063	0.47823	238.3	5.1	224.5	3.9	349	51	224.5	3.9	0.290698	
IRA_1511_1.FIN62	41	0.916	0.279	0.015	0.03695	0.00096	0.017218	250	12	233.8	6	380	130	233.8	6	1.091703	
IRA_1511_1.FIN80	258	1.312	0.2704	0.0058	0.03789	0.00051	0.60996	242.8	4.6	239.7	3.2	260	42	239.7	3.2	0.762195	
IRA_1511_1.FIN27	300	2.03	0.2589	0.0051	0.03812	0.00051	0.12255	234.3	4	241.1	3.2	188	53	241.1	3.2	0.492611	
IRA_1511_1.FIN46	761	91.9	0.2972	0.0084	0.0404	0.0023	0.083347	264.2	6.6	256	14	334	92	256	14	0.010881	
IRA_1511_1.FIN20	495	4.34	0.2971	0.0046	0.0415	0.00043	0.43704	264	3.6	262.1	2.7	281	33	262.1	2.7	0.230415	
IRA_1511_1.FIN57	900	7.22	0.323	0.012	0.0429	0.0017	0.76844	283.9	9	271	11	433	83	271	11	0.138504	
IRA_1511_1.FIN97	325	1.85	0.3156	0.0083	0.0441	0.001	0.69211	280.5	6.4	278.3	6.4	289	45	278.3	6.4	0.540541	
IRA_1511_1.FIN92	783	3.53	0.3178	0.0069	0.04439	0.0009	0.58035	280.1	5.3	280	5.6	290	60	280	5.6	0.283286	
IRA_1511_1.FIN130	103.4	0.868	0.311	0.01	0.04499	0.00097	0.017567	274.2	7.8	283.6	6	181	76	283.6	6	1.152074	
IRA_1511_1.FIN7	440	1.305	0.3523	0.0073	0.04526	0.00052	0.37098	306.2	5.5	285.3	3.2	495	40	285.3	3.2	0.766284	
IRA_1511_1.FIN43	843	48.7	0.349	0.013	0.0453	0.0015	0.83672	303.7	9.9	285.5	9.4	476	67	285.5	9.4	0.020534	
IRA_1511_1.FIN21	1001	3.08	0.336	0.012	0.04548	0.00087	0.62938	294.2	9.1	286.7	5.4	339	64	286.7	5.4	0.324675	
IRA_1511_1.FIN144	253	2.09	0.3504	0.0067	0.04596	0.00064	0.35028	304.8	5	289.6	3.9	410	42	289.6	3.9	0.478469	
IRA_1511_1.FIN13	34.1	0.805	0.355	0.018	0.0465	0.0012	0.15723	309	13	293.2	7.2	440	110	293.2	7.2	1.242236	
IRA_1511_1.FIN56	347	16	0.343	0.011	0.0473	0.0012	0.74967	300.2	8.3	297.7	7.2	348	52	297.7	7.2	0.0625	
IRA_1511_1.FIN122	370	1.892	0.3504	0.0075	0.04752	0.00059	0.40401	305.5	5.8	299.2	3.6	328	47	299.2	3.6	0.528541	
IRA_1511_1.FIN95	124.1	1.154	0.348	0.01	0.0476	0.00089	0.31388	303.2	7.8	299.8	5.5	329	69	299.8	5.5	0.866551	
IRA_1511_1.FIN136	693	78.4	0.3531	0.005	0.04805	0.00075	0.36497	307.5	3.6	302.5	4.6	333	36	302.5	4.6	0.012755	
IRA_1511_1.FIN3	428	5.08	0.356	0.012	0.0482	0.0011	0.49616	309.1	8.9	303.4	6.9	349	70	303.4	6.9	0.19685	
IRA_1511_1.FIN149	376	0.751	0.3572	0.0069	0.04827	0.00065	0.31752	309.9	5.1	303.9	4	338	44	303.9	4	1.331558	
IRA_1511_1.FIN146	89.2	1.222	0.348	0.011	0.0483	0.0011	0.017929	302.6	8.5	304.2	7	321	91	304.2	7	0.818331	
IRA_1511_1.FIN103	476.3	4.153	0.352	0.0089	0.04895	0.00073	0.36886	306.1	6.7	308.1	4.5	271	52	308.1	4.5	0.24079	
IRA_1511_1.FIN69	590	133	0.359	0.012	0.04908	0.00099	0.54869	311.1	9.1	308.9	6.1	303	70	308.9	6.1	0.007519	
IRA_1511_1.FIN25	667	1.51	0.3559	0.0068	0.04934	0.00081	0.81565	310.9	5.2	310.4	4.9	297	24	310.4	4.9	0.662252	
IRA_1511_1.FIN37	469	7.24	0.3578	0.0061	0.04932	0.00054	0.26025	311.2	4.4	310.4	3.3	309	41	310.4	3.3	0.138122	
IRA_1511_1.FIN147	801	1.54	0.3627	0.0071	0.04938	0.00081	0.67675	314	5.3	310.7	5	316	33	310.7	5	0.649351	
IRA_1511_1.FIN12	371	1.7	0.365	0.0078	0.04946	0.00066	0.44126	315.7	5.8	311.2	4.1	355	46	311.2	4.1	0.588235	
IRA_1511_1.FIN155	387	2.16	0.3682	0.0067	0.04984	0.00057	0.42988	318.1	5	313.5	3.5	360	41	313.5	3.5	0.462963	
IRA_1511_1.FIN106	527	1.758	0.365	0.006	0.0499	0.00075	0.65548	315.8	4.5	313.9	4.6	299	30	313.9	4.6	0.568828	
IRA_1511_1.FIN32	626	9.43	0.409	0.047	0.0503	0.0029	0.60479	346	32	316	18	560	170	316	18	0.106045	
IRA_1511_1.FIN24	448	1.849	0.3686	0.0082	0.0505	0.001	0.72887	319.4	6.2	317.4	6.2	279	34	317.4	6.2	0.540833	
IRA_1511_1.FIN121	171	1.346	0.3672	0.0082	0.05065	0.0008	0.27153	317.2	6.1	318.5	4.9	285	52	318.5	4.9	0.742942	
IRA_1511_1.FIN49	215	1.449	0.3663	0.0096	0.05094	0.00069	0.1254	317.8	6.9	320.3	4.3	298	61	320.3	4.3	0.690131	
IRA_1511_1.FIN81	381	2.66	0.3733	0.0051	0.05117	0.00055	0.16402	322	3.8	321.7	3.4	331	35	321.7	3.4	0.37594	
IRA_1511_1.FIN30	110.5	1.468	0.378	0.018	0.0516	0.0014	0.38078	330	14	324.5	8.8	325	93	324.5	8.8	0.681199	
IRA_1511_1.FIN124	220.1	9.92	0.3841	0.0097	0.05229	0.00095	0.40246	330.6	7.2	328.5	5.8	334	50	328.5	5.8	0.100806	
IRA_1511_1.FIN127	417	1.291	0.3757	0.0066	0.05235	0.00064	0.51127	323.7	4.9	328.9	3.9	290	34	328.9	3.9	0.774593	
IRA_1511_1.FIN151	193.3	1.343	0.374	0.012	0.0525	0.0016	0.12153	322.4	9.2	329.6	9.5	283	96	329.6	9.5	0.744602	

IRA_1511_1.FIN118	608	20.6	0.414	0.01	0.0528	0.0013	0.83046	352	7.2	331.6	8	473	37	331.6	8	0.048544
IRA_1511_1.FIN58	564	4.31	0.3911	0.0062	0.05291	0.00066	0.16554	335	4.5	332.4	4	364	38	332.4	4	0.232019
IRA_1511_1.FIN40	185.6	5.35	0.4154	0.0095	0.0549	0.0013	0.52757	352.5	6.8	344.3	7.7	370	57	344.3	7.7	0.186916
IRA_1511_1.FIN89	197.8	1.325	0.409	0.015	0.0552	0.001	0.53144	348	11	346.5	6.1	350	68	346.5	6.1	0.754717
IRA_1511_1.FIN141	722	2.03	0.409	0.0085	0.0566	0.0016	0.69848	348	6.2	355.1	9.5	333	45	355.1	9.5	0.492611
IRA_1511_1.FIN18	546	48	0.445	0.011	0.0588	0.001	0.61716	373.8	7.7	368.4	6.1	405	44	368.4	6.1	0.020833
IRA_1511_1.FIN4	189.7	1.859	0.491	0.015	0.0619	0.0018	0.78772	405	10	387	11	460	56	387	11	0.537924
IRA_1511_1.FIN154	505	3.9	0.4848	0.0076	0.0621	0.0012	0.4678	401.3	5.2	388.3	7	481	42	388.3	7	0.25641
IRA_1511_1.FIN111	250	13.62	0.479	0.013	0.0623	0.0015	0.35146	396.9	9	389.4	8.9	420	61	389.4	8.9	0.073421
IRA_1511_1.FIN137	942	61.6	0.47	0.0093	0.0634	0.0014	0.7961	391.1	6.4	396.5	8.8	335	27	396.5	8.8	0.016234
IRA_1511_1.FIN17	577	46	0.4867	0.0065	0.06351	0.00099	0.40735	402.6	4.4	396.9	6	436	37	396.9	6	0.021739
IRA_1511_1.FIN105	200	5.06	0.496	0.017	0.0636	0.0018	0.32912	409	12	397	11	452	86	397	11	0.197628
IRA_1511_1.FIN31	465	29.5	0.505	0.013	0.0641	0.0017	0.65541	414.6	8.5	400	10	483	40	400	10	0.033898
IRA_1511_1.FIN6	919	10.8	0.489	0.013	0.0647	0.002	0.51301	403.6	9.1	404	12	409	54	404	12	0.092593
IRA_1511_1.FIN64	200.1	1.981	0.515	0.013	0.0658	0.0013	0.47436	421.5	8.5	410.9	7.9	465	58	410.9	7.9	0.504796
IRA_1511_1.FIN84	784	7.83	0.502	0.01	0.0663	0.0016	0.71424	413	7.1	414.1	9.7	431	44	414.1	9.7	0.127714
IRA_1511_1.FIN67	820	3.45	0.54	0.012	0.0671	0.0014	0.45462	438.1	7.6	418.9	8.4	517	57	418.9	8.4	0.289855
IRA_1511_1.FIN8	228.6	4.34	0.543	0.011	0.06817	0.0008	0.43973	441.4	7.3	425.1	4.8	522	42	425.1	4.8	0.230415
IRA_1511_1.FIN139	639	23.3	0.553	0.011	0.0684	0.0013	0.39129	447	7.4	426.2	8	562	56	426.2	8	0.042918
IRA_1511_1.FIN129	243	6.07	0.5443	0.0093	0.06982	0.0008	0.40934	440.9	6.1	435	4.8	465	36	435	4.8	0.164745
IRA_1511_1.FIN15	566	6.25	0.578	0.018	0.0699	0.002	0.32079	463	12	435	12	578	84	435	12	0.16
IRA_1511_1.FIN63	376	2.41	0.576	0.01	0.0706	0.0011	0.4989	461.3	6.4	439.7	6.7	547	35	439.7	6.7	0.414938
IRA_1511_1.FIN42	225.9	9.54	0.578	0.013	0.073	0.0015	0.11903	462.9	8.4	454	9.3	526	72	454	9.3	0.104822
IRA_1511_1.FIN52	178	4.983	0.564	0.011	0.0733	0.001	0.39646	454.6	6.8	456.2	6.2	422	44	456.2	6.2	0.200682
IRA_1511_1.FIN73	318.2	5.79	0.5763	0.0091	0.07366	0.00098	0.45315	461.8	5.9	458.1	5.9	482	33	458.1	5.9	0.172712
IRA_1511_1.FIN159	214	5.1	0.576	0.013	0.074	0.001	0.46382	462.6	8.5	460.3	6.3	513	45	460.3	6.3	0.196078
IRA_1511_1.FIN5	297.7	5.86	0.5787	0.0083	0.0742	0.0018	0.37275	463.5	5.4	461	11	456	49	461	11	0.170648
IRA_1511_1.FIN93	290.1	5.34	0.5898	0.0076	0.07496	0.00077	0.08494	470.5	4.8	465.9	4.6	481	37	465.9	4.6	0.187266
IRA_1511_1.FIN119	260	4.33	0.604	0.022	0.0752	0.0023	0.69691	480	14	468	14	535	61	468	14	0.230947
IRA_1511_1.FIN44	369	19.9	0.609	0.018	0.076	0.0011	0.43235	483	12	471.9	6.9	549	66	471.9	6.9	0.050251
IRA_1511_1.FIN19	218	13.53	0.581	0.02	0.0761	0.0018	0.53361	468	12	473	11	438	69	473	11	0.07391
IRA_1511_1.FIN112	474	2.801	0.599	0.0075	0.07685	0.0007	0.39832	476.4	4.8	477.3	4.2	490	25	477.3	4.2	0.357015
IRA_1511_1.FIN99	256	5.108	0.648	0.013	0.0802	0.0013	0.50253	508.1	8.4	497.6	7.8	552	43	497.6	7.8	0.195771
IRA_1511_1.FIN11	183.9	2.841	0.674	0.014	0.08047	0.00093	0.007746	522.5	8.5	498.9	5.6	633	52	498.9	5.6	0.351989
IRA_1511_1.FIN108	293	2.46	0.634	0.02	0.0806	0.0029	0.74611	498	12	504	16	475	50	504	16	0.406504
IRA_1511_1.FIN33	269.6	6.87	0.63	0.025	0.0815	0.0028	0.30402	496	16	505	17	470	100	505	17	0.14556
IRA_1511_1.FIN134	103.7	0.5746	0.655	0.014	0.0819	0.0011	0.22635	511.4	8.6	507.3	6.5	529	53	507.3	6.5	1.740341
IRA_1511_1.FIN160	444	1.655	0.6845	0.0095	0.08558	0.00092	0.4409	529.3	5.7	529.3	5.4	516	33	529.3	5.4	0.60423
IRA_1511_1.FIN47	598	1.09	0.724	0.014	0.0863	0.0018	0.75136	552.5	8.2	534	11	641	35	534	11	0.917431
IRA_1511_1.FIN85	685.5	2.095	0.698	0.012	0.0867	0.0016	0.56314	537.4	6.9	535.9	9.2	575	37	535.9	9.2	0.477327
IRA_1511_1.FIN9	111	2.21	0.717	0.017	0.0878	0.0018	0.43143	548.7	9.9	543	10	626	50	543	10	0.452489
IRA_1511_1.FIN117	244	1.853	0.756	0.025	0.0884	0.0015	0.10289	571	14	546	8.9	666	76	546	8.9	0.539665
IRA_1511_1.FIN35	164	2.16	0.787	0.051	0.0895	0.0028	0.29187	588	29	553	17	720	140	553	17	0.462963
IRA_1511_1.FIN128	208.4	2.138	0.788	0.024	0.0902	0.0028	0.53994	590	14	556	17	703	61	556	17	0.467727
IRA_1511_1.FIN152	581	1.188	0.735	0.014	0.0902	0.0018	0.62663	560.5	7.8	556	10	585	35	556	10	0.841751
IRA_1511_1.FIN140	293	2.02	0.756	0.012	0.09097	0.00097	0.35267	571.3	7.1	561.2	5.8	621	35	561.2	5.8	0.49505
IRA_1511_1.FIN68	355	1.576	0.761	0.018	0.0938	0.0016	0.74756	576.2	9.8	577.9	9.3	559	36	577.9	9.3	0.634518
IRA_1511_1.FIN82	1039	1.45	0.796	0.015	0.0974	0.0017	0.9004	594.8	8.5	599	9.9	573	16	599	9.9	0.689655
IRA_1511_1.FIN38	962	3.8	0.817	0.012	0.0982	0.0012	0.74116	607.1	6.6	604.1	7	608	21	604.1	7	0.263158
IRA_1511_1.FIN28	148.7	1.116	0.871	0.017	0.101	0.0015	0.232	635.6	9.5	620	9	738	42	620	9	0.896057
IRA_1511_1.FIN120	87.4	1.458	0.857	0.019	0.1023	0.0027	0.44476	628	10	628	16	650	100	628	16	0.685871
IRA_1511_1.FIN16	196.8	1.674	0.857	0.019	0.1024	0.0019	0.16113	628	10	629	11	605	48	629	11	0.597372
IRA_1511_1.FIN138	698	15.36	0.889	0.018	0.1026	0.0016	0.51979	645.4	9.5	629.8	9.6	692	33	629.8	9.6	0.065104
IRA_1511_1.FIN50	54.2	0.7393	0.885	0.02	0.1033	0.0017	0.14395	643	11	633	10	680	58	633	10	1.352631
IRA_1511_1.FIN91	36.5	1.873	0.904	0.051	0.1035	0.0029	0.38587	652	27	635	17	660	110	635	17	0.533903
IRA_1511_1.FIN109	125.1	0.995	0.871	0.015	0.1038	0.0019	0.6144	635.7	8.3	636	11	646	36	636	11	1.005025
IRA_1511_1.FIN156	179	1.019	1.101	0.021	0.1224	0.0019	0.5618	755	10	744	11	775	32	744	11	0.981354
IRA_1511_1.FIN74	175	1.511	1.101	0.022	0.1225	0.0028	0.66556	753	11	744	16	792	40	744	16	0.661813
IRA_1511_1.FIN70	158.9	2.09	1.079	0.022	0.1228	0.0033	0.4289	743	11	747	19	738	56	747	19	0.478469
IRA_1511_1.FIN34	279	2.474	1.205	0.016	0.1297	0.0013	0.42956	802.5	7.3	786	7.3	855	26	786	7.3	0.404204
IRA_1511_1.FIN72	110.1	1.155	1.438	0.046	0.1481	0.0037	0.46853	903	19	890	21	1000	69	1000	69	0.865801
IRA_1511_1.FIN53	72.2	0.783	1.684	0.031	0.1651	0.0026	0.11031	1003	11	985	15	1007	42	1007	42	1.277139
IRA_1511_1.FIN45	298.4	1.028	1.496	0.029	0.1468	0.0016	0.29617	928	12	882.9	8.8	1024	39	1024	39	0.972763
IRA_1511_1.FIN23	351	1.77	4.121	0.041	0.2909	0.0035	0.66979	1657.9	8.3	1646	18	1664	18	1664	18	0.564972
IRA_1511_1.FIN100	123	0.892	6.103	0.094	0.3583	0.0052	0.45416	1990	14	1974	25	1986	36	1986	36	1.121076
IRA_1511_1.FIN2	124	5.42	4.978	0.083	0.2833	0.0058	0.7861	1818	14	1611	30	2074	22	2074	22	0.184502
IRA_1511_1.FIN10	531	6.85	8.999	0.072	0.414	0.0044	0.75142	2337.6	7.3	2236	20	2428	12	2428	12	0.145985
IRA_1511_1.FIN123	106.4	0.495	10	0.17	0.4522	0.0071	0.68198	2434	16	2404	31	2472	23	2472	23	2.020202
IRA_1511_1.FIN86	49.5	2.45	11.01	0.53	0.484	0.016	0.48559	2521	45	2542	70	2527	71	2527	71	0.408163
IRA_1511_1.FIN157	96.1	1.446	8.47	0.19	0.353	0.011	0.78481	2286	22	1947	50	2593	30	2593	30	0.691563
IRA_1511_1.FIN79	38.1	1.118	10.92	0.24	0.457	0.012	0.42635	2520	22	2424	54	2607	39	2607	39	0.894454

Sample Name:	IRA1512							207/235		206/238		207/206		Best age			
Grain	[U] ppm	U/Th	207/235	2σ error	206/238	2σ error	RHO	Age (Ma)	2σ error	Age (Ma)	2σ error	Age (Ma)	2σ error	(Ma)	2σ error	Th/U	Rim
IRA1512_21.FIN2	805	0.781	0.2467	0.0056	0.03579	0.00057	0.48917	223.8	4.5	226.7	3.6	227	48	226.7	3.6	1.28041	
IRA1512_33.FIN2	740	0.804	0.2519	0.0045	0.0361	0.00048	0.42149	227.9	3.6	228.6	3	248	37	228.6	3	1.243781	
IRA1512_108.FIN2	685	0.776	0.2513	0.0051	0.03625	0.00055	0.69937	227.3	4.2	229.5	3.4	234	35	229.5	3.4	1.28866	
IRA1512_16.FIN2	569	0.875	0.2686	0.0069	0.03659	0.00052	0.58202	241.1	5.5	231.6	3.2	351	43	231.6	3.2	1.142857	
IRA1512_28.FIN2	875	0.597	0.2573	0.0057	0.03658	0.00067	0.13316	232.4	4.6	231.6	4.2	246	57	231.6	4.2	1.675042	
IRA1512_99.FIN2	302	0.581	0.2595	0.0056	0.03663	0.00037	0.11302	234.4	4.4	231.9	2.3	264	49	231.9	2.3	1.72117	
IRA1512_84.FIN2	521	0.841	0.2597	0.0047	0.03685	0.00037	0.27444	234.2	3.8	233.3	2.3	217	39	233.3	2.3	1.189061	
IRA1512_106.FIN2	419.6	0.838	0.2557	0.0043	0.03705	0.00032	0.19363	231	3.5	234.5	2	208	42	234.5	2	1.193317	
IRA1512_20.FIN2	646	0.6749	0.2734	0.0041	0.03755	0.00037	0.3238	245.3	3.2	237.6	2.3	344	37	237.6	2.3	1.481701	
IRA1512_71.FIN2	768	1.706	0.266	0.0043	0.03765	0.00035	0.4448	239.6	3.5	238.2	2.2	278	34	238.2	2.2	0.586166	
IRA1512_29.FIN2	481	0.608	0.2658	0.0054	0.0377	0.00032	0.13912	239.1	4.3	238.5	2	244	42	238.5	2	1.644737	
IRA1512_9.FIN2	614	0.642	0.2654	0.005	0.03797	0.0004	0.38921	238.7	4	240.2	2.5	206	38	240.2	2.5	1.557632	
IRA1512_109.FIN2	705	1.092	0.2654	0.0038	0.03812	0.00032	0.20263	238.8	3.1	241.2	2	223	36	241.2	2	0.915751	
IRA1512_107.FIN2	426	0.813	0.267	0.005	0.03819	0.0004	0.42586	240.1	4	241.6	2.5	253	40	241.6	2.5	1.230012	
IRA1512_74.FIN2	375	1.519	0.263	0.014	0.03847	0.00064	0.18094	236	11	243.3	4	190	110	243.3	4	0.658328	
IRA1512_47.FIN2	1035	1.407	0.2734	0.0039	0.03858	0.00033	0.41431	245.6	3.2	244	2	260	31	244	2	0.710732	
IRA1512_36.FIN2	1066	1.646	0.2741	0.0034	0.03892	0.00031	0.32567	246.1	2.7	246.1	1.9	249	27	246.1	1.9	0.607533	
IRA1512_98.FIN2	32.27	11.2	0.283	0.017	0.0391	0.00086	0.042894	254	13	247.2	5.3	330	120	247.2	5.3	0.089286	
IRA1512_89.FIN2	59.2	1.876	0.268	0.015	0.04	0.00079	0.027387	240	12	252.8	4.9	120	110	252.8	4.9	0.533049	
IRA1512_6.FIN2	530	1.2045	0.3745	0.0065	0.04983	0.00039	0.19261	322.7	4.8	313.4	2.4	371	39	313.4	2.4	0.83022	
IRA1512_72.FIN2	964	10.8	0.391	0.017	0.0501	0.0019	0.70644	335	13	315	12	493	69	315	12	0.092593	
IRA1512_65.FIN2	165.3	1.874	0.4112	0.0097	0.0542	0.00069	0.1216	351.4	6.9	340.2	4.2	405	59	340.2	4.2	0.533618	
IRA1512_51.FIN2	404.8	2.598	0.64	0.01	0.07976	0.00072	0.28437	502.1	6.5	494.7	4.3	521	35	494.7	4.3	0.384911	
IRA1512_49.FIN2	650	21	0.656	0.023	0.0824	0.0035	0.80197	512	14	510	21	515	67	510	21	0.047619	
IRA1512_87.FIN2	611	1.307	0.69	0.012	0.0832	0.0015	0.64787	532.1	7.5	514.9	8.9	592	27	514.9	8.9	0.765111	
IRA1512_94.FIN2	1284	1.966	0.6959	0.0086	0.0858	0.0013	0.54982	536	5.2	530.7	7.4	539	28	530.7	7.4	0.508647	
IRA1512_60.FIN2	83	0.4645	0.701	0.023	0.0878	0.0014	0.24491	540	14	543.6	8	502	70	543.6	8	2.152853	
IRA1512_78.FIN2	262	1.378	0.709	0.037	0.0881	0.0016	0.87337	544	21	544	9.7	540	77	544	9.7	0.725689	
IRA1512_61.FIN2	659	12.26	0.736	0.013	0.0884	0.0015	0.55365	562.2	7.8	545.8	8.9	615	35	545.8	8.9	0.081566	
IRA1512_92.FIN2	341	1.39	0.763	0.012	0.0906	0.0011	0.46052	575.3	6.9	558.7	6.6	650	35	558.7	6.6	0.719424	
IRA1512_86.FIN2	35.8	0.842	0.779	0.035	0.0954	0.0019	0.3058	582	20	589	11	523	92	589	11	1.187648	
IRA1512_115.FIN2	754	3.85	0.7849	0.0094	0.09603	0.00096	0.60785	587.9	5.4	591	5.7	566	24	591	5.7	0.25974	
IRA1512_114.FIN2	88.6	0.948	0.794	0.019	0.0969	0.0011	0.34866	592	11	595.9	6.7	570	48	595.9	6.7	1.054852	
IRA1512_105.FIN2	357.3	2.01	0.8	0.011	0.09791	0.00087	0.39912	596.8	6.5	602.1	5.1	598	31	602.1	5.1	0.497512	
IRA1512_48.FIN2	871	3.99	0.813	0.02	0.0999	0.0022	0.61676	606	12	614	13	576	47	614	13	0.250627	
IRA1512_17.FIN2	315	0.422	0.839	0.014	0.1001	0.0011	0.37673	618.2	8	614.8	6.2	623	37	614.8	6.2	2.369668	
IRA1512_2.FIN2	296	1.749	0.857	0.014	0.1013	0.0011	0.58874	629.3	7.7	622.1	6.5	639	26	622.1	6.5	0.571755	
IRA1512_68.FIN2	121.6	2.089	0.864	0.018	0.1019	0.0012	0.22336	632.8	9.8	626.6	6.8	673	47	626.6	6.8	0.478698	
IRA1512_5.FIN2	41.2	0.771	0.85	0.035	0.1024	0.0023	0.35228	622	19	628	13	580	82	628	13	1.297017	
IRA1512_82.FIN2	332	3.993	0.863	0.014	0.1024	0.0013	0.75132	631.8	7.6	628.6	7.7	646	32	628.6	7.7	0.250438	
IRA1512_83.FIN2	155	1.317	0.859	0.016	0.1027	0.0012	0.57898	628.4	8.6	629.9	7.3	611	41	629.9	7.3	0.759301	
IRA1512_4.FIN2	231.7	2.05	0.859	0.012	0.10279	0.00065	0.16336	630	6.6	631.1	3.8	603	32	631.1	3.8	0.487805	
IRA1512_76.FIN2	333	1.76	0.863	0.014	0.1029	0.0012	0.53112	631.2	7.6	631.5	6.8	672	31	631.5	6.8	0.568182	
IRA1512_15.FIN2	69.4	0.951	0.859	0.021	0.1033	0.0015	0.25654	627	11	633.4	8.5	603	51	633.4	8.5	1.051525	
IRA1512_67.FIN2	536	2.081	0.8638	0.0088	0.10384	0.00096	0.50972	631.9	4.8	636.8	5.6	646	24	636.8	5.6	0.480538	
IRA1512_7.FIN2	127	2.908	0.864	0.022	0.1039	0.0017	0.47698	634	12	637	10	613	48	637	10	0.343879	
IRA1512_88.FIN2	234	0.848	0.878	0.011	0.10398	0.00099	0.29632	639	6.1	637.6	5.8	632	29	637.6	5.8	1.179245	
IRA1512_118.FIN2	565	1.197	0.883	0.011	0.10473	0.00085	0.62711	642.1	6.1	642	4.9	645	26	642	4.9	0.835422	
IRA1512_90.FIN2	176	1.651	0.893	0.021	0.1048	0.0015	0.46092	648	11	642.6	8.7	661	42	642.6	8.7	0.605694	
IRA1512_111.FIN2	334	1.597	0.897	0.018	0.1067	0.0015	0.49451	649.7	9.7	653.2	8.6	685	45	653.2	8.6	0.626174	
IRA1512_1.FIN2	427	0.821	0.905	0.011	0.107	0.0011	0.49878	654.4	5.9	655.3	6.1	616	22	655.3	6.1	1.218027	
IRA1512_79.FIN2	478	2.97	0.967	0.048	0.1092	0.0043	0.89152	685	25	668	25	739	72	668	25	0.3367	
IRA1512_116.FIN2	150.6	1.967	0.955	0.019	0.11072	0.00091	0.29435	681.3	9.8	676.9	5.3	692	41	676.9	5.3	0.508388	
IRA1512_40.FIN2	232	1.194	0.945	0.015	0.11178	0.00097	0.22555	675.7	7.8	683	5.6	663	34	683	5.6	0.837521	
IRA1512_56.FIN2	154.1	3.54	0.949	0.016	0.1123	0.0013	0.28437	677.5	8.6	686.1	7.4	636	39	686.1	7.4	0.282486	
IRA1512_74.FIN2	522	1.768	0.995	0.017	0.1131	0.0011	0.36487	701	8.7	690.9	6.5	763	36	690.9	6.5	0.565611	
IRA1512_23.FIN2	194.6	0.682	1.096	0.022	0.1208	0.0012	0.12623	751	10	734.9	6.7	807	48	734.9	6.7	1.466276	
IRA1512_119.FIN2	888	3.33	1.0547	0.009	0.12117	0.00099	0.5385	731.3	4.5	737.2	5.7	720	17	737.2	5.7	0.3003	
IRA1512_14.FIN2	80.5	0.885	1.09	0.022	0.1224	0.0014	0.06405	747	11	744.4	7.8	734	47	744.4	7.8	1.129944	

IRA1512_101.FIN2	340	0.361	1.098	0.017	0.1227	0.0015	0.4522	751.8	8.4	745.8	8.8	795	32	745.8	8.8	2.770083
IRA1512_70.FIN2	306	1.786	1.112	0.017	0.1233	0.0013	0.29448	758.7	8.2	749.4	7.5	800	34	749.4	7.5	0.55991
IRA1512_97.FIN2	265.3	0.737	1.106	0.016	0.1235	0.0014	0.62366	755.5	7.6	750.4	7.9	785	25	750.4	7.9	1.356852
IRA1512_45.FIN2	223	1.12	1.128	0.015	0.126	0.0013	0.30077	766.9	7.2	765	7.6	766	32	765	7.6	0.892857
IRA1512_96.FIN2	89.5	0.931	1.121	0.028	0.1263	0.0016	0.2987	764	14	766.7	9.4	765	47	766.7	9.4	1.074114
IRA1512_18.FIN2	88.2	2.668	1.101	0.026	0.1264	0.0015	0.19814	755	12	767	8.7	744	48	767	8.7	0.374813
IRA1512_41.FIN2	31.8	1.261	1.169	0.054	0.1265	0.0051	0.64906	782	26	767	29	857	86	767	29	0.793021
IRA1512_113.FIN2	343	3.31	1.144	0.013	0.1269	0.00088	0.53596	774.4	6	770.1	5	789	23	770.1	5	0.302115
IRA1512_103.FIN2	314	1.14	1.15	0.016	0.1288	0.0011	0.47754	777.1	7.4	781	6.2	779	26	781	6.2	0.877193
IRA1512_44.FIN2	421	1.793	1.207	0.014	0.1342	0.0011	0.54745	804.6	6.7	811.5	6.3	798	24	811.5	6.3	0.557724
IRA1512_38.FIN2	270	1.16	1.232	0.031	0.1349	0.0019	0.62454	814	14	816	11	812	42	816	11	0.862069
IRA1512_80.FIN2	251.6	1.46	1.314	0.023	0.1396	0.002	0.66332	852.3	9.7	842	11	892	29	842	11	0.684932
IRA1512_73.FIN2	114.2	1.535	1.283	0.024	0.1396	0.0016	0.24107	838	11	843.1	8.7	838	42	843.1	8.7	0.651466
IRA1512_77.FIN2	186.9	1.652	1.313	0.026	0.1414	0.0018	0.60503	852	11	854	11	844	35	844	11	0.605327
IRA1512_53.FIN2	158.6	4.28	1.31	0.029	0.1401	0.0023	0.70458	849	13	845	13	852	31	845	13	0.233645
IRA1512_43.FIN2	373	22.5	1.403	0.046	0.1485	0.0044	0.5778	888	19	892	25	861	51	861	51	0.044444
IRA1512_31.FIN2	108.3	0.628	1.333	0.022	0.1435	0.0019	0.27843	858.9	9.6	864	11	874	36	874	36	1.592357
IRA1512_120.FIN2	91.7	2.02	1.423	0.033	0.1497	0.0026	0.53501	900	14	899	15	912	40	912	40	0.49505
IRA1512_25.FIN2	179.1	2.07	1.54	0.028	0.1587	0.0019	0.48903	945	11	949	10	920	32	920	32	0.483092
IRA1512_93.FIN2	58.9	1.61	1.558	0.037	0.1604	0.0026	0.31407	952	15	958	15	935	53	935	53	0.621118
IRA1512_95.FIN2	540	6.22	1.497	0.013	0.1547	0.0012	0.51246	929.2	5.3	927.6	7	936	17	936	17	0.160772
IRA1512_63.FIN2	104	0.81	1.528	0.026	0.159	0.0014	0.37768	941	10	951.3	7.9	938	33	938	33	1.234568
IRA1512_24.FIN2	68.8	2.067	1.604	0.037	0.1647	0.002	0.25902	973	14	983	11	949	46	949	46	0.483793
IRA1512_22.FIN2	232.5	0.91	1.469	0.021	0.1513	0.002	0.46244	917.1	8.7	908	11	953	28	953	28	1.098901
IRA1512_19.FIN2	1269	40.3	1.467	0.017	0.1501	0.0019	0.69412	916.3	6.9	901	11	958	20	958	20	0.024814
IRA1512_75.FIN2	55.4	2.008	1.459	0.032	0.1485	0.003	0.49037	915	13	892	17	962	42	962	42	0.498008
IRA1512_110.FIN2	416	2.91	1.551	0.015	0.1571	0.0013	0.25437	951.1	6	940.8	7.2	965	24	965	24	0.343643
IRA1512_102.FIN2	203	1.77	1.612	0.033	0.1655	0.0025	0.76972	974	13	987	14	974	23	974	23	0.564972
IRA1512_66.FIN2	75	1.182	1.561	0.036	0.1564	0.0029	0.47456	954	15	936	16	978	46	978	46	0.846024
IRA1512_50.FIN2	86.1	1.088	1.631	0.035	0.1642	0.0017	0.25925	980	13	979.7	9.2	979	43	979	43	0.919118
IRA1512_58.FIN2	225.8	1.53	1.566	0.026	0.1587	0.0018	0.57965	956	10	949.6	9.9	984	30	984	30	0.653595
IRA1512_112.FIN2	114.9	1.453	1.746	0.032	0.1747	0.0024	0.5517	1025	12	1037	13	999	31	999	31	0.688231
IRA1512_30.FIN2	493.4	1.917	1.793	0.024	0.1776	0.0016	0.48687	1045.9	8.7	1053.8	8.8	1042	27	1042	27	0.521648
IRA1512_62.FIN2	232	1.405	1.853	0.024	0.1824	0.0017	0.62271	1064.5	8.7	1079.9	9.4	1043	23	1043	23	0.711744
IRA1512_35.FIN2	561	1.917	1.569	0.013	0.1524	0.0011	0.57334	957.7	5	914.3	6.4	1060	17	1060	17	0.521648
IRA1512_55.FIN2	168	0.604	1.821	0.031	0.1767	0.0018	0.63472	1051	11	1049	9.9	1068	27	1068	27	1.655629
IRA1512_64.FIN2	269.1	1.335	1.825	0.019	0.1761	0.0014	0.48109	1054.8	6.8	1045.6	7.8	1074	19	1074	19	0.749064
IRA1512_3.FIN2	105.5	1.136	1.739	0.033	0.1661	0.0028	0.48499	1022	12	990	15	1087	39	1087	39	0.880282
IRA1512_34.FIN2	74.7	1.927	2.078	0.037	0.1988	0.0028	0.56071	1141	13	1170	15	1089	33	1089	33	0.518941
IRA1512_11.FIN2	732	3.15	1.86	0.018	0.1739	0.0016	0.56746	1066.5	6.5	1033.3	8.7	1112	18	1112	18	0.31746
IRA1512_78.FIN2	444	2.015	2.332	0.026	0.1978	0.0015	0.59648	1221.6	8	1163.2	7.9	1338	18	1338	18	0.496278
IRA1512_72.FIN2	50.3	0.541	4.188	0.09	0.2903	0.0044	0.55424	1672	17	1642	22	1727	36	1727	36	1.848429
IRA1512_10.FIN2	76.2	0.913	5.428	0.065	0.3459	0.0033	0.61628	1891	11	1914	16	1856	19	1856	19	1.09529
IRA1512_52.FIN2	134.2	0.575	5.463	0.052	0.3437	0.0024	0.49405	1893.8	8.3	1904	11	1881	16	1881	16	1.73913
IRA1512_81.FIN2	16.8	1.71	5.75	0.32	0.347	0.019	0.84454	1921	49	1910	90	1911	65	1911	65	0.584795
IRA1512_69.FIN2	152.9	1.418	5.377	0.048	0.3297	0.0029	0.55675	1882	7.7	1838	14	1949	16	1949	16	0.705219
IRA1512_32.FIN2	327	1.129	6.268	0.051	0.3736	0.0027	0.72249	2014.5	7.3	2046	13	1991	12	1991	12	0.88574
IRA1512_37.FIN2	48.2	0.28	5.97	0.13	0.3563	0.0054	0.64071	1971	18	1964	26	2009	28	2009	28	3.571429
IRA1512_59.FIN2	134.7	2.81	5.89	0.12	0.3367	0.0075	0.88528	1957	18	1869	36	2068	19	2068	19	0.355872
IRA1512_85.FIN2	185.6	1.864	8.537	0.094	0.3846	0.004	0.68218	2290	10	2097	19	2439	15	2439	15	0.536481
IRA1512_81.FIN2	59.5	2.91	11.36	0.41	0.511	0.018	0.88287	2550	34	2657	78	2452	27	2452	27	0.343643
IRA1512_26.FIN2	120.5	1.037	11.197	0.093	0.4932	0.0042	0.5964	2542.5	7.2	2584	18	2510	13	2510	13	0.96432
IRA1512_27.FIN2	583	2.367	11.019	0.092	0.4863	0.0046	0.6527	2523.9	7.8	2554	20	2511	12	2511	12	0.422476
IRA1512_13.FIN2	107.1	3.93	9.48	0.15	0.4146	0.0061	0.3814	2385	15	2236	28	2512	29	2512	29	0.254453
IRA1512_54.FIN2	97.2	1.39	10.96	0.12	0.4794	0.0049	0.69135	2520.3	9.9	2524	22	2517	13	2517	13	0.719424
IRA1512_37.FIN2	47.2	0.641	10.37	0.33	0.447	0.011	0.79123	2480	34	2380	49	2555	38	2555	38	1.560062
IRA1512_46.FIN2	212	1.551	11.55	0.2	0.4843	0.0071	0.94606	2567	16	2551	33	2576	12	2576	12	0.644745
IRA1512_42.FIN2	174	1.094	11.76	0.26	0.4908	0.0087	0.63139	2584	21	2573	38	2590	33	2590	33	0.914077
IRA1512_117.FIN2	149	1.75	12.99	0.14	0.5216	0.0049	0.58984	2682	10	2705	21	2655	14	2655	14	0.571429
IRA1512_39.FIN2	184.6	4.66	12.61	0.12	0.4942	0.0047	0.6245	2650.6	8.8	2588	20	2699	13	2699	13	0.214592
IRA1512_100.FIN2	209.4	1.316	26.86	0.24	0.6797	0.0062	0.73272	3377.7	8.8	3342	24	3401	10	3401	10	0.759878

Sample Name:	IRA1513							207/235		206/238		207/206		Best age			
Grain	[U] ppm	U/Th	207/235	2σ error	206/238	2σ error	RHO	Age (Ma)	2σ error	Age (Ma)	2σ error	Age (Ma)	2σ error	(Ma)	2σ error	Th/U	Rim
IRA_1513_1.FIN113	2377	293	0.0472	0.0031	0.00694	0.00024	0.38355	46.9	3.1	44.6	1.5	330	130	44.6	1.5	0.003413	rim
IRA_1513_1.FIN139	765	211	0.0484	0.0043	0.00701	0.00033	0.44443	48	4.1	45	2.1	290	160	45	2.1	0.004739	rim
IRA_1513_1.FIN138	1970	172	0.0456	0.0011	0.00703	0.00011	0.12075	45.3	1.1	45.17	0.72	70	61	45.17	0.72	0.005814	rim
IRA_1513_1.FIN133	1103	216	0.0465	0.0023	0.00728	0.00034	0.21182	46.1	2.3	46.7	2.2	150	250	46.7	2.2	0.00463	rim
IRA_1513_1.FIN4	2820	47.4	0.0536	0.0026	0.00744	0.00017	0.52964	53.1	2.5	47.8	1.1	303	93	47.8	1.1	0.021097	rim
IRA_1513_1.FIN116	4690	406	0.0545	0.001	0.00823	0.00013	0.48929	53.85	0.99	52.84	0.84	129	37	52.84	0.84	0.002463	rim
IRA_1513_1.FIN2	2365	60.6	0.0628	0.0027	0.00904	0.00033	0.76333	61.9	2.6	58	2.1	257	65	58	2.1	0.016502	rim
IRA_1513_1.FIN46	1860	29.2	0.0637	0.0041	0.00917	0.00054	0.37366	62.6	3.9	58.8	3.4	210	160	58.8	3.4	0.034247	rim
IRA_1513_1.FIN53	1044	17.42	0.0715	0.0042	0.00986	0.00026	0.58158	70.1	4	63.2	1.7	330	120	63.2	1.7	0.057405	rim
IRA_1513_1.FIN94	1427	157	0.072	0.014	0.0102	0.001	0.38022	70	13	65.4	6.5	220	380	65.4	6.5	0.006369	rim
IRA_1513_1.FIN135	690	35.5	0.0859	0.0067	0.01188	0.00045	0.33724	83.6	6.2	76.1	2.8	310	160	76.1	2.8	0.028169	
IRA_1513_1.FIN141	1490	29.5	0.0915	0.0027	0.01283	0.00037	0.60926	88.9	2.5	82.2	2.4	275	54	82.2	2.4	0.033898	
IRA_1513_1.FIN104	1095	16.5	0.0951	0.0046	0.01298	0.00039	0.63504	92.2	4.2	83.2	2.5	358	94	83.2	2.5	0.060606	
IRA_1513_1.FIN60	1170	15.9	0.0944	0.0062	0.01329	0.00029	0.41877	91.6	5.7	85.1	1.9	250	170	85.1	1.9	0.062893	
IRA_1513_1.FIN71	1410	24	0.0999	0.005	0.01363	0.0007	0.59615	96.7	4.6	87.3	4.5	320	110	87.3	4.5	0.041667	
IRA_1513_1.FIN13	1650	23	0.1028	0.0071	0.01403	0.00063	0.62338	99.4	6.5	89.8	4	320	140	89.8	4	0.043478	
IRA_1513_1.FIN39	2208	9.73	0.12	0.0066	0.01693	0.00076	0.53523	115	6	108.2	4.8	250	79	108.2	4.8	0.102775	
IRA_1513_1.FIN29	428	4.43	0.233	0.011	0.0309	0.0011	0.59538	212.6	8.9	196.3	7.2	435	77	196.3	7.2	0.225734	
IRA_1513_1.FIN144	572	4.26	0.2367	0.0076	0.0316	0.0014	0.33981	215.6	6.2	200.6	9	300	110	200.6	9	0.234742	
IRA_1513_1.FIN47	908	6.94	0.2275	0.0082	0.03182	0.00063	0.60445	209.4	7.1	201.9	3.9	316	61	201.9	3.9	0.144092	
IRA_1513_1.FIN18	870	4.67	0.2475	0.0072	0.03185	0.00083	0.82073	224.3	5.9	202.1	5.2	454	41	202.1	5.2	0.214133	
IRA_1513_1.FIN140	207	1.088	0.269	0.013	0.03598	0.00055	0.36147	241	11	227.8	3.4	430	120	227.8	3.4	0.919118	
IRA_1513_1.FIN147	237	1.52	0.2693	0.0062	0.03752	0.00059	0.36067	242	5	237.4	3.6	292	50	237.4	3.6	0.657895	
IRA_1513_1.FIN40	413	2.586	0.3356	0.0075	0.04639	0.00079	0.38604	293.7	5.7	292.3	4.8	311	54	292.3	4.8	0.386698	
IRA_1513_1.FIN54	233	1.95	0.355	0.011	0.04753	0.00078	0.1874	307.8	7.9	299.3	4.8	357	71	299.3	4.8	0.512821	
IRA_1513_1.FIN15	519	2.68	0.3461	0.0069	0.04814	0.00091	0.36158	301.7	5.2	303.1	5.6	309	55	303.1	5.6	0.373134	
IRA_1513_1.FIN3	430	5.61	0.387	0.02	0.0487	0.0019	0.26721	332	15	307	11	510	120	307	11	0.178253	
IRA_1513_1.FIN108	420	2.496	0.3541	0.0062	0.04904	0.00059	0.48429	308.2	4.6	308.6	3.6	316	36	308.6	3.6	0.400641	
IRA_1513_1.FIN64	537	3.853	0.3795	0.0068	0.0497	0.0011	0.51639	326.6	5	312.6	6.6	441	44	312.6	6.6	0.259538	
IRA_1513_1.FIN93	320	1.662	0.3658	0.0063	0.05003	0.00069	0.4716	317	4.8	314.7	4.2	340	37	314.7	4.2	0.601685	
IRA_1513_1.FIN27	198.5	1.767	0.3625	0.0073	0.05038	0.00081	0.33702	313.8	5.4	316.8	5	281	49	316.8	5	0.565931	
IRA_1513_1.FIN31	253.6	3.302	0.3626	0.0068	0.05042	0.0007	0.087834	314	5.1	317.1	4.3	287	49	317.1	4.3	0.302847	
IRA_1513_1.FIN145	267	2.025	0.3742	0.0078	0.05113	0.00089	0.4106	322.5	5.8	321.4	5.4	343	45	321.4	5.4	0.493827	
IRA_1513_1.FIN123	587	3.74	0.436	0.012	0.0535	0.0015	0.72244	367.1	8.1	335.6	8.9	601	37	335.6	8.9	0.26738	
IRA_1513_1.FIN88	419	15.3	0.446	0.016	0.0578	0.0022	0.81092	377.7	9	362	14	480	59	362	14	0.065359	
IRA_1513_1.FIN14	252.7	3.11	0.451	0.01	0.05792	0.00099	0.40206	378.5	7.3	363	6	453	49	363	6	0.321543	
IRA_1513_1.FIN95	274	8.49	0.489	0.013	0.0624	0.0011	0.61522	403.9	8.8	390	7	505	48	390	7	0.117786	
IRA_1513_1.FIN65	140.1	5.61	0.486	0.021	0.0625	0.0022	0.53641	408	14	391	14	415	96	391	14	0.178253	
IRA_1513_1.FIN131	114.2	3.274	0.535	0.017	0.0654	0.0012	0.40483	434	11	408.1	7.3	567	63	408.1	7.3	0.305437	
IRA_1513_1.FIN50	148.5	3.8	0.512	0.016	0.0656	0.0018	0.51611	421	10	410	11	481	54	410	11	0.263158	
IRA_1513_1.FIN112	238	2.539	0.525	0.015	0.0659	0.0014	0.6318	429.6	9.8	412.9	8.1	518	44	412.9	8.1	0.393856	
IRA_1513_1.FIN142	194	3.13	0.506	0.014	0.0662	0.0011	0.44615	416.9	9.6	413.5	6.7	457	57	413.5	6.7	0.319489	
IRA_1513_1.FIN6	274	1.858	0.52	0.0086	0.0678	0.0013	0.38545	425	5.7	422.8	7.6	453	52	422.8	7.6	0.538213	
IRA_1513_1.FIN48	143.1	3.6	0.526	0.014	0.0685	0.0014	0.75213	431	10	426.8	8.7	470	38	426.8	8.7	0.277778	
IRA_1513_1.FIN52	302.2	7	0.5412	0.0097	0.069	0.001	0.28916	438.9	6.4	430.2	6.3	503	37	430.2	6.3	0.142857	
IRA_1513_1.FIN61	144.6	3.188	0.527	0.014	0.0691	0.0016	0.38757	429.5	9.6	431.8	9.3	415	61	431.8	9.3	0.313676	
IRA_1513_1.FIN11	170	1.168	0.573	0.026	0.0693	0.0023	0.84347	465	17	432	14	619	51	432	14	0.856164	
IRA_1513_1.FIN68	127.3	1.136	0.604	0.04	0.0701	0.0015	0.068724	479	25	436.7	9.1	690	160	436.7	9.1	0.880282	
IRA_1513_1.FIN137	244	2.865	0.564	0.011	0.07014	0.00093	0.52451	454.1	6.8	436.9	5.6	569	34	436.9	5.6	0.34904	
IRA_1513_1.FIN96	221	8.93	0.5456	0.0083	0.0704	0.001	0.19414	441.8	5.4	438.4	6.1	473	37	438.4	6.1	0.111982	
IRA_1513_1.FIN132	212.3	1.96	0.561	0.011	0.0709	0.0012	0.37041	451.5	7	441.2	7.4	508	41	441.2	7.4	0.510204	
IRA_1513_1.FIN148	197	6.02	0.5489	0.0092	0.07131	0.00088	0.23741	443.9	6	444	5.3	452	40	444	5.3	0.166113	
IRA_1513_1.FIN83	471	3.137	0.5565	0.0072	0.07138	0.00081	0.29113	449.1	4.7	444.4	4.9	483	33	444.4	4.9	0.318776	
IRA_1513_1.FIN72	137.7	3.742	0.564	0.014	0.0718	0.0011	0.29312	453.5	8.8	446.9	6.8	473	51	446.9	6.8	0.267237	
IRA_1513_1.FIN124	356	7.38	0.618	0.02	0.0719	0.0021	0.13498	488	13	447	13	689	54	447	13	0.135501	
IRA_1513_1.FIN126	158.3	2.2	0.5497	0.009	0.07207	0.0008	0.46926	445.3	6.1	448.6	4.8	443	36	448.6	4.8	0.454545	
IRA_1513_1.FIN44	173.2	5.71	0.5594	0.0093	0.0723	0.00086	0.35067	450.8	6	449.9	5.2	462	44	449.9	5.2	0.175131	
IRA_1513_1.FIN143	158.8	2.852	0.5583	0.009	0.07239	0.00083	0.3609	450.1	5.9	450.5	5	439	39	450.5	5	0.350631	
IRA_1513_1.FIN36	239	3.106	0.562	0.011	0.07286	0.00093	0.54976	452.2	7	453.3	5.6	451	35	453.3	5.6	0.321958	
IRA_1513_1.FIN100	197.3	1.62	0.584	0.011	0.0747	0.0011	0.482	468.7	6.3	464.2	6.6	478	41	464.2	6.6	0.617284	
IRA_1513_1.FIN33	46.1	2.806	0.685	0.028	0.0771	0.0022	0.051407	531	16	479	13	783	97	479	13	0.356379	

IRA_1513_1.FIN105	44	0.927	0.669	0.038	0.0794	0.0029	0.49542	522	22	493	18	600	100	493	18	1.078749
IRA_1513_1.FIN92	206	3.511	0.681	0.022	0.0794	0.0021	0.080237	527	14	493	13	682	95	493	13	0.284819
IRA_1513_1.FIN98	175	4.5	0.671	0.026	0.0807	0.0028	0.6705	521	16	500	17	608	65	500	17	0.222222
IRA_1513_1.FIN59	52.8	2.109	0.673	0.03	0.0849	0.005	0.4611	526	20	525	30	560	120	525	30	0.474158
IRA_1513_1.FIN119	123	2.724	0.737	0.014	0.0875	0.0013	0.41135	559.8	8.1	540.6	7.7	650	43	540.6	7.7	0.367107
IRA_1513_1.FIN24	208.3	1.125	0.724	0.015	0.0887	0.0019	0.36015	552.6	8.7	548	11	589	56	548	11	0.888889
IRA_1513_1.FIN25	207.9	1.019	0.73	0.013	0.0892	0.0013	0.18574	556.4	7.6	550.6	7.5	589	49	550.6	7.5	0.981354
IRA_1513_1.FIN58	318	2.733	0.788	0.021	0.0901	0.002	0.62541	589	12	556	12	705	54	556	12	0.365898
IRA_1513_1.FIN75	116.4	13.5	0.994	0.071	0.0936	0.0041	0.95025	616	26	569	24	973	47	569	24	0.074074
IRA_1513_1.FIN22	101	22.1	0.799	0.028	0.0928	0.0033	0.96833	590	17	573	20	653	22	573	20	0.045249
IRA_1513_1.FIN30	775	3.98	0.852	0.013	0.0945	0.0017	0.64641	625.4	7.2	582	9.9	785	31	582	9.9	0.251256
IRA_1513_1.FIN86	219.5	2.113	0.775	0.041	0.0946	0.0043	0.7457	582	23	582	26	584	80	582	26	0.473261
IRA_1513_1.FIN77	105.4	2.536	0.835	0.032	0.0955	0.0036	0.26106	623	21	588	21	740	110	588	21	0.394322
IRA_1513_1.FIN41	185	1.004	0.846	0.017	0.0991	0.0014	0.45446	621.7	9.4	608.8	8.1	644	34	608.8	8.1	0.996016
IRA_1513_1.FIN81	158	0.683	0.808	0.017	0.0995	0.0015	0.50495	602.5	9.1	611.3	8.7	597	39	611.3	8.7	1.464129
IRA_1513_1.FIN115	82.5	1.387	0.819	0.019	0.1008	0.0017	0.26937	607	10	618.8	9.9	607	56	618.8	9.9	0.720981
IRA_1513_1.FIN121	142.1	4.75	0.843	0.025	0.1012	0.0027	0.8504	622	14	621	16	651	44	621	16	0.210526
IRA_1513_1.FIN19	98.6	0.955	0.846	0.017	0.1026	0.0014	0.33552	621.6	9.3	629.7	8.4	577	45	629.7	8.4	1.04712
IRA_1513_1.FIN38	162	1.95	0.867	0.02	0.1027	0.0018	0.25722	636	11	630	11	652	55	630	11	0.512821
IRA_1513_1.FIN37	176.6	2.35	0.882	0.016	0.1035	0.0014	0.19313	643.1	8.7	634.9	8.3	675	46	634.9	8.3	0.425532
IRA_1513_1.FIN28	343.9	4.13	0.953	0.015	0.105	0.002	0.75396	679.5	7.6	644	12	797	23	644	12	0.242131
IRA_1513_1.FIN7	121.2	1.017	0.875	0.016	0.1057	0.0016	0.33432	639	8.2	647.5	9.5	610	39	647.5	9.5	0.983284
IRA_1513_1.FIN129	244	2.486	0.899	0.013	0.1067	0.001	0.35746	651	7.2	653.8	6.1	659	31	653.8	6.1	0.402253
IRA_1513_1.FIN107	104.9	1.877	0.923	0.032	0.1068	0.002	0.50609	666	18	654	12	722	64	654	12	0.532765
IRA_1513_1.FIN23	233	4.686	0.961	0.011	0.1109	0.0012	0.48594	683.6	5.5	678.1	7.1	725	26	678.1	7.1	0.213402
IRA_1513_1.FIN134	74	5.22	1.007	0.022	0.1131	0.0018	0.28415	707	11	691	11	774	56	691	11	0.191571
IRA_1513_1.FIN102	229	1.134	1.084	0.044	0.1155	0.0037	0.64778	750	20	704	21	877	57	704	21	0.881834
IRA_1513_1.FIN103	171.9	2.207	1.134	0.029	0.1219	0.0026	0.66872	769	14	741	15	856	40	741	15	0.453104
IRA_1513_1.FIN117	94.1	0.895	1.09	0.032	0.1228	0.0023	0.050364	748	16	746	13	802	74	746	13	1.117318
IRA_1513_1.FIN110	130	1.169	1.298	0.026	0.1331	0.002	0.61953	844	12	805	11	976	41	805	11	0.855432
IRA_1513_1.FIN51	21.3	1.38	1.529	0.081	0.1635	0.0049	0.11589	938	32	981	28	810	110	810	28	0.724638
IRA_1513_1.FIN55	286	1.107	1.261	0.022	0.1351	0.0031	0.50906	828	10	816	18	850	40	816	18	0.903342
IRA_1513_1.FIN89	153.3	1.171	1.359	0.033	0.1386	0.0027	0.45927	871	14	837	15	927	52	837	15	0.853971
IRA_1513_1.FIN62	27.6	0.475	1.358	0.054	0.1395	0.0048	0.085438	869	23	841	27	920	120	841	27	2.105263
IRA_1513_1.FIN82	42.1	0.644	1.491	0.034	0.1541	0.0023	0.28044	927	13	923	13	935	48	935	48	1.552795
IRA_1513_1.FIN69	138	0.3586	1.594	0.032	0.1602	0.0024	0.3397	969	12	958	13	970	42	970	42	2.788622
IRA_1513_1.FIN128	122	3.84	1.542	0.029	0.1563	0.002	0.56895	946	12	936	11	993	29	993	29	0.260417
IRA_1513_1.FIN56	139	1.163	1.41	0.037	0.142	0.0033	0.69851	894	15	856	19	993	36	993	36	0.859845
IRA_1513_1.FIN80	242	1.0493	1.561	0.016	0.1571	0.0016	0.21804	955.8	6.6	940.7	9	1003	29	1003	29	0.953016
IRA_1513_1.FIN101	96.1	0.4746	1.61	0.031	0.1602	0.0023	0.40795	973	12	958	13	1012	41	1012	41	2.107038
IRA_1513_1.FIN70	154.1	0.918	1.693	0.03	0.1659	0.0021	0.36977	1009	11	989	12	1044	36	1044	36	1.089325
IRA_1513_1.FIN99	126	1.239	1.769	0.027	0.1736	0.0023	0.54549	1033.6	9.9	1032	13	1051	29	1051	29	0.807103
IRA_1513_1.FIN73	41.05	3.553	1.89	0.068	0.1836	0.0057	0.0728	1076	24	1086	31	1062	94	1062	94	0.281452
IRA_1513_1.FIN63	69.9	1.272	1.604	0.049	0.1533	0.0041	0.52388	971	19	919	23	1092	56	1092	56	0.786164
IRA_1513_1.FIN12	205	3.788	1.856	0.023	0.1765	0.0021	0.62414	1065.4	8	1048	11	1097	29	1097	29	0.263992
IRA_1513_1.FIN111	150.6	1.039	4.977	0.069	0.323	0.0055	0.69659	1815	12	1804	27	1847	24	1847	24	0.962464
IRA_1513_1.FIN45	218	1.681	4.89	0.17	0.311	0.012	0.86591	1799	29	1745	61	1866	22	1866	22	0.594884
IRA_1513_1.FIN26	143.4	2.169	3.799	0.061	0.2399	0.005	0.64379	1594	14	1390	25	1875	28	1875	28	0.461042
IRA_1513_1.FIN66	133.7	1.691	5.82	0.11	0.3428	0.0064	0.78457	1948	16	1899	31	1997	18	1997	18	0.591366
IRA_1513_1.FIN120	53	0.829	5.49	0.2	0.309	0.012	0.80131	1897	31	1733	58	2104	29	2104	29	1.206273
IRA_1513_1.FIN17	307.2	1.062	7.382	0.06	0.3732	0.0035	0.54957	2158.5	7.3	2044	16	2261	14	2261	14	0.94162
IRA_1513_1.FIN84	278.9	1.355	9.38	0.12	0.3786	0.0057	0.7311	2375	11	2069	27	2640	17	2640	17	0.738007
IRA_1513_1.FIN146	136.7	1.052	13.47	0.17	0.5166	0.0084	0.7673	2714	11	2684	36	2734	16	2734	16	0.95057

Sample Name:	IRA1514							207/235		206/238		207/206		Best age			
Grain	[U] ppm	U/Th	207/235	2σ error	206/238	2σ error	RHO	Age (Ma)	2σ error	Age (Ma)	2σ error	Age (Ma)	2σ error	(Ma)	2σ error	Th/U	Rim
IRA_1514_105.FIN2	1201	0.886	0.1947	0.0033	0.02598	0.00029	0.58067	180.5	2.8	165.4	1.8	378	33	165.4	1.8	1.128668	
IRA_1514_51.FIN2	1202	0.733	0.2363	0.0049	0.03196	0.00073	0.76936	215.2	4	202.8	4.5	339	32	202.8	4.5	1.364256	
IRA_1514_48.FIN2	320.1	0.957	0.2456	0.006	0.03226	0.00067	0.38079	222.8	4.9	204.6	4.2	441	63	204.6	4.2	1.044932	
IRA_1514_2.FIN2	180.9	1.132	0.241	0.011	0.03307	0.0008	0.32674	219	8.8	209.7	5	328	91	209.7	5	0.883392	
IRA_1514_106.FIN2	466	0.846	0.2408	0.0054	0.03431	0.00044	0.2558	218.9	4.4	217.5	2.8	249	49	217.5	2.8	1.182033	
IRA_1514_63.FIN2	460.5	1.023	0.2527	0.0044	0.03519	0.00047	0.35805	228.6	3.6	222.9	3	294	38	222.9	3	0.977517	
IRA_1514_58.FIN2	539	0.791	0.2583	0.0042	0.03552	0.00034	0.22425	233.1	3.3	225	2.1	314	38	225	2.1	1.264223	
IRA_1514_82.FIN2	545	0.772	0.2483	0.0047	0.03588	0.00048	0.46991	225	3.8	227.2	3	214	39	227.2	3	1.295337	
IRA_1514_113.FIN2	552	0.747	0.2509	0.0044	0.03622	0.00039	0.33244	227.8	3.5	229.3	2.5	199	36	229.3	2.5	1.338688	
IRA_1514_26.FIN2	531	0.772	0.256	0.0054	0.03638	0.00053	0.31992	231.1	4.4	230.4	3.3	264	50	230.4	3.3	1.295337	
IRA_1514_10.FIN2	300	0.693	0.2508	0.0052	0.03641	0.00038	0.023959	227.4	4.2	230.5	2.4	179	49	230.5	2.4	1.443001	
IRA_1514_95.FIN2	357	1.013	0.2539	0.0052	0.03646	0.00039	0.28871	229.8	4.2	230.8	2.4	200	45	230.8	2.4	0.987167	
IRA_1514_59.FIN2	360.3	0.931	0.2573	0.0052	0.03676	0.0004	0.11912	232.2	4.2	232.7	2.5	248	46	232.7	2.5	1.074114	
IRA_1514_120.FIN2	449	0.859	0.2482	0.0044	0.03683	0.00041	0.37029	225.3	3.5	233.1	2.6	163	39	233.1	2.6	1.164144	
IRA_1514_14.FIN2	488	0.863	0.258	0.0047	0.03708	0.00047	0.33692	232.8	3.8	234.7	2.9	237	40	234.7	2.9	1.158749	
IRA_1514_91.FIN2	671	0.6905	0.2592	0.0039	0.03718	0.0004	0.27397	234.2	3.1	235.3	2.5	223	37	235.3	2.5	1.448226	
IRA_1514_49.FIN2	591	0.888	0.2571	0.0039	0.03721	0.00053	0.13569	232.5	3.1	235.5	3.3	205	43	235.5	3.3	1.126126	
IRA_1514_21.FIN2	680	0.715	0.2601	0.0043	0.03722	0.00052	0.21357	234.6	3.4	235.6	3.2	195	43	235.6	3.2	1.398601	
IRA_1514_94.FIN2	310	0.985	0.2623	0.0059	0.03731	0.00041	0.20527	236.6	4.8	236.1	2.6	246	51	236.1	2.6	1.015228	
IRA_1514_60.FIN2	320	1.134	0.2635	0.0065	0.03744	0.00039	0.43191	237.6	5.3	236.9	2.5	269	51	236.9	2.5	0.881834	
IRA_1514_98.FIN2	773	3.934	0.498	0.011	0.0609	0.0012	0.37795	410.1	7.5	382.5	7.5	564	44	382.5	7.5	0.254194	
IRA_1514_46.FIN2	307	2.978	0.5541	0.0088	0.07048	0.00088	0.13331	448.2	5.8	439	5.3	479	41	439	5.3	0.335796	
IRA_1514_104.FIN2	428.5	3.084	0.5583	0.0087	0.07116	0.00072	0.44914	450.6	5.6	443.1	4.3	447	31	443.1	4.3	0.324254	
IRA_1514_53.FIN2	206	3.41	0.636	0.022	0.0738	0.0018	0.49221	500	13	459	11	653	60	459	11	0.293255	
IRA_1514_5.FIN2	306.6	4.63	0.675	0.013	0.0789	0.0018	0.35233	523.4	7.9	489	11	646	52	489	11	0.215983	
IRA_1514_80.FIN2	258.3	3.033	0.672	0.011	0.08338	0.00095	0.39012	521.2	6.9	516.2	5.6	553	40	516.2	5.6	0.329707	
IRA_1514_116.FIN2	270	6.18	0.705	0.015	0.085	0.0014	0.59977	540.8	8.7	525.9	8.3	619	36	525.9	8.3	0.161812	
IRA_1514_77.FIN2	164	1.832	0.661	0.015	0.0851	0.0011	0.25637	514.4	9.1	526.6	6.6	474	47	526.6	6.6	0.545852	
IRA_1514_98.FIN2	368.6	2.351	0.706	0.019	0.0853	0.0019	0.77904	542	11	528	11	579	34	528	11	0.425351	
IRA_1514_93.FIN2	80.6	0.62	0.715	0.024	0.0892	0.002	0.61245	549	15	550	12	596	59	550	12	1.612903	
IRA_1514_38.FIN2	232	0.758	0.739	0.018	0.0899	0.002	0.61718	560	11	554	12	597	46	554	12	1.319261	
IRA_1514_13.FIN2	194	2.06	0.759	0.014	0.0921	0.0016	0.31029	572.2	8.3	567.9	9.6	571	48	567.9	9.6	0.485437	
IRA_1514_17.FIN2	228.3	0.592	0.812	0.017	0.0942	0.0015	0.44813	603.8	9.3	580.3	8.6	675	36	580.3	8.6	1.689189	
IRA_1514_100.FIN2	230	40.6	0.776	0.014	0.09502	0.00093	0.23975	583.1	7.6	585.1	5.5	575	40	585.1	5.5	0.024631	
IRA_1514_4.FIN2	161.6	1.237	0.811	0.015	0.0952	0.0012	0.18259	602	8.6	585.9	7	659	45	585.9	7	0.808407	
IRA_1514_107.FIN2	12.59	0.772	0.825	0.055	0.0958	0.0035	0.11838	607	30	589	20	700	150	589	20	1.295337	
IRA_1514_65.FIN2	709	5.34	0.806	0.012	0.0958	0.0011	0.73345	600.5	6.9	589.9	6.4	643	20	589.9	6.4	0.187266	
IRA_1514_89.FIN2	1203	7.871	0.7978	0.0074	0.09583	0.00087	0.59703	595.4	4.2	589.9	5.1	617	18	589.9	5.1	0.127049	
IRA_1514_76.FIN2	87.5	0.625	0.852	0.024	0.0964	0.001	0.065698	625	13	593	6	743	61	593	6	1.6	
IRA_1514_35.FIN2	590	4.82	0.798	0.014	0.0976	0.0014	0.75003	595.9	8	600	8.2	610	24	600	8.2	0.207469	
IRA_1514_114.FIN2	423	2.808	0.844	0.016	0.0999	0.0013	0.66785	622.5	9	613.8	7.3	648	29	613.8	7.3	0.356125	
IRA_1514_72.FIN2	73.2	2.911	0.826	0.019	0.1	0.0012	0.14594	610	11	614.3	7.1	602	56	614.3	7.1	0.343525	
IRA_1514_1.FIN2	46.8	1.237	0.893	0.028	0.1001	0.0014	0.38261	645	15	614.9	8.1	754	64	614.9	8.1	0.808407	
IRA_1514_111.FIN2	191	0.767	0.84	0.02	0.1003	0.0015	0.60609	618	11	615.7	8.7	618	39	615.7	8.7	1.303781	
IRA_1514_16.FIN2	196	0.982	0.832	0.015	0.1016	0.0012	0.29035	615.7	7.9	623.6	6.9	595	43	623.6	6.9	1.01833	
IRA_1514_108.FIN2	248.6	2.21	0.846	0.021	0.1017	0.0022	0.70547	625	12	624	13	625	37	624	13	0.452489	
IRA_1514_25.FIN2	288	5.88	0.855	0.016	0.1019	0.002	0.58392	627.4	8.8	625	12	637	38	625	12	0.170068	
IRA_1514_57.FIN2	129.2	1.165	0.859	0.015	0.1022	0.0011	0.21438	628.5	8.1	627.2	6.4	620	39	627.2	6.4	0.858369	
IRA_1514_112.FIN2	155	1.034	0.862	0.018	0.1026	0.0011	0.37501	630.2	9.9	629.7	6.6	613	46	629.7	6.6	0.967118	
IRA_1514_29.FIN2	87.5	2.635	0.877	0.021	0.1042	0.0014	0.32415	643	11	638.7	8.4	636	47	638.7	8.4	0.379507	
IRA_1514_78.FIN2	337	1.885	0.885	0.015	0.1043	0.0014	0.33508	642.8	7.8	641.3	8.1	654	36	641.3	8.1	0.530504	
IRA_1514_43.FIN2	37	11.3	0.876	0.036	0.1056	0.0026	0.36999	636	19	647	15	557	85	647	15	0.088496	
IRA_1514_70.FIN2	353	1.347	0.972	0.021	0.1069	0.0025	0.65047	688	11	654	15	841	42	654	15	0.74239	
IRA_1514_30.FIN2	65	3.138	0.907	0.022	0.107	0.0016	0.27268	653	11	655.3	9.1	652	53	655.3	9.1	0.318674	
IRA_1514_39.FIN2	169.1	1.231	0.892	0.015	0.1075	0.00094	0.30516	647.4	8	658.2	5.5	623	37	658.2	5.5	0.812348	
IRA_1514_45.FIN2	338.5	5.663	0.9389	0.0087	0.1095	0.0011	0.28833	672	4.5	669.9	6.3	682	24	669.9	6.3	0.176585	
IRA_1514_71.FIN2	46.32	1.92	0.987	0.044	0.1103	0.0028	0.53144	696	23	674	16	777	85	674	16	0.520833	

IRA_1514_40.FIN2	100.6	3.51	0.941	0.023	0.1105	0.0017	0.36243	671	12	675.5	9.9	677	51	675.5	9.9	0.2849
IRA_1514_15.FIN2	154	2.83	0.973	0.024	0.1115	0.0016	0.2469	689	12	681.3	9.1	685	55	681.3	9.1	0.353357
IRA_1514_27.FIN2	268	4.878	0.957	0.012	0.11215	0.00092	0.21318	681.9	6.4	685.2	5.4	660	31	685.2	5.4	0.205002
IRA_1514_33.FIN2	383	5.4	0.978	0.022	0.1127	0.0026	0.65375	691	11	688	15	713	43	688	15	0.185185
IRA_1514_119.FIN2	115.4	2.723	1.012	0.02	0.1142	0.0015	0.42174	709	10	697.1	8.8	738	39	697.1	8.8	0.367242
IRA_1514_64.FIN2	240.1	2.712	1.035	0.017	0.1163	0.0012	0.53447	721.5	8.7	709.2	6.7	736	30	709.2	6.7	0.368732
IRA_1514_68.FIN2	80	0.857	1.008	0.024	0.1168	0.0015	0.11065	707	12	711.9	8.6	676	56	711.9	8.6	1.166861
IRA_1514_34.FIN2	820	12.8	1.043	0.06	0.1176	0.0062	0.88558	722	29	716	36	765	53	716	36	0.078125
IRA_1514_44.FIN2	136.9	2.56	1.019	0.017	0.1185	0.0011	0.52238	713.4	8.7	721.9	6.5	689	37	721.9	6.5	0.390625
IRA_1514_110.FIN2	338	31.9	1.077	0.03	0.1223	0.0023	0.86564	743	14	743	13	736	30	743	13	0.031348
IRA_1514_103.FIN2	66.5	0.523	1.112	0.03	0.1255	0.0017	0.18673	758	15	761.9	9.7	748	62	761.9	9.7	1.912046
IRA_1514_55.FIN2	72.3	0.869	1.117	0.023	0.1255	0.0015	0.066867	760	11	763	8.6	752	52	763	8.6	1.150748
IRA_1514_32.FIN2	124.9	0.864	1.2	0.031	0.1275	0.0023	0.39149	802	15	774	13	845	50	774	13	1.157407
IRA_1514_31.FIN2	99.9	3.03	1.237	0.03	0.1283	0.0021	0.27579	817	13	778	12	944	52	778	12	0.330033
IRA_1514_36.FIN2	305	2.15	1.146	0.015	0.1283	0.0016	0.19103	774.9	7.1	778.9	9.4	761	34	778.9	9.4	0.465116
IRA_1514_115.FIN2	173.3	2.025	1.178	0.02	0.1289	0.0022	0.40066	790.6	9.4	781	12	786	39	781	12	0.493827
IRA_1514_61.FIN2	533	4.42	1.262	0.026	0.1296	0.0019	0.64686	827	12	786	11	948	31	786	11	0.226244
IRA_1514_54.FIN2	450	2.207	1.235	0.017	0.1337	0.0016	0.46502	816.8	8	808.5	9.2	838	29	808.5	9.2	0.453104
IRA_1514_79.FIN2	155	2.309	1.227	0.022	0.134	0.0014	0.35644	811	10	810.4	8.2	814	36	810.4	8.2	0.433088
IRA_1514_8.FIN2	132.2	2.02	1.252	0.021	0.1341	0.001	0.21557	825.9	9.4	811.4	6	839	37	811.4	6	0.49505
IRA_1514_56.FIN2	218	1.032	1.364	0.017	0.1466	0.0014	0.31683	874.1	7	881.6	7.9	836	25	836	7.9	0.968992
IRA_1514_28.FIN2	86.7	1.609	1.327	0.028	0.1429	0.0019	0.15512	857	13	863	11	853	50	853	50	0.621504
IRA_1514_81.FIN2	190	1.679	1.464	0.019	0.1529	0.0017	0.27945	915.6	7.8	917.1	9.5	911	30	911	30	0.595593
IRA_1514_90.FIN2	93.1	1.573	1.559	0.028	0.1613	0.0017	0.25918	955	11	963.8	9.3	912	38	912	38	0.635728
IRA_1514_85.FIN2	550	6.8	1.495	0.02	0.1552	0.0014	0.52358	930.5	8	929.9	8	917	23	917	23	0.147059
IRA_1514_109.FIN2	380	2.52	1.425	0.052	0.1494	0.0039	0.92888	896	23	897	22	932	38	932	38	0.396825
IRA_1514_47.FIN2	23.8	2.88	1.628	0.056	0.1685	0.0028	0.3224	981	21	1003	15	943	65	943	65	0.347222
IRA_1514_24.FIN2	182.7	2.152	1.459	0.025	0.1484	0.0016	0.52288	913	10	891.7	9.1	967	31	967	31	0.464684
IRA_1514_42.FIN2	60.3	1.71	1.666	0.058	0.1652	0.004	0.63837	991	22	985	22	970	57	970	57	0.584795
IRA_1514_50.FIN2	243	1.127	1.645	0.019	0.1665	0.0018	0.21204	987.6	7.4	992.4	9.9	979	29	979	29	0.887311
IRA_1514_84.FIN2	132	7.69	1.414	0.028	0.1422	0.0019	0.53593	896	12	857	11	991	35	991	35	0.130039
IRA_1514_67.FIN2	194.5	0.956	1.671	0.029	0.1651	0.0029	0.57432	998	11	984	16	995	33	995	33	1.046025
IRA_1514_3.FIN2	196	0.768	1.642	0.023	0.1635	0.0015	0.29518	985.4	9	976.1	8.1	996	25	996	25	1.302083
IRA_1514_101.FIN2	195.6	1.259	1.564	0.019	0.157	0.0011	0.41019	955.5	7.7	940.2	6.2	999	24	999	24	0.794281
IRA_1514_52.FIN2	131.6	1.505	1.617	0.022	0.1611	0.0021	0.25819	975.8	8.6	963	12	1007	35	1007	35	0.664452
IRA_1514_19.FIN2	130	1.137	1.739	0.034	0.1724	0.0036	0.47548	1022	13	1025	20	1011	47	1011	47	0.879507
IRA_1514_7.FIN2	308	1.818	1.503	0.03	0.1509	0.003	0.4892	930	12	906	17	1016	43	1016	43	0.550055
IRA_1514_20.FIN2	67.2	0.508	1.825	0.038	0.1766	0.0025	0.54314	1052	13	1048	14	1041	38	1041	38	1.968504
IRA_1514_22.FIN2	368	1.619	1.823	0.019	0.1761	0.0019	0.51727	1053.4	6.8	1045	10	1054	20	1054	20	0.617665
IRA_1514_41.FIN2	1179	9.77	2.515	0.036	0.1874	0.0024	0.74518	1277	11	1107	13	1578	18	1578	18	0.102354
IRA_1514_74.FIN2	110	1.289	4.712	0.079	0.3076	0.0045	0.63793	1771	14	1728	22	1811	24	1811	24	0.775795
IRA_1514_23.FIN2	405	1.839	4.44	0.08	0.2812	0.0052	0.73057	1721	15	1599	27	1858	26	1858	26	0.543774
IRA_1514_12.FIN2	398	1.332	5.282	0.04	0.3359	0.0033	0.4415	1865.4	6.5	1867	16	1861	17	1861	17	0.750751
IRA_1514_69.FIN2	294	3.27	5.345	0.062	0.3397	0.0045	0.61333	1875.8	9.8	1884	22	1871	19	1871	19	0.30581
IRA_1514_88.FIN2	456	1.19	5.558	0.032	0.348	0.0026	0.40917	1909.4	4.9	1925	13	1897	13	1897	13	0.840336
IRA_1514_37.FIN2	293.2	9.84	4.648	0.091	0.2875	0.0047	0.71781	1756	16	1628	23	1900	26	1900	26	0.101626
IRA_1514_75.FIN2	166	2.86	5.81	0.17	0.356	0.0079	0.85717	1942	27	1961	38	1920	30	1920	30	0.34965
IRA_1514_18.FIN2	84.1	0.4157	4.748	0.089	0.2859	0.0032	0.43083	1774	16	1621	16	1929	31	1929	31	2.405581
IRA_1514_97.FIN2	212.2	1.516	4.732	0.065	0.2886	0.0035	0.69621	1772	11	1634	17	1945	19	1945	19	0.659631
IRA_1514_99.FIN2	43.2	0.419	5.43	0.11	0.3255	0.0057	0.34001	1889	17	1816	28	1949	36	1949	36	2.386635
IRA_1514_118.FIN2	268.8	0.8219	6.048	0.086	0.3596	0.0053	0.77483	1982	12	1980	25	1977	16	1977	16	1.216693
IRA_1514_102.FIN2	124.1	0.678	5.979	0.061	0.3404	0.0025	0.5449	1973.2	8.7	1888	12	2050	16	2050	16	1.474926
IRA_1514_96.FIN2	125.3	1.173	6.75	0.12	0.3179	0.004	0.75667	2076	16	1779	20	2398	19	2398	19	0.852515
IRA_1514_73.FIN2	773	11.1	10.02	0.15	0.4536	0.007	0.87708	2435	14	2410	31	2469	18	2469	18	0.09009
IRA_1514_11.FIN2	162.5	1.263	9.66	0.16	0.418	0.007	0.54559	2402	15	2250	32	2519	27	2519	27	0.791766
IRA_1514_66.FIN2	117.4	1.275	11.006	0.09	0.4775	0.0034	0.34664	2523.1	7.6	2516	15	2524	16	2524	16	0.784314
IRA_1514_83.FIN2	342	3.35	9.639	0.088	0.4135	0.0064	0.54063	2400.3	8.4	2233	28	2546	21	2546	21	0.298507
IRA_1514_6.FIN2	394	1.999	10.92	0.13	0.4572	0.0099	0.63001	2515	11	2424	44	2574	27	2574	27	0.50025
IRA_1514_9.FIN2	891	13.8	9.23	0.18	0.3595	0.0092	0.39971	2358	18	1978	43	2683	40	2683	40	0.072464
IRA_1514_86.FIN2	262.7	1.783	26.52	0.22	0.6763	0.0042	0.63459	3367.6	8.2	3332	16	3385	10	3385	10	0.560852

Sample Name:	IRA1801							207/235		206/238		207/206		Best age			
Grain	[U] ppm	U/Th	207/235	2σ error	206/238	2σ error	RHO	Age (Ma)	2σ error	Age (Ma)	2σ error	Age (Ma)	2σ error	(Ma)	2σ error	Th/U	Rim
IRA1801_80.FIN2	3300	100	0.049	0.0021	0.00668	0.00019	0.19594	48.6	2.1	42.9	1.2	340	100	42.9	1.2	0.01	rim
IRA1801_16.FIN2	4290	32.2	0.0583	0.0028	0.00768	0.00021	0.29759	57.5	2.7	49.3	1.4	411	97	49.3	1.4	0.031056	rim
IRA1801_127.FIN2	2780	58.3	0.0635	0.004	0.00878	0.00043	0.8097	62.5	3.8	56.3	2.7	323	86	56.3	2.7	0.017153	rim
IRA1801_34.FIN2	1630	14	0.0638	0.0038	0.00948	0.0006	0.61397	62.7	3.6	60.8	3.9	170	110	60.8	3.9	0.071429	rim
IRA1801_41.FIN2	1840	15.2	0.0868	0.0052	0.01202	0.0004	0.36409	84.4	4.8	77	2.6	290	100	77	2.6	0.065789	rim
IRA1801_21.FIN2	1256	9.35	0.1204	0.0072	0.0159	0.0011	0.66576	115.4	6.5	101.9	7.2	420	120	101.9	7.2	0.106952	rim
IRA1801_75.FIN2	1188	1.432	0.256	0.01	0.03473	0.00054	0.71018	231	7.9	220.1	3.3	317	62	220.1	3.3	0.698324	
IRA1801_55.FIN2	699	4.85	0.2508	0.0037	0.03558	0.0003	0.30232	227.1	3	225.4	1.9	244	33	225.4	1.9	0.206186	
IRA1801_108.FIN2	1345	2.01	0.2556	0.0054	0.03733	0.00047	0.2293	231	4.3	236.3	2.9	253	50	236.3	2.9	0.497512	
IRA1801_49.FIN2	1033	3.526	0.2647	0.0072	0.0376	0.00058	0.26703	238.3	5.8	237.9	3.6	232	70	237.9	3.6	0.283607	
IRA1801_18.FIN2	143	2.22	0.309	0.03	0.0377	0.0016	0.37738	273	24	238	10	590	250	238	10	0.45045	
IRA1801_125.FIN2	808	2.564	0.2633	0.004	0.03784	0.00036	0.14143	237.2	3.2	239.4	2.2	229	33	239.4	2.2	0.390016	
IRA1801_85.FIN2	1951	5.27	0.3277	0.0078	0.03992	0.00094	0.61328	287.7	5.9	252.3	5.8	578	45	252.3	5.8	0.189753	
IRA1801_76.FIN2	1105	20.61	0.3146	0.0055	0.04016	0.00066	0.82341	277.5	4.3	253.8	4.1	464	29	253.8	4.1	0.04852	
IRA1801_32.FIN2	873	11.92	0.33	0.017	0.0411	0.0028	0.37182	289	13	259	18	550	140	259	18	0.083893	
IRA1801_88.FIN2	466	2.89	0.343	0.015	0.045	0.0014	0.33793	300	11	283.9	8.5	410	120	283.9	8.5	0.346021	
IRA1801_23.FIN2	937	2.02	0.3668	0.0071	0.04939	0.00081	0.10063	317.2	5.3	310.7	5	364	52	310.7	5	0.49505	
IRA1801_12.FIN2	437	2.462	0.372	0.011	0.05043	0.00088	0.29948	322.7	9.2	317.2	5.4	360	71	317.2	5.4	0.406174	
IRA1801_33.FIN2	532	4.67	0.399	0.019	0.0521	0.0018	0.29889	341	14	327	11	440	110	327	11	0.214133	
IRA1801_5.FIN2	648	3.32	0.4274	0.0076	0.05492	0.00072	0.51922	362	5.2	344.7	4.4	452	35	344.7	4.4	0.301205	
IRA1801_78.FIN2	310.3	1.824	0.43	0.019	0.0567	0.0016	0.65468	362	13	355.7	9.4	382	72	355.7	9.4	0.548246	
IRA1801_126.FIN2	333	4.95	0.437	0.012	0.0577	0.0011	0.40536	367.5	8.7	361.8	6.8	418	60	361.8	6.8	0.20202	
IRA1801_88.FIN2	448	4.9	0.455	0.02	0.0601	0.0023	0.60259	381	14	376	14	400	76	376	14	0.204082	
IRA1801_51.FIN2	367.2	4.25	0.506	0.014	0.063	0.0011	0.61956	414.8	9.4	393.8	6.5	527	47	393.8	6.5	0.235294	
IRA1801_11.FIN2	393.8	2.162	0.498	0.012	0.06467	0.00083	0.2534	409.7	7.9	403.9	5	437	52	403.9	5	0.462535	
IRA1801_59.FIN2	257	3.76	0.567	0.013	0.06456	0.00074	0.20814	455.2	8.8	404.2	4.8	739	57	404.2	4.8	0.265957	
IRA1801_64.FIN2	268.5	2.474	0.486	0.016	0.0649	0.0015	0.63937	401	11	405.3	8.9	412	57	405.3	8.9	0.404204	
IRA1801_84.FIN2	692	10.28	0.5038	0.0058	0.06516	0.00064	0.47663	414	3.9	406.9	3.9	453	23	406.9	3.9	0.097276	
IRA1801_119.FIN2	301	2.071	0.536	0.011	0.06717	0.00081	0.28544	434.7	7.4	419	4.9	501	45	419	4.9	0.482859	
IRA1801_99.FIN2	452	3.62	0.529	0.011	0.06741	0.00071	0.12092	430.9	7.3	420.5	4.3	457	46	420.5	4.3	0.276243	
IRA1801_26.FIN2	634	1.454	0.541	0.015	0.0677	0.0016	0.56819	438	10	421.9	9.9	535	58	421.9	9.9	0.687758	
IRA1801_85.FIN2	224	1.77	0.578	0.05	0.0678	0.0044	0.7861	461	32	422	27	680	91	422	27	0.564972	
IRA1801_131.FIN2	640	7.42	0.532	0.01	0.06834	0.00096	0.20405	432.9	7	426.1	5.8	451	49	426.1	5.8	0.134771	
IRA1801_47.FIN2	622	4.85	0.5198	0.0098	0.06843	0.00089	0.51581	424.6	6.6	426.6	5.4	409	37	426.6	5.4	0.206186	
IRA1801_72.FIN2	311	2.61	0.523	0.012	0.06861	0.00093	0.21612	426.9	8	427.8	5.6	427	49	427.8	5.6	0.383142	
IRA1801_93.FIN2	318.6	5.01	0.523	0.013	0.06917	0.0009	0.21959	426.4	8.7	431.1	5.4	437	57	431.1	5.4	0.199601	
IRA1801_39.FIN2	201.8	2.487	0.592	0.016	0.0707	0.0011	0.33018	471	10	440.1	6.8	631	56	440.1	6.8	0.402091	
IRA1801_113.FIN2	347	7.12	0.5478	0.0085	0.07081	0.00068	0.26085	443	5.5	441	4.1	441	36	441	4.1	0.140449	
IRA1801_73.FIN2	375	1.287	0.565	0.011	0.07122	0.00095	0.37022	454	7.3	443.5	5.7	494	44	443.5	5.7	0.777001	
IRA1801_100.FIN2	292	5.4	0.551	0.018	0.0714	0.0011	0.30385	445	12	444.3	6.3	431	69	444.3	6.3	0.185185	
IRA1801_71.FIN2	58.6	0.945	0.571	0.032	0.0714	0.0014	0.18173	455	20	444.5	8.6	480	110	444.5	8.6	1.058201	
IRA1801_21.FIN2	224.3	2.195	0.562	0.018	0.0716	0.0012	0.14733	452	12	445.7	7.1	483	75	445.7	7.1	0.455581	
IRA1801_134.FIN2	234.1	4.44	0.548	0.013	0.07172	0.00079	0.40813	442.6	8.5	446.4	4.7	391	48	446.4	4.7	0.225225	
IRA1801_53.FIN2	446	4.239	0.553	0.012	0.0718	0.00099	0.52898	446.6	8.1	447	6	450	42	447	6	0.235905	
IRA1801_96.FIN2	327	3.114	0.671	0.04	0.0724	0.0028	0.69248	520	25	450	17	810	93	450	17	0.32113	
IRA1801_111.FIN2	283.6	3.05	0.564	0.013	0.07267	0.00074	0.1545	453.4	8.3	452.2	4.4	439	52	452.2	4.4	0.327869	
IRA1801_87.FIN2	488	3.78	0.5712	0.0069	0.07279	0.00053	0.21986	458.4	4.5	452.9	3.2	472	28	452.9	3.2	0.26455	
IRA1801_103.FIN2	164	6	0.574	0.032	0.0728	0.0014	0.14282	460	20	453.2	8.6	480	130	453.2	8.6	0.166667	
IRA1801_65.FIN2	378	3.906	0.55	0.016	0.0729	0.001	0.42609	444	10	453.9	6.1	438	58	453.9	6.1	0.256016	
IRA1801_13.FIN2	660	1.625	0.561	0.011	0.073	0.001	0.27486	451.6	7.1	454	6.3	439	42	454	6.3	0.615385	
IRA1801_91.FIN2	391	1.108	0.573	0.01	0.07315	0.0007	0.41291	459.3	6.6	455	4.2	464	38	455	4.2	0.902527	
IRA1801_44.FIN2	524	6.14	0.566	0.021	0.0734	0.0013	0.18817	454	15	456.6	7.8	463	54	456.6	7.8	0.162866	
IRA1801_107.FIN2	293.6	4.762	0.572	0.013	0.0734	0.001	0.34522	458.7	8.4	456.8	6	454	49	456.8	6	0.209996	
IRA1801_82.FIN2	298	1.379	0.566	0.015	0.0737	0.0012	0.43522	454.4	9.6	458.1	7.3	436	54	458.1	7.3	0.725163	
IRA1801_60.FIN2	169.1	7.14	0.561	0.011	0.07369	0.00072	0.32658	450.8	7.4	458.3	4.3	415	44	458.3	4.3	0.140056	
IRA1801_95.FIN2	378	2.791	0.587	0.017	0.0741	0.0015	0.50034	468	11	460.7	9.2	497	63	460.7	9.2	0.358295	
IRA1801_15.FIN2	943	4.45	0.5717	0.009	0.07447	0.0007	0.27516	458.8	5.8	463	4.2	445	36	463	4.2	0.224719	
IRA1801_8.FIN2	443	8.01	0.574	0.019	0.0744	0.002	0.17805	460	12	463	12	432	87	463	12	0.124844	
IRA1801_50.FIN2	185	2.815	0.575	0.016	0.0746	0.0012	0.042449	459	10	463.5	7.4	430	58	463.5	7.4	0.35524	
IRA1801_69.FIN2	163.3	3.14	0.566	0.011	0.0754	0.00078	0.046555	454.2	7.4	469.1	4.6	395	46	469.1	4.6	0.318471	
IRA1801_94.FIN2	290	2.97	0.59	0.011	0.07599	0.00083	0.030694	470.1	7	472.1	5	425	46	472.1	5	0.3367	
IRA1801_33.FIN2	238.8	2.024	0.593	0.014	0.07649	0.00091	0.14352	471.6	9.2	475.1	5.4	451	57	475.1	5.4	0.494071	
IRA1801_110.FIN2	387	2.351	0.604	0.011	0.07654	0.00064	0.13565	479.4	7.2	475.4	3.8	486	43	475.4	3.8	0.425351	
IRA1801_67.FIN2	282	2.45	0.582	0.011	0.07666	0.00085	0.16538	465.2	6.8	476.1	5.1	442	46	476.1	5.1	0.408163	
IRA1801_98.FIN2	141	1.396	0.6	0.017	0.0767	0.0011	0.24464	476	11	476.2	6.3	445	63	476.2	6.3	0.716332	
IRA1801_31.FIN2	410	3.411	0.61	0.016	0.0768	0.001	0.65035	482.5	9.7	477.1	6.1	501	51	477.1	6.1	0.293169	
IRA1801_70.FIN2	275.8	3.04	0.608	0.015	0.0776	0.0012	0.3216	481.1	9.4	481.8	7	495	49	481.8	7	0.328947	
IRA1801_41.FIN2	79.3	2.68	0.651	0.039	0.0781	0.0017	0.42747	507	24	485	10	590	130	485	10	0.373134	
IRA1801_52.FIN2	259.3	1.761	0.629	0.018	0.0792	0.0016	0.70487	494	11	491.1	9.4	512	46	491.1	9.4	0.567859	
IRA1801_58.FIN2	195.5	5.4	0.769	0.027	0.0874	0.0024	0.69294	577	16	540	14	736	55	540	14	0.185185	

IRA1801_34.FIN2	59.2	1.595	0.714	0.025	0.0875	0.0017	0.085336	544	15	541	10	582	90	541	10	0.626959
IRA1801_20.FIN2	203.6	1.357	0.713	0.02	0.0901	0.0012	0.14363	545	12	555.9	6.8	497	64	555.9	6.8	0.73692
IRA1801_45.FIN2	776	7.35	0.776	0.014	0.0905	0.0014	0.64298	582.7	8.2	558.5	8.5	659	29	558.5	8.5	0.136054
IRA1801_106.FIN2	191	1.237	0.756	0.031	0.0913	0.0023	0.77927	569	18	563	14	580	58	563	14	0.808407
IRA1801_32.FIN2	192.2	1.779	0.745	0.023	0.0917	0.0017	0.22056	564	13	565	10	561	69	565	10	0.562114
IRA1801_101.FIN2	569	1.413	0.755	0.015	0.092	0.0015	0.47638	570.6	8.4	567	8.7	592	42	567	8.7	0.707714
IRA1801_4.FIN2	409	2.915	0.776	0.022	0.0935	0.0018	0.65859	582	12	576	11	601	48	576	11	0.343053
IRA1801_117.FIN2	142	3.172	0.878	0.022	0.0961	0.0014	0.31963	640	12	592.1	7.9	800	52	592.1	7.9	0.315259
IRA1801_17.FIN2	343	0.891	0.777	0.019	0.0965	0.0016	0.28527	583	11	594.1	9.6	554	56	594.1	9.6	1.122334
IRA1801_46.FIN2	473	0.3145	0.797	0.013	0.09714	0.00091	0.26126	594.7	7.2	597.6	5.4	586	34	597.6	5.4	3.17965
IRA1801_81.FIN2	189.1	0.655	0.826	0.016	0.098	0.0012	0.4018	610.2	8.8	602.7	6.9	638	38	602.7	6.9	1.526718
IRA1801_42.FIN2	443	2.61	0.868	0.014	0.0989	0.0017	0.31834	634.1	7.9	607.9	9.9	723	42	607.9	9.9	0.383142
IRA1801_54.FIN2	188.2	3.29	0.819	0.025	0.0993	0.002	0.50947	606	14	610	11	594	57	610	11	0.303951
IRA1801_122.FIN2	231.2	2.426	0.838	0.018	0.0997	0.0011	0.079638	617	10	612.6	6.4	640	51	612.6	6.4	0.412201
IRA1801_86.FIN2	90	0.617	0.858	0.026	0.1014	0.0015	0.22826	627	14	622.7	8.6	621	66	622.7	8.6	1.620746
IRA1801_120.FIN2	241.3	2.847	0.857	0.015	0.1016	0.001	0.3932	627.2	8.1	623.7	6	624	35	623.7	6	0.351247
IRA1801_29.FIN2	475.8	0.784	0.847	0.013	0.10228	0.00097	0.42212	622.1	7.1	627.7	5.7	600	31	627.7	5.7	1.27551
IRA1801_109.FIN2	79.5	0.996	0.843	0.04	0.1023	0.0021	0.20309	618	22	628	12	588	92	628	12	1.004016
IRA1801_22.FIN2	119.6	1.336	0.906	0.023	0.1052	0.0015	0.15397	655	12	644.5	9	676	59	644.5	9	0.748503
IRA1801_128.FIN2	26.71	3.02	0.879	0.041	0.1063	0.0019	0.029636	634	22	651	11	555	92	651	11	0.331126
IRA1801_9.FIN2	175	1.054	0.888	0.019	0.10646	0.00095	0.02273	644	10	652.1	5.6	589	52	652.1	5.6	0.948767
IRA1801_104.FIN2	93.8	1.716	0.901	0.034	0.1078	0.0025	0.29841	650	18	660	15	600	84	660	15	0.582751
IRA1801_44.FIN2	236.9	2.765	0.967	0.027	0.1104	0.0018	0.5762	686	14	675	11	721	60	675	11	0.361664
IRA1801_7.FIN2	304	3.16	0.947	0.024	0.1106	0.0016	0.25928	675	12	676.3	9.4	657	56	676.3	9.4	0.316456
IRA1801_62.FIN2	89.9	1.801	0.942	0.025	0.1108	0.0018	0.10583	672	13	677	10	680	65	677	10	0.555247
IRA1801_123.FIN2	315	1.303	0.926	0.015	0.11089	0.00087	0.2901	664.6	7.9	677.9	5.1	627	34	677.9	5.1	0.76746
IRA1801_114.FIN2	45.83	1.132	1.002	0.033	0.1118	0.0015	0.15104	703	16	683	8.8	733	70	683	8.8	0.883392
IRA1801_130.FIN2	237	1.434	0.986	0.037	0.1119	0.003	0.36824	696	19	684	17	739	81	684	17	0.69735
IRA1801_116.FIN2	188.4	44	0.971	0.024	0.114	0.002	0.38501	688	12	696	11	652	52	696	11	0.022727
IRA1801_97.FIN2	165.4	0.628	1.022	0.029	0.1151	0.0016	0.1955	714	14	702.3	9.4	725	61	702.3	9.4	1.592357
IRA1801_38.FIN2	144.2	1.23	0.992	0.019	0.1157	0.0015	0.23076	698.3	9.6	705.8	8.5	677	45	705.8	8.5	0.813008
IRA1801_127.FIN2	199.7	2.226	0.993	0.017	0.1165	0.0011	0.31852	699.5	8.7	710.1	6.5	677	36	710.1	6.5	0.449236
IRA1801_37.FIN2	261	1.996	1.061	0.025	0.1204	0.0016	0.34707	733	12	732.8	9.3	747	50	732.8	9.3	0.501002
IRA1801_14.FIN2	584	1.499	1.088	0.021	0.1223	0.0025	0.75011	747	10	744	14	769	31	744	14	0.667111
IRA1801_129.FIN2	185.1	1.662	1.104	0.026	0.1247	0.0011	0.48269	755	13	757.7	6.3	760	47	757.7	6.3	0.601685
IRA1801_16.FIN2	35.3	1.244	1.144	0.086	0.1309	0.0053	0.60377	765	42	792	30	760	120	792	30	0.803859
IRA1801_1.FIN2	205.9	1.379	1.386	0.039	0.1343	0.0027	0.28519	881	17	812	15	1055	61	812	15	0.725163
IRA1801_48.FIN2	34.5	1.11	1.359	0.069	0.1463	0.0031	0.24223	866	29	880	18	820	110	820	18	0.900901
IRA1801_63.FIN2	158	2.572	1.247	0.019	0.1371	0.0012	0.25003	821.3	8.6	828.1	7	829	33	828.1	7	0.388802
IRA1801_77.FIN2	199	0.48	1.322	0.051	0.1405	0.0043	0.747	853	23	847	24	859	56	847	24	2.083333
IRA1801_35.FIN2	290.3	1.72	1.393	0.024	0.1471	0.0018	0.35588	885	10	885	10	897	36	897	36	0.581395
IRA1801_124.FIN2	196	0.249	1.526	0.023	0.1569	0.0014	0.39381	939.7	9	939.4	7.9	950	29	950	29	4.016064
IRA1801_95.FIN2	318	1.203	1.648	0.026	0.1648	0.0018	0.26457	988	10	983	10	974	35	974	35	0.831255
IRA1801_115.FIN2	91.2	0.66	1.721	0.048	0.1726	0.0029	0.13165	1014	18	1026	16	978	66	978	66	1.515152
IRA1801_56.FIN2	198.3	0.935	1.73	0.027	0.1724	0.0017	0.26382	1018.5	9.8	1025	9.5	1007	32	1007	32	1.069519
IRA1801_57.FIN2	85	0.885	1.666	0.045	0.1653	0.0023	0.33991	993	17	986	13	1027	51	1027	51	1.129944
IRA1801_3.FIN2	557	1.149	1.818	0.028	0.1791	0.0024	0.21674	1051	10	1062	13	1030	36	1030	36	0.870322
IRA1801_28.FIN2	111.1	1	1.698	0.041	0.1675	0.0025	0.086287	1006	15	998	14	1035	52	1035	52	1
IRA1801_89.FIN2	87.7	0.626	1.781	0.045	0.1744	0.0025	0.25644	1037	17	1036	14	1041	56	1041	56	1.597444
IRA1801_6.FIN2	80.2	1.605	1.884	0.034	0.1831	0.0023	0.16933	1076	12	1084	13	1045	41	1045	41	0.623053
IRA1801_132.FIN2	341	1.472	1.586	0.031	0.1529	0.0025	0.69006	963	12	917	14	1059	29	1059	29	0.679348
IRA1801_43.FIN2	511	1.328	1.842	0.023	0.1767	0.0021	0.69101	1060	8.1	1051	12	1077	20	1077	20	0.753012
IRA1801_105.FIN2	152.4	0.7783	2.046	0.034	0.1927	0.0019	0.41276	1130	11	1136	10	1107	31	1107	31	1.284852
IRA1801_90.FIN2	70.6	1.526	1.661	0.039	0.1565	0.0023	0.4674	991	15	937	13	1123	49	1123	49	0.655308
IRA1801_118.FIN2	590	0.685	4.082	0.052	0.2858	0.0028	0.62341	1649	10	1620	14	1678	18	1678	18	1.459854
IRA1801_24.FIN2	1397	2.852	3.777	0.055	0.2482	0.004	0.74745	1587	12	1429	21	1814	20	1814	20	0.350631
IRA1801_83.FIN2	196.8	1.014	5.45	0.049	0.3474	0.0026	0.49289	1892	7.7	1922	12	1859	14	1859	14	0.986193
IRA1801_10.FIN2	164.1	2.107	5.841	0.063	0.3541	0.0032	0.43579	1951.5	9.3	1954	15	1942	19	1942	19	0.474608
IRA1801_133.FIN2	405.9	6.1	5.23	0.26	0.31	0.011	0.94733	1857	44	1738	57	1990	32	1990	32	0.163934
IRA1801_8.FIN2	643	1.098	5.144	0.089	0.3007	0.0059	0.67113	1843	15	1694	29	2002	26	2002	26	0.910747
IRA1801_135.FIN2	249	1.357	4.53	0.13	0.2632	0.0066	0.75554	1732	23	1505	33	2006	26	2006	26	0.73692
IRA1801_79.FIN2	274	1.533	7.01	0.068	0.3904	0.0036	0.70577	2111.6	8.6	2124	17	2092	13	2092	13	0.652316
IRA1801_112.FIN2	330	2.546	7.549	0.079	0.4178	0.0045	0.66532	2178.2	9.4	2250	20	2105	16	2105	16	0.392773
IRA1801_25.FIN2	523	6.08	7.377	0.072	0.4025	0.0032	0.66403	2157.5	8.7	2180	15	2141	13	2141	13	0.164474
IRA1801_30.FIN2	508	2.029	8.439	0.076	0.4239	0.0044	0.58206	2278.7	8.2	2278	20	2279	16	2279	16	0.492854
IRA1801_121.FIN2	218.1	2.37	8.16	0.11	0.3862	0.0041	0.45965	2247	12	2104	19	2381	23	2381	23	0.421941
IRA1801_80.FIN2	947	2.99	11.25	0.13	0.4735	0.0056	0.79534	2543	11	2498	24	2564	14	2564	14	0.334448
IRA1801_102.FIN2	248	0.821	10.59	0.2	0.4464	0.0069	0.88898	2484	19	2377	31	2570	15	2570	15	1.218027
IRA1801_40.FIN2	155.4	1.682	10.95	0.19	0.4641	0.0073	0.70208	2517	16	2457	32	2580	21	2580	21	0.59453
IRA1801_2.FIN2	51.38	1	11.81	0.16	0.4951	0.0054	0.32393	2587	13	2592	23	2586	24	2586	24	1
IRA1801_61.FIN2	221	0.529	11.07	0.24	0.468	0.011	0.82118	2528	20	2475	47	2596	24	2596	24	1.890359
IRA1801_36.FIN2	97.6	0.764	11.62	0.22	0.4785	0.0071	0.64317	2573	17	2520	31	2627	24	2627	24	1.308901
IRA1801_92.FIN2	205.5	2.914	13.02	0.1	0.4571	0.0036	0.56484	2680.8	7.6	2426	16	2863	12	2863	12	0.343171

Sample Name:	IRA1802							207/235		206/238		207/206		Best age			
Grain	[U] ppm	U/Th	207/235	2σ error	206/238	2σ error	RHO	Age (Ma)	2σ error	Age (Ma)	2σ error	Age (Ma)	2σ error	(Ma)	2σ error	Th/U	Rim
IRA1802_95.FIN2	3780	76.7	0.053	0.0022	0.00783	0.00038	0.63625	52.4	2.1	50.3	2.4	185	83	50.3	2.4	0.013038	rim
IRA1802_78.FIN2	3350	77	0.0552	0.002	0.00784	0.00026	0.56501	54.5	2	50.4	1.6	264	75	50.4	1.6	0.012987	rim
IRA1802_80.FIN2	2780	48.3	0.0582	0.0032	0.00804	0.00033	0.68619	57.4	3	51.6	2.1	299	87	51.6	2.1	0.020704	rim
IRA1802_2.FIN2	1894	15	0.068	0.0052	0.00909	0.00033	0.69069	66.7	4.9	58.3	2.1	360	110	58.3	2.1	0.066667	rim
IRA1802_130.FIN2	2780	13.2	0.0657	0.0022	0.00947	0.00032	0.82037	64.6	2.1	60.8	2	216	55	60.8	2	0.075758	rim
IRA1802_42.FIN2	4140	43.9	0.0701	0.0047	0.01015	0.0007	0.78201	68.7	4.5	65.1	4.5	215	93	65.1	4.5	0.022779	rim
IRA1802_79.FIN2	2310	20.4	0.0704	0.0062	0.01034	0.00078	0.8591	68.9	5.9	66.3	5	120	74	66.3	5	0.04902	rim
IRA1802_47.FIN2	1150	27.7	0.093	0.014	0.01197	0.00093	0.59993	90	13	76.7	5.9	400	240	76.7	5.9	0.036101	rim
IRA1802_17.FIN2	3240	11.7	0.0977	0.0069	0.01287	0.00067	0.72206	94.6	6.4	82.5	4.2	410	110	82.5	4.2	0.08547	rim
IRA1802_100.FIN2	2620	49.5	0.1078	0.0068	0.01391	0.00063	0.74351	103.8	6.2	89	4	440	100	89	4	0.020202	rim
IRA1802_50.FIN2	1721	14.6	0.11	0.004	0.01485	0.00053	0.56257	105.9	3.6	95	3.3	357	74	95	3.3	0.068493	rim
IRA1802_2.FIN2	271.4	1.562	0.233	0.013	0.03168	0.00083	0.18029	212	10	201.1	5.2	300	120	201.1	5.2	0.640205	
IRA1802_78.FIN2	289	1.57	0.222	0.017	0.0321	0.0012	0.52934	202	14	203.8	7.5	190	140	203.8	7.5	0.636943	
IRA1802_21.FIN2	517	2.508	0.247	0.015	0.0324	0.0025	0.40278	224	12	206	16	440	170	206	16	0.398724	
IRA1802_38.FIN2	1030	1.385	0.2347	0.0066	0.03273	0.00068	0.36128	213.9	5.4	207.6	4.2	265	60	207.6	4.2	0.722022	
IRA1802_28.FIN2	1069	1.65	0.235	0.01	0.0337	0.001	0.83976	213.7	8.3	213.4	6.3	200	52	213.4	6.3	0.606061	
IRA1802_13.FIN2	276.3	1.175	0.25	0.017	0.0348	0.0015	0.53036	225	14	220.7	9.2	280	120	220.7	9.2	0.851064	
IRA1802_31.FIN2	1103	10.46	0.262	0.011	0.0349	0.0011	0.80268	235.8	8.8	221	6.9	340	56	221	6.9	0.095602	
IRA1802_55.FIN2	523	1.115	0.2602	0.0068	0.03628	0.00045	0.090204	234.6	5.4	229.7	2.8	277	60	229.7	2.8	0.896861	
IRA1802_9.FIN2	569	1.693	0.2584	0.0083	0.03676	0.00055	0.19243	233.1	6.7	232.7	3.4	246	70	232.7	3.4	0.590667	
IRA1802_70.FIN2	492	0.858	0.2638	0.0079	0.03695	0.00054	0.52129	237.4	6.3	233.9	3.3	281	67	233.9	3.3	1.165501	
IRA1802_79.FIN2	412	0.797	0.2671	0.0087	0.03768	0.00051	0.072768	240	6.9	238.4	3.2	267	74	238.4	3.2	1.254705	
IRA1802_98.FIN2	110.1	1.783	0.282	0.012	0.03789	0.00071	0.27692	251.2	9.8	239.7	4.4	345	89	239.7	4.4	0.560852	
IRA1802_33.FIN2	383.9	1.085	0.2704	0.0084	0.03805	0.00061	0.39465	242.6	6.8	240.7	3.8	229	63	240.7	3.8	0.921659	
IRA1802_105.FIN2	1053	0.566	0.271	0.006	0.03808	0.00052	0.45316	243.4	4.8	240.9	3.2	254	47	240.9	3.2	1.766784	
IRA1802_64.FIN2	400	1.116	0.2733	0.0071	0.03849	0.00069	0.60332	244.9	5.6	243.4	4.3	250	45	243.4	4.3	0.896057	
IRA1802_97.FIN2	227.5	1.153	0.2745	0.0078	0.03938	0.00049	0.014954	245.8	6.2	249	3	218	64	249	3	0.867303	
IRA1802_110.FIN2	308	1.12	0.2887	0.0095	0.03965	0.0007	0.10783	257.2	7.5	250.6	4.3	309	83	250.6	4.3	0.892857	
IRA1802_66.FIN2	461	1.852	0.2715	0.0083	0.03989	0.0006	0.63801	244.9	6.2	252.1	3.7	201	55	252.1	3.7	0.539957	
IRA1802_117.FIN2	841	0.846	0.2891	0.0072	0.0403	0.00068	0.00783	257.8	5.6	254.7	4.2	294	68	254.7	4.2	1.182033	
IRA1802_40.FIN2	606	1.007	0.2947	0.0065	0.04111	0.00051	0.4715	262	5.1	259.7	3.2	272	44	259.7	3.2	0.993049	
IRA1802_8.FIN2	521.1	0.855	0.2998	0.0061	0.04112	0.00041	0.16029	266	4.7	259.7	2.5	328	46	259.7	2.5	1.169591	
IRA1802_7.FIN2	597	0.582	0.2948	0.006	0.04166	0.00039	0.1001	262.1	4.7	263.1	2.4	261	48	263.1	2.4	1.718213	
IRA1802_68.FIN2	210.3	0.916	0.32	0.012	0.04196	0.00086	0.34992	281.6	9.4	264.9	5.3	429	82	264.9	5.3	1.091703	
IRA1802_72.FIN2	218	1.01	0.308	0.011	0.04243	0.00087	0.21431	272.2	8.4	267.8	5.3	317	80	267.8	5.3	0.990099	
IRA1802_118.FIN2	465	1.906	0.3535	0.0096	0.04567	0.00082	0.42596	307	7.1	287.9	5.1	465	59	287.9	5.1	0.524659	
IRA1802_104.FIN2	280.7	7.48	0.399	0.016	0.0473	0.0011	0.59259	340	12	298.1	6.9	605	73	298.1	6.9	0.13369	
IRA1802_49.FIN2	1524	2.392	0.3627	0.0077	0.04812	0.00071	0.37178	314.1	5.8	303	4.3	404	47	303	4.3	0.41806	
IRA1802_45.FIN2	822	1.45	0.496	0.019	0.0553	0.0016	0.77362	407	13	347.1	9.5	745	50	347.1	9.5	0.689655	
IRA1802_116.FIN2	1188	6.27	0.51	0.013	0.0614	0.0015	0.74167	417.9	8.9	384.3	9.4	621	39	384.3	9.4	0.15949	
IRA1802_32.FIN2	115.2	1.198	0.54	0.033	0.063	0.0017	0.40231	437	21	394	10	640	120	394	10	0.834725	
IRA1802_26.FIN2	1166	2.161	0.509	0.013	0.0631	0.0021	0.53914	417.5	8.7	395	13	564	66	395	13	0.462749	
IRA1802_27.FIN2	1057	1.262	0.503	0.01	0.06526	0.0009	0.52152	413.5	6.8	407.5	5.4	442	34	407.5	5.4	0.792393	
IRA1802_58.FIN2	581	2.34	0.52	0.014	0.0669	0.0013	0.444	425	9.4	417.7	8	445	66	417.7	8	0.42735	
IRA1802_101.FIN2	341.5	2.024	0.542	0.018	0.0683	0.0018	0.39411	439	12	426	11	500	72	426	11	0.494071	
IRA1802_41.FIN2	654	1.308	0.548	0.011	0.06953	0.00097	0.33045	443.2	7	433.3	5.9	505	46	433.3	5.9	0.764526	
IRA1802_37.FIN2	463	2.789	0.538	0.013	0.0697	0.0012	0.40804	436.5	8.4	434.5	7.2	418	51	434.5	7.2	0.358551	
IRA1802_4.FIN2	732	4.36	0.554	0.01	0.07052	0.00077	0.48098	447.3	6.7	439.3	4.6	481	36	439.3	4.6	0.229358	
IRA1802_102.FIN2	199	1.667	0.542	0.015	0.0707	0.0012	0.34725	438.6	9.7	440.1	7.3	413	59	440.1	7.3	0.59988	
IRA1802_121.FIN2	332.9	1.349	0.552	0.012	0.07108	0.00083	0.38151	445.6	7.7	442.6	5	436	45	442.6	5	0.74129	
IRA1802_10.FIN2	263	1.261	0.592	0.021	0.0711	0.0021	0.5039	471	14	443	13	651	77	443	13	0.793021	
IRA1802_71.FIN2	299	1.694	0.546	0.01	0.07126	0.00071	0.40663	442	6.5	443.7	4.3	431	34	443.7	4.3	0.590319	
IRA1802_34.FIN2	382	4.55	0.5607	0.0096	0.07136	0.00078	0.3889	451.5	6.3	444.3	4.7	451	37	444.3	4.7	0.21978	
IRA1802_53.FIN2	257.6	1.364	0.544	0.015	0.07152	0.00085	0.40059	440	10	445.2	5.1	406	57	445.2	5.1	0.733138	
IRA1802_50.FIN2	350	1.408	0.567	0.016	0.07296	0.00099	0.30296	455	10	453.9	5.9	465	61	453.9	5.9	0.710227	
IRA1802_84.FIN2	351	1.613	0.5604	0.0089	0.07345	0.00068	0.17535	451.3	5.8	456.9	4.1	421	38	456.9	4.1	0.619963	
IRA1802_88.FIN2	475	5.79	0.5658	0.0091	0.07418	0.00073	0.24649	454.8	5.9	461.3	4.4	422	37	461.3	4.4	0.172712	
IRA1802_23.FIN2	504.7	1.213	0.605	0.02	0.0744	0.0018	0.45001	480	13	463	11	582	69	463	11	0.824402	
IRA1802_127.FIN2	475	3.99	0.5764	0.0081	0.07471	0.00082	0.45	461.8	5.2	464.4	4.9	450	31	464.4	4.9	0.250627	
IRA1802_85.FIN2	276.1	1.536	0.591	0.024	0.0748	0.0013	0.17483	471	15	464.9	7.6	504	92	464.9	7.6	0.651042	
IRA1802_39.FIN2	613	1.345	0.584	0.01	0.07506	0.00075	0.10899	466.7	6.6	466.5	4.5	456	43	466.5	4.5	0.743494	

IRA1802_54.FIN2	563	4.774	0.587	0.01	0.07647	0.00088	0.46143	469.8	6.2	475	5.3	443	37	475	5.3	0.209468
IRA1802_57.FIN2	313.4	2.088	0.589	0.011	0.07704	0.00092	0.329	469.9	7	478.4	5.5	429	41	478.4	5.5	0.478927
IRA1802_90.FIN2	217	2.8	0.591	0.013	0.0778	0.001	0.40501	471	8	482.6	6.1	410	41	482.6	6.1	0.357143
IRA1802_20.FIN2	296	5.9	0.611	0.011	0.07808	0.0009	0.32255	483.3	7	484.6	5.4	477	41	484.6	5.4	0.169492
IRA1802_119.FIN2	254.5	2.184	0.604	0.016	0.0781	0.0014	0.21767	479	10	484.8	8.2	434	65	484.8	8.2	0.457875
IRA1802_75.FIN2	407.9	1.858	0.621	0.0097	0.07977	0.00074	0.2165	490.1	6	494.7	4.4	472	36	494.7	4.4	0.538213
IRA1802_128.FIN2	531	1.369	0.732	0.031	0.0836	0.0018	0.25774	557	17	518	11	715	63	518	11	0.73046
IRA1802_124.FIN2	210	1.064	0.697	0.019	0.0848	0.0013	0.2613	536	11	524.5	7.9	563	60	524.5	7.9	0.93985
IRA1802_47.FIN2	84.3	2.059	0.718	0.035	0.0873	0.0021	0.29182	546	20	540	12	558	99	540	12	0.485673
IRA1802_95.FIN2	74.6	1.52	0.726	0.063	0.0886	0.0057	0.79344	553	35	546	34	590	100	546	34	0.657895
IRA1802_36.FIN2	410	1.915	0.722	0.021	0.089	0.0021	0.38892	551	12	549	13	539	65	549	13	0.522193
IRA1802_35.FIN2	406	2.384	0.766	0.017	0.092	0.0013	0.40756	576.5	9.6	567.2	7.9	582	45	567.2	7.9	0.419463
IRA1802_104.FIN2	96	3.11	0.789	0.066	0.0926	0.0036	0.75821	587	36	571	21	620	120	571	21	0.321543
IRA1802_91.FIN2	652	109	0.752	0.01	0.0928	0.00096	0.63439	568.8	5.9	572	5.7	563	24	572	5.7	0.009174
IRA1802_114.FIN2	1066	13.8	0.787	0.015	0.0929	0.0015	0.68109	588.9	8.6	572.8	8.8	661	32	572.8	8.8	0.072464
IRA1802_111.FIN2	117.1	2.35	0.885	0.044	0.0955	0.0032	0.7304	641	24	588	19	825	68	588	19	0.425532
IRA1802_81.FIN2	228.3	1.745	0.796	0.018	0.0973	0.0015	0.45998	595	10	598.5	8.9	586	45	598.5	8.9	0.573066
IRA1802_63.FIN2	237	0.858	0.822	0.012	0.0995	0.001	0.46946	609.2	7.2	611.1	6.2	604	31	611.1	6.2	1.165501
IRA1802_44.FIN2	483	2.16	0.911	0.029	0.0996	0.0025	0.77676	656	15	612	15	805	38	612	15	0.462963
IRA1802_123.FIN2	641	1.638	0.849	0.013	0.10125	0.00099	0.58606	623.9	7.4	621.7	5.8	612	28	621.7	5.8	0.610501
IRA1802_17.FIN2	126.7	1.646	0.84	0.023	0.1013	0.0016	0.42668	617	13	622.1	9.3	595	62	622.1	9.3	0.607533
IRA1802_108.FIN2	315	5.86	0.88	0.019	0.1026	0.0013	0.41572	640	10	629.7	7.8	666	45	629.7	7.8	0.170648
IRA1802_99.FIN2	367.4	3.29	0.93	0.026	0.1038	0.0023	0.83368	666	14	637	14	765	33	637	14	0.303951
IRA1802_87.FIN2	205.4	1.112	0.935	0.037	0.105	0.0013	0.65634	666	17	643.5	7.7	726	56	643.5	7.7	0.899281
IRA1802_125.FIN2	277	2.278	0.918	0.024	0.1072	0.0021	0.6033	661	13	656	12	673	43	656	12	0.438982
IRA1802_14.FIN2	509	1.143	0.968	0.069	0.1075	0.0023	0.52039	680	29	658	14	800	98	658	14	0.874891
IRA1802_46.FIN2	480	3.24	1.021	0.021	0.1111	0.0024	0.37223	714	10	679	14	842	51	679	14	0.308642
IRA1802_96.FIN2	224	2.27	1.168	0.095	0.1134	0.0084	0.95884	780	46	692	49	1059	43	692	49	0.440529
IRA1802_120.FIN2	437.4	1.269	0.969	0.011	0.11402	0.0009	0.30769	687.7	5.7	696	5.2	647	25	696	5.2	0.788022
IRA1802_69.FIN2	174.4	2.45	0.943	0.014	0.1142	0.0012	0.41865	674	7.5	697.3	7.2	617	34	697.3	7.2	0.408163
IRA1802_12.FIN2	270	2.082	1.158	0.057	0.1178	0.007	0.68574	779	27	718	40	975	89	718	40	0.480307
IRA1802_89.FIN2	831	3.479	1.013	0.013	0.118	0.0014	0.52905	709.7	6.5	719.1	8.1	690	26	719.1	8.1	0.287439
IRA1802_93.FIN2	416	4.3	1.079	0.017	0.1199	0.0016	0.43107	742.7	8.4	729.6	9.4	794	33	729.6	9.4	0.232558
IRA1802_62.FIN2	127	0.897	1.051	0.024	0.1215	0.0017	0.3002	728	12	739.3	9.8	688	49	739.3	9.8	1.114827
IRA1802_30.FIN2	488	2.36	1.199	0.033	0.1266	0.003	0.65413	799	15	768	17	880	45	768	17	0.423729
IRA1802_22.FIN2	286	1.48	1.148	0.031	0.1273	0.0024	0.43507	776	15	772	14	804	53	772	14	0.675676
IRA1802_56.FIN2	569	1.685	1.301	0.015	0.1439	0.0011	0.36252	846	6.4	866.7	6	803	21	803	6	0.593472
IRA1802_94.FIN2	222	0.5528	1.301	0.029	0.133	0.0025	0.65391	844	13	805	14	961	36	805	14	1.808973
IRA1802_103.FIN2	565	0.753	1.246	0.018	0.1343	0.0016	0.58712	821.2	8.2	812.3	9	836	26	812.3	9	1.328021
IRA1802_106.FIN2	378	0.584	1.222	0.026	0.1346	0.0025	0.60238	810	12	814	14	797	40	814	14	1.712329
IRA1802_25.FIN2	496	1.644	1.32	0.024	0.1435	0.0022	0.52891	854	10	864	12	840	34	840	12	0.608273
IRA1802_80.FIN2	90.5	1.482	1.346	0.034	0.142	0.002	0.27268	864	15	856	11	904	54	904	54	0.674764
IRA1802_86.FIN2	101.3	1.717	1.428	0.029	0.1488	0.0015	0.10775	899	12	894.3	8.6	917	43	917	43	0.582411
IRA1802_126.FIN2	104.5	1.494	1.724	0.037	0.1724	0.0018	0.31832	1016	14	1025	9.7	987	42	987	42	0.669344
IRA1802_11.FIN2	242.4	0.884	1.609	0.028	0.1631	0.0024	0.49693	973	11	974	13	996	34	996	34	1.131222
IRA1802_100.FIN2	243.4	2.86	1.617	0.061	0.1612	0.0057	0.90655	973	22	962	31	1000	41	1000	41	0.34965
IRA1802_59.FIN2	143	1.01	1.783	0.053	0.1785	0.0033	0.64407	1037	19	1059	18	1002	47	1002	47	0.990099
IRA1802_122.FIN2	175.2	1.479	1.645	0.058	0.1615	0.0036	0.70796	985	22	965	20	1015	52	1015	52	0.676133
IRA1802_60.FIN2	185.8	4.99	1.778	0.041	0.1758	0.0027	0.59753	1036	15	1044	15	1040	39	1040	39	0.200401
IRA1802_74.FIN2	114.3	0.967	1.592	0.046	0.1563	0.0026	0.39443	968	17	936	15	1048	52	1048	52	1.034126
IRA1802_115.FIN2	265.1	0.835	1.666	0.041	0.163	0.0032	0.41216	995	16	973	17	1060	49	1060	49	1.197605
IRA1802_129.FIN2	535	1.739	1.795	0.035	0.1687	0.0026	0.63572	1041	13	1007	14	1119	30	1119	30	0.575043
IRA1802_29.FIN2	505	1.924	1.991	0.046	0.1859	0.0038	0.65202	1112	15	1099	21	1138	36	1138	36	0.519751
IRA1802_65.FIN2	235.5	3.67	2.882	0.085	0.2448	0.0044	0.56836	1376	22	1412	23	1332	50	1332	50	0.27248
IRA1802_15.FIN2	58.2	2.032	2.472	0.088	0.2058	0.0078	0.2797	1260	25	1205	42	1371	85	1371	85	0.492126
IRA1802_112.FIN2	202	0.949	4.57	0.1	0.2924	0.0059	0.85346	1741	18	1653	30	1850	22	1850	22	1.053741
IRA1802_3.FIN2	306.6	0.7144	5.14	0.051	0.3258	0.0028	0.62756	1842	8.4	1818	14	1866	14	1866	14	1.399776
IRA1802_18.FIN2	256.8	0.701	5.407	0.075	0.3395	0.004	0.92418	1885	12	1884	19	1901	18	1901	18	1.426534
IRA1802_61.FIN2	162	0.816	5.37	0.14	0.3345	0.0071	0.80846	1878	22	1860	34	1911	26	1911	26	1.22549
IRA1802_109.FIN2	197	0.775	6.42	0.54	0.379	0.034	0.94319	2031	72	2070	160	1997	52	1997	52	1.290323
IRA1802_19.FIN2	319.7	3.18	9.96	0.15	0.4554	0.0057	0.68832	2429	14	2418	25	2442	23	2442	23	0.314465
IRA1802_92.FIN2	329	1.74	10.48	0.34	0.477	0.015	0.91311	2476	30	2512	66	2454	23	2454	23	0.574713

Bibliography

Abdelsalam, M.G., Liegeois, J.P., and Stern, R.J., 2002. The Saharan metacraton. J. Afr. Earth Sci., v. 34, no. 3–4, p. 119–136. doi:10.1016/S0899-5362 (02)00013-1.

Agostini, S., Doglioni, C., Innocenti, F., Manetti, P. and Tonarini, S., 2010. On the geodynamics of the Aegean rift. Tectonophysics, 488(1-4), pp.7-21.

Altherr, R. Kreuzer, H., Wendt, I., Lenz, H., Wagner, G., Keller, J., Harre, W., and Hohndorf, A. 1982. A late Oligocene/early Miocene high-temperature belt in the Attic-Cycladic Crystalline Complex (SE Pelagonian, Greece). Geol. Jahrb., E23, 97-164.

Altherr, R., Kreuzer, H., Lenz, H., Wendt, I., Harre, W., & Dürr, S. 1994. Further evidence for a Late Cretaceous low-pressure/high-temperature terrane in the Cyclades, Greece. Chemie der Erde, 54, 319–328.

Anders, B., Reischmann, T., Poller, U., Kostopoulos, D. 2005. Age and origin of granitic rocks from the eastern Vardar Zone: new constraints on the evolution of the Internal Hellenides. J. Geol. Soc. London, 162, 857–870. https://doi.org/10.1144/0016-764904-077.

Anders, B., Reischmann, T., Kostopoulos, D., Poller, U. 2006. The oldest rocks of Greece: first evidence for a Precambrian terrane within the Pelagonian Zone. Geol. Mag., 143, 41–58. DOI: https://doi.org/10.1017/S0016756805001111.

Anders, B., Reischmann, T., Kostopoulos, D. 2007. Zircon geochronology of basement rocks from the Pelagonian Zone, Greece: constraints on the pre-Alpine evolution of the westernmost Internal Hellenides. Int. J. Earth Sci., 96, 639–661. https://doi.org/10.1007/s00531-006-0121-7.

Andriessen, P.A.M., Banga, G., and Hebeda, E.H. 1987. Isotopic age study of pre-Alpine rocks in the basal units on Naxos, Sikinos and Ios, Greek Cyclades. Geol. Mijnb., 66(3), pp.3-14.

Armijo, R., Meyer, B., Hubert, A. and Barka, A. 1999. Westward propagation of the North Anatolian fault into the northern Aegean: Timing and kinematics. Geology, 27(3), pp.267-270.

Aubouin, J., Bonneau, M., & Celet, P. 1970. Contribution à la géologie des Hellènides: le Gavrovo, le Pinde et la zone ophiolique subpélagonienne. Soc. Géol. Nord.

Augier, R., Jolivet, L., Gadenne, L., Lahfid, A., and Driussi, O. 2014. Exhumation kinematics of the Cycladic Blueschists unit and back-arc extension, insight from the Southern Cyclades (Sikinos and Folegandros Islands, Greece). Tectonics, 34(1), 152–185. https://doi.org/10.1002/2014TC003664.

Avdis, V. & Triantaphyllis, M. 1994. Geological Map, sheets Iraklia and Schinoussa, Scale 1: 50 000. – Department of Geology and Geological Mapping, Athens.

Avigad, D., and Garfunkel, Z. 1991. Uplift and exhumation of high-pressure metamorphic terranes: The example of the Cycladic blueschists belt (Aegean Sea). Tectonophysics 188, 357–372. https://doi.org/10.1016/0040-1951(91)90464-4.

Avigad, D. 1998. High-pressure metamorphism and cooling on SE Naxos (Cyclades, Greece). European J. Mineral., 10, 1309-1319.

Avigad, D., Ziv, A. and Garfunkel, Z. 2001. Ductile and brittle shortening, extension-parallel folds and maintenance of crustal thickness in the central Aegean (Cyclades, Greece). Tectonics, 20(2), pp.277-287.

Avigad, D., Stern, R.J., Beyth, M., Miller, N. and McWilliams, M.O. 2007. Detrital zircon U–Pb geochronology of Cryogenian diamictites and Lower Paleozoic sandstone in Ethiopia (Tigrai): age constraints on Neoproterozoic glaciation and crustal evolution of the southern Arabian–Nubian Shield. Precambrian Res., 154(1-2), pp.88-106.

Avigad, D., Gerdes, A., Morag, N., Bechstadt, T. 2012. Coupled U–Pb– Hf of detrital zircons of Cambrian sandstones from Morocco and Sardinia: implications for provenance and Precambrian crustal evolution of north Gondwana. Gondwana Res., 21, 690–703.

Baldwin, S. L. 1996. Contrasting PTt histories for blueschists from the western Baja Terrane and the Aegean: Effects of synsubduction exhumation and backarc extension. Washington DC Am. Geophys. Union, Geophys. Monogr. Ser., 96, pp.135-141.

Baldwin, S. L., & Lister, G. S. 1998. Thermochronology of the South Cyclades Shear Zone, Ios, Greece: Effects of ductile shear in the argon partial retention zone. J. Geophys. Res., 103:7315–7336. doi:10.1029/97JB03106.

Bargnesi, E.A., Stockli, D.F., Mancktelow, N., and Soukis, K. 2013. Miocene core complex development and coeval supradetachment basin evolution of Paros, Greece, insights from (U–Th)/He thermochronometry. Tectonophysics, 595, 165-182. https://doi.org/10.1016/j.tecto.2012.07.015.

Baud, A., Jenny. C., Papanikolaou. D., Sideris. C., and Stampfli. G.M. 1990. New observations on Permian stratigraphy in Greece and geodynamic interpretation. Bull. Geol. Soc. Greece, 25(1): 187-206.

Baumgartner, P.O. 1985. Jurassic sedimentary evolution and nappe emplacement in the Argolis Peninsula (Peloponnesus, Greece). Mém. Soc. Helv. Sci. Nat., 99, 1–111.

Beaudoin, A., Laurent, V., Augier, R., Jolivet, L., Lahfid, A., Arbaret, L., Rabillard, A., Menant, A. 2015. The Ikaria high-temperature metamorphic core complex (Cyclades, Greece): geometry, kinematics and thermal structure. J. Geodyn., 92, 18–41. https://doi.org/10.1016/j.jog.2015.09.004.

Behrmann, J.H., Seckel, C. 2007. Structures, flow stresses, and estimated strain rates in metamorphic rocks of the Small Cyclades Islands Iraklia and Schinoussa (Aegean Sea, Greece). Geotectonica Res. 95, 1–11.

Blake, M.C., Geyssant, J., Kienast, J.R., Lepvrier, C., Maluski, H., Papanikolaou, D. 1981. A geologic reconnaissance of the Cycladic Blueschist Belt, Greece. Geol. Soc. Am. Bull., 92 (I), 247–254. https://doi.org/10.1130/0016-7606(1981)92<247:AGROTC>2.0.CO;2.

Böger, H. 1983. Stratigraphische und tektonische Verknuepfungen kontinentaler Sedimente des Neogens im Aegais-Raum. Geol. Rundsch., 72, 771–813. https://doi.org/10.1007/BF01848344.

Bolhar, R., Ring, U., & Allen, C. M. 2010. An integrated zircon geochronological and geochemical investigation into the Miocene plutonic evolution of the Cyclades, Aegean Sea, Greece: Part 1: Geochronology. Contr. Mineral. Petrol., 160(5), 719-742.

Bonneau, M. 1984. Correlation of the Hellenic nappes in the south-east Aegean and their tectonic reconstruction. In: Dixon, J.E., Robertson, A.H.F. (Eds.). The Geological Evolution of the Eastern Mediterranean. Special Publication of the Geological Society of London. Blackwell Sci. Publ., Oxford, pp. 517–527.

Bonneau, M., and Kienast, J. R. 1982. Subduction, collision et schistes bleus; l'exemple de l'Egee (Grece). Bull. Soc. geol. Fr., 7(4), 785–791.

Bortolotti, V., Carras, N., Chiari, M., Fazzuoli, M., Marcucci, M., Photiades, A., Principi, G. 2003. The Argolis peninsula in the palaeogeographic and geodynamic frame of the Hellenides. Ofioliti, 28(2), 79–94. https://doi.org/10.4454/ofioliti.v28i2.196.

Bortolotti, V., Chiari, M., Marroni, M., Pandolfi, L., Principi, G., Saccani, E. 2013. Geodynamic evolution of ophiolites from Albania and Greece (Dinaric-Hellenic belt): one, two, or more oceanic basins? Int. J. Earth Sci., 102, 783–811. https://doi.org/10.1007/s00531-012-0835-7.

Bousquet R, Oberhδnsli R, Goffe B, Wiederkehr M, Koller F, SchmidSM, Schuster R, Engi M, Berger A, Martinotti G. 2008. Metamorphism of metasediments in the scale of an orogen: a key to the Tertiary geodynamic evolution of the Alps. In: Siegesmund S, Froitzheim N (eds) Tectonic aspect of the Alpine-Dinaride-Carpathian system, vol 298. Geol. Soc. Spec. Publ. London, pp 393–411

Brichau, S., Ring, U., Ketcham, R.A., Carter, A., Stockli, D., and Brunel, M. 2006. Constraining the long-term evolution of the slip rate for a major extensional fault system in the central Aegean, Greece, using thermochronology. Earth Planet. Sci. Lett., 241(1-2), 293-306. https://doi.org/10.1016/j.epsl.2005.09.065.

Brichau, S., Ring, U., Carter, A., Monié, P., Bolhar, R., Stockli, D., Brunel, M. 2007. Extensional faulting on Tinos Island, Aegean Sea, Greece: How many detachments? Tectonics, 26, TC4009. https://doi.org/10.1029/2006TC001969.

Brichau, S., Thomson, S., and Ring, U. 2010. Thermochronometric constraints on the tectonic evolution of the Serifos detachment, Aegean Sea, Greece. Int. J. Earth Sci., 99(2), 379-393. https://doi.org/10.1007/s00531-008-0386-0.

Bröcker, M. 1990. Die Blauschiefer-Grünschiefer-Assoziation der Insel Tinos (Kykladen, Griechenland) und ihre kontaktmetamorphe Überprägung. Geotektonische Forschungen, 74, 1-107.

Bröcker, M., Kreuzer, H., Matthews, A., and Okrusch, M. 1993. 40Ar/39Ar and oxygen isotope studies of polymetamorphism from Tinos Island, Cycladic blueschist belt, Greece: J. Metamorph. Geol., 11, 223–240. doi:10.1111/j.1525-1314.1993. tb00144. x.

Bröcker, M., and Franz, L. 1998. Rb–Sr isotope studies on Tinos Island (Cyclades, Greece): additional time constraints for metamorphism, extent of infiltration-controlled overprinting and deformational activity. Geol. Mag., 135, 369–382.

Bröcker, M. and Enders, M. 1999. U–Pb zircon geochronology of unusual eclogite-facies rocks from Syros and Tinos (Cyclades, Greece). Geol. Mag., 136(2), pp.111-118.

Bröcker, M., and Keasling, A. 2006. Ionprobe U-Pb zircon ages from the high-pressure/low-temperature mélange of Syros, Greece: Age diversity and the importance of pre-Eocene subduction. J. Metamorph. Geol., 24(7), 615–631. https://doi.org/10.1111/j.1525-1314.2006.00658.x.

Bröcker, M., and Pidgeon, R.T. 2007. Protolith Ages of Meta-igneous and Metatuffaceous Rocks from the Cycladic Blueschist Unit, Greece: Results of a Reconnaissance U-Pb Zircon Study. J. Geol., 115, 83–98. https://doi.org/10.1086/509269.

Bröcker, M., Baldwin, S., and Arkudas, R. 2013. The geological significance of 40Ar/39Ar and Rb-Sr white mica ages from Syros and Sifnos, Greece: A record of continuous (re)crystallization during exhumation? J. Metamorph. Geol., 31, 629–646. https://doi.org/10.1111/jmg.12037.

Bröcker, M., Huyskens, M., and Berndt, J. 2016. U–Pb dating of detrital zircons from Andros, Greece: constraints for the time of sediment accumulation in the northern part of the Cycladic blueschist belt. Geol. J., 51(3), 354–367. https://doi.org/10.1002/gj.2634.

Brodhag, S., Gracia-Calvo, M. & Schiwek, P., 2003: Geologie und Tektonik der Insel Iraklia/Kykladen (Griechenland). – Unpubl.nMapping Report, Univ. Freiburg, 76 pp.

Buick, I.S. 1991. The late Alpine evolution of an extensional shear zone, Naxos, Greece. J. Geol. Soc., 148(1), 93-103.

Brun, J.P. and Sokoutis, D. 2010. 45 m.y. of Aegean crust and mantle flow driven by trench retreat. Geology 38 (9), 815–818. https://doi.org/10.1130/G30950.1.

Burkhard, M. 1992. Calcite twins, their geometry, appearance and significance as stress-strain markers and indicators of tectonic regime: a review. J. Struct. Geol. 15, 351–368.

Buick, I.S. 1991. The late Alpine evolution of an extensional shear zone, Naxos, Greece. J. Geol. Soc., 148(1), 93-103. https://doi.org/10.1144/gsjgs.148.1.0093.

Buick, I.S., Holland, T.J.B. 1989. The P-T-t path associated with crustal extension, Naxos, Cyclades. In: Daly, J.S., Cliff, R.A., Yardley, B.W.D., (eds): The evolution of metamorphic belts. Geol. Soc. London Spec. Publ., 40, 365 371.

Cao, S.Y., Neubauer, F., Bernroider, F., Genser, J., Liu, J., Friedl, G., 2017. Low-grade retrogression of a high-temperature metamorphic core complex: Naxos, Cyclades, Greece. Geol. Soc. Am. Bull., 129, 93–117. https://doi.org/10.1130/B31502.1.

Cassinis, G., Perotti, C., Santi, G. 2018. Post-Variscan Verrucano-like deposits in Italy, and the onset of the alpine tectono-sedimentary cycle. Earth Sci. Rev., 185, 476–497. https://doi.org/10.1016/j.earscirev.2018.06.021.

Celet, P. Ferriere, J. 1978. Les Hellenides internes: le Pelagonien. Eclogae Geol. Helv. 71(3):467–495.

Chatzaras, V., Xypolias, P., Kokkalas, S., and Koukouvelas I. 2011. Oligocene–Miocene thrusting in central Aegean: insights from the Cycladic island of Amorgos, Geol. Journal, 46, 619–636. doi:10.1002/gj.1304.

Chatzaras, V., Dörr, W., Gerdes, A., Krahl, J., Xypolias, P., Zulauf, G. 2016. Tracking the late Paleozoic to early Mesozoic margin of northern Gondwana in the Hellenides: paleotectonic constraints from U–Pb detrital zircon ages. Int. J. Earth Sci., (Geol. Rundsch.), 105, 1881–1899. DOI:10.1007/s00531-016-1298-z.

Cisneros, M., Barnes, J.D., Behr, W.M.; Kotowski, A.J.; Stockli, D.F.; Soukis, K. 2021. Insights from elastic thermobarometry into exhumation of high-pressure metamorphic rocks from Syros, Greece. Solid Earth, 12, 1335–1355.

Clément, B., 1968. Observations sur le Trias du Pateras et du Parnis en Attique (Grèce). CR somm. des Séances, SGF, fasc, *9*, pp.332-334.

Clift, P.D. 1996. Accretion tectonics of the Neotethyan Ermioni Complex, Peloponnesos, Greece. J. Geol. Soc. London, 153, 745-757. https://doi.org/10.1144/gsjgs.153.5.0745.

Coleman, M., Dubosq, R., Schneider, D.A., Grasemann, B. and Soukis, K. 2019. Along-strike consistency of an extensional detachment system, West Cyclades, Greece. Terra Nova, 31(3), 220-233. DOI: 10.1111/ter.12388.

Coleman, M.J., Schneider, D.A., Grasemann, B., Soukis, K., Lozios, S. and Hollinetz, M.S. 2020. Lateral Termination of a Cycladic-Style Detachment System (Hymittos, Greece). Tectonics, 39, e2020TC006128. https://doi.org/10.1029/2020TC006128.

De Bono, A. 1998. Pelagonian margins in central Evia Island (Greece). Stratigraphy and geodynamic evolution. Unpublished on line PhD thesis, Lausanne, 114 pp. http://www.ss.unil.ch/publications/pdf/phd_debono.pdf.

De Bono, A., Martini, R., Zaninetti, L., Hirsch, F., Stampfli, G.M., Vavassis, I. 2001 Permo-Triassic stratigraphy of the Pelagonian zone in central Evia island (Greece). Eclogae Geol. Helv. 94, 289–311. https://archive-ouverte.unige.ch/unige:40868.

Denèle, Y., Lecomte, E., Jolivet, L., Lacombe, O., Labrousse, L., Huet, B., Le Pourhiet, L. 2011. Granite intrusion in a metamorphic core complex: the example of the Mykonos laccolith (Cyclades, Greece). Tectonophysics 501, 52–70. https://doi.org/10.1016/j.tecto.2011.01.013.

Dickinson, W. R., and Gehrels, G. E. 2009. Use of U-Pb ages of detrital zircons to infer maximum depositional ages of strata: A test against a Colorado Plateau Mesozoic database. Earth Planet. Sci. Lett., *288*(1–2), 115–125.

Doglioni, C., Busatta, C., Bolis, G., Marianini, L., and Zanella, M. 1996. Structural evolution of the eastern Balkans (Bulgaria). Marine Petrol. Geol., 13 (2), 225-251.

Doglioni, C., Harabaglia, P., Merlini, S., Mongelli, F., Peccerillo, A., Piromallo, C. 1999. Orogens and slabs vs their direction of subduction. Earth-Sci. Rev. 45, 167–208.

Doglioni, C., Carminati, E., Cuffaro, M., and Scrocca, D. 2007. Subduction kinematics and dynamic constraints. Earth Sci. Rev., 83 (3-4), 125-175. https://doi.org/10.1016/j.earscirev.2007.04.001.

Dörr, W., Zulauf, G., Gerdes, A., Lahaye, J., Kowalczyk, G. 2015. A hidden Tonian basement in the eastern Mediterranean: Age constraints from U–Pb data of magmatic and detrital zircons of the External Hellenides (Crete and Peloponnesus). Precambrian Res., 258, 83–108. https://doi.org/10.1016/j.precamres.2014.12.015.

Dubois, R., and Bignot, G. 1979. Présence d'un 'hardground' nummulitique au sommet de la série Cretacée d'Almyropotamos (Eubée méridionale, Grèce): Consequences. C. R. Acad. Sci., Série II 289, 993–995.

Duchene, S., Aissa, R., Vanderhaeghe, O. 2006. Pressure-temperature-time evolution of metamorphic rocks from Naxos (Cyclades, Greece): constraints from thermobarometry and Rb/Sr dating. Geodin. Acta, 19, 301–321.

Dürr, S., Altherr, R., Keller, J., Okrusch, M., Seidel, E. 1978. The Median Aegean Crystalline Belt: Stratigraphy, structure, metamorphism, magmatism, in: Closs, H. et al. (Eds.), Alps, Apennines, Hellenides. IUCG Sci. Rep. 38, 455–477.

Dürr, S. 1985. Geological Map of Greece, 1:50.000, Amorgos–Donousa Sheet. Institute of Geological and Mining Research, Athens.

El-Bialy, M.Z. 2020. Precambrian basement complex of Egypt. In The Geology of Egypt (pp. 37-79). Springer, Cham. https://doi.org/10.1007/978-3-030-15265-9_2.

Encinas, A., Sagripanti, L., Rodríguez, M.P., Orts, D., Anavalon, A., Giroux, P., Otero, J., Echaurren, A., Zambrano, P., and Valencia, V. 2021. Tectonosedimentary evolution of

the Coastal Cordillera and Central Depression of south-Central Chile (36◦30'-42◦S). Earth Sci. Rev., 213 103465. https://doi.org/10.1016/j.earscirev.2020.103465.

Engel, M., and Reischmann, T. 1998. Single zircon geochronology of orthogneisses from Paros, Greece. Bull. Geol. Soc. Greece, 32(3), pp. 91–99.

Eyal, M., Litvinovsky, B., Jahn, B.M., Zanvilevich, A. and Katzir, Y. 2010. Origin and evolution of post-collisional magmatism: coeval Neoproterozoic calc-alkaline and alkaline suites of the Sinai Peninsula. Chem. Geol., 269(3-4), pp.153-179. https://doi.org/10.1016/j.chemgeo.2009.09.010.

Faccenda, M., Gerya, T. V., & Chakraborty, S. 2008. Styles of post-subduction collisional orogeny: influence of convergence velocity, crustal rheology and radiogenic heat production. Lithos, 103, 257–287.

Faccenna, C., Jolivet, L., Piromallo, C. and Morelli, A. 2003. Subduction and the depth of convection in the Mediterranean mantle. J. Geoph. Res.: Solid Earth, 108(B2).

Ferriere, J. 1982. Paleogeographies et tectoniques superposees dans les Hellenides Internes au niveau de l'Othrys et du Pelion (Grece). Soc. Geol. Nord. Publ. 8:1–970.

Ferriere, J., Reynaud, J.Y., Pavlopoulos, A., Bonneau, M., Migiros, G., Chanier, F., Gardin, S. 2004. Geologic evolution and geodynamic controls of the Tertiary intramontane piggyback Meso-Hellenic basin, Greece. Bull. Soc. Géol. Fr., 175, 361–381. https://doi.org/10.2113/175.4.361.

Ferriere J., Chanier, F., Ditbanjong, P. 2012. The Hellenic ophiolites: eastward or westward obduction of the Maliac Ocean, a discussion. Int. J. Earth Sci., (Geol. Rundsch.), 101, 1559–1580. https://doi.org/10.1007/s00531-012-0797-9.

Ferriere J, Chanier F, Baumgartner PO, Caridroit M, Bout-Roumazeilles V, Graveleau F, Danelian T, Ventalon S. 2015. The evolution of the Triassic–Jurassic oceanic lithosphere: insights from the supra-ophiolitic series of othris (continental Greece), Bull. Soc. Geol. France 186(6):71–84.

Ferriere, J., Baumgartner, P.O., and Chanier, F. 2016. The Maliac Ocean: the origin of the Tethyan Hellenic ophiolites. Int. J. Earth Sci., (Geol. Rundsch.), 105, 1941–1963. https://doi.org/10.1007/s00531-016-1303-6.

Festa, A., Ogata, K., Pini, G.A., Dilek, Y. and Alonso, J.L. 2016. Origin and significance of olistostromes in the evolution of orogenic belts: A global synthesis. Gondwana Res., 39, pp.180-203. https://doi.org/10.1016/j.gr.2016.08.002.

Finetti, I. 1982. Structure, stratigraphy and evolution of central Mediterranea. *Boll. Geof.Teor. App.*, *24*(96), pp.247-315.

Flansburg, M.E., Stockli, D.F., Poulaki, E.M., and Soukis, K. 2019. Tectono-magmatic and stratigraphic evolution of the Cycladic Basement, Ios Island, Greece. Tectonics, 38, 2291–2316. https://doi.org/10.1029/2018tc005436.

Fleury, J. J. 1980. Evolution d'une platforme et d'un bassin dans leur cadre alpin: les zones de Gavrovo-Tripolitza et du Pinde-Olonos. Soc. Géol. Nord, Spec. Publ., 4, 651.

Franz, L., Okrusch, M., Seidel, E. and Kreuzer, H. 2005. Polymetamorphic evolution of pre-Alpidic basement relics in the external Hellenides, Greece. Neues Jb. Mineral. -Abh., 181(2), pp.147-172. DOI:10.1127/0077-7757/2005/0013.

Forster, M. A., and Lister, G. S. 1999. Detachment faults in the Aegean core complex of Ios, Cyclades, Greece. Geol. Soc., London, Spec. Publ., 154(1), 305–323. https://doi.org/10.1144/GSL.SP.1999.154.01.14.

Forster, M., and Lister, G. 2009. Core-complex-related extension of the Aegean lithosphere initiated at the Eocene-Oligocene transition. J. Geophys. Res., 114, B02401. https://doi.org/10.1029/2007JB005382.

Forster, M.A. and Lister, G.S. 2005. Several distinct tectono-metamorphic slices in the Cycladic eclogite–blueschist belt, Greece. Contr. Mineral. Petrol., 150(5), pp.523-545.

Forte, A.M., Bailey, C.M., 2007. Testing the utility of the porphyroclast hyperbolic distribution method of kinematic vorticity analysis. J. Struct. Geol. 29, 983e1001.

Fossen, H., Tikoff, B. 1997. Forward modelling of non-steady-state deformation and the 'minimum strain path'. J. Struct. Geol. 19, 987–996.

Fossen, H., 2000. Extensional tectonics in the Caledonides: synorogenic or postorogenic? Tectonics 19, 213–224.

Fossen, H., Cavalcante, G.C.G., 2017. Shear zones – a review. Earth Sci. Rev. 171, 434–455.

Fossen, H., Cavalcante, G. G. C., Pinheiro, L. R. V., Archanjo, J. C. 2019. Deformation – Progressive or multiphase? J. Struct. Geol., 125, 82-99. https://doi.org/10.1016/j.jsg.2018.05.006.

Fytrolakis, N., Papanikolaou, D., Panagopoulos, A. 1981. Stratigraphy and structure of Amorgos Island, Aegean Sea. Ann. Géol. Pays Hellén., vol. 30, pp. 455–472.

Gautier, P., Brun, J.P., and Jolivet, L., 1993. Structure and kinematics of Upper Cenozoic extensional detachment on Naxos and Paros (Cyclades Islands, Greece): Tectonics, 12(5), 1180-1194. https://doi.org/10.1029/93TC01131.

Gautier, P., and Brun, J.P. 1994. Crustal-scale geometry and kinematics of late-orogenic extension in the central Aegean (Cyclades and Ewia Island). Tectonophysics, 238(1-4), 399-424. DOI:10.1016/0040-1951(94)90066-3.

Gerogiannis, N., and Xypolias, P. 2017. Retroward extrusion of high-pressure rocks: An example from the Hellenides (Pelion Blueschist Nappe, NW Aegean). Terra Nova, 29, 372–381. DOI:10.1111/ter.12297.

Gerogiannis, N., Xypolias, P., Chatzaras, V., Aravadinou, E., Papapavlou, K., 2019. Deformation within the Cycladic subduction-exhumation channel: new insights from the enigmatic Makrotantalo nappe (Andros, Aegean). Int. J. Earth Sci. 108, 817–843.

Gerogiannis, N., Aravadinou, E., Chatzaras, V., and Xypolias, P. 2021. Calcite pseudomorphs after aragonite: A tool to unravel the structural history of high-pressure marbles (evia island, Greece). J. Struct. Geol., 148, 104373. https://doi.org/10.1016/j.jsg.2021.104373.

Glodny, J., and Ring, U. 2022. The cycladic blueschist unit of the hellenic subduction orogen: Protracted high-pressure metamorphism, decompression and reimbrication of a diachronous nappe stack. Earth Sci. Rev., 224, 103883. https://doi.org/10.1016/j.earscirev.2021.103883.

Godfriaux, I., 1968. Etude géologique de la région de l'Olympe (Grèce) (Doctoral dissertation, Universite de Lille.).

Godfriaux, I. and Ricou, L.E. 1991. Direction et sens de transport associes au cherriage synmetamorphe sur l'Olympe. Bull. Soc. Geol. Greece 25(1), pp.207-229.

Goffe, B. and Chopin, C. 1986. High-pressure metamorphism in the Western Alps: zoneography of metapelites, chronology and consequences. Schw. Mineral. Petrograph. Mitt., 66, 41–52.

Grasemann, B., Schneider, D.A., Stockli, D.F., and Iglseder, C. 2012. Miocene bivergent crustal extension in the Aegean: Evidence from the western Cyclades (Greece). Lithosphere, 4(1), 23-39. https://doi.org/10.1130/L164.1.

Grasemann, B., Huet, B., Schneider, D.A., Rice, A.H.N., Lemonnier, N. and Tschegg, C. 2018. Miocene postorogenic extension of the Eocene synorogenic imbricated Hellenic subduction channel: New constraints from Milos (Cyclades, Greece). GSA Bulletin, 130(1-2), pp.238-262. DOI:10.1130/B31731.1.

Grasemann, B., Schneider, D.A., Soukis, K., Roche, V., Hubmann B. 2021. Paleogeographic position of the central Dodecanese Islands, southeastern Greece: The push-pull of Pelagonia. GSA Bulletin. https://doi.org/10.1130/B36095.1

Hart, N.R., Stockli, F.D., and Hayman, N.W. 2016. Provenance evolution during progressive rifting and hyperextension using bedrock and detrital zircon U-Pb geochronology, Mauléon Basin, western Pyrenees. Geosphere, 12(4), 1166-1186. https://doi.org/10.1130/GES01273.1.

Henjes-Kunst, F., and Kreuzer, H. 1982. Isotopic dating of pre-alpidic rocks from the island of Ios (Cyclades, Greece). Contr. Mineral. Petrol., 80(3), 245–253. https://doi.org/10.1007/BF00371354.

Hinsken, T., Bröcker, M., Berndt, J., and Gärtner, C. 2016. Maximum sedimentation ages and provenance of metasedimentary rocks from Tinos Island, Cycladic blueschist belt, Greece. Int. J. Earth Sci., 105(7), 1923–1940. https://doi.org/10.1007/s00531-015-1258-z.

Hippert, J., and Tohver, E. 1999. On the development of zones of reverse shearing in mylonitic rocks. J. Struct. Geol., 21, 1603-1614.

Hooft, E.E., Nomikou, P., Toomey, D.R., Lampridou, D., Getz, C., Christopoulou, M.E., O'Hara, D., Arnoux, G.M., Bodmer, M., Gray, M. and Heath, B.A. 2017. Backarc tectonism, volcanism, and mass wasting shape seafloor morphology in the Santorini-Christiana-Amorgos region of the Hellenic Volcanic Arc. Tectonophysics, 712, pp.396-414. https://doi.org/10.1016/j.tecto.2017.06.005.

Hoskin, P.W.O. and Schaltegger, U. 2003. The composition of zircon and igneous and metamorphic petrogenesis. In Reviews in Mineralogy and Geochemistry; Mineral. Soc. Am., Washington, DC, USA, Volume 53, pp. 27–55.

Huet, B., Labrousse, L., and Jolivet, L. 2009. Thrust or detachment? exhumation processes in the Aegean: Insight from a field study on Ios (Cyclades, Greece). Tectonics, 28(3), 1–27. https://doi.org/10.1029/2008TC002397.

Huet, B., Labrousse, L., Monjé, P., Malvoisin, B., & Jolivet, L. 2014. Coupled phengite 40Ar-39Ar geochronology and thermobarometry: PTt evolution of Andros Island (Cyclades, Greece). Geol. Mag., 152(4), 711–727. https://doi.org/10.1017/S0016756814000661.

Ishii, K. 1992. Partitioning of non-coaxiality in deforming layered rock masses. Tectonophysics 210, 33e43.

Jackson, S.E., Pearson, N.J., Griffin, W.L., and Belousova, E.A. 2004. The application of laser ablation - inductively coupled plasma - mass spectrometry to in situ U – Pb zircon geochronology. Chem.Geol., 211(1-2),47-69. https://doi.org/10.1016/j.chemgeo.2004.06.017.

Jacobshagen, V., Skala, W. 8s Wallrecher, E. 1976. Observations sur le developpement tectonique des Sporades du Nord. Bull. Soc. Geol. France 18, 281-6

Jacobshagen, V. 1986. Geologie von Griechenland: Berlin and Stuttgart, Begruder Borntaeger.

Jamieson, R. A., & Beaumont, C. 2013. On the origin of orogens. Geol. Soc. Am. Bull., 125 (11 12), 1671–1702. https://doi.org/10.1130/B30855.1.

Jansen, J.B.H., Schuiling, R.D. 1976. Metamorphism on Naxos: petrology and geothermal gradients. Am. J. Sci., 276 (10), 1225–1253.

Jansen, J.B.H. 1977. Metamorphism on Naxos, Greece (Doctoral dissertation) Utrecht Univ., Utrecht, Netherlands.

Jiang, D., Williams, P.F., 1998. High strain zones: a unified model. J. Struct. Geol. 20, 1105e1120.

Jolivet, L., Goffé, B., Monié, P., Truffert-Luxey, C., Patriat, M. and Bonneau, M. 1996. Miocene detachment in Crete and exhumation P-T-t paths of high-pressure metamorphic rocks. Tectonics, 15(6), pp.1129-1153.

Jolivet, L., and Faccenna, C. 2000. Mediterranean extension and the Africa-Eurasia collision. Tectonics 19:1095–1106. doi:10.1029/2000TC900018.

Jolivet, L., Faccenna, C., Goffé, B., Burov, E. and Agard, P. 2003. Subduction tectonics and exhumation of high-pressure metamorphic rocks in the Mediterranean orogens. Am. J. Sci., 303(5), pp.353-409.

Jolivet, L., Famin, V., Mehl, C., Parra, T., Aubourg, C., Hébert, R., Philippot, P., Whitney, D.L. and Teyssier, C., 2004. Strain localization during crustal-scale boudinage to form extensional metamorphic domes in the Aegean Sea. Special papers - Geol. Soc. Am., pp.185-210.

Jolivet, L., and Brun, J.P. 2010. Cenozoic geodynamic evolution of the Aegean. Int. J. Earth Sci., (Geol. Rundsch.), 99(1), 109–138. https://doi.org/10.1007/s00531-008-0366-4.

Jolivet, L., Lecomte, E., Huet, B., Denèle, Y., Lacombe, O., Labrousse, L., Le Pourhiet, L., Mehl, C. 2010. The North Cycladic detachment system. Earth Planet. Sci. Lett., 289, 87–104. https://doi.org/10.1016/j.epsl.2009.10.032.

Jolivet, L., Faccenna, C., Huet, B., Labrousse, L., Le Pourhiet, L., Lacombe, O., Lecomte, E., Burov, E., Denèle, Y., Brun, J.P. and Philippon, M., Paul, A., Salaün, G., Karabulut, H., Piromallo, C., Monié, P., Gueydan, F., Okay, A., Oberhänsli, R., Pourteau, A., Augier, R., Gadenne, L. and Driussi, O. 2013. Aegean tectonics: Strain localisation, slab tearing and trench retreat. Tectonophysics, 597, pp. 1-33. https://doi.org/10.1016/j.tecto.2012.06.011.

Jolivet, L., Menant, A., Sternai, P., Rabillard, A., Arbaret, L., Augier, R., Laurent, V., Beaudoin, A., Grasemann, B., Huet, B. and Labrousse, L. 2015. The geological signature of a slab tear below the Aegean. Tectonophysics, 659, pp.166-182.

Jolivet, L., Sautter, V., Moretti, I., Vettor, T., Papadopoulou, Z., Augier, R., Denèle, Y. and Arbaret, L. 2021. Anatomy and evolution of a migmatite-cored extensional metamorphic dome and interaction with syn-kinematic intrusions, the Mykonos-Delos-Rheneia MCC. J. Geodyn., 144, p.101824.

Katsikatsos, G. 1979. La structure tectonique de Γ Attique et de Γ ile d' Eubee, Proc. 6th Coll. Geol. Aegean Region, 1, 211 -228.

Katzir, Y., Matthews, A., Garfunkel, Z., and Schliestedt, M. 1996. The tectonometamorphic evolution of a dismembered ophiolite (Tinos, Cyclades, Greece). Geol. Mag., 133, 237–254. doi:10.1017/S0016756800008992.

Keay, S. (1998). The geological evolution of the Cyclades, Greece: constraints from SHRIMP U-Pb geochronology. PhD Thesis. Research School of Earth Science, Australian National University, Canberra, Australia DOI:10.25911/5d66671ad2b2f.

Keay, S., Lister, G., Buick, I. 2001. The timing of partial melting, Barrovian metamorphism and granite intrusion in the Naxos metamorphic core complex Cyclades, Aegean Sea, Greece. Tectonophysics, 342, 275–312. https://doi.org/10.1016/S0040-1951(01)00168-8.

Keay, S., and Lister, G. 2002. African provenance for the metasediments and meta-igneous rocks of the Cyclades, Aegean Sea, Greece. Geology, 30(3), 235–238. https://doi.org/10.1130/0091-7613(2002)030<0235:APFTMA>2.0.CO;2.

Keiter, M., Ballhaus, C., & Tomaschek, F. 2011. A new geological map of the Island of Syros (Aegean Sea, Greece): Implications for lithostratigraphy and structural history of the Cycladic Blueschist Unit. Geol. Soc. Am., Vol. 481.

Kotowski, A.J., Behr, W.M., Cisneros, M., Stockli, D.F., Soukis, K., Barnes, J. and Ortega-Arroyo, D., 2020. Subduction, underplating, and return flow recorded in the Cycladic Blueschist Unit exposed on Syros Island, Greece. Earth and Space Science Open Archive ESSOAr. https://doi.org/10.1002/essoar.10504307.1.

Kotowski, A.J., Cisneros, M., Behr, W.M., Stockli, D.F., Soukis, K., Barnes, J. and Ortega-Arroyo, D., 2022. Subduction, underplating, and return flow recorded in the Cycladic Blueschist Unit exposed on Syros Island, Greece. Tectonics, 41, e2020TC006528. https://doi.org/10.1029/2020TC006528.

Koutsovitis, P., Soukis, K., Voudouris, P., Lozios, S., Ntaflos, T., Stouraiti, C., and Koukouzas N. 2021. The Late Cretaceous magmatic arc of the south Aegean: Geodynamic implications from petrological and geochemical studies of granitoids from Anafi island (Cyclades – Greece). Int. Geol. Rev., 1-24, DOI:10.1080/00206814.2021.1884906.

Kroner, U. and Romer, R. L. 2013. Two plates – Many subduction zones: The Variscan orogeny reconsidered. Gondwana Res. 24, 298–329. http://dx.doi.org/10.1016/j.gr.2013.03.001.

Kydonakis, K., Gallagher, K., Brun, J.P., Jolivet, M., Gueydan, F., Kostopoulos, D. 2014. Upper Cretaceous exhumation of the western Rhodope Metamorphic Province (Chalkidiki Peninsula, northern Greece). Tectonics, 33 (6), 1113–1132. http://dx.doi.org/10.1002/2014TC003572.

Lagos, M., Scherer, E. E., Tomaschek, F., Münker, C., Keiter, M., Berndt, J., & Ballhaus, C. 2007. High precision Lu–Hf geochronology of Eocene eclogite-facies rocks from Syros, Cyclades, Greece. Chem. Geol., 243(1-2), 16-35.

Laskari, S., Soukis, K., Stockli, D. F., Lozios, S., and Zambetakis-Lekkas, A. 2022a. Reconstructing the southern Pelagonian domain in the Aegean Sea: Insights from U-Pb detrital zircon analysis, lithostratigraphic and structural study, and zircon (U-Th)/He thermochronology on Amorgos Island (SE Cyclades, Greece). Gondwana Res., 106, 329–350. https://doi.org/10.1016/j.gr.2022.02.007.

Laskari, S., Soukis, K., Lozios, S., Stockli, D.F., Poulaki E.M., Stouraiti, C. 2022b. Structural Study and Detrital Zircon Provenance Analysis of the Cycladic Blueschist Unit Rocks from Iraklia Island: From the Paleozoic Basement Unroofing to the Cenozoic Exhumation. Minerals, 12, 83. https://doi.org/10.3390/min12010083.

Laskou, M., and Economou, M. 1991. Platinum group elements and gold concentrations in Greek bauxites. Geol. Balc., 21(2), pp.65-77.

Laurent, V., Beaudoin, A., Jolivet, L., Arbaret, L., Augier, R., Rabillard, A., Menant, A. 2015. Interrelations between extensional shear zones and synkinematic intrusions: the example of Ikaria Island (NE Cyclades, Greece). Tectonophysics, 651-652, 152–171. http://dx.doi.org/10.1016/j.tecto.2015.03.020.

Laurent, V., Jolivet, L., Roche, V., Augier, R., Scaillet, S. and Cardello, G.L. 2016. Strain localization in a fossilized subduction channel: Insights from the Cycladic Blueschist Unit (Syros, Greece). Tectonophysics, 672, pp.150-169.

Laurent, V., Lanari, P., Naïr, I., Augier, R., Lahfid, A., & Jolivet, L. 2018. Exhumation of eclogite and blueschist (Cyclades, Greece): Pressure-temperature evolution determined by thermobarometry and garnet equilibrium modelling. J. Metamorph. Geol., 36(6), 769–798. https://doi.org/10.1111/jmg.12309.

Lekkas, S., Skourtsos, Em., Soukis, K., Kranis, H., Lozios, S.G., Alexopoulos, A. and Koutsovitis, P. 2011. Late Miocene detachment faulting and crustal extension in SE Attica (Greece). Geoph. Res. Abstr., (Vol. 13, pp. EGU-2011-EGU13016).

Le Pichon, X., Lallemant, S.J., Chamot-Rooke, N., Lemeur, D. and Pascal, G. 2002. The Mediterranean Ridge backstop and the Hellenic nappes. Marine Geol., 186(1-2), pp.111-125.

Linnemann, U., Ouzegane, K., Drareni, A., Hofmann, M., Becker, S., Gärtner, A. and Sagawe, A. 2011. Sands of West Gondwana: an archive of secular magmatism and plate interactions—a case study from the Cambro-Ordovician section of the Tassili Ouan Ahaggar (Algerian Sahara) using U–Pb–LA-ICP-MS detrital zircon ages. Lithos, 123(1-4), pp.188-203.

Lips, A.L.W., White, S.H. and Wijbrans, J.R. 1998. 40Ar/39Ar laserprobe direct dating of discrete deformational events: a continuous record of early Alpine tectonics in the Pelagonian Zone, NW Aegean area, Greece. Tectonophysics, 298(1-3), pp.133-153.

Lister G.S., Banga, G., and Feenstra, A. 1984. Metamorphic core complexes of cordilleran type in the Cyclades, Aegean Sea, Greece. Geology, 12, 221-225. https://doi.org/10.1130/0091-7613(1984)12<221:MCCOCT>2.0.CO;2.

Lister, G. S., and Forster, M. A. 2016. White mica 40Ar/39Ar age spectra and the timing of multiple episodes of high-P metamorphic mineral growth in the Cycladic eclogite–blueschist belt, Syros, Aegean Sea, Greece. J. Metamorph. Geol., 34(5), 401–421.

Löwen, K., Bröcker, M., and Berndt, J. 2015. Depositional ages of clastic metasediments from Samos and Syros, Greece: Results of a detrital zircon study. Int. J. Earth Sci., 104(1), 205–220.https://doi.org/10.1007/s00531-014-1058-x.

Malandri, C., Soukis, K., Maffione, M., Özkaptan, M., Vassilakis, E., Lozios, S., & van Hinsbergen, D. J. 2017. Vertical-axis rotations accommodated along the Mid-Cycladic

lineament on Paros Island in the extensional heart of the Aegean orocline (Greece). Lithosphere, 9(1), 78–99. https://doi.org/10.1130/L575.1.

Maluski, H., Bonneau, M., Kienast, J.R. 1987. Dating themetamorphic events in the Cycladic area: 39Ar/40Ar data from metamorphic rocks of the island of Syros (Greece). Bull. Soc. Géol. Fr, 8, 833–842. https://doi.org/10.2113/gssgfbull.III.5.833.

Marsh, J.H., and Stockli, D.F. 2015. Zircon U-Pb and trace element zoning characteristics in an anatectic granulite domain: Insights from LASS-ICP-MS depth profiling. Lithos, 239, 170–185. https://doi.org/10.1016/j.lithos.2015.10.017.

Martha, S.O., Dörr, W., Gerdes, A., Petschick, R., Schastok, J., Xypolias, P., and Zulauf, G. 2016. New structural and U–Pb zircon data from Anafi crystalline basement (Cyclades, Greece): constraints on the evolution of a Late Cretaceous magmatic arc in the Internal Hellenides. Int. J. Earth Sci. (Geol Rundsch), 105(7), 2031-2060. https://doi.org/10.1007/s00531-016-1346-8.

Martha, S. O., Dörr, W., Gerdes, A., Krahl, J., Linckens, J., and Zulauf, G. 2017. The tectonometamorphic and magmatic evolution of the Uppermost Unit in central Crete (Melambes area): constraints on a Late Cretaceous magmatic arc in the Internal Hellenides (Greece). Gondwana Res., 48, 50–71, doi:10.1016/j.gr.2017.04.004.

Martha, S., Zulauf, G., Dörr, W., Binck, J., Nowara, P., and Xypolias, P. 2018. The tectonometamorphic evolution of the Uppermost Unit south of the Dikti Mountains, Crete. Geol. Mag., 1-24, Cambridge University Press doi:10.1017/S0016756818000328.

Martin, L., Duchêne, S., Deloule, E. and Vanderhaeghe, O. 2006. The isotopic composition of zircon and garnet: A record of the metamorphic history of Naxos, Greece. Lithos, 87(3-4),pp.174-192.

Martin, L.A., Duchêne, S., Deloule, E. and Vanderhaeghe, O. 2008. Mobility of trace elements and oxygen in zircon during metamorphism: consequences for geochemical tracing. Earth Planet. Sci. Lett., 267(1-2), pp.161-174.

Mavrogonatos, C., Magganas, A., Kati, M., Bröcker, M. and Voudouris, P., 2021. Ophicalcites from the Upper Tectonic Unit on Tinos, Cyclades, Greece: mineralogical, geochemical and isotope evidence for their origin and evolution. Int. J. Earth Sci. (Geol Rundsch), 110(3), pp.809-832, https://doi.org/10.1007/s00531-021-01991-4.

Mcclusky, S., Balassanian, S., Barka, A., Demir, C., Ergintav, S., Georgiev, I., Gurkan, O., Hamburger, M., Hurst, K., Kahle, H. and Kastens, K. 2000. Global Positioning System constraints on plate kinematics and dynamics in the eastern Mediterranean and Caucasus. J. Geophy. Res.: Solid Earth, 105(B3), pp.5695-5719.

McGrath, A., Stouraiti, C., Windley, B. 2017. Geochemistry of mylonitic gneisses from the Cycladic Basement Unit (Paros and Serifos, Aegean Sea): Implications for protoliths of the high-grade gneisses. Int. J. Earth Sci., 106, 2067–2089.

Meinhold, G., Kostopoulos, D., Frei, D., Himmerkus, F., Reischmann, T. 2010. U–Pb LASF-ICP-MS zircon geochronology of the Serbo- Macedonian Massif, Greece: palaeotectonic constraints for Gondwana-derived terranes in the Eastern Mediterranean. Int. J. Earth Sci., 99, 813–832. https://doi.org/10.1007/s00531-009-0425-5.

Meinhold, G., Morton, A.C., Avigad, D. 2013. New insights into peri-Gondwana paleogeography and the Gondwana super-fan system from detrital zircon U–Pb ages. Gondwana Res., 23, 661–665. doi:10.1016/j.gr.2012.05.003.

Melidonis, N.G., 1980. The geological structure and mineral deposits of Tinos island (Cyclades, Greece). The geology of Greece, 13, pp.1-80.

Menant, A., Jolivet, L., Augier, R. and Skarpelis, N. 2013. The North Cycladic Detachment System and associated mineralization, Mykonos, Greece: Insights on the evolution of the Aegean domain. Tectonics, 32(3), pp.433-452.

Menant, A., Jolivet, L., Vrielynck, B. 2016. Kinematic reconstructions and magmatic evolution illuminating crustal and mantle dynamics of the eastern Mediterranean region since the late Cretaceous. Tectonophysics, 675, 103-140. https://doi.org/10.1016/j.tecto.2016.03.007.

Minoux, L. 1980. Stratigraphie, structure et métamorphisme de l'île d'Amorgos (Cyclades, Grèce). Ph.D. Thesis, University of Pierre et Marie Curie.

Mizera, M. and Behrmann, J.H. 2016. Strain and flow in the metamorphic core complex of Ios Island (Cyclades, Greece). Int. J. Earth Sci., 105(7), pp.2097-2110.

Mposkos, E.D. and Kostopoulos, D.K. 2001. Diamond, former coesite and supersilicic garnet in metasedimentary rocks from the Greek Rhodope: a new ultrahigh-pressure metamorphic province established. Earth Planet. Sci. Lett., 192(4), pp.497-506.

Papadopoulos, G., and Pavlides, B.S. 1992. The large 1956 earthquake in the South Aegean: Macroseismic field configuration, faulting, and neotectonics of Amorgos Island. Earth Planet. Sci. Lett., 113(3), 383-396. https://doi.org/10.1016/0012-821X(92)90140-Q.

Papanikolaou, D.J. 1977. On the structural geology and tectonics of Paros Island (Aegean Sea). Ann. Geol. Pays Hellén., 28, 450–464.

Papanikolaou, D.J. 1978. Contribution to the geology of Aegean Sea. The Island of Andros. Ann. Géol. Pays Hellén., 29, 477–553.

Papanikolaou, D.J. 1979. Unités tectoniques et phases de déformations dans l'ile de Samos, Mer Egée, Grèce. Bull. Soc. Géol. Fr., 7(6), pp.745-762.

Papanikolaou D. 1980. Contribution to the geology of Aegean Sea. The island of Paros, Ann. Géol. Pays Hellén., 30(1), 65-96.

Papanikolaou, D. 1987. Tectonic evolution of the Cycladic blueschist belt (Aegean Sea, Greece). In: Helgeson H.C. (ed.) Chemical transport in metasomatic processes. D. Reidel Publ. Com., Dordrecht, 429–450.

Papanikolaou, D., Bargathi, H., Dabovski, C., Dimitriu, R., El-Hawat, A., Ioane, D., Kranis, H., Obeidi, A., Oaie, G., Seghedi, A., Zagorchev, I. 2004. Transect VII. The Transmed Atlas, Cavazza, et al. (Eds.), Springer.

Papanikolaou, D.J. and Royden, L.H. 2007. Disruption of the Hellenic arc: Late Miocene extensional detachment faults and steep Pliocene-Quaternary normal faults—Or what happened at Corinth?. Tectonics, 26(5).

Papanikolaou, D. 2009. Timing of tectonic emplacement of the ophiolites and terrane paleogeography in the Hellenides. Lithos, 108(1–4), 262–280. https://doi.org/10.1016/j.lithos.2008.08.003.

Papanikolaou, D. 2013. Tectonostratigraphic models of the Alpine terranes and subduction history of the Hellenides. Tectonophysics, 595–596, 1–24. http://dx.doi.org/10.1016/j.tecto.2012.08.008.

Papanikolaou, D.I. 2021. The Geology of Greece. 345pp, Springer Nature. https://doi.org/10.1007/978-3-030-60731-9.

Passchier, C.W. 1998. Monoclinic model shear zones. J. Struct. Geol. 20, 1121e1137.

Passchier, C.W., Trouw, R.A.J. 2005. Microtectonics, second ed. Springer, Berlin.

Passchier, C.W., and Coelho, S. 2006. An outline of shear-sense analysis in high-grade rocks. Gondwana Res., 10(1-2), pp.66-76.

Paton, C., Woodhead, J.D., Hellstrom, J.C., Hergt, J. M., Greig, A., and Maas, R. 2010. Improved laser ablation U-Pb zircon geochronology through robust downhole fractionation correction. Geochem., Geophys., Geosyst., 11(3) Q0AA06, doi:10.1029/2009GC002618.

Patzak, M., Okrusch, M., Kreuzer, H. 1994. The Akrotiri unit on the island of Tinos, Cyclades, Greece: Witness to a lost terrane of Late Cretaceous age. Neues Jb. Geol. Paläontol. Abh., 194(2), pp.211–252.

Peillod, A., Ring, U., Glodny, J., Skelton, A. 2017. An Eocene/Oligocene blueschist−/greenschist-facies P-T loop from the Cycladic Blueschist unit on Naxos island, Greece: deformation-related reequilibration vs thermal relaxation. J. Metamorph. Geol., 35, 805–830. https://doi.org/10.1111/jmg.12256.

Pe-Piper, G., and Piper, D.J.W. 2002. The igneous rocks of Greece. The anatomy of an orogen. Geol. Mag., 140(3), pp.357–357.

Petrus, J.A., and Kamber, B.S. 2012. VizualAge: A novel approach to laser ablation ICP-MS U-Pb geochronology data reduction. Geostand. Geoanal. Res., 36(3), 247-270. https://doi.org/10.1111/j.1751-908X.2012.00158.x.

Philippon, M., Brun, J.P. and Gueydan, F. 2012. Deciphering subduction from exhumation in the segmented Cycladic Blueschist unit (Central Aegean, Greece). Tectonophysics, 524, pp.116-134.

Philippon, M., Brun, J.P., Gueydan, F. and Sokoutis, D. 2014. The interaction between Aegean back-arc extension and Anatolia escape since Middle Miocene. Tectonophysics, 631, pp.176-188.

Photiades A., and Skourtsis-Coroneou V. 1994. Stratigraphic and paleogeographic evolution of the Northern Argolis (Greece) during the Cretaceous-Paleogene. Bull. Geol. Soc. Greece, 30(2), pp. 135-146.

Photiades, A., and Keay, S. 2003. Geological and geochronological data for Sikinos and Folegandros metamorphic units (Cyclades, Greece): their tectono-stratigraphic significance. Bull. Geol. Soc. Greece, 35, pp.35-45.

Poulaki, E.M., Stockli, D.F., Flansburg, M.E., and Soukis, K. 2019. Zircon U-Pb chronostratigraphy and provenance of the Cycladic Blueschist Unit and Cycladic Basement on Sikinos and Ios Islands, Greece. Tectonics. https://doi.org/10.1029/2018TC005436.

Poulaki, E.M., Stockli, D.F., Flansburg, M.E., Gevedon, M.L., Stockli, L.D., Barnes, J.D., Soukis, K., Kitajima, K. and Valley, J.W. 2021. Zircon U-Pb and geochemical signatures in high-pressure, low-temperature metamorphic rocks as recorders of subduction zone processes, Sikinos and Ios islands, Greece. Chem. Geol., 582, p.120447. https://doi.org/10.1016/j.chemgeo.2021.120447.

Pourteau, A., Bousquet, R., Vidal, O., Plunder, A., Duesterhoeft, E., Candan, O., Oberhansli, R. 2014. Multistage growth of Fe–Mg–carpholite and Fe–Mg–chloritoid, from field evidence to thermodynamic modelling. Contrib. Mineral. Petrol. 168:1090. DOI: 10.1007/s00410-014-1090-7.

Putlitz, B., Cosca, M.A. and Schumacher, J.C. 2005. Prograde mica 40Ar/39Ar growth ages recorded in high pressure rocks (Syros, Cyclades, Greece). Chem. Geol., 214(1-2), pp.79-98.

Reinecke, T., Altherr, R., Hartung, B., Hatzipanagiotou, K., Kreuzer, H., Harre, W., Klein, H., Keller, J., Geenen, E., Böger, H. 1982. Remnants of a late Cretaceous high temperature belt on the island of Anafi (Cyclades, Greece). Neues Jb. Mineral. Abh., 145, 157–182.

Reiners, P.W., Spell, T.L., Nicolescu, S., and Zanetti, K.A. 2004. Zircon (U-Th)/He thermochronometry: He diffusion and comparisons with 40Ar/39Ar dating. Geochim. Cosmoch. Acta, **68**(8), 1857-1887.

Reiners, P.W. 2005. Zircon (U-Th)/He thermochronometry. in: Reiners, P.W., Ehlers, T.A. (Eds.), Low-Temperature Thermochronology: Techniques, Interpretations, and Applications. Rev. Mineral. Geochem., 58, 151-179. https://doi.org/10.2138/rmg.2005.58.6.

Reischmann, T. 1998. Pre alpine origin of tectonic units from the metamorphic complex of Naxos, Greece, identified by single zircon Pb/Pb dating. Bull. Geol. Soc. Greece, 32(3), pp.101–111.

Reischmann, T., Kostopoulos, D.K., Loos, S., Anders, B., Avgerinas, A. and Sklavounos, S.A., 2001. Late Palaeozoic magmatism in the basement rocks southwest of Mt. Olympos, Central Pelagonian Zone, Greece: remnants of a Permo-Carboniferous magmatic arc. Bull. Geol. Soc. Greece, 34(3), pp.985-993.

Richter, D., Müller, C., and Risch H. 1996. Die Flysch-Zonen Griechenlands XI. Neue Daten zur Stratigraphie und Paläogeographie des Flysches und seiner Unterlagen in der Pelagonischen Zone (Griechenland). Neu. Jb. Geol. Paläontol. Abh., 201, 3, 327.366.

Ricou, L.E., Burg, J.P., Godfriaux, I. and Ivanov, Z. 1998. Rhodope and Vardar: the metamorphic and the olistostromic paired belts related to the Cretaceous subduction under Europe. Geodin. Acta, 11(6), pp.285-309.

Rimmelé, G., Oberhänsli, R., Goffé, B., Jolivet, L., Candan, O., Çetinkaplan, M. 2003. First evidence of high-pressure metamorphism in the ‘‘Cover Series’’ of the southern Menderes Massif. Tectonic and metamorphic implications for the evolution of SW Turkey. Lithos, 71 (2003) 19– 46. doi:10.1016/S0024-4937(03)00089-6.

Ring, U., Laws, S., Bernet, M. 1999. Structural analysis of a complex nappe sequence and late-orogenic basins from the Aegean Island of Samos, Greece. J. Struct. Geol., 21, 1575–1601. https://doi.org/10.1016/S0191-8141(99)00108-X.

Ring, U., Layer, P.W., Reischmann, T. 2001. Miocene high-pressure metamorphism in the Cyclades and Crete, Aegean Sea, Greece: evidence for large-magnitude displacement on the Cretan detachment. Geology, 29(5), pp.395– 398. https://doi.org/10.1130/0091-7613(2001)029<0395:MHPMIT>2.0.CO;2.

Ring, U., and Layer, P.W. 2003. High-pressure metamorphism in the Aegean, eastern Mediterranean: underplating and exhumation from the Late Cretaceous until the Miocene to Recent above the retreating Hellenic subduction zone. Tectonics, 22 (3). https://doi.org/10.1029/2001TC001350.

Ring, U., Thompson, S. & Brocker, M. 2003. Fast extension but little exhumation: The Vari detachment in the Cyclades, Greece. Geol. Mag., 140 (3), 245–252.

Ring, U., Thomson, S., Rosenbaum, G. 2009. Timing of the Amorgos detachment system and implications for detachment faulting in the southern Aegean Sea, Greece. In: Extending a Continent: Architecture, Rheology and Heat Budget, Ring, U., Wernicke, B. (eds). Geol. Soc. London, Spec. Publ., 321, 169–178. https://doi.org/10.1144/SP321.8.

Ring, U., Glodny, J., Will, T., and Thomson, S. 2010. The Hellenic Subduction System: High-Pressure Metamorphism, Exhumation, Normal Faulting, and Large-Scale Extension. Ann. Rev. Earth Planet. Sci., 38(1), 45–76. https://doi.org/10.1146/annurev.earth.050708.170910.

Ring, U., Glodny, J., Will, T.M., Thomson, S. 2011. Normal faulting on Sifnos and the south Cycladic detachment system, Aegean Sea, Greece. J. Geol. Soc., 168, 751–768. https://doi.org/10.1144/0016-76492010-064.

Ring, U., Glodny, J., Pelliod A., Skelton A. 2018. The timing of high-temperature conditions and ductile shearing in the footwall of the Naxos extensional fault system, Aegean Sea, Greece. Tectonophysics, 700, 108-130. https://doi.org/10.1016/j.tecto.2018.09.001.

Ring, U., Pantazides, H., Glodny, J. and Skelton, A., 2020. Forced return flow deep in the subduction channel, Syros, Greece. Tectonics, 39(1), p.e2019TC005768, https://doi.org/10.1029/2019TC005768.

Robertson, A.H.F., Clift, P.D., Degnan, P.J., Jones, G. 1991. Palaeogeographic and palaeotectonic evolution of the Eastern Mediterranean Neotethys. Palaeogeogr. Palaeoclim. Palaeoecol., 87, 289–343. https://doi.org/10.1016/0031-0182(91)90140-M.

Robertson, A.H.F., Dixon, J.E., Brown, S., Collins, A., Morris, A., Pickett, E.A., Sharp, I., Ustaömer, T. 1996. Alternative tectonic models for the Late Palaeozoic–Early Tertiary development of Tethys in the Eastern Mediterranean region. In: Morris, A., Tarling, D.H. (eds) Palaeomagnetism and tectonics of the Mediterranean region. Geol. Soc. London, Spec. Publ., 105, 239–263. https://doi.org/10.1144/GSL.SP.1996.105.01.22.

Robertson, A.H. 2002. Overview of the genesis and emplacement of Mesozoic ophiolites in the Eastern Mediterranean Tethyan region. Lithos, 65(1-2), pp.1-67.

Robertson, A.H.F. 2004, Development of concepts concerning the genesis and emplacement of Tethyan ophiolites in the East Mediterranean and Oman regions: Earth Sci. Rev., v. 66, p. 331–387.

Robertson, A.H.F. 2006. Sedimentary evidence from the south Mediterranean region (Sicily, Crete, Peloponnese, Evia) used to test alternative models for the regional tectonic setting of Tethys during Late Palaeozoic–Early Mesozoic time. In: Robertson, A.H.F., Mountrakis, D. (eds) Tectonic development of the eastern Mediterranean region. Geol. Soc. London, Spec. Publ., 260, 91–154. https://doi.org/10.1144/GSL.SP.2006.260.01.06.

Robertson, A.H.F. 2012. Late Palaeozoic–Cenozoic tectonic development of Greece and Albania in the context of alternative reconstructions of Tethys in the Eastern Mediterranean region. Int. Geol. Rev., 54(4), 373–454. https://doi.org/10.1080/00206814.2010.543791.

Roche, V., Jolivet, L., Papanikolaou, D., Bozkurt, E., Menant, A. and Rimmele, G., 2019. Slab fragmentation beneath the Aegean/Anatolia transition zone: Insights from the tectonic and metamorphic evolution of the Eastern Aegean region. Tectonophysics, 754, pp. 101-129. https://doi.org/10.1016/j.tecto.2019.01.016.

Rosenbaum, G., Ring, U., Kühn, A. 2007. Tectonometamorphic evolution of high-pressure rocks from the island of Amorgos (Central Aegean, Greece). J. Geol. Soc. London, 164, 425–438. https://doi.org/10.1144/0016-76492006-005.

Royden, L. H. 1993. Evolution of retreating subduction boundaries formed during continental collision, Tectonics, 12(3), 629–638, doi:10.1029/92TC02641.

Royden, L. H., and Burchfiel, B. C. 1989. Are systematic variations in thrust belt style related to plate boundary processes? (the western Alps versus the Carpathians). Tectonics 8, 51-62.

Royden, L.H. and Papanikolaou, D.J., 2011. Slab segmentation and late Cenozoic disruption of the Hellenic arc. Geochem., Geophy., Geosyst., 12(3).

Rubatto, D. 2002. Zircon trace element geochemistry: Partitioning with garnet and link between U-Pb ages and metamorphism. Chem. Geol., 184, 123–138.

Sánchez-Gómez, M., Avigad, D., and Heimann, A. 2002. Geochronology of clasts in allochthonous Miocene sedimentary sequences on Mykonos and Paros Islands: implications for back-arc extension in the Aegean Sea. J. Geol. Soc., 159, 45-60. https://doi.org/10.1144/0016-764901031.

Schenker, F.L., Burg, J.P., Kostopoulos, D., Moulas, E., Larionov, A. and von Quadt, A. 2014. From Mesoproterozoic magmatism to collisional Cretaceous anatexis: Tectonomagmatic history of the Pelagonian Zone, Greece. Tectonics, 33(8), pp.1552-1576.

Schenker, F.L., Fellin, M.G. and Burg, J.P. 2015. Polyphase evolution of Pelagonia (northern Greece) revealed by geological and fission-track data. Solid Earth, 6(1), pp.285-302.

Schermer, E.R. 1990. Mechanisms of blueschist creation and preservation in an A-type subduction zone, Mount Olympos region, Greece. Geology, 18(11), pp.1130-1133.

Schermer, E.R. 1993. Geometry and kinematics of continental basement deformation during the Alpine orogeny, Mt. Olympos region, Greece. J. Struct. Geol., 15(3-5), pp.571-591.

Scherreiks, R., Bosence, D., BouDagher-Fadel, M., Melendez, G., Baumgartner, P.O. 2010. Evolution of the Pelagonian carbonate platform complex and the adjacent oceanic realm in response to plate tectonic forcing (Late Triassic and Jurassic), Evvoia, Greece. Int. J. Earth Sci., 99, 1317–1334. https://doi.org/10.1007/s00531-009-0461-1.

Schneider, D.A., Grasemann, B., Lion, A., Soukis, K., Draganits, E. 2018. Geodynamic significance of the Santorini Detachment System (Cyclades, Greece). Terra Nova 30, 414–422, DOI:410.1111/ter.12357.

Seidel, E., Kreuzer, H., and Harre, W. 1982. A Late Oligocene/ Early Miocene high pressure belt in the External Hellenides. Geol. Jahrb., 23, 165-206.

Seman, S., Stockli, D.F., and Soukis, K. 2017. The provenance and internal structure of the Cycladic Blueschist Unit revealed by detrital zircon geochronology, Western Cyclades, Greece. Tectonics, 36, 1407–1429 https://doi.org/10.1002/2016TC004378.

Seybold, L., Dörr, W., Trepmann, C.A., and Krahl, J. 2020. New constraints from U–Pb dating of detrital zircons on the palaeogeographic origin of metasediments in the Talea Ori, central Crete. Geol. Mag., 157, 1383–1408. DOI:10.1017/S0016756819001365.

Shaked, Y., Avigad, D. and Garfunkel, Z. 2000. Alpine high-pressure metamorphism at the Almyropotamos Window (southern Evia, Greece). Geol. Mag., 137(4):367-380. DOI:10.1017/S001675680000426X.

Sharman, G.R., Sharman, J.P. and Sylvester, Z., 2018. DetritalPy: A Python-based toolset for visualizing and analysing detrital geo-thermochronologic data. The Depositional Record, *4*(2), pp.202-215. https://doi.org/10.1002/dep2.45.

Singleton, J.S., Stockli, D.F., Gans, P.B. and Prior, M.G. 2014. Timing, rate, and magnitude of slip on the Buckskin-Rawhide detachment fault, west central Arizona. Tectonics, 33(8), pp.1596-1615. https://doi.org/10.1002/2013TC003517.

Sláma, J., Košler, J., Condon, D.J., Crowley, J.L., Gerdes, A., Hanchar, J.M. and Schaltegger, U. 2008. Plešovice zircon—a new natural reference material for U–Pb and Hf isotopic microanalysis. Chem. Geol., 249 (1-2), 1-35. https://doi.org/10.1016/j.chemgeo.2007.11.005.

Soukis, K. and Papanikolaou, D., 2004. Contrasting geometry between Alpine and late- to post-Alpine tectonic structures in Anafi Island (Cyclades). Bull. Geol. Soc. Greece, 36(4), 1688–1696. https://doi.org/10.12681/bgsg.16575.

Soukis, K. and Stockli, D.F. 2013. Structural and thermochronometric evidence for multi-stage exhumation of southern Syros, Cycladic islands, Greece. Tectonophysics, 595, 148-164. https://doi.org/10.1016/j.tecto.2012.05.017.

Stampfli, G.M. and Borel, G.D. 2002. A plate tectonic model for the Paleozoic and Mesozoic constrained by dynamic plate boundaries and restored synthetic oceanic isochrons. Earth Planet. Sci. Lett., 196(1–2), 17–33. https://doi.org/10.1016/S0012-821X(01)00588-X.

Stampfli, G.M., Vavassis, I, De Bono, A., Rosselet, F., Matti, B., and Bellini, M. 2003. Remnants of the Paleotethys oceanic suture-zone in the western Tethyan area. Stratigraphic and structural evolution on the Late Carboniferous to Triassic continental and marine successions in Tuscany (Italy): regional reports and general correlation. Boll. Soc. Geol. Ital., vol.2, pp. 1-24.

Stampfli, G.M. and Borel, G.D. 2004. The TRANSMED transects in space and time: constraints on the paleotectonic evolution of the Mediterranean domain. In The TRANSMED Atlas. The Mediterranean region from crust to mantle (pp. 53-80). Springer, Berlin, Heidelberg.

Stampfli, G.M., Hochard, C., Vérard, C., Wilhelm, C., von Raumer, J. 2013. The formation of Pangea. Tectonophysics, 593, 1–19. https://doi.org/10.1016/j.tecto.2013.02.037.

Stephan, T., Kroner, U.W.E. and Romer, R.L. 2019. The pre-orogenic detrital zircon record of the Peri-Gondwanan crust. Geol. Mag., 156(2), pp.281-307. doi:10.1017/S0016756818000031.

Stockli, D.F. 2005. Application of low-temperature thermochronometry to extensional tectonic settings, in: Reiners, P.W., Ehlers, T.A. (Eds.), Low-Temperature Thermochronology: Techniques, Interpretations, and Applications. Rev. Mineral. Geochem., 58, 441–448. https://doi.org/10.2138/rmg.2005.58.16.

Stouraiti, C., Mitropoulos, P., Tarney, J., Barreiro, B., McGrath, A.M., Baltatzis, E. 2010. Geochemistry and petrogenesis of late Miocenegranitoids, Cyclades, southern Aegean: Nature of source components. Lithos, 114, 337–352.

Stouraiti, C., Pantziris, I., Vasilatos, C., Kanellopoulos, C., Mitropoulos, P., Pomonis, P., Chiaradia, M. 2017. Ophiolitic remnants from the upper and intermediate structural unit of the Attic-Cycladic Crystalline Belt (Aegean, Greece): Fingerprinting geochemical affinities of magmatic precursors. Geosciences, 7, 14.

Stouraiti, C.; Baziotis, I.; Asimow, P.D.; Downes, H. 2018. Geochemistry of the Serifos calc-alkaline granodiorite pluton, Greece: Constraining the crust and mantle contributions to I-type granitoids. Int. J. Earth Sci., 107, 1657–1688.

Tataris, A., Kallergis, G., Kounis, G., Bizon, G. and Christodoulou, G., 1970. Nafplion sheet in scale 1: 50,000, Geological map of Greece. Inst. Geol. Subsurf. Res., Athens, Greece.

Theodoropoulos, D. 1979. Samos island. Geological map of Greece, scale 1/50000. Inst. Geol. Subsurf. Res., Athens, Greece.

Theye, T., Seidel, E. & Vidal, O. 1992. Carpholite, sudoite, and chloritoid in low-grade high-pressure metapelites from Crete and the Peloponnese, Greece. European J. Mineral., 4, 487–507.

Theye, T., Chopin, C., Grevel, K.D., Ockenga, E. 1997. The assemblage diaspore+quartz in metamorphic rocks: a petrological, experimental and thermodynamic study. J. Metamorph. Geol., 15, 17–28. https://doi.org/10.1111/j.1525-1314.1997.1501050.x.

Thigpen, J. R., Law, R.D., Merschat, A.J., and Stowell, H.H. 2017. Linkages and feedbacks in orogenic systems: An introduction, *in* Law, R.D., Thigpen, J.R., Merschat, A.J., and Stowell, H.H., eds., Linkages and Feedbacks in Orogenic Systems: Geol. Soc. Am. Mem. 213, p. v–xiii. doi:10.1130/2017.1213(00).

Thomson, S.N., Stockhert, B., and Brix, M.R. 1998. Thermochronology of the high-pressure metamorphic rocks of Crete, Greece: implications for the speed of tectonic processes. Geology 26(3), 259–62, doi:10.1130/0091-7613(1998)026<0259:TOTHPM>2.3.CO;2.

Thomson, S.N., Ring, U., Brichau, S., Glodny, J. and Will, T.M., 2009. Timing and nature of formation of the Ios metamorphic core complex, southern Cyclades, Greece. Geol. Soc. London, Spec. Publ., 321(1), pp.139-167. https://doi.org/10.1144/SP321.7.

Tomaschek, F., Kennedy, A., Keay, S., Ballhaus, C. 2001. Geochronological constraints on Carboniferous and Triassic magmatism in the Cyclades: SHRIMP U–Pb ages of zircons from Syros, Greece. J. Confer. Abstr., vol.6, No.1, p. 315.

Tomaschek, F., Kennedy, A.K., Villa, I.M., Lagos, M., Ballhaus, C. 2003. Zircons from Syros, Cyclades, Greece - recrystallization and mobilization of zircon during high pressure metamorphism. J. Petrol., 44, 1977–2002.

Tsampouraki-Kraounaki, K., Sakellariou, D., Rousakis, G., Morfis, I., Panagiotopoulos, I., Livanos, I., Manta, K., Paraschos, F. and Papatheodorou, G. 2021. The Santorini-Amorgos Shear Zone: Evidence for Dextral Transtension in the South Aegean Back-Arc Region, Greece. Geosciences, 11(5), p.216. https://doi.org/10.3390/geosciences11050216.

Underhill, J.R. 1989. Late Cenozoic deformation of the Hellenide foreland, western Greece. Geol. Soc. Am. Bull., 101(5), pp.613-634.

Uunk, B., Brouwer, F., de Paz-Alvarez, M., van Zuilen, K., Huybens, R., van't Veer, R., and Wijbrans, J. 2022. Consistent detachment of supracrustal rocks from a fixed subduction depth in the cyclades. Earth Planet. Sci. Lett., 584, 117479. https://doi.org/10.1016/j.epsl.2022.117479.

Urai, J.L., Schuiling, R.D., and Jansen, J.B.H. 1990. Alpine deformation on Naxos (Greece). Geol. Soc. London, Spec. Publ., 54(1), 509–522. https://doi.org/10.1144/GSL.SP.1990.054.01.47.

Van der Maar, P. A. 1981. Metamorphism on Ios and the geological history of the southern Cyclades, Greece (Doctoral dissertation, Utrecht University).

Van der Maar, P. A., & Jansen, J. B. H. 1983. The geology of the polymetamorphic complex of Ios, Cyclades, Greece and its significance for the Cycladic Massif. Int. J. Earth Sci., 72(1), 283–299. https://doi.org/10.1007/BF01765910.

Van Hinsbergen, D.J.J., Hafkenscheid, E., Spakman, W., Meulenkamp, J.E., Wortel, R. 2005. Nappe stacking resulting from subduction of oceanic and continental lithosphere below Greece. Geology, 33 (4), 325-328. https://doi.org/10.1130/G20878.1.

Van Hinsbergen, D.J.J., Zachariasse, W.J., Wortel, M.J.R. and Meulenkamp, J.E. 2005b. Underthrusting and exhumation: A comparison between the External Hellenides and the "hot" Cycladic and "cold" South Aegean core complexes (Greece). Tectonics, 24(2).

Van Hinsbergen, D.J. and Schmid, S.M. 2012. Map view restoration of Aegean–West Anatolian accretion and extension since the Eocene. Tectonics, 31(5).

Van Hinsbergen, D.J., Torsvik, T.H., Schmid, S.M., Maţenco, L.C., Maffione, M., Vissers, R.L., Gürer, D. and Spakman, W. 2020. Orogenic architecture of the Mediterranean region

and kinematic reconstruction of its tectonic evolution since the Triassic. Gondwana Res., 81, pp.79-229.

Von Quadt, A., Moritz, R., Peytcheva, I. and Heinrich, C.A., 2005. 3: Geochronology and geodynamics of Late Cretaceous magmatism and Cu–Au mineralization in the Panagyurishte region of the Apuseni–Banat–Timok–Srednogorie belt, Bulgaria. Ore Geol. Rev., 27(1-4), pp.95-126.

Vandenberg, L. C., and Lister, G. S. 1996. Structural analysis of basement tectonites from the Aegean metamorphic core complex of Ios, Cyclades, Greece. J. Struct. Geol., 18(12), 1437–1454. https://doi.org/10.1016/S0191-8141(96)00068-5.

Vavassis, I., De Bono, A., Stampfli, G.M., Giorgis, D., Valloton, A., Amelin, Y. 2000. U–Pb and Ar–Ar geochronological data from Pelagonian basement in Evia (Greece): geodynamic implications for the evolution of the Paleotethys. Schw. Mineral. Petrograph. Mitteil., 80, 21–43.

Vermeesch, P. 2018. IsoplotR: a free and open toolbox for geochronology. Geosci. Front., v.9, p.1479-1493. doi:10.1016/j.gsf.2018.04.001.

Walcott, C.R. and White, S.H. 1998. Constraints on the kinematics of post-orogenic extension imposed by stretching lineations in the Aegean region. Tectonophysics, 298(1-3), pp.155-175.

Wijbrans, J.R., and McDougall, I. 1988. Metamorphic evolution of the Attic Cycladic Metamorphic belt on Naxos (Cyclades, Greece) utilizing 40Ar/39Ar age spectrum measurements. J. Metamorph. Geol., 6 (1988) 57 I-594. https://doi.org/10.1111/j.1525-1314.1988.tb00441.x.

Willett, S., Beaumont, C. and Fullsack, P. 1993. Mechanical model for the tectonics of doubly vergent compressional orogens. Geology, 21(4), pp.371-374. doi:10.1130/0091-7613(1993)021<0371:MMFTTO>2.3.CO;2.

Wolfe, M. R., and Stockli, D. F. 2010. Zircon (U–Th)/He thermochronometry in the KTB drill hole, Germany, and its implications for bulk He diffusion kinetics in zircon. Earth Planet, Sci. Lett., *295*(1-2), 69-82. https://doi.org/10.1016/j.crte.2016.01.001.

Xypolias, P., Kokkalas, S., & Skourlis, K. 2003. Upward extrusion and subsequent transpression as a possible mechanism for the exhumation of HP/LT rocks in Evia Island (Aegean Sea, Greece). J. Geodyn., 35(3), 303-332.

Xypolias, P., Dörr, W., Zulauf, G. 2006. Late Carboniferous plutonism within the pre-Alpine basement of the External Hellenides (Kithira, Greece): evidence from U–Pb zircon dating. J. Geol. Soc. London, 163, 539–547. https://doi.org/10.1144/0016-764904-114.

Xypolias, P., Chatzaras, V. and Koukouvelas, I.K., 2007. Strain gradients in zones of ductile thrusting: insights from the External Hellenides. J. Struct. Geol., 29(9), pp.1522-1537.

Xypolias, P. 2010. Vorticity analysis in shear zones: a review of methods and applications. J. Struct. Geol. 32, 2072–2092.

Xypolias, P., Iliopoulos, I., Chatzaras, V., and Kokkalas, S. 2012. Subduction- and exhumation-related structures in the Cycladic Blueschists: Insights from south Evia Island (Aegean region, Greece). Tectonics, 31, TC2001. https://doi.org/10.1029/2011TC002946.

Žák J., Svojtkab M., Hajnaa J., and Ackermanb, L. 2020. Detrital zircon geochronology and processes in accretionary wedges. Earth Sci. Rev., 207 (2020) 103214 https://doi.org/10.1016/j.earscirev.2020.103214.

Zanchetta, S., Garzanti, E., Doglioni, C., & Zanchi, A. 2012. The Alps in the Cretaceous: a doubly vergent pre-collisional orogen. Terra Nova, 24, 351–356.

Zanchetta, S., Malusa, G. M., and Zanchi, A. 2015. Precollisional development and Cenozoic evolution of the Southalpine retrobelt (European Alps). Lithosphere, 7(6), 662-681. doi:10.1130/L466.1.

Zeffren, S., Avigad, D., Heimann, A. and Gvirtzman, Z. 2005. Age resetting of hanging wall rocks above a low-angle detachment fault: Tinos Island (Aegean Sea). Tectonophysics, 400(1-4), pp.1-25.

Zlatkin, O., Avigad, D., and Gerdes, A. 2018. New Detrital Zircon Geochronology from the Cycladic Basement (Greece): Implications for the Paleozoic Accretion of Peri-Gondwanan Terranes to Laurussia. Tectonics, 37(12), 4679–4699. https://doi.org/10.1029/2018TC005046.

Zulauf, G., Romano, S.S., Dörr, W., and Fiala, J. 2007. Crete and the Minoan Terranes: age constraints from U–Pb dating of detrital zircons. In: Linnemann, U., Nance, R.D., Kraft, P, Zulauf G (eds) The evolution of the Rheic Ocean: from Avalonian to Cadomian active margin to Alleghenian-Variscan collission. Geol. Soc. Am. Spec. Pap., 423, p.401. https://doi.org/10.1130/2007.2423(19).

Zulauf, G., Klein, T., Kowalczyk, G., Krahl, J., and Romano, S.S. 2008. The Mirsini Syncline of eastern Crete, Greece: a key area for understanding pre-Alpine and Alpine orogeny in the eastern Mediterranean. Z. Dtsch Ges. Geowiss., 159, 3, 399-414. DOI: 10.1127/1860-1804/2008/0159-0399.

Zulauf, G., Dörr, W., Fisher-Spurlock, S.C., Gerdes, A., Chatzaras, V., and Xypolias, P. 2015. Closure of the Paleo-Tethys in the External Hellenides: Constraints from U-Pb ages of magmatic and detrital zircons (Crete). Gondwana Res., 28(2), 642–667. http://dx.doi.org/10.1016/j.gr.2014.06.011.

Zulauf, G., Dörr, W., Marko L., and Krahl J. 2018. The late Eo-Cimmerian evolution of the external Hellenides: constraints from microfabrics and U–Pb detrital zircon ages of Upper Triassic (meta)sediments (Crete, Greece). Int. J. Earth Sci., 107(7), 2859-2894. doi:10.1007/s00531-018-1632-8.